

SPECTROSCOPY-BASED QUANTIFICATION OF CHROMOPHORES AND
SCATTERING IN NEAR INFRARED TOMOGRAPHY

A Thesis
Submitted to the Faculty
in partial fulfillment of the requirements for the
degree of

Doctor of Philosophy

by

Subhadra Srinivasan

Thayer School of Engineering
Dartmouth College
Hanover, New Hampshire

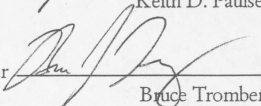
May 2005

Examining Committee:

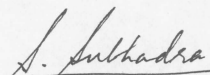
Chairman 
Brian W. Pogue, Ph.D.

Member 
Hamid Dehghani, Ph.D.

Member 
Keith D. Paulsen, Ph.D.

Member 
Bruce Tromberg, Ph.D.

Charles K. Barlowe, Ph.D.
Dean of Graduate Studies


(Signature of Author)

SPECTROSCOPY-BASED QUANTIFICATION OF CHROMOPHORES AND
SCATTERING IN NEAR INFRARED TOMOGRAPHY

A Thesis
Submitted to the Faculty
in partial fulfillment of the requirements for the
degree of

Doctor of Philosophy

by

Subhadra Srinivasan

Thayer School of Engineering
Dartmouth College
Hanover, New Hampshire

May 2005

Examining Committee:

Chairman _____
Brian W. Pogue, Ph.D.

Member _____
Hamid Dehghani, Ph.D.

Member _____
Keith D. Paulsen, Ph.D.

Member _____
Bruce Tromberg, Ph.D.

Charles K. Barlowe, Ph.D.
Dean of Graduate Studies

(Signature of Author)

Thayer School of Engineering
Dartmouth College

“Spectroscopy-based Quantification of Chromophores and
Scattering in Near Infrared Tomography”

Subhadra Srinivasan

Doctor of Philosophy

Committee

Brian W. Pogue
Hamid Dehghani
Keith D. Paulsen
Bruce Tromberg

ABSTRACT

Near infrared (NIR) imaging offers unique functional information relating to metabolic status of tissue, and this makes it a potentially useful imaging modality for diagnosis of breast cancer. The image reconstruction process traditionally involved obtaining amplitude and phase measurements of light reflectance along the periphery of the breast, used with a finite-element model of the diffusion equation to obtain maps of tissue absorption and reduced scattering coefficients. These were spectrally de-convolved to obtain images of total hemoglobin, oxygen saturation, water and scatter. In this thesis, different priors were investigated to improve the ill-posed image reconstruction problem. Spatial priors were investigated through a multi-stage recovery procedure, where the spatial location of abnormalities was obtained through a varying regularization scheme. In an alternate approach, use of spectral *a-priori* information was embedded into the reconstruction, through the absorption and scattering behavior of chromophores and scatterers, as a functional of wavelength. The latter approach enhanced the quantification of the spectroscopy-based

parameters significantly (which were obtained directly by coupling multi-wavelength measurements) as well as improved the images qualitatively by reducing the high-frequency spatial noise. The spectral approach, validated in simulations and experimental data, was then applied to study clinical data from female volunteers with mammographically-detected abnormalities; and results indicated that contrast mechanisms related to angiogenesis, hypoxia, cell proliferation and cellular microenvironment, were obtainable through tomographic images of NIR functional parameters.

ACKNOWLEDGEMENTS

I have had the wonderful opportunity to work with a great mentor and advisor in Brian Pogue. Brian has been a constant source of support and encouragement over these past four years and has played a key role in shaping my work. He demonstrates the process of research through example: of not taking any idea for granted, but exploring, studying and interpreting it in innovative ways. He has always encouraged me to pursue new ideas, while providing invaluable guidance in the research undertaken. Being a novice in the area, I found his guidance and endless patience invaluable. His open door policy created an atmosphere for healthy debate and is greatly appreciated. On occasions when I was frustrated by minutia, he would show me the bigger picture. Always positive and with a smile, Brian worked seamlessly towards my deadlines, in spite of being such a busy person. His confidence in my work through objective evaluation and support over the years has finally helped me to completion.

Prof Paulsen never ceases to amaze me with his invaluable comments in spite of his demanding schedule. He has a way of hitting the nub, and reaching the core of a problem right-away followed by valuable suggestions. I have felt exhilaration every time he has read through my paper and approved it because of the high standard he maintains. My heart-felt thanks to Dr. Hamid Dehghani for all his support and encouragement. Hamid has been an incredible teacher, explaining the principles of image reconstruction in simple terms, when I was a beginner. His perspective has improved my work considerably. I have also learnt some neat testing, debugging and coding techniques in Matlab from him.

I would like to thank Dr. Shudong for her input on the tomography system and all the patient studies; she demonstrates by example the importance of dealing with clinical data. It was a pleasure working with Ben Brooksby on a wonderful collaboration, and my sincere thanks to Xiaomei Song, Xin Wang, Heng Xu and Qianqian Fang for useful discussions. Many thanks to Dr. Steve Poplack for the mammogram interpretations and Christine Kogel for sharing that information with me in a timely manner. I would also like to thank Jennifer Gibson for the statistical analysis used in this thesis and Dr. Wendy Wells for useful feedback on my papers. I'm grateful to Dr. Bruce Tromberg, my external examiner for his thoughtful suggestions on my proposal and for being on my committee in spite of a busy schedule. My gratitude goes to Professor Daniel Lynch and Professor Elsa Garmire, in whom I have gained valuable role-models.

It was wonderful having some special friends Karen, Christina, Nirmal, Navin, Scott, Summer and others in Thayer. I'm forever indebted to my close friends at Dartmouth, who have always been there for me through this journey, Thanks Viji, Dhana, Sarah and Naomi.

All this would not have been possible without the blessings and love of my parents and my adorable sister Preethi, who kept up my morale during my downs, and supported me with all their heart, in my decisions. My gratitude to my in-laws, two amazing people with huge hearts, I'm lucky to have in my life. Thanks to my wonderful, dear husband, Abhi, for his endless patience in proof-reading my thesis, helping me with formatting, for his incredible and ever-lasting support, his love and for reminding me everyday, how beautiful life is.

TABLE OF CONTENTS

ABSTRACT	ii
ACKNOWLEDGEMENTS	iv
LIST OF FIGURES	x
LIST OF TABLES	xxi
1. INTRODUCTION	1
Thesis Overview	8
2. THEORY	10
2.1 Introduction	10
2.2 Instrumentation	10
2.3 Image Reconstruction	12
2.4 Spectral Fitting: Beer's law	18
2.5 Spectral Fitting: Scatter Theory	20
2.6 Conclusion	21
3. MEASUREMENT OF MOLAR ABSORPTION SPECTRA	22
3.1 Introduction	22
3.2 Materials and Methods	23
3.2.1 <i>Diffuse Optical Tomography System</i>	23
3.2.2 <i>Phantom Experiments</i>	24
3.2.3 <i>Oxygen Dissociation curve</i>	27
3.3 Results	28
3.3.1 <i>Molar Absorption Spectra</i>	28
3.3.2 <i>Oxygen Dissociation (Hill) Curve</i>	32
3.4. Discussion	33
4. INTERPRETATION OF SPECTRAL DATA IN NORMAL PATIENTS	35
4.1 Introduction	35

4.2 Materials and Methods.....	38
4.2.1 Tomography system.....	38
4.2.2 Spectral Estimation of Physiologic Parameters.....	39
4.2.3 Human Subjects.....	40
4.3 Results.....	40
4.3.1 System Calibration and Accuracy Testing.....	40
4.3.2 Subject Demographic Information.....	41
4.3.3 NIR-information Relative to Age, BMI, Breast Diameter.....	43
4.3.4 NIR Information Relative to Radiographic Density.....	46
4.3.5 Trends Between NIR Parameters.....	47
4.4 Discussion.....	50
5. MULTI-STAGE RECONSTRUCTION APPROACH FOR IMPROVED QUANTIFICATION OF SMALL OBJECTS.....	54
5.1 Introduction.....	54
5.2 Methods.....	57
5.2.1 Step 1: Levenberg-Marquart reconstruction algorithm.....	57
5.2.2 Step 2: Two region regularization.....	58
5.2.3 Step 3: Region based reconstruction using spatial information from step 2	60
5.3 Results.....	60
5.3.1 The advantage of a priori information.....	61
5.3.2 Application of three stage reconstruction.....	64
5.3.3 Clinical abnormality: absorption and scattering heterogeneity in different positions.....	72
5.4 Discussion.....	76
6. ERROR MODELS: INTERPRETING EFFECTS OF ERROR IN ABSORPTION IN CHROMOPHORE CONCENTRATIONS' RECOVERY.....	79
6.1 Introduction.....	79
6.2 Materials and Methods.....	81
6.3 Results.....	82

6.3.1 <i>Negative Bias in Recovery of μ_a</i>	82
6.3.2 <i>Random Error Propagation Model: Effects of Increasing Wavelengths</i>	83
6.3.3 <i>Parabolic Error Propagation Models: Incorporating Negative Bias</i>	86
6.4 Discussion	90
7. SPECTRALLY CONSTRAINED DIRECT CHROMOPHORE & SCATTERING	
RECONSTRUCTION	91
7.1 Introduction	91
7.2 Methods	94
7.2.1 <i>Conventional Technique: Individual Optical Properties Recovery at</i>	
<i>Separate Wavelengths</i>	94
7.2.2 <i>Spectral Fitting: Beer's law and Scatter Theory</i>	96
7.2.3 <i>Spectrally Constrained Direct Chromophore and Scattering Reconstruction</i>	
.....	96
7.3 Results	100
7.3.1 <i>Effect of Noise in Amplitude and Phase Measurements</i>	100
7.3.2 <i>Tumor-simulating Phantom results</i>	103
7.3.3 <i>Reduced Standard Deviation in Homogeneous Experimental Data</i>	106
7.3.4 <i>Scattering Parameter Validation</i>	109
7.3.5 <i>Oxygen Saturation Validation</i>	111
7.3.6 <i>Total Hemoglobin Validation</i>	113
7.3.7 <i>Application to Heterogeneous Experimental Measurements: Phantom</i>	
<i>Study</i>	115
7.3.8 <i>Variation of Hemoglobin in Heterogeneous Phantom Experiment</i>	118
7.3.9 <i>Variation of Scattering in Heterogeneous Phantom Experiments</i>	120
7.3.10 <i>Addition of Wavelengths: Case Study</i>	124
7.4 Discussion	128
8. CHARACTERIZATION OF BREAST TUMORS IN-VIVO USING SPECTRALLY	
CONSTRAINED DIRECT RECONSTRUCTION.....	137
8.1 Introduction	137
8.2 Methods	140

8.3 Results	141
<i>8.3.1 Case Studies 1, 2&3: Infiltrating Ductal Carcinomas (IDCs)</i>	141
<i>8.3.2 Case Study 4: Fibrosis</i>	151
<i>8.3.3 Case Study 5 & 6: Fibrocystic Disease (FCD)</i>	153
8.4 Discussion	158
9. COMBINATION OF SPECTRAL AND SPATIAL <i>A-PRIORI</i> INFORMATION	163
9.1 Introduction	163
9.2 Materials and Methods.....	164
<i>9.2.1 Instrumentation</i>	164
<i>9.2.2 Image Reconstruction</i>	165
9.3 Results	167
<i>9.3.1 Heterogeneous Phantom Experiments: Test Case</i>	167
<i>9.3.2 Application to Clinical Data from Normal Subject</i>	171
9.4 Discussion	173
10. ANALYSIS OF NORMAL PATIENT DATA USING SPECTRALLY CONSTRAINED DIRECT RECONSTRUCTION	176
10.1 Introduction	176
10.2 Methods	177
10.3 Results	177
<i>10.3.1 Patient Demographic Information</i>	177
<i>10.3.2 Correlations between functional and demographic parameters</i>	178
<i>10.3.3 Correlations between functional parameters and radiographic density</i> ..	180
<i>10.3.4 Correlations between the functional parameters</i>	183
10.4 Discussion	185
11. CONCLUDING REMARKS.....	188
APPENDIX A.....	191
APPENDIX B.....	192
REFERENCES	196

LIST OF FIGURES

Figure 1-1: Absorption spectra of oxyhemoglobin, water and melanin (from Boulnois³, Hale and Query⁴). Optical window exists between 600 and 1000nm where absorption from oxyhemoglobin and water are low, permitting penetration through centimeters of tissue..... 2

Figure 2-1: (a) Instrumentation of the optical tomography frequency domain system⁴³ showing the three planes of optical fibers in a radial configuration, through which light is passed and detected at six wavelengths. (b) the patient bed that the volunteers use for being imaged⁴⁴; the instrumentation in (a) is placed under this bed. 12

Figure 2-2: (a) mesh containing 1785 nodes used to generate the field for a single source, shown as a logarithmic intensity plot in (b) for a homogeneous domain with optical properties $\mu_a = 0.01 \text{ mm}^{-1}$ and $\mu_s = 1 \text{ mm}^{-1}$. The mesh in (a) was used to reconstruct all the images shown in this work, with appropriately varied diameter. 15

Figure 2-3: Absorption characteristics⁷⁶ of the main absorbers, oxyhemoglobin (HbO₂), deoxyhemoglobin (Hb) and water (60% to fit on same scale) in breast tissue. The six wavelengths used in the imaging system are marked as gray bold lines..... 20

Figure 3-1: Absorption coefficients at 785nm obtained by measurements on fully oxygenated phantom solution with increasing amounts of whole blood. 29

Figure 3-2: Measured molar absorption spectra of oxyhemoglobin, calculated from tissue-simulating phantom experiments with increasing amounts of whole blood. (b) Molar absorption spectrum of de-oxyhemoglobin, calculated in the same manner, and (c) absorption spectra of 100% water, found from the offset in the phantom experiments. 30

Figure 3-3 (a). Mean molar absorption spectra of oxyhemoglobin, in comparison with standard literature spectra obtained from Prahl⁷⁶. (b) Mean molar absorption spectrum of de-oxyhemoglobin, in comparison with spectra obtained from Prahl. (c) Mean absorption spectra of 100% water, found from the offset in the phantom experiments, in comparison with standard values from Hale and Query⁴. 31

Figure 3-4(a) A plot of the calculated oxygen dissociation curve from both homogeneous and heterogeneous estimates as a function of solution oxygen partial pressure (pO_2) is shown, as measured in tissue simulating phantoms that were degassed of oxygen, and extinction spectra derived in Figure 3 were used. The theoretical curve was obtained from ⁹³ (b) the hemoglobin and water variation with pO_2 in the same experiment are shown, which are nearly constant, since these were not varied in this experiment.33

Figure 4-1: Measured absorption and transport (or reduced) scattering coefficient spectrum of a single subject’s breast tissue. The data points represent the average value throughout the breast, and the lines are the best-model fits to the data. The equation for scattering shows the parameters for the optimal fit to the scattering power equation.42

Figure 4-2: Hb_T concentration (in micromolar units) is plotted against subject BMI by using data from both breasts. The solid line is a linear regression to the data showing a statistically significant correlation ($P = 0.04$ in Table 4.4).43

Figure 4-3: (a) Water fraction (percentage) is plotted as a function of subject breast size, showing data points for both breasts as measured in the NIR imaging array. The solid line is a linear regression to the data. (b) Scattering power and amplitude are plotted against breast diameter. Amplitude has a statistically significant correlation ($P = 0.04$ in Table 4).44

Figure 4-4: (a) Oxygen saturation is plotted as a function of subject age, with a linear regression line shown. (b) Scattering power is plotted as a function of subject age, with data points for left and right breasts included. The solid line represents linear regression to the data and presents a statistically significant correlation (Table 4.4).45

Figure 4-5: NIR scattering power and amplitude are plotted as a function of the four radiographic density classifications with average values from all patients shown by the shaded bars and the standard deviation between subjects shown as the error bars. A significant difference exists between fatty and extremely dense categories for both parameters (Table 5). Hetero: heterogeneous; Ext.: extremely.47

Figure 4-6: Subject NIR parameter oxygen saturation is plotted against Hb_T49

Figure 4-7: Scattering power versus Hb_T . for the normal patient pool of data.49

Figure 5-1: (a) Average reconstructed absorption coefficients plotted as a function of contrast for heterogeneities of different diameters compared to the true values, which

illustrate the bias error as the size of the heterogeneity decreases. (b) Same as Figure 5.1(a) for 10mm and 20mm heterogeneities using region-based reconstruction with a priori information on the position and size of the inclusion.....	63
Figure 5-2: (a) The average reconstructed absorption coefficients in the heterogeneity are shown for the 10mm diameter anomaly, obtained using the original reconstruction (stage 1) and using a final step of the three stage reconstruction. These are compared against the true values for differing contrast levels. (b) same, using a 15mm diameter anomaly. (c) using a 20mm diameter anomaly.....	66
Figure 5-3: (a) Comparison of average reconstructed absorption coefficient in the heterogeneity for the 15mm anomaly, obtained using just step 1, using steps 1 and 3, without step 2, and using the sequence of steps 1, 2 and 3, which shows the advantage of the sequence of three stage algorithm.(b) Projection error versus iteration number for the three steps of the reconstruction algorithm, when recovering an image from simulated data for a 15mm diameter anomaly with a contrast of 2.2 with the background.....	68
Figure 5-4: (a) Average reconstructed absorption coefficient in the inclusion for different positions of a 10mm region obtained from the original reconstruction (stage 1 only) and the final step of the 3-stage algorithm. Results are also compared with true values. The measurement data was simulated and the position of the inclusion was varied from a location 10mm from edge to the center, in increments of 3 mm. (b) same, for experimental data is used from a 10 mm object. The position was varied from a location 10mm from edge to the center, in increments of 4 mm.....	69
Figure 5-5: (a) Average reconstructed absorption coefficient in the inclusion for different positions of a 20mm anomaly (similar to Figure 5.4) using simulated data; (b) for experimental data. The position of the inclusion was varied from 10mm from the edge to the center, in increments of 3 mm.....	71
Figure 5-6: (a), (b), (c): Reconstructed images from the three stages of reconstruction, respectively, using simulated measurement data with 1% Gaussian-noise generated from a phantom with background properties of: $\mu_a = 0.01 \text{ mm}^{-1}$ and $\mu_s = 1.0 \text{ mm}^{-1}$ and a 15mm absorption object near 6 o'clock with $\mu_a = 0.020 \text{ mm}^{-1}$ and 15 mm scattering object with $\mu_s = 1.5 \text{ mm}^{-1}$ near 12 o'clock.....	73

Figure 5-7: (a), (b), (c) Reconstructed images from the three stages of the reconstruction, using clinical data at 785nm wavelength from the left breast of a subject having an intraductal carcinoma in the lower region of the breast. The measurements were recorded 30mm from the nipple..... 75

Figure 6-1: Reconstructed absorption coefficient for different sized inclusions, as a function of the contrast relative to the background absorption. These are simulated data with region of interest values taken from the final images. 82

Figure 6-2:(a) The percent error in the calculated total hemoglobin value is estimated based upon spectral fitting with random errors assumed in the absorption coefficient, showing how the error would change with different numbers of wavelengths used in the measurements. In (b) the same error propagation calculation is shown for oxygen saturation and in (c) for water content..... 85

Figure 6-3: Error in recovery of μ_a as a function of contrast between the anomaly and background absorption for different inclusion sizes, shows a parabolic trend, with saturation at higher contrasts, due to inability of the reconstruction to recover steep changes between anomaly and background. 87

Figure 6-4:(a) Error in recovery of μ_a for different wavelengths as calculated from the reconstructed images; the different lines are for varying S_tO_2 from 100% to 0% in steps of 5%; (b) shows the true contrast available in μ_a between the anomaly and background, suggesting that the increasing error in (a) for lower S_tO_2 is because of the higher contrast (due to de-oxyhemoglobin absorption) available at 661nm. 88

Figure 6-5: Error propagation in hemoglobin, oxygen saturation and water, is shown with the bias error model implemented, with current six wavelengths available. 89

Figure 7-1: Recovered mean values with standard deviation error bars are shown for (a) hemoglobin, (b) oxygen saturation (SO_2), (c) water (%), (d) scatter amplitude, and (e) scatter power. These were estimated from the interior of a homogeneous field, reconstructed with different levels of noise in the original data. Values for the new spectrally-constrained reconstruction are shown alongside results from the conventional approach. 102

Figure 7-2: Recovered NIR parameter images are shown for a heterogeneous phantom with true values in the top row, as reconstructed from simulated data with 1% random

Gaussian noise added. The middle row shows images obtained using the spectrally-constrained reconstruction and the bottom row shows the same set of images using the conventional method of applying least squares fitting to images of absorption and reduced scattering coefficients, and then sequentially fitting for chromophore images.

.....104

Figure 7-3: Mean and standard deviations from the images recovered using both spectrally constrained reconstruction and the conventional method are shown for the test phantom used in Figure 1, with increasing amounts of random Gaussian noise as the abscissa. The results are average values taken from the region of the heterogeneity, for (a) Hb_T in μM , (b) S_tO_2 in %, (c) water in %, (d) scatter amplitude and (e) scatter power. The background values were observed to stay constant for both methods.....105

Figure 7-4: Recovered mean values with standard deviation error bars are shown in (a) from reconstructed data with a 90 mm diameter liquid phantom containing 1% Intralipid with $9.3 \mu M$ total hemoglobin. Values for the spectrally constrained reconstruction are shown alongside those obtained with the conventional reconstruction approach and the true theoretical values. In (b) the images from this phantom are shown for comparison, with the spectrally-constrained reconstruction (top row), the conventional reconstruction (middle row) and profile plots from the mid-plane of these images (bottom row).....108

Figure 7-5: Recovered mean values are shown from a series of phantoms where the scattering coefficient was systematically varied through differing concentrations of Intralipid, between 0.75% and 1.5%. The estimated scattering power and amplitudes are shown in (a) and the reduced scattering coefficients at 661 and 785 nm are shown in (b). The total hemoglobin, which did not vary, is shown in (c) along with a line corresponding to the theoretical value. In (d) the oxygen saturation and water values are shown, which also did not vary. Both have theoretical estimates of 100%. Error bars represent the standard deviation of all pixels within the interior 60 mm of the region imaged.....110

Figure 7-6: Estimated mean values are shown from homogeneous reconstructions of a phantom with varying oxygen partial pressure (pO_2) of the solution, induced by addition of yeast. The oxygen saturation is shown in (a) along with the theoretical estimate from the Hill curve. The total hemoglobin and % water are shown in (b), with

the theoretically estimated values of 18 μM and 100% respectively, and should not vary with changes in oxygenation. The scatter power and amplitude are shown in (c) and should not vary, and the reduced scattering coefficient at 785 nm is also shown in (d).

.....112

Figure 7-7: The reconstructed mean and standard deviation values are shown from phantoms with varying concentrations of blood where total hemoglobin is graphed in (a) alongside the theoretical value shown by a dotted line. The recovered values of oxygen saturation (%), water (%), scattering amplitude (a) and scattering power (b) are shown in (b), all of which are not expected to vary with changes in total % blood. The scatter parameters are multiplied by 100 to allow them to be displayed on the same graph as oxygen saturation and water.114

Figure 7-8: Comparison of images obtained with the spectrally constrained direct chromophore reconstruction and the conventional technique of independent optical property at separate wavelengths recovery on measurements from a gelatin phantom with a 2.5cm inclusion. The gelatin phantom contained whole blood and TiO_2 for scattering and the inclusion was filled with 4% pig blood and 0.75% Intralipid in buffered saline. The expected images are shown in the top row for Hb_T (μM), oxygen saturation (%), water (%), scatter amplitude and scatter power. The spectral method images appear in the second row while conventional technique images are located in the bottom-most row.116

Figure 7-9: Images of a gelatin phantom whose inclusion Hb_T concentration was varied from 20-44 μM . Top row shows true images for Hb_T . Images obtained by application of spectral priors appear in second row while the bottom row contains the images resulting from the conventional technique. The images for all other parameters (oxygen saturation, water and scatter) remained nearly constant with the Hb_T change.118

Figure 7-10: The mean and standard deviation in the anomaly region from images recovered by spectrally constrained direct reconstruction and conventional separate wavelengths property recovery following change in hemoglobin concentration in the anomaly for (a) Hb_T (μM). The other parameters did not vary as shown by (b) Oxygen saturation (%) and water (%) for both methods; (c) scatter amplitude and power for spectral method and (d) scatter amplitude and power for conventional procedure.120

Figure 7-11: Following variation in scattering by imaging a gelatin phantom whose inclusion Intralipid concentration was varied from 0.75 to 1.75% in steps of 0.25%. Top row shows true images for scatter amplitude (in units of $10^{-3b}(\text{mm})^{b-1}$, b being scatter power) with images obtained by application of spectral priors in second row and bottom row containing these images for the conventional technique. The images for all other parameters (Hb_T, oxygen saturation, water and scatter) stayed nearly constant with this change.121

Figure 7-12: The mean and standard deviation in the anomaly region for scatter amplitude and scatter power from images recovered by (a) spectrally constrained direct reconstruction and (b) conventional separate wavelengths property recovery, following change in Intralipid concentration in the anomaly. Scatter power is expected to stay constant with this change with linear variation in scatter amplitude. The other parameters did not vary as shown by (c) Hb_T(μM) and (d) Oxygen saturation (%) and water (%) for both methods.123

Figure 7-13: The molar absorption spectra for the absorbing chromophores^{4,76} (oxyhemoglobin-HbO₂, de-oxyhemoglobin-Hb and water (multiplied by 10 to fit on the same scale) is shown in Figure. The gray bold lines show the current six wavelengths of use and the blue dotted lines with labels show the wavelengths added to these, to study the behavior of the spectral reconstruction to increasing number of wavelengths.125

Figure 7-14: Top row shows the true images (Hb_T (μM), Oxygen saturation (%), water (%), scatter amplitude and scatter power) for the test phantom used to generate frequency domain measurements. Middle row shows the images recovered by the spectral technique using six of the wavelengths (currently in use in the clinical instrumentation) and bottom row shows the images obtained by the use of fourteen wavelengths almost uniformly distributed in the range 660-960nm which includes the six wavelengths used for middle row images.126

Figure 7-15: (a) Average and standard deviation for each of the NIR parameters in their respective heterogeneities, obtained by FWHM segmentation on the images. The images were recovered by the spectral reconstruction for two cases: current six wavelengths used in the clinical imager and the extension to 14 wavelengths uniformly sampling the entire range of 660-960nm. The test phantom consisted of five

heterogeneities (one for each NIR parameter) with 1% random Gaussian noise in the simulated frequency domain data. (b) shows the background recovered means with standard deviations alongside true values.....128

Figure 8-1: (a) left craniocaudal mammogram and (b) magnified close-up mediolateral mammogram from the left breast of a 73yr old woman with a 2.5cm spiculated mass (marked with black arrows) diagnosed as infiltrating ductal carcinoma by core-needle biopsy (patient ID #1035). (c) top row shows images for $Hb_T(\mu M)$, $S_tO_2(\%)$, water (%), scatter amplitude and scatter power obtained using the spectrally constrained direct chromophore reconstruction; bottom row shows the images of the same using the conventional separate wavelength approach. Images in top row correspond well with tumor location (given as 2:30 clock face position, close to the periphery) from the mammogram.....142

Figure 8-2: The average for the five NIR parameters along with standard deviation in the region of the tumor and the background (for the patient corresponding to Figure 8.1). The tumor was defined by segmentation of the images obtained from the spectrally constrained direct chromophore reconstruction using the FWHM criterion. The tumor exhibits increases in total hemoglobin (Hb_T), water and scatter with decreases in oxygenation, compared to the surrounding tissue.145

Figure 8-3: (a) left craniocaudal mammogram, (b) magnified view of mammogram and (c) ultrasound images from the left breast of a 37yr old woman with a 3cm irregular mass (indicated with black arrows) centrally located at 6:30 on the clock face; diagnosed as infiltrating ductal carcinoma through biopsy (patient ID #1077) (d) images for $Hb_T(\mu M)$, $S_tO_2(\%)$, water (%), scatter amplitude and scatter power obtained using the spectrally constrained direct chromophore reconstruction. The tumor is most clearly visible in the Hb_T image.....146

Figure 8-4: The average and standard deviation for the five NIR parameters in the region of the tumor and the background (for patient corresponding to Figure 6). The tumor was defined by segmentation of the images obtained using the spectrally constrained direct chromophore reconstruction and FWHM criterion. The tumor exhibits an increase in total hemoglobin (Hb_T) and water, with decreases in oxygenation, compared to the surrounding tissue.148

Figure 8-5: (a) Left craniocaudal mammogram, (b) left mediolateral oblique mammogram for a 73 yr old subject, revealed two abnormalities close to each other in the lower outer left breast, diagnosed by excision biopsy as infiltrating ductal carcinoma and 2.5cm in size (patient ID #2034). The mass is indicated with black arrows. (c) NIR tomographic images obtained using amplitude and phase measurements at the periphery of the breast and the spectrally constrained reconstruction approach. The tumor is visible in total hemoglobin, water and scatter as a localized increase and in oxygen saturation, as a decrease.....149

Figure 8-6: The average and standard deviation for total hemoglobin, oxygen saturation, water and scatter amplitude (a) and power (b) (multiplied by 100 to fit in the same Figure) obtained from the images in 8.5(c) The tumor was segmented using a FWHM criterion from the scatter power image, which shows the cancer most clearly, corresponding to location from mammogram.150

Figure 8-7: (a) Left craniocaudal mammogram, (b) left mediolateral oblique mammogram magnified for a 49 yr old subject showing a 2.7cm mass in the 2:30 clock position, diagnosed by core biopsy as the benign condition, fibrosis (patient ID #2135) (c) NIR tomographic images obtained by applying the spectral reconstruction on the frequency domain data from the plane closest to the chest wall containing the tumor. The tumor is most clearly discernible in total hemoglobin and scatter in the 3:00 clock position with oxygen saturation and water having almost homogeneous images.152

Figure 8-8: The average for the five NIR parameters along with standard deviation, in the region of the tumor and the background for a subject with fibrosis (mammogram and NIR images in Figure 8.7). The tumor exhibits a small increase in total hemoglobin (10%) and a larger increase in scatter amplitude (22%) with respect to the surrounding tissue; other NIR parameters do not show much change.....153

Figure 8-9: (a) Left craniocaudal mammogram, (b) left mediolateral oblique mammogram for a 49 yr old subject, showing an 7 x 5 mm ill-defined mass at 12:00 clock position, diagnosed by stereotactic guided biopsy as the benign condition, FCD (patient ID #1079). (c) Recovered images for the NIR parameters are shown as reconstructed with the spectral approach, using frequency domain data from the periphery of the breast. Contrast is observed at location of the lesion, in total hemoglobin and water, and no decrease in oxygen saturation is observed. (d) Mean values and standard deviation, in

the tumor (segmented using FWHM criterion as for previous cases) and surrounding tissue; most dominant contrast is in water.	154
Figure 8-10(a) Right craniocaudal and (b) right mediolateral oblique mammograms for a 61 yr old subject (patient ID #1059). The mammograms showed no abnormality. Ultrasound revealed a 1.1cm lesion at the 9:30 clock position diagnosed as FCD. (c) top row shows the images obtained using the spectral reconstruction for the right breast; bottom row shows the images for the contralateral normal breast. Both show a trend of decreasing oxygenation corresponding to an increasing hemoglobin; likely occurring as a result of fibroglandular tissue rather than tumor location.	157
Figure 8-11: Average and standard deviation in the benign lesion (discussed in Figure 8.10) and the surrounding tissue. The tumor was segmented using the FWHM criterion on the NIR images; while a decrease in oxygenation is observed, this may be due to fibroglandular tissue. Water shows a contrast and scatter as well, over the background.	158
Figure 8-12: The average total hemoglobin and standard deviation in the location of the lesions from 12 tumors imaged in-vivo (7 cancers and 5 benign lesions) including the case-studies reported in this paper, plotted against vessel density in the tumor obtained from pathology, indicates a possible correlation.	160
Figure 9-1: (a) Photograph of gelatin phantom used to provide a priori information regarding position of anomaly; (b) Reconstructed images of total hemoglobin concentration (μM), percent hemoglobin oxygen saturation, water fraction, scattering amplitude, and scattering power, for the gelatin phantom, using algorithms which incorporate different degrees of a priori information. The top row shows the true values, the second shows the reconstruction which uses no priors, the third uses spatial constraints, the fourth uses spectral constraints, and the bottom uses both spectral and spatial priors.....	168
Figure 9-2: Mean reconstructed values of $[\text{Hb}_T]$ (μM), S_tO_2 (%), Water (%), A, and b, in the region of the inclusion using four algorithms. As the total hemoglobin concentration in the phantom cavity increases, so does the reconstructed value. When the blood concentration is high, the best results are achieved when both spectral and spatial priors are used in the reconstruction, with spectral priors following close. As expected, S_tO_2 , water, a, and b within the cavity remain constant for each solution (not shown here).	

Generally, when no priors are used, the standard deviation of the property values within the region is the highest.171

Figure 9-3:(a) MRI of a healthy 43yr old female volunteer, used to provide spatial priors regarding tissue boundaries, for the reconstruction; (b)Breast tissue property images estimated using four different reconstruction methods. First (top), only the outer boundary of the imaging domain, and the location of the optical fiber measurement sites are specified. Second, a spatially constrained algorithm was used. Third, spectral constraints were applied and chromophore concentrations and scattering parameters were reconstructed directly. Fourth (bottom), both spatial and spectral constraints were combined.....172

Figure 10-1:(a) Total hemoglobin plotted against BMI and (b) Water plotted against BMI using data from left and right breasts, for 60 healthy subjects. Both showed a statistically significant correlation ($p < 0.001$ for (a) and $p = 0.005$ for (b)).180

Figure 10-2:(a) Scatter amplitude versus diameter and (b) scatter power versus age; both showed statistically significant correlations with p values < 0.001 and 0.005 respectively.181

Figure 10-3: (a) NIR scatter power as a function of radiographic density: the average for the subjects in each category is plotted along with standard deviation. Statistical analysis showed that scatter power could separate fatty from heterogeneous dense and extremely dense category, with a p-values 0.01 and 0.006 . (b) Water as a function of radio-density: water could separate scattered from heterogeneously dense and extremely dense categories with p values 0.03 and 0.005 respectively.183

Figure 10-4:(a) Water versus total hemoglobin and (b) scatter power versus water; both showed statistically significant correlations with p-values < 0.001184

LIST OF TABLES

Table 4-1: Mean, standard deviation, and total range of the subject clinical and NIR parameters	41
Table 4-2: Pearson correlation coefficients (r) and P values for three clinical parameters	42
Table 4-3: Mean values of standardized effects for subject age, BMI, and breast diameter for each of the four radiographic density categories and a global P value for differences in mean effects in these variables among the density categories	43
Table 4-4: Estimated partial correlations relative to demographic parameters of breast diameter, subject age, and BMI, along with confidence intervals and P values for testing for a nonzero partial correlation.	46
Table 4-5: A comparison of mean standardized values for NIR properties among radiographic density groups and statistical P values for difference from the fatty group.	48
Table 4-6: Correlation coefficients among the derived NIR properties with corresponding P values for testing for the presence of an association between properties	49
Table 5-1 The average reconstructed parameters for the three stages of reconstruction quantified from regions in the final images, when applied to the simulated data shown in Figure 5.6.	74
Table 5-2: The average reconstructed parameters from the three stages of reconstruction when applied to an image from the clinical data, discussed in Figure 5.7.	75
Table 10-1: Average and standard deviation for demographic and NIR parameters from 60 normal subjects.....	178
Table 10-2: Estimated partial correlations with standard error of NIR parameters relative to demographic factors such as age, BMI and breast diameter.....	179
Table 10-3: Results of statistical analysis testing for separation of the radiographic density categories using NIR parameters	182
Table 10-4: Correlation coefficients among the derived NIR properties with corresponding p-values.....	184

1. Introduction

“The results indicate that a ‘window’ for effective transmission of near IR light exists in biological materials and that cerebral Hb-HbO₂ steady states, the blood volume, the redox state of cytochrome a, a₃, and thereby oxygen sufficiency can be monitored noninvasively.” -*Frans F. Jobsis*, Science 198(4323), Dec 1977.

“While nuclear MR imaging, positron emission tomography (PET), and ultrasonography (US) provide separate morphologic and biochemical parameters, the NIR optical method is outstanding for its simplicity, economy, and ... high specificity.” -*Britton Chance*, Guest Editorial in Academic Radiology, 8(3), March 2001.

When light is passed through biological tissues, in addition to reflection at the boundary (due to refractive index mismatch between air and the tissue), absorption and scattering events occur within the tissue. The relative strengths of these processes depend on the wavelength of light as well as the properties of the tissue medium. The primary light absorbers in tissue (also called chromophores) are oxy and de-oxyhemoglobin, water, melanin and lipids, and these have a distinct spectra, shown in Figure 1. Depending on the function to be probed, appropriate wavelengths can be used for tissue interrogation. In the

ultraviolet and infrared (wavelength, $\lambda > 2000\text{nm}$), absorption (by hemoglobin and water respectively) dominates and hence, the penetration of light is limited up to a few cell layers¹. Between 600 and 1000nm however, an optical window exists (see Figure 1) where the low absorption of hemoglobin and water along with high scattering, allows photons to propagate in a random walk, through up to a dozen centimeters of tissue. The field of optical imaging in this near infra red (NIR) window gained momentum after Jobsis (1977), utilized measurements in this region, at two wavelengths appropriately placed, and showed that non-invasive monitoring of the oxy and de-oxy hemoglobin equilibrium was possible².

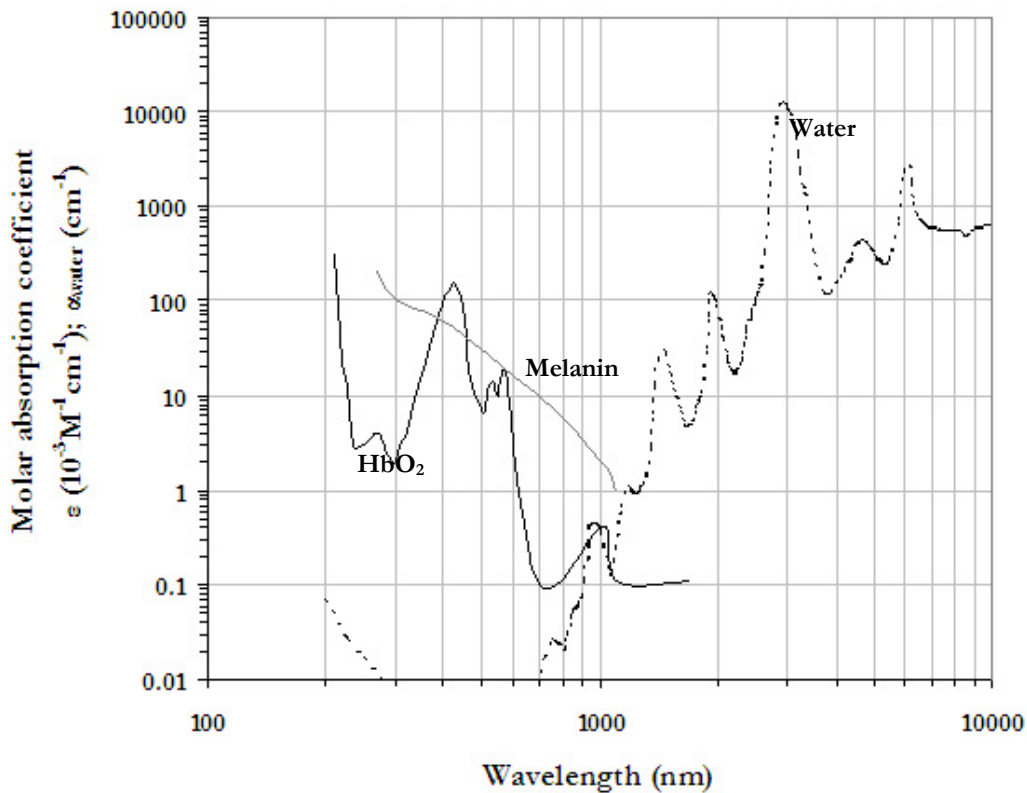


Figure 1-1: Absorption spectra of oxyhemoglobin, water and melanin (from Boulnois³, Hale and Querry⁴). Optical window exists between 600 and 1000nm where absorption from oxyhemoglobin and water are low, permitting penetration through centimeters of tissue.

Optical imaging holds considerable promise as a functional imaging modality providing multifaceted directions of research, relating to diagnosis of disease, probing of different tissue (breast⁵⁻⁷ brain⁸⁻¹⁰, muscle¹¹, forearm¹², skin¹³), therapeutic applications such as monitoring chemotherapy¹⁴ and light-sensitive treatments such as photodynamic therapy^{15, 16}; Further aspects such as availability of high contrast¹⁷ and scattering information as well as the non-invasive nature and inexpensiveness of the technique make the modality attractive for researchers in a clinical setting.

The concept of using light in the near infrared wavelength band for breast imaging, was explored nearly 75 years ago, when breast tissue was illuminated with light (diaphanography or transillumination)¹⁸ ; however clinical results were overwhelmed by scattering effects and low specificity^{19, 20}. Optical Imaging regained prominence after Jobsis's discovery; and since then, this field of non-invasive imaging has experienced sustained growth and development toward clinically viable imaging systems. Developments in the past two decades resulted in sophisticated instrumentation that obtains measurements around the breast at multiple detector locations using multiple sources; and nonlinear computational methods for light propagation models that provide image reconstruction. Together with knowledge of absorption spectra, these allow recovery of tissue functional parameters such as hemoglobin, oxygenation and water fraction in tissue.

NIR optical imaging has a unique niche in the diagnosis of breast cancer. Current methods for screening and diagnosing breast cancer are mammography, MRI and ultrasound. Mammography, the screening modality of choice suffers from a high false positive rate²¹ and community practice has shown that almost 80% of the women who

undergo biopsy as a result of a screening mammogram-detected abnormality do not have cancer²². Mammography has reduced sensitivity in women with denser breasts²³ and this density factor is responsible for mammography failure in younger women (40-49 yrs)²⁴. Mammography as well as MR and ultrasound rely largely on structural features of abnormalities rather than functional information and their inherent tumor-background contrast is in the order of 10%²⁵.

In optical imaging, the dominant contrast resulting from high-contrast (assessed up to 200%²⁵) available from heme in the blood, leads to images which are related to intrinsic pathophysiologic processes such as angiogenesis and hypoxia. Increased hemoglobin levels at the location of the tumor due to neovascularization²⁶, causes increased optical absorption^{6, 27, 28}, although scattering mechanisms also occur which may hold diagnostic promise as well. Tissue hypoxia typically found in malignant tumors²⁶ is recorded in the oxygen saturation images of the breast, and water content images are also anticipated to provide additional information in cases such as fibroadenoma²⁷ or fibrocystic disease. Recent studies have suggested that structural information related to density of the breast and risk of cancer may also be available through NIR optical tomography^{25, 29-31}.

Pregnancy, age, and hormonal factors are some factors which can result in changes in the physiological state of the breast tissue which can be monitored noninvasively using NIR. During the menstrual cycle, blood flow may increase by 50% at time of ovulation(midcycle) and remains high until menstruation³². MR imaging has shown elevated water content and mean volumetric fibroglandular fraction during menses³³. Consistent with these, using NIR spectroscopy, Shah et al⁷ showed an increase in de-oxyhemoglobin of up to

48.3% and in water of up to 28.1% during the luteal phase, by monitoring a single subject through different phases of the cycle. In addition, total hemoglobin and water content was observed to be higher in pre-menopausal women compared to post-menopausal; with the latter showing higher lipid content³⁴. Studies have shown that hemoglobin from optical imaging is statistically inversely correlated to the body mass index⁵, and water content may be related to the breast size³¹. Such studies (documented in more detail in *Chapter 4*) are representative of the fact that using information from optical absorption and scattering, NIR may be able to track and quantify variations in the breast physiology.

Through the 1990s, the field of NIR imaging saw several advances in experimental³⁵⁻⁴⁰ and model-based theory^{41, 42} which permitted various studies to be carried out in clinical settings. Dartmouth researchers were part of this effort, developing and testing a frequency domain imaging device, which provided a measure of transmitted and reflected light from the breast, through amplitude and phase measurements. This has been extensively documented by McBride et al^{43, 44} and was used to image normal and abnormal women to study NIR images. The ability to recover optical images from such measurements was also developed concurrently^{41, 45} and was based on a computational finite element model of the diffusion approximation to model light propagation. This allowed recovery of absorption and reduced scattering coefficients at the wavelengths used for interrogation of breast tissue. Dehghani et al⁴⁶ developed a toolbox (NIRFAST) which implemented this scheme in MATLAB for both 2-D and 3-D applications, to be used by the Dartmouth group for image recovery. This was the starting point for the work presented in this thesis.

The focus of this thesis has been to improve the qualitative and quantitative characterization of breast tissue using NIR parameters. Researchers agree that spatial resolution of optical imaging is limited by the dominance of scattering^{41, 47, 48}, making the image reconstruction a difficult problem with a cost on the quantitative accuracy that cannot be overcome without a priori information regarding the imaging domain. Several studies have used *a-priori* information about the size and position of the tumor to enhance the quantitative accuracy of absorption and scattering of tumors as demonstrated by Schweiger et al⁴⁹, Pogue et al⁵⁰, Dehghani et al^{51, 52}, which would be especially useful in imaging of small objects. However, the *a-priori* information is typically obtained from MRI and requires a combined MRI-NIR system, which is currently unavailable in most cases. A multi-step procedure has been investigated in this thesis, to improve the quantitative accuracy available in absorption coefficients, by using the existing reconstruction to provide *a-priori* information, and targets improved quantification of small objects. The results from implementation of the algorithm to experimental and simulated data look promising and show improved quantification consistently; however, they emphasize the hypothesis that though the resolution achievable through NIR can be improved by zoning approaches, there is a finite limit to this improvement. Any inaccuracy in quantification of absorption coefficients affects the resultant chromophore concentrations. Hence, the ability to quantify hemoglobin, oxygen saturation and water suffers, and this poses a limit on the reliability and diagnostic capability of optical tomography.

Current research systems for NIR tomography use multi-wavelengths⁵³ to capture the spectral features of hemoglobin, oxy-hemoglobin, water and lipids (the primary absorbers in breast tissue). The multi-wavelength data acquisition capability permitted

recovery of chromophore concentrations and extended indices such as hemoglobin, oxygen saturation, scatter amplitude and scatter power^{6, 28}. However, in so far, this was done by a linear least squares fit which did not utilize the spectral behavior in the recovery of the optical properties themselves. The concept of *a-priori* information is extended to a novel reconstruction approach presented here, that implements the expected spectral shapes of the chromophore and scattering models into the image formation process, thereby adding a spectral constraint into the reconstruction. The approach presented here uses simultaneously all six wavelengths of frequency domain measurements and incorporates the Beer's law for absorption and the approximation to Mie theory for scattering as constraints thereby reducing the solution space as well as the number of parameters to be reconstructed for and hence creates a more robust and stable algorithm.

Of equal importance is the characterization of breast tissue, both in normal and diseased tissue, using the optical parameters. This has been done by our group^{25, 31} and researchers elsewhere^{5, 27, 54, 55} in order to correlate the in-vivo clinical optical information with established physiological and patho-physiological parameters. Each of the new approaches investigated here has been used for this purpose, and used to interpret the NIR parameters so obtained, after suitably validating the methods in simulations and systematic experiments. The bulk average approach was used for normal tissue to study trends relating optical parameters to demographic information such as age, breast size, body mass index and radiographic density. In the case of volunteers with abnormalities, the images were used to zone in on the tumor and study the quantitative values in the region of interest, establishing possible diagnostic indicators, along with correlations to mammographic features and pathology measures such as blood vessel density.

Thesis Overview

The chapters in this thesis have been chronologically arranged and include validation studies in simulations and experiments; and application to clinical data, for each reconstruction approach presented as well.

Chapter 2 presents an overview of the theory behind image reconstruction, which forms the basis for much of the work.

Chapter 3 deals with the calibration of spectral information obtained through the optical tomography system, by measuring the molar absorption spectra for the clinical system through systematic experiments; this is followed by *chapter 4* dealing with implementation of this calibration to study trends from a normal patient pool of 24 subjects, establishing statistically significant correlations between NIR and demographic parameters.

Chapter 5 proposes and investigates a multi-step reconstruction procedure of zoning in on a tumor and hence improving the quantification of absorption coefficients in the imaging process. This has been tested in simulations, experiments and clinical data from a single subject with abnormality; and involves a variation in regularization to provide *a priori* information.

Chapter 6 establishes the significance of obtaining accurate quantification in absorption coefficients by investigating the tradeoffs in chromophore concentrations' accuracy for different levels of error. This was carried out by suitable error models mimicking observed trends in quantitative accuracy and also shows the importance of increasing number of wavelengths of interrogation

This is followed by *Chapter 7* which introduces a novel reconstruction approach that supersedes the recovery of optical coefficients; and instead directly recovers chromophore

concentrations and scatter parameters by incorporation of spectral priors into the reconstruction process and parameter reduction. This is validated in simulations and controlled experiments.

Chapter 8 is a study of images obtained from patients with abnormalities, when the direct spectral reconstruction was applied for image recovery. This chapter establishes some diagnostic indicators and features of carcinomas, fibrosis and fibrocystic disease as seen through optical tomographic images.

Chapter 9 is an extension of the *a priori* information: the results from collaboration with Ben Brooksby, bringing together spectral and spatial priors, the latter obtainable through MR structure. Improved spatial resolution is observable here, in experiments and clinical data.

Chapter 10 includes an addendum by evaluating additional trends obtained in normal clinical data by application of spectral priors.

Chapter 11 forms the conclusions of the thesis along with future directions of research. The *Appendix* includes phantom recipe as well as details of the reconstruction tool box including file-naming conventions and general instructions for users.

2. Theory

2.1 Introduction

Obtaining hemoglobin, oxygen saturation, water and scatter images of the breast using diffuse optical tomography is a three stage process: 1) obtaining measurements of transmitted and reflected light from the breast; 2) applying a model of light propagation to recover the bulk optical properties of the breast such as absorption and reduced scattering coefficients; 3) estimating concentrations of the underlying molecular chromophores in the tissue using their known spectral signatures. Each of these three stages is described below, more detailed for steps 2 and 3, which form the main framework for this thesis. The data acquisition process of the device was also used for obtaining experimental measurements and clinical data, and hence is explained below, albeit in lesser detail.

2.2 Instrumentation

Typically the measurements for optical imaging are obtained by passing light through tissue and collecting some measure of light propagation from the boundary of the domain (the breast in our case). The measured data can be in the frequency domain where the amplitude and phase of an intensity modulated light signal is measured, after transmission

through tissue^{43, 56} or time domain where the temporal characteristics of light are measured by passing an ultra-short light pulse through tissue³⁵. In addition continuous-wave measurements⁵⁷ exist, which allow broadband interrogation with intensity measurements, but no phase information, making the separation of absorption and scatter difficult. Indeed, studies^{58, 59} have shown that absorption and scatter can be determined uniquely only for frequency not equal to zero and hence some broad band systems use frequency domain instrumentation in addition, to provide scattering information⁶⁰.

The current system built at Dartmouth and documented by McBride et al^{43, 44} is a multi-wavelength frequency domain instrument allowing amplitude and phase measurement along the periphery of the breast. Briefly, the automated NIR tomography device was constructed to perform cross-sectional imaging of the breast by means of fiber optic bundles. The fibers arranged in a circular array (with both radial and vertical degrees of freedom) have the capability to collect data in three slices of tissue from sets of 16 source and 15 detector locations (see Figure 2.1). Intensity modulated light (at 100MHz) at six discrete wavelengths between 660 and 850 nm is used to allow multi-spectral interrogation of the breast. Detection is accomplished by high-gain, high-bandwidth photomultiplier tubes, and the detected light is electrically mixed with a reference signal to yield a low-frequency (500 Hz) signal that is recorded by the computer. The measured data are calibrated to account for small offsets due to source–detector fiber transmission, alignment characteristics, and errors in discretization or model–data mismatch. By fitting the measurements to a homogenous calculation of the diffusion equation on a circular geometry (of relevant size), an initial estimate of the optical properties can be obtained. This initial

estimate is used in the reconstruction on which the calibrated data are processed by a finite-element model of the optical diffusion equation in the frequency domain.



Figure 2-1: (a) Instrumentation of the optical tomography frequency domain system⁴³ showing the three planes of optical fibers in a radial configuration, through which light is passed and detected at six wavelengths. (b) the patient bed that the volunteers use for being imaged⁴⁴; the instrumentation in (a) is placed under this bed.

2.3 Image Reconstruction

Light undergoes absorption and scattering processes when passed through tissue and its propagation can be modeled with multiple-scattering electromagnetic theory, as well as the radiative transfer theory. Multiple scattering electromagnetic theory is based on the fluctuation of permittivity of the medium so that the behavior of the electric field can then be described by Maxwell's equations⁶¹. While mathematically rigorous, this analytical theory has found limited application in the field of tissue optics because of its complexity and lack of readily available solutions for non-specific shapes and densities⁶². The radiative transfer theory deals directly with the transport of energy through a medium containing the particles and is arrived at by considering the radiant energy balance in an elemental volume and angular space of tissue^{61, 62}. While analytical solutions⁶¹⁻⁶³ to this equation exist, approximate solutions have found to be more practical in applications. The Monte Carlo simulation is one such promising method and is used to track the trajectory of photons in tissue, based on

suitable probability distributions^{61, 64}. Though Monte Carlo simulations provide accurate solutions, its main drawback is that it is computationally expensive and time consuming. The radiative transfer equation can be reduced to a set of coupled differential equations, which have the solution for radiance in terms of orthogonal polynomials (legendre's polynomials in this case)⁶¹. When truncated to N terms, these equations (of order N+1) are termed as P_N equations of which the diffusion approximation is the P₁ model⁶¹.

In the diffusion approximation, the assumption is that the diffuse intensity encounters many particles and is scattered almost uniformly in all directions, and therefore its angular distribution is almost uniform isotropic⁶². This equation exists under the assumption that scatter dominates over absorption which is true in the case of several tissue types, including the human breast, in the wavelength region of 650-1350 nm⁴⁷. This differential equation is written as^{62, 65} :

$$-\nabla \cdot \kappa(r) \nabla \Phi(r, \omega) + \left(\mu_a(r) + \frac{i\omega}{c} \right) \Phi(r, \omega) = q_0(r, \omega) \quad (2.1)$$

where $\Phi(r, \omega)$ is the isotropic fluence at modulation frequency ω and position r , $\kappa(r)$ is the diffusion coefficient, $\mu_a(r)$ is the absorption coefficient, c is the speed of light in the medium and $q_0(r, \omega)$ is an isotropic source. The diffusion coefficient can be written as

$$\kappa(r) = \frac{1}{3[\mu_a(r) + \mu_s'(r)]} \quad (2.2)$$

where μ_s' is the reduced scattering coefficient. It is known that the diffusion approximation holds only for the region far from the boundary and the source (at least one scattering distance away)⁶². For this reason, the source (Gaussian) in the current application is modeled

one scattering distance from the boundary, inside the domain, so that the scattering in the tissue can be approximated to be isotropic everywhere.

Equation 2.1 can be solved using standard numerical techniques. The Finite element model (FEM), one such technique, offers considerable flexibility in handling complex and inhomogeneous geometries and has been applied here at Dartmouth and by researchers elsewhere^{41, 48}. The forward solver obtains the fluence for a given distribution of optical properties by applying suitable boundary conditions, type III (Robin-type) in our case given as^{46, 66}:

$$\Phi(\gamma) + \frac{\kappa(r)}{\alpha} \hat{n} \cdot \nabla \Phi(\gamma) = 0 \quad (2.3)$$

where α incorporates the reflection at the boundary due to refractive index change and \hat{n} is the outer normal at the boundary at a point γ . Figure 2.2 shows the field obtained by solving Equation 2.1 for a homogeneous domain ($\mu_a = 0.01 \text{ mm}^{-1}$, $\mu'_s = 1 \text{ mm}^{-1}$), when one of the sources is used, along with the source-detector locations and the mesh (for domain diameter 86mm) containing triangular elements and 1785 nodes utilized for this and all simulations shown ahead. Typically, 1% random Gaussian noise (as percentage of each measurement) was added to such simulated data, to mimic the experimental setting⁴³, when used to assess a given reconstruction algorithm.

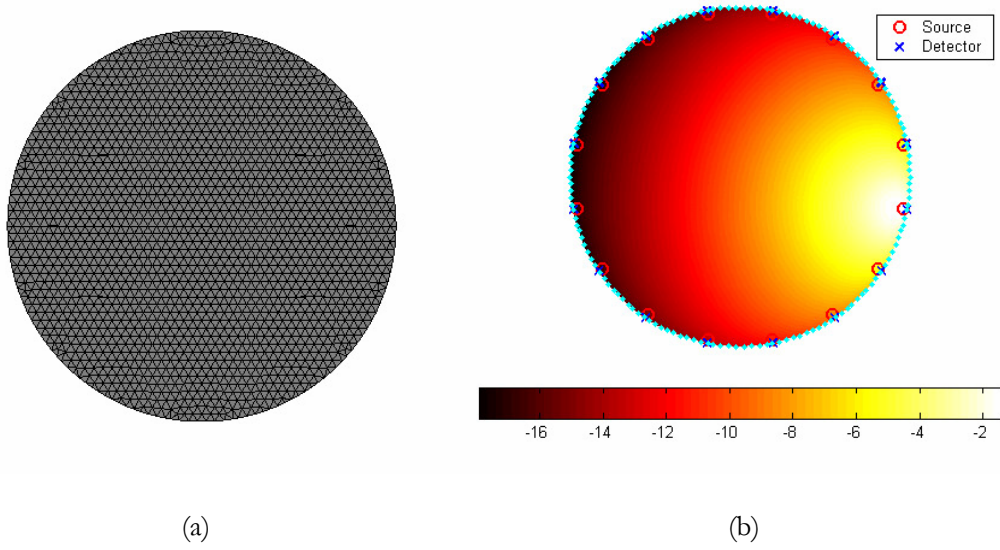


Figure 2-2: (a) mesh containing 1785 nodes used to generate the field for a single source, shown as a logarithmic intensity plot in (b) for a homogeneous domain with optical properties $\mu_a = 0.01 \text{ mm}^{-1}$ and $\mu_s = 1 \text{ mm}^{-1}$. The mesh in (a) was used to reconstruct all the images shown in this work, with appropriately varied diameter.

In NIR tomography, boundary measurements are taken and the inverse problem of obtaining the images of the optical properties from this data has to be solved. Typically, this is done through an iterative procedure where an objective function containing some measure of the difference between the measured and the model data, is sought to be minimized. In our case, the least-squares functional to be minimized is:

$$\chi^2 = \sum_{j=1}^M (\Phi_j^{meas} - \Phi_j^{cal})^2, \quad (2.4)$$

where M is the total number of measurements at each wavelength, and Φ_j^{meas} and Φ_j^{cal} are the measured and calculated fluence respectively, at the boundary for each measurement point j . The gradient-based iterative procedure used here is based on the Newton's method which has been applied to several inverse problems^{67, 68}. Assuming that a solution for the

optical properties exists, close to an initial estimate μ_0 , the Gauss-Newton method, based on the Taylor's series expansion, gives the new search direction or update, as

$$\mathfrak{J}\partial\mu = \partial\Phi, \quad (2.5)$$

where $\partial\Phi$ refers to the change in boundary data, \mathfrak{J} is the Jacobian, the matrix containing the sensitivity of the boundary data to a change in optical property μ_a and diffusion coefficient κ given by $\mathfrak{J} = [\mathfrak{J}_{\mu_a}; \mathfrak{J}_{\kappa}]$ and $\partial\mu$ is the update in the optical properties given by $\partial\mu = [\partial\mu_a; \partial\kappa]$. The Gauss-Newton method has the properties of the Newton method but is different in the calculation of the Hessian (matrix containing second derivatives) which is calculated from first derivatives. In accordance with the local convergence behavior of the Newton's method, the reconstruction is sensitive to the initial estimate of the parameters, which are given by a homogeneous pre-fitting algorithm. This algorithm calculates the bulk properties on a mesh of homogeneous circular geometry using Newton Raphson minimization with the finite element model of diffusion equation, starting with an initial guess based on the analytical solution for infinite medium⁶⁹. Detailed derivations are available in references^{45, 48}.

This inverse problem based on the diffusion equation is a non-linear ill-posed problem (a well-posed problem was defined in the Hadamard sense as a problem whose solution existed, was unique and a continuous function of the data (was stable); an ill-posed was one which lacked any of these properties^{70, 71}). Uniqueness of μ_a and μ_s' for the optical tomography problem has been established for frequency domain measurements, for an appropriately close initial guess, if not reconstructing independently for refractive index⁵⁸. However, regarding stability, matrix \mathfrak{J} in Equation 2.5 is generally ill-conditioned such that

the solution $\partial\mu$ is known to be overwhelmed by data and rounding errors. While, theoretically such problems are not solvable, *a-priori* estimates (in the form of regularization) can yield solutions close to the true answer. Many regularization techniques have been studied for the purpose of obtaining stable solutions from ill-posed problems⁷¹. Multiplying Equation 2.5 by \mathfrak{S}^T to make the matrix square in the number of parameter estimates, we get

$$\mathfrak{S}^T \mathfrak{S} \partial\mu = \mathfrak{S}^T (\Phi_{meas} - \Phi_{cal}) \quad (2.6)$$

The Levenberg Marquardt regularization scheme then gives the solution by iteratively solving for:

$$\partial\mu = (\mathfrak{S}^T \mathfrak{S} + \lambda I)^{-1} \mathfrak{S}^T (\Phi_{meas} - \Phi_{cal}) \quad (2.7)$$

where I is the identity matrix and λ is the regularizing factor that stabilizes the solution. The convergence properties of this method have been established in Kaltenbacher⁶⁷, and the advantage of Newton's rapid convergence is retained⁷². The sequencing approach for λ as introduced by Marquart^{72,73} depends on the projection error and can be written as

$$\lambda(k+1) = \begin{cases} \frac{\lambda(k)}{l}, & \chi^2(k) \leq \chi^2(k-1) \\ \lambda(k)l, & \chi^2(k) > \chi^2(k-1) \end{cases} \quad (2.8)$$

where l is a constant ($l = \sqrt{10}$ was found empirically to be reasonable for the problem and is used for all future purposes), and χ^2 is the projection error. The value of λ in Equation 2.7 obviously determines the nature of the relationship. If λ is too high, it dominates the relationship in Equation (2.7) and successive iterations do not yield much change in the update vector. However, if this damping factor is too small, then the problem will be dominated by noise in the data. In our studies, we have found empirically that a starting

value of λ in the range of 1000 to 1 reasonably recovers the optical images⁷⁴, and noise begins to dominate for starting regularization values below 1. A dual mesh scheme⁷⁵ has been used for all the reconstructions, where the Jacobian is calculated on a fine mesh (1785 nodes) and mapped onto a coarse mesh (425 nodes) to minimize the number of unknowns being estimated in equation 2.7. The reconstruction was terminated when the projection error was within 2% of the previous iteration's error; given by

$$\left| \frac{\chi_k^2 - \chi_{k-1}^2}{\chi_{k-1}^2} \right| \leq 0.02 \quad (2.9)$$

This typically occurs at 10-12 iterations for NIRFAST, and all the reconstructions in this thesis have begun with $\lambda = 10$.

2.4 Spectral Fitting: Beer's law

The image reconstruction is to be carried out for the six wavelengths currently used in the frequency domain instrumentation, to yield absorption and reduced scattering coefficient maps at each wavelength. Assuming the main absorbers in the tissue to be oxy-hemoglobin (HbO₂), de-oxyhemoglobin (Hb) and water and knowing their molar absorption spectra (absorption per unit concentration) at the six wavelengths, one can calculate each of their contributions to the absorption using the Beer's law. This is given as:

$$\mu_a(\lambda) = \sum_{i=1}^3 \varepsilon_i(\lambda) c_i \quad (2.10)$$

where ε_i is the molar absorption spectra and c_i is the concentration of the i^{th} chromophore at wavelength λ . This can be written in matrix form as

$$\mu_a = [\varepsilon]c \quad (2.11)$$

so that c , the concentration of chromophores, is calculated in a least squares constrained fit by putting the absorption coefficients at different wavelengths in the vector on the left hand side and the molar absorption spectra for the chromophores for the corresponding wavelengths on the right hand side. Figure 2.3 shows this spectral behavior for Hb, HbO₂ and water obtained from literature^{4, 76, 77} for the 600-1000nm range. The molar absorption spectra was also independently calculated for the current six wavelengths of use, with systematic experiments on the imaging system. This is detailed in *Chapter 3*. This approach of using values estimated by the system compensates for any offsets from the theoretical values; yet there was little difference between our experimental and theoretical estimates of molar absorption coefficients. By fitting for the concentrations, total hemoglobin is then calculated as $Hb_T = HbO_2 + Hb$ (in μM), and oxygen saturation as $S_tO_2 = HbO_2 / Hb_T \times 100$ (in %); the contribution from other chromophores such as lipids has been found to be negligible, as the wavelengths used here were limited to less than 850 nm where lipid is a weak absorber²⁷. The constraints on the fitting process were (i) for Hb_T to be non-negative and below $200\mu M$ (each of Hb and HbO₂ to be less than $100 \mu M$), (ii) oxygen saturation to be in the range $[0, 100\%]$ and (iii) water to be in the range $[0, 100\%]$. The availability of six wavelengths (greater than the number of chromophores) and the constraints on the fit in Equation 2.11 allow for reasonably good accuracy in the concentrations so derived. This accuracy can be further enhanced with introduction of wavelengths beyond 850nm, where stronger water features can be captured. However, the overall quantification of these chromophores also depends substantially on the accuracy of the absorption coefficients themselves, as explained in *Chapter 6*, and hence a direct spectral reconstruction approach would be more beneficial in quantitative improvement (see *chapter 7*).

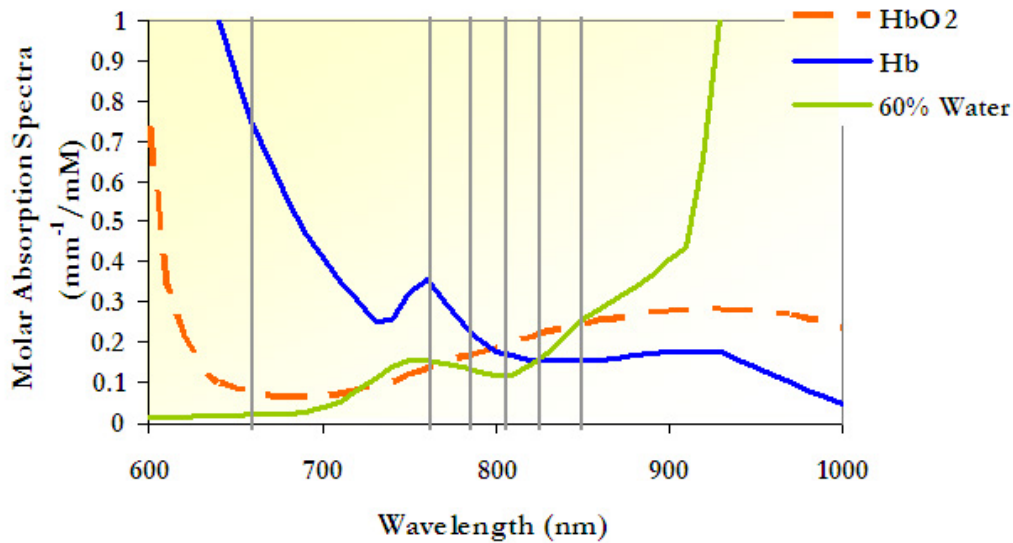


Figure 2-3: Absorption characteristics⁷⁶ of the main absorbers, oxyhemoglobin (HbO₂), deoxyhemoglobin (Hb) and water (60% to fit on same scale) in breast tissue. The six wavelengths used in the imaging system are marked as gray bold lines.

2.5 Spectral Fitting: Scatter Theory

The scattering coefficients also provide physiological information, relating to molecular level changes. Scattering occurs due to cells and their organelles such as nuclei and mitochondria as well as refractive index mismatch between the organelles and across membranes. The size, distribution and volume fraction of the particles as well as the change in refractive index have been shown to affect the scattering spectra⁷⁸⁻⁸⁰. Mie theory predicts the behavior of this scattering with wavelength, when the scatterer size is comparable to, or larger than the wavelength of light, with the assumption that these scatterers are homogeneous dielectric spheres. Studies have shown that a simpler approximation to Mie theory fits the scattering spectra reasonably well, given by^{81,82}:

$$\mu_s' = a\lambda^{-b} \quad (2.12)$$

This fit was used to derive scatter amplitude (a) and scatter power (b) images with wavelength in μm , using the μ'_s images at the six wavelengths obtained from the image reconstruction. The coefficient μ'_s has units mm^{-1} and b is dimensionless, so that a has units given by $10^{-3b}(\text{mm})^{b-1}$. Scattering power is governed by the shape or slope of scattering which is predominantly affected by the size^{83, 84}; the amplitude relates to the number density of the scatterers. Together, these two parameters may reflect variations in breast structural composition due to different cellular, organelle and structural sizes/densities for fatty and glandular tissue. Though scatterers in tissue are not necessarily homogeneous spheres as assumed in deriving Equation 2.12, studies on red blood cells and yeast have shown this to be a reasonable approximation since measurements of μ'_s in these cells show similar trends as Mie theory^{85, 86}.

2.6 Conclusion

Using the procedure detailed in this chapter and following the sequence of data acquisition through the frequency domain instrumentation, image reconstruction through a finite element model to the diffusion approximation and spectral fitting to Beer's law and scatter theory, the images of total hemoglobin, oxygen saturation, water, scatter amplitude and scatter power for the whole breast in tomographic slices, are obtainable. This has been used in the following chapters in this thesis, to study the quantification of these NIR parameters and the information they yield, as corresponding to physiologic changes and pathology.

3. Measurement of Molar Absorption Spectra

3.1 Introduction

The absorption of near infra red light by breast tissue is primarily due to de-oxyhemoglobin, oxyhemoglobin and water. After obtaining the internal spatial absorption coefficients through measurements on the breast periphery and image reconstruction, the concentrations of oxy and de-oxy hemoglobin and water (the primary absorbers in breast tissue at the wavelengths of measurements) are obtained as images through a de-convolution process which uses the spectral signatures (called molar absorption spectra or absorption per unit concentration) of these absorbers in breast tissue.

Wray et al⁷⁷ found the near infrared hemoglobin spectra at various oxygenation levels from cuvette studies of lysed human red cells. This spectra has also been measured by Cope⁸⁷, in a similar way, in his Ph.D thesis. Zijlstra et al⁸⁸ have determined the millimolar absorptivities of the clinically relevant derivatives of fetal and adult human hemoglobin in the visible and near-infrared spectral range. The optical constants for water were found by Hale and Quarry⁴ and several others^{3, 89}. Hence, the extinction spectra for the chromophores of interest have been found in the past by different groups through chemical and clinical

experiments. However, these literature values also differ from each other, as for example, there is 11.7% difference between the values of Wray et al and Cope for the oxyhemoglobin spectra. The molar absorption coefficients would yield the chromophore concentrations without error, if the absorption coefficients are estimated without error. However, algorithms to convert light attenuation into corresponding concentrations, which seem to perform adequately in one system can apparently generate unrealistic results when transferred to another system as found by Matcher et al⁹⁰. Most imaging systems introduce systemic errors in obtaining the absorption coefficients, which maybe either due to the measuring system or the reconstruction procedure. These errors have to be compensated for, and this can be done by using molar absorption spectra specific to the imaging system, which can be measured systematically by a simple procedure.

The aim of the study carried out in this chapter was to obtain the molar absorption measured within the Dartmouth imaging system and to obtain oxygen dissociation curve to establish the sensitivity of the imaging system to low oxygen pressures and validate the measured molar absorption spectra. In this study, all measurements were carried out using the frequency domain diffuse tomography system with multiple source detectors in a radial configuration to image the whole uncompressed breast, and the optical parameters are obtained by carrying out a non-linear gradient based iterative reconstruction algorithm.

3.2 Materials and Methods

3.2.1 Diffuse Optical Tomography System

The optical tomography system for which the molar absorption spectra is to be measured, has been described in *Chapter 2*. This imaging system allows frequency domain

measurements (amplitude and phase) of light fluence to be obtained from the boundary of the breast (or breast-mimicking phantoms). The amplitude and phase undergo calibration to account for any instrumental offsets or model-data mismatch, and the calibrated data is reconstructed to yield absorption and reduced scattering coefficient maps. The image reconstruction is based on the frequency domain diffusion equation used to model light propagation in highly scattering media^{35, 91} (details in *Chapter 2*), and the core of the reconstruction scheme is a Newton-Raphson minimization method for iteratively updating the optical property parameters based on minimization of the standard sum of squared differences between the measured and calculated optical radiance at specific detector locations. This type of error is a measure of the fit of the model to the measured data, and is often referred to as the projection error and is commonly used as a surrogate measure of the convergence of the algorithm.

From the absorption coefficients(μ_a) and knowing the molar absorption spectra (ϵ), the concentration of the chromophores (oxyhemoglobin-[HbO₂], de-oxyhemoglobin-[Hb] and water-[H₂O]) can be obtained by a linear least squares constrained fit (Equation 2.11) The total hemoglobin (Hb_T) is given by ([Hb_T] = [HbO₂] + [Hb]) and oxygen saturation (S_tO₂) is given by (S_tO₂ = ([HbO₂] / [Hb_T] × 100 %). The relation between the reduced scattering coefficient μ'_s , and wavelength (λ) is derived by an approximation to the Mie scattering theory given by Equation 2.12^{81, 92}.

3.2.2 Phantom Experiments

To obtain accurate concentrations of the chromophores, it is necessary to have an accurate set of molar absorption spectra for the major absorbers, in this case, de-

oxyhemoglobin, oxyhemoglobin and water. The molar absorption spectra have to be measured specifically within the system being used, to compensate for any systemic errors in the model-based estimation of concentrations. Phantom measurements are often performed on tissue-simulating objects, and a standard solution-based phantom is a mixture of Intralipid and blood³⁷. The Intralipid provides Mie-like scatterer to simulate the light scattering from cells in the tissue⁹². Intralipid-based solutions were prepared with 1% lipid fraction, by volume, in sterile saline with whole blood added in varying concentrations. This solution was held in a plastic cup and positioned in the imaging array to mimic the scattering and absorption properties of the tissue. Measurements were carried out at each specific blood concentration level and then the blood concentration was increased successively between 0% and 1%, in steps of 0.2%. By imaging the liquid phantom multiple times, the absorption coefficients at six wavelengths were obtained at each of the multiple blood concentrations, after reconstruction.

The same type of solution was prepared again and deoxygenated by addition of yeast, and the experiment was repeated for completely deoxygenated hemoglobin. The slopes from the graphs of μ_a versus blood concentration for oxygenated and deoxygenated solutions at each wavelength, yield the molar absorption coefficients for oxygenated and deoxygenated blood. These values are converted to the corresponding values for oxyhemoglobin and deoxyhemoglobin by simply dividing by the hemoglobin concentration within the blood sample (determined by measurement in a clinical co-oximeter system⁵³). At each of the different wavelengths the molar absorption coefficient is then known. The molar absorption due to pure water is also given by extrapolation of the data to zero blood concentration at each wavelength. The experiments have been carried out four times for oxygenated and

deoxygenated solution, to obtain repeatable data sets, and the calculated mean values has been used as the molar absorption spectra for the imaging system. Different sets of molar absorption spectra can also be obtained depending on the type of reconstruction algorithms used (the calculation was repeated for the spectral approach in *Chapter 7*).

Since the phantom under consideration is homogeneous, different types of reconstruction procedures can be used to generate the absorption coefficients. Mainly, there are two types of reconstruction estimates used in this study.

- 1) Heterogeneous estimate: In this procedure, reconstruction is carried out iteratively to obtain simultaneous maps of the absorption and scattering coefficients everywhere. The mean absorption coefficient of the whole image is then used to obtain the molar absorption spectra. Ideally, the reconstruction should result in a homogeneous image for μ_a . However, because of the hyper-sensitivity of the reconstruction to regions close to the boundary (where measurements are taken), certain boundary artifacts are introduced in the image. Including these boundary nodal values in computing the mean for the absorption coefficient may introduce some error in its estimation. Hence a second way to obtain the homogeneous absorption coefficient is to calculate the absorption coefficient by specifying a region of interest within the image, which excludes the boundary artifacts, and taking the mean of the absorption coefficients in the region of interest. This yields a more accurate value for the absorption coefficient, which when used to calculate the molar absorption spectra, gives more accuracy.
- 2) Homogeneous bulk estimate: In this procedure, a region based reconstruction is carried out where the phantom is considered as a single homogeneous region and

reconstruction is carried out iteratively to simultaneously calculate a global value for the absorption and scattering coefficients. The absorption coefficient obtained this way is quantitatively more accurate because it excludes any image artifacts or errors in region definition that may arise in the spatially-varying reconstruction and also makes use of the fact that the measurements have been done on a homogeneous phantom.

In this way, two different sets of absorption coefficients have been calculated, by using heterogeneous estimation of the inner domain with boundary artifact correction, and a bulk homogeneous estimation. Using the processing explained above, two sets of molar absorption spectra have been calculated, which are suitably used for studies depending on the type of reconstruction used for the study. The molar absorption spectra obtained this way vary slightly since each compensates for the error in the estimated parameters introduced by the particular reconstruction scheme.

3.2.3 Oxygen Dissociation curve

To test the sensitivity of the system to low pO_2 values, which are typically found in tumors, the next step was to find the oxygen dissociation curve (i.e. Hill curve) for the clinical system. This involved obtaining the oxygen saturation values for the complete range of pO_2 values from 150mm to 0mm Hg. This was carried out by using a liquid phantom solution of 1% Intralipid and 1% whole blood in saline. The pO_2 was measured independently using a chemical microelectrode, after calibration of the electrode overnight in saline solution. By varying the pO_2 gradually, using a small amount of yeast and making measurements over the period of time, till the pO_2 reduced to zero, a complete set of data over the required range was obtained. Reconstruction of the data and use of the appropriate

calculated molar extinction spectra depending on type of estimate used for the absorption coefficients, results in values of oxygen saturation, total hemoglobin and water concentration.

3.3 Results

3.3.1 Molar Absorption Spectra

The molar absorption coefficients have been obtained by the slope-offset method described in *Section 3.2.2*. The absorption coefficients at 785nm, obtained from measurements on a completely oxygenated homogeneous phantom, are plotted against blood concentration in Figure 3.1. The slope from the linear fit to the data points is divided by the hemoglobin content measured to give the molar absorption coefficient for oxyhemoglobin at 785nm and the offset shown is the absorption due to water at 785nm. The absorption coefficients in Figure 3.1 have been determined using the homogeneous estimate scheme. In this way, the values are obtained at all six wavelengths, and for both oxygenated and deoxygenated hemoglobin phantom solution.

Figure 3.2 shows the measured extinction spectra for (a) oxyhemoglobin (b) deoxyhemoglobin and (c) water, obtained from our tomography system using homogeneous estimate. These data show the results from three repeated measures of these values, and the mean of set at a given wavelength was used as the standard value. It was estimated that these calculated values have a standard deviation error of 6% for both homogeneous and heterogeneous estimates.

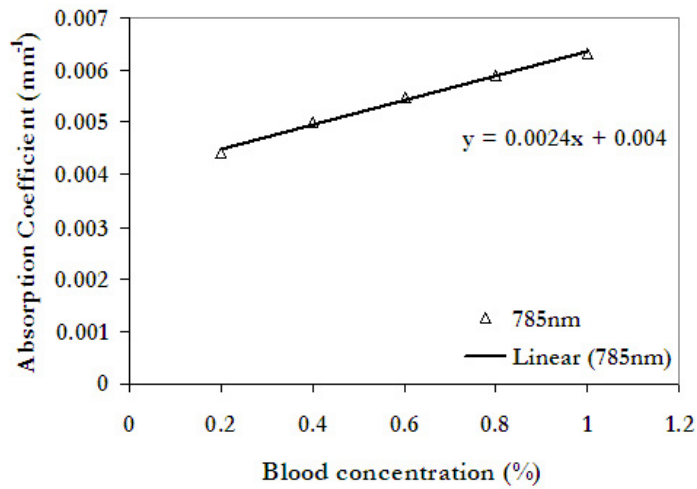
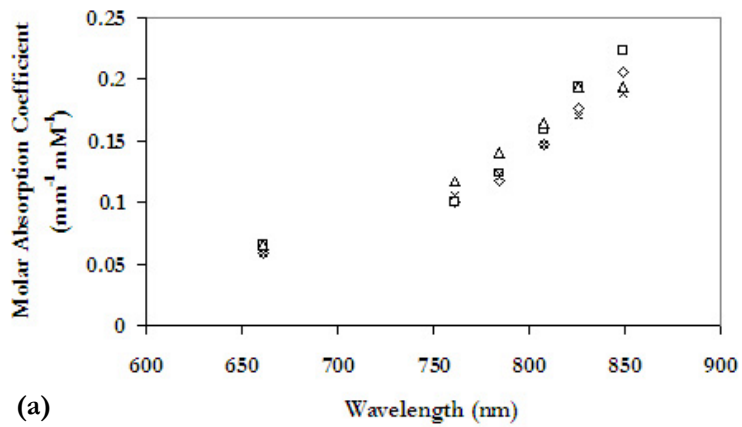
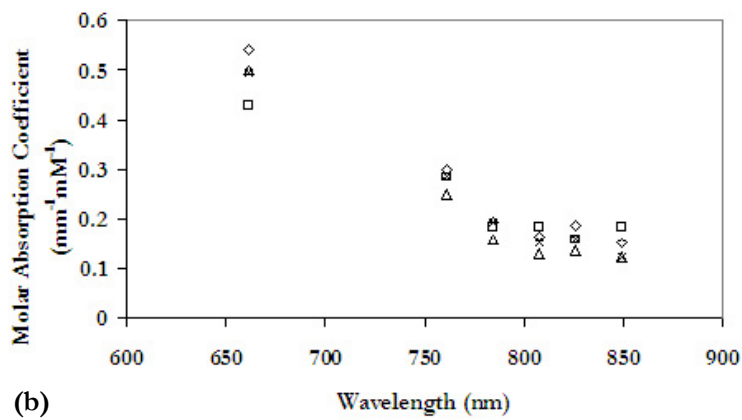


Figure 3-1: Absorption coefficients at 785nm obtained by measurements on fully oxygenated phantom solution with increasing amounts of whole blood.

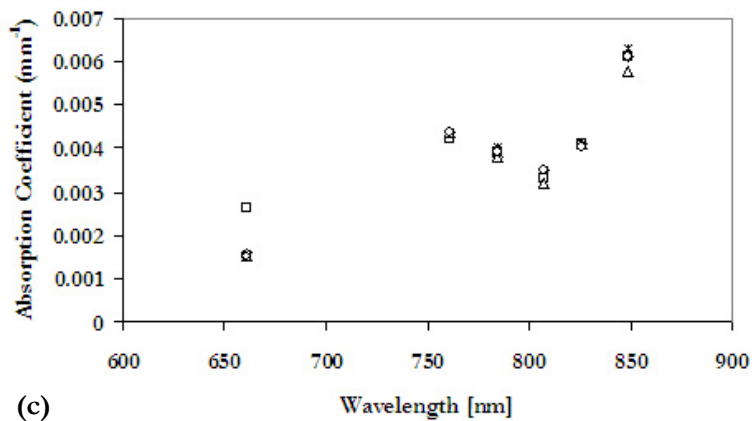
Figure 3.3 shows the molar absorption spectra for oxy-hemoglobin, hemoglobin and water obtained from both the homogeneous estimate and heterogeneous estimate, and the corresponding values from literature^{4, 76}. Depending on the type of reconstruction being used, the corresponding molar absorption coefficients are used in other phantom and patient studies.



(a)



(b)



(c)

Figure 3-2: Measured molar absorption spectra of oxyhemoglobin, calculated from tissue-simulating phantom experiments with increasing amounts of whole blood. (b) Molar absorption spectrum of de-oxyhemoglobin, calculated in the same manner, and (c) absorption spectra of 100% water, found from the offset in the phantom experiments.

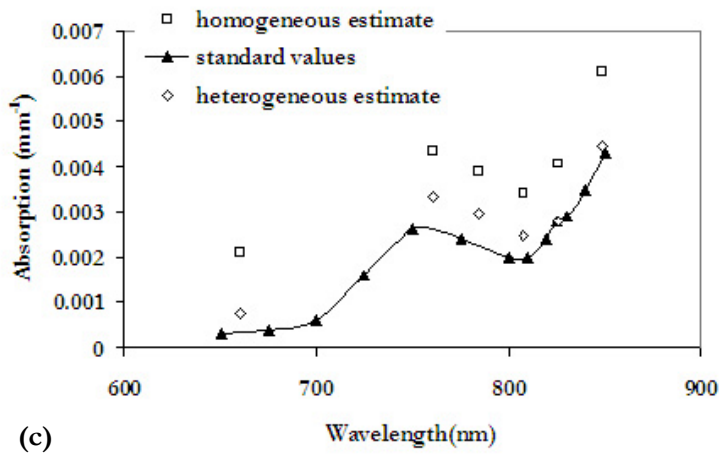
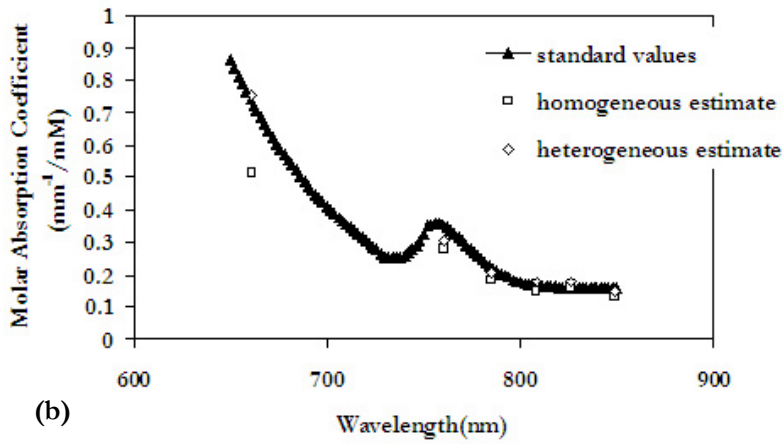
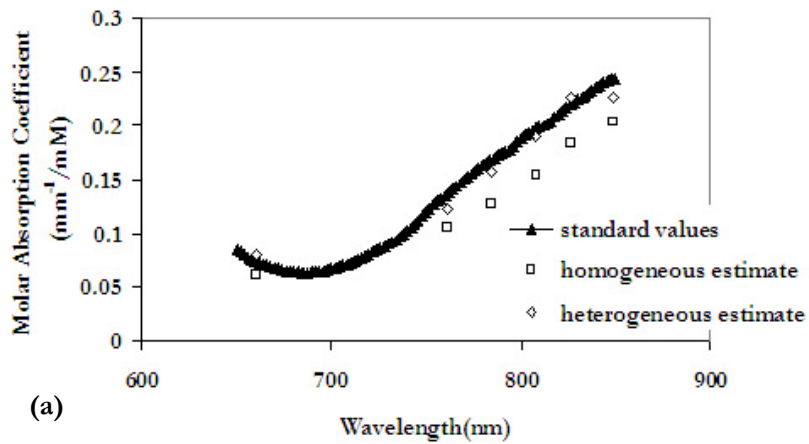


Figure 3-3 (a). Mean molar absorption spectra of oxyhemoglobin, in comparison with standard literature spectra obtained from Prahl⁷⁶. (b) Mean molar absorption spectrum of de-oxyhemoglobin, in comparison with spectra obtained from Prahl. (c) Mean absorption spectra of 100% water, found from the offset in the phantom experiments, in comparison with standard values from Hale and Query⁴.

3.3.2 Oxygen Dissociation (Hill) Curve

In validation tests, these calculated molar absorption coefficients were used to recover the properties of test tissue-simulating phantoms of varying oxygen saturation. Phantoms were deoxygenated with the addition of yeast, and measurements of absorption and scattering versus solution pO_2 were recorded at multiple times during the deoxygenating process. The absorption coefficient data obtained from homogeneous or heterogeneous estimates was spectrally decomposed into concentrations of water, oxy-hemoglobin and de-oxyhemoglobin using the corresponding molar absorption spectra, and from these the oxygen saturation was calculated. The Hill curve characteristic of oxygen dissociation from hemoglobin is shown in Figure 3.4 (a), along with the total hemoglobin and water values with variation in pO_2 , in Figure 3.4(b). The oxygen saturation values obtained using a homogeneous estimate and least squares constrained fit, is estimated to be accurate with a mean error of 7.6 % with the worst accuracy near zero pO_2 and higher accuracy above the 80% saturation value. The higher error at low pO_2 values is likely due to higher noise in measurements due to the high absorption of de-oxyhemoglobin. For the values computed from heterogeneous estimate, the oxygen saturation values are accurate with a mean error of 4.8 %. Estimates of total hemoglobin only vary by 5% for both homogeneous reconstruction, and heterogeneous reconstruction, when oxygen saturation varies, and estimates of water concentration vary by less than 10% for both over the range of pO_2 values.

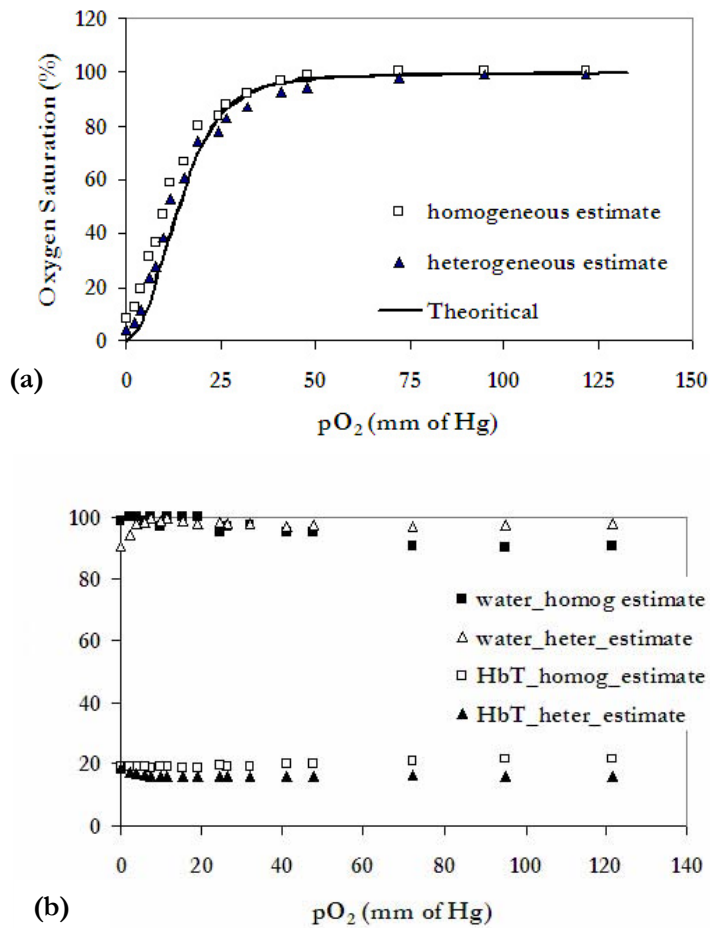


Figure 3-4(a) A plot of the calculated oxygen dissociation curve from both homogeneous and heterogeneous estimates as a function of solution oxygen partial pressure (pO_2) is shown, as measured in tissue simulating phantoms that were degassed of oxygen, and extinction spectra derived in Figure 3 were used. The theoretical curve was obtained from ⁹³ (b) the hemoglobin and water variation with pO_2 in the same experiment are shown, which are nearly constant, since these were not varied in this experiment.

3.4. Discussion

The goal of this part of the study has been to ensure that the best quantitative accuracy is possible when imaging with the Dartmouth clinical NIR system, and the three absorption-derived measurements are separated well, without significant model-derived cross talk. The molar absorption coefficients have been derived experimentally and their

accuracy has been investigated through phantom experiments. The absorption coefficients increase linearly with blood concentration and this is accurately depicted by the tomography system, and hence the procedure of obtaining the slope and offsets from a linear fit is well justified. The molar absorption coefficients for oxyhemoglobin and de-oxyhemoglobin calculated using the heterogeneous estimate, shows good agreement with the literature values with a mean error of 7.6%, and this fact shows the robustness of the nonlinear reconstruction used, when the boundary artifacts are removed. For the homogeneous estimate, this value is higher, at 23%, which may be because of the nature of the reconstruction in trying to find a single global value for the absorption and scattering coefficients which satisfies the measurements. The homogeneous estimate has been found useful in the past to study trends in optical properties in various studies where the global parameters are used instead of the average parameters, and in such cases, it is necessary to have molar absorption spectra which takes into account the difference between the global estimates and the heterogeneous estimates.

The Hill curve data plotted in Figures 3.4 confirms that oxygen saturation can be imaged while simultaneously imaging Hb_T and water accurately, and the data suggests that a level of less than 10% error is incurred in this situation, independent of type of reconstruction used.

Overall this chapter has shown that usage of the measured molar absorption spectra yields results in agreement with theory as shown by the Hill curve data. The spectra is used in all the future studies to investigate the various parameters and information obtained from NIR tomography.

4. Interpretation of Spectral data in Normal Patients

4.1 Introduction

The breast is a highly heterogeneous and dynamically complex organ whose characteristics depend upon factors such as age, hormonal status, habitus, family and medical history and genetics^{32, 94, 95}. Normal breast tissue changes considerably during development, pregnancy and menopause as well as through the menstrual cycle. It has been documented that blood flow can increase up to 50% at the time of ovulation; and by the end of the monthly cycle, some women may undergo breast enlargement up to 20% due to increased vascularity and water content³². Total blood content can vary up to a factor of 5 or more between women based upon their body fat content, making the breast one of the most physiologically variable tissues in the human body. With near-infrared (NIR) spectral imaging hemoglobin concentration, oxygen saturation and water content can yield information about the current physiological state of the normal breast.

The range of NIR technologies that have been used to measure breast tissue varies significantly, yet the findings for breast composition with NIR are fairly consistent, as summarized here. Suzuki et al⁹⁶ studied the spectral transmission of normal breast in a

Japanese population with a time-resolved optical system using a single wavelength and showed variations in absorption and scattering properties with age and body-mass index (BMI). Quaresima et al⁹⁷ investigated spectral fitting of chromophores in the breasts of five subjects and reported variations in Hb_T, S_tO₂, water and lipids in the ranges of Hb_T = 2.9-20.4 μM, S_tO₂ = 0-90%, water fraction = 11-74% and lipid fraction = 26-90%. Cerussi et al⁹⁸ acquired measurements from 28 subjects at seven wavelengths using a frequency domain photon migration system to sample at the depth of a few centimeters in normal breast tissue. They found differences in composition between premenopausal and postmenopausal superficial breast tissue and correlations in water and lipid content with age. Pogue et al⁶ presented results, again using spectra from the literature, to evaluate measurements at four or five wavelengths from a frequency domain system that imaged the whole breast. They reported typical quantitative values for hemoglobin concentration ranging from 10 to 60μM. Shah et al⁷ described spectroscopy studies of superficial breast tissue in 14 subjects using measurements at four wavelengths and showed differences in the physiological properties between premenopausal, postmenopausal and women using hormone replacement therapy treatment where the hemoglobin content of premenopausal breast tissue was found to be highest relative to subjects with hormone replacement therapy treatment and postmenopausal tissue which were intermediate and lowest of the three groups, respectively. Durduran et al⁵ in a study of the healthy breast evaluated 52 volunteers in a parallel plate transmission geometry using three wavelengths of continuous-wave measurements. Their results showed correlation of BMI with blood volume and μ'_s under the assumption that the breast water fraction was fixed at 31%.

All of these results have been based upon either constraining the chromophores being considered in the analysis (e.g. fixed water fraction) or using complete spectral estimation but with data from only the superficial portion of the breast (e.g. NIR spectroscopy). In the study reported in this chapter and published in Srinivasan et al³¹, measurements of the whole breast have been achieved with spectral decomposition requiring no assumptions about chromophore concentrations. Molar absorption spectra were also determined with the imaging system used for clinical data collection. Specifically, a frequency domain diffuse tomography system recorded intensity and phase shift of light signals through the breast in three contiguous 1 centimeter sections where a diffusion model of light transport underpins the estimation of the absorption (μ_a) and transport scattering (μ_s') coefficients. The absorption coefficient spectra, $\mu_a(\lambda)$, are used to infer the concentrations of hemoglobin, oxyhemoglobin and water using the extinction spectra of these constituents while the scattering coefficient spectra, $\mu_s'(\lambda)$, are fit with a simplified Mie theory to derive scattering power and amplitude estimates that are related to structural particle size and density in the breast^{6,44}.

In this chapter, a cohort of 24 normal subjects with different radiographic densities was imaged with the goal of achieving accurate spectral analysis of the whole breast. The molar absorption spectra specific to hemoglobin, oxyhemoglobin and water were measured directly in the tomographic system to compensate for systemic errors or offsets related to image reconstruction, described in the previous chapter. The system sensitivity to low partial oxygen pressure (pO_2) and low Hb_T values has been systematically tested, and a spectral fitting procedure was adopted which provided the best quantitative estimate of the

optically-derived physiological parameters in the normal breast. In particular, the spectrally-decomposed concentrations were tested for correlation to each subject's BMI and radiographic density. These measurements mark one of the first efforts in in-vivo quantitative interpretation of the whole breast concentrations of Hb_T , S_tO_2 , water and optical scattering. The long term goal of this investigation of NIR in the breast is to explore the typical composition of and variability in the normal tissues which can be measured with NIR tomography and to determine which of the imaged quantities may be used as markers of disease (i.e. breast carcinoma), risk of disease, or response to therapeutic intervention.

4.2 Materials and Methods

4.2.1 Tomography system

Details of the imaging system design can be found in previous publications^{99, 100}, and in *Chapter 2*, but the salient features of the instrumentation are outlined here. The automated frequency domain NIRS device was constructed to perform cross-sectional imaging of the breast via fiber optic bundles by collecting data in three slices of tissue from sets of 16 source and 15 detector locations per slice. All source-detector fibers are arranged in a circular array and light at six discrete wavelengths between 660nm and 850nm was used to allow multi-spectral interrogation of the breast. Light detection was accomplished by high gain, high bandwidth photomultiplier tubes, and the amplitude and phase shift of the measured, suitably heterodyned signal was recorded for each source/detector pair.

The measured data was calibrated to account for small offsets due to source-detector fiber transmission and alignment characteristics as well as errors in discretization or model-data mismatch. By fitting the measurements to a homogenous calculation of the diffusion

equation on a circular geometry (of relevant size), an initial estimate of the optical properties can be obtained. This initial estimate is used in the reconstruction where the calibrated data is processed by a finite element model of the optical diffusion equation in the frequency domain. The absorption and reduced scattering coefficients at each point in the reconstructed image of the breast are obtained by minimization of the difference between the measured and calculated fluence rate intensity and phase. An in-depth description of the reconstruction can be found in *Chapter 2* of this thesis. Instead of a complete absorption map of heterogeneous regions, it is possible to segment the reconstructed image into zones to obtain quantitatively accurate estimates for these individual areas within the breast. The approach has been applied previously in theoretical studies incorporating *a-priori* information^{49, 50, 101}. This concept can be extended to consider the entire breast as a single region in order to estimate the best possible quantitative bulk value for the entire tissue. This was described in the previous chapter as the ‘homogeneous bulk estimate’; this kind of analysis will not be helpful in recovering heterogeneities, but will provide the best estimate of average optical properties as it minimizes image artifacts or errors arising from region definition that may occur in a spatially-varying reconstruction. This was used to obtain the bulk average optical properties for all the subjects imaged here.

4.2.2 Spectral Estimation of Physiologic Parameters

After reconstruction of absorption and scattering coefficient images at all six wavelengths, the absorption coefficient spectra at each location within the reconstructed image, are converted to hemoglobin concentration, oxygen saturation and water maps using the Beer’s law and approximation to Mie theory. These have been detailed in *Chapter 2* and briefly involve a least squares fit to the respective relationships.

4.2.3 Human Subjects

In this study, the spectral analysis of breast composition was carried out on data measured from the breasts of 24 normal female subjects. The clinical examinations were approved by the institutional committee for the protection of human subjects, and written consent was obtained from all participating women. The age range was 41 to 75 years. Nine of the women were premenopausal, while 15 were postmenopausal. Nine of the postmenopausal women were taking some form of hormone replacement therapy. The participants had differing radiographic density and none of the subjects were known to have any form of breast disease at the time of examination. The NIR breast examinations were carried out following procedures described previously in *Chapter 2*. Additional subject specific information was collected including age, breast size, body-mass index and radiographic density as interpreted from a recent mammography exam. The statistical analysis was carried out by biostatisticians (Jennifer Gibson and Tor Tosteson, Dartmouth Hitchcock Medical Center, Lebanon, NH) to test for correlations between the demographic and NIR parameters.

4.3 Results

4.3.1 System Calibration and Accuracy Testing

To validate the spectral decomposition of total absorption and scattering spectra into concentrations of hemoglobin, water and scattering parameters, a comprehensive series of tissue-simulating phantom studies were completed. These are documented in *Chapter 3* and allowed quantitative values to be derived for extinction spectra of (a) oxy-hemoglobin (b)

deoxyhemoglobin and (c) water obtained from our tomography system. The results from repeated measurements indicated a standard deviation error of 6% in the ability to estimate molar absorption coefficients. These coefficients represent the most accurate estimate of the molar absorption determined from the specific imaging system at Dartmouth. These coefficients were validated by obtaining the oxygen dissociation curve described in *Chapter 3*.

4.3.2 Subject Demographic Information

The left and right breasts of 24 normal subjects were imaged using the NIR tomography system. A typical example of absorption and scattering coefficient data collected from the breast of one volunteer is shown in Figure 4.1. From these spectral measurements, five parameters were derived from the NIR reconstruction and fitting: total tissue hemoglobin (Hb_T), tissue oxygen saturation (S_tO_2), water concentration, scattering power and scattering amplitude.

Table 4-1: Mean, standard deviation, and total range of the subject clinical and NIR parameters

Property	Mean± SD	Total Range
Age (yrs)	53.5 ± 10	41 : 74
Breast diameter (mm)	80 ± 13	49 : 102
BMI (kg/m ²)	25 ± 4	19 : 34
Total hemoglobin (μM)	22 ± 8	9 : 41
Oxygen Saturation(%)	58 ± 9	32 : 75
Water (%)	48 ± 12	21 : 82

Table 4.1 shows the mean, standard deviation, and range in the age, breast diameter, BMI, and NIR physiological parameters for all subjects. The clinical parameters turned out

to have statistically significant correlations with one another, although at generally low levels, as shown in Table 4.2. Association between these subject characteristics and the discrete classification of radiographic density was assessed by a one-way ANOVA (Table 4.3), comparing the standardized means of age, BMI, and breast diameter. In each case, a strong relationship with radiographic density was demonstrated.

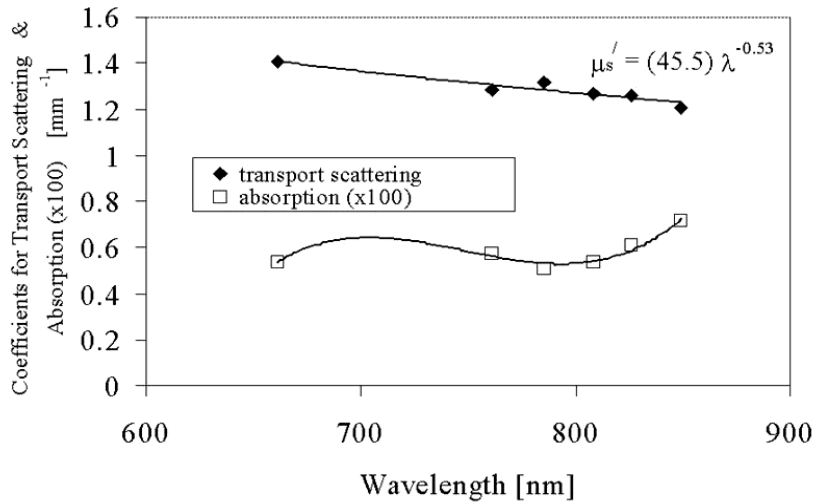


Figure 4-1: Measured absorption and transport (or reduced) scattering coefficient spectrum of a single subject's breast tissue. The data points represent the average value throughout the breast, and the lines are the best-model fits to the data. The equation for scattering shows the parameters for the optimal fit to the scattering power equation.

Table 4-2: Pearson correlation coefficients (r) and P values for three clinical parameters

Parameter	R	P
Age & BMI	0.31	0.03
Age & Diameter	0.39	0.006
BMI & Diameter	0.69	<0.001

Table 4-3: Mean values of standardized effects for subject age, BMI, and breast diameter for each of the four radiographic density categories and a global P value for differences in mean effects in these variables among the density categories

Outcome	Fatty	Scattered	HD	ED	p-value
Age	0.29	1.03	-0.36	-0.05	0.009
BMI	0.82	0.12	-0.27	-0.91	0.002
Diameter	1.05	0.20	-0.50	-0.25	<.001

4.3.3 NIR-information Relative to Age, BMI, Breast Diameter

To investigate how the NIR parameters relate to the clinical indicators of breast composition, they were tested for correlation with each of the subject demographic parameters. The most significant correlations are plotted for BMI, breast diameter, subject age, and radiographic density in Figs. 4.2–4.5.

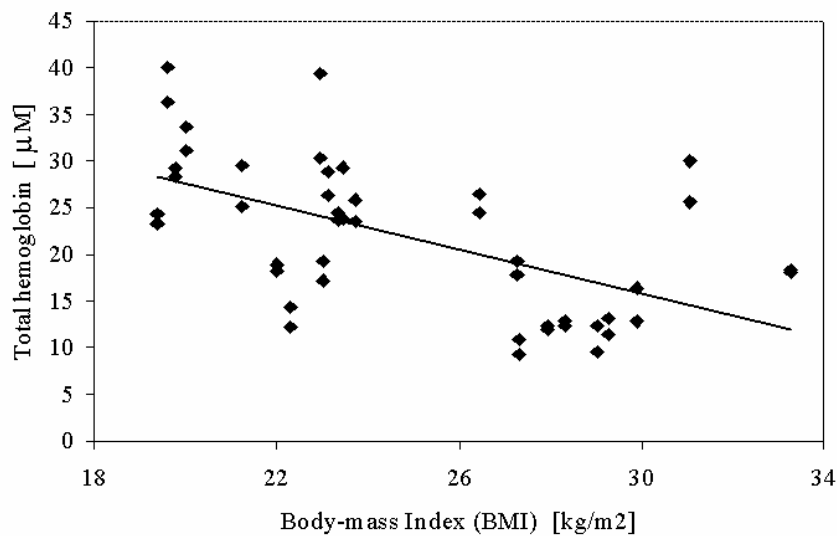
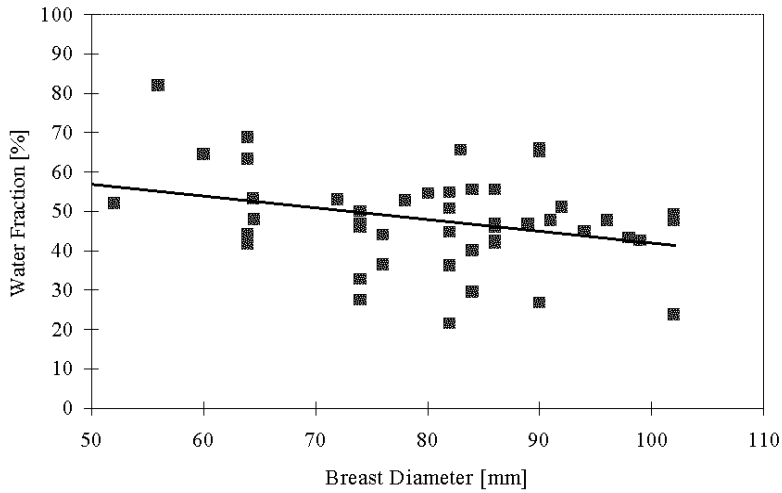
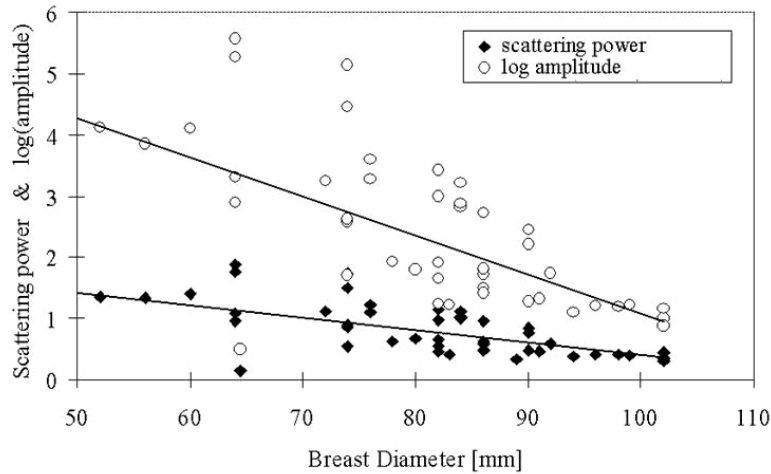


Figure 4-2: Hb_T concentration (in micromolar units) is plotted against subject BMI by using data from both breasts. The solid line is a linear regression to the data showing a statistically significant correlation ($P = 0.04$ in Table 4.4).



(a)

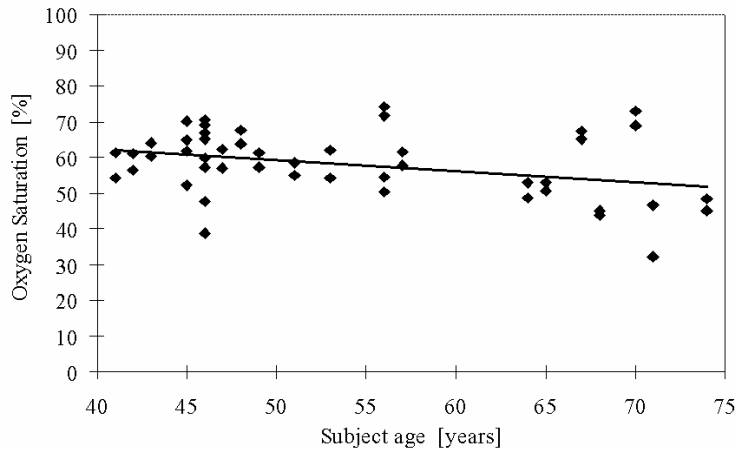


(b)

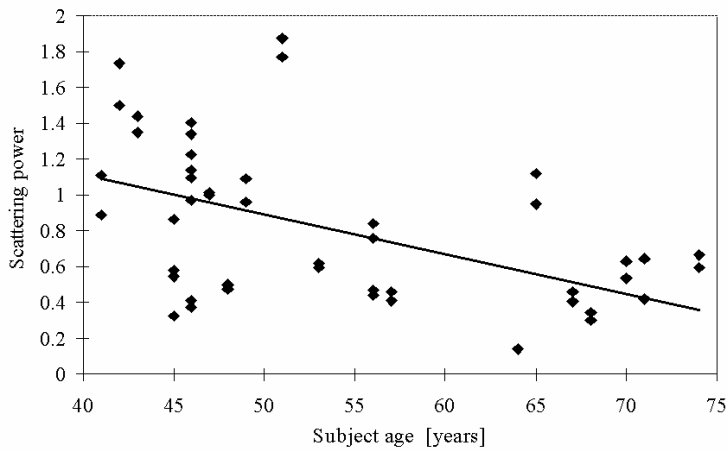
Figure 4-3: (a) Water fraction (percentage) is plotted as a function of subject breast size, showing data points for both breasts as measured in the NIR imaging array. The solid line is a linear regression to the data. (b) Scattering power and amplitude are plotted against breast diameter. Amplitude has a statistically significant correlation ($P = 0.04$ in Table 4).

Table 4.4 shows partial correlations between the five NIR parameters and the three clinical subject factors. These correlations were computed by using a random-effects regression model with the standardized NIR parameter as an outcome. Data from both left and right breasts were included with allowance for a possible correlation. The NIR

parameters correlate differently to the clinical factors. Hb_T correlates significantly to BMI, whereas S_tO_2 and water correlate most significantly to age and breast diameter, respectively. The data are plotted in a representative graph in Fig. 4.2, which shows Hb_T as a function of BMI. Fig. 4.3 shows the correlations of breast diameter with water fraction plotted in Fig. 4.3a and scattering parameters plotted in Fig. 4.3b. Some indication existed that S_tO_2 may be most strongly correlated to age, as plotted in Fig. 4.4a, but the P value was 0.06. The scattering power was significantly correlated to subject age, with $P = 0.05$, as plotted in Fig. 4.4b.



(a)



(b)

Figure 4-4: (a) Oxygen saturation is plotted as a function of subject age, with a linear regression line shown. (b) Scattering power is plotted as a function of subject age, with data points for left and right breasts included. The solid line represents linear regression to the data and presents a statistically significant correlation (Table 4.4).

Table 4-4: Estimated partial correlations relative to demographic parameters of breast diameter, subject age, and BMI, along with confidence intervals and P values for testing for a nonzero partial correlation.

NIR Property	Subject Parameter	95% Confidence interval	p-value
Hb _T	Diameter	-0.08 (-0.39, 0.24)	0.64
Hb _T	Age	-0.13 (-0.48, 0.21)	0.46
Hb _T	BMI	-0.43 (-0.81, -0.04)	0.04
SO ₂ %	Diameter	0.21 (-0.24, 0.67)	0.37
SO ₂ %	Age	-0.46 (-0.92, -0.00)	0.06
SO ₂ %	BMI	-0.19 (-0.71, 0.33)	0.48
Water %	Diameter	-0.43 (-0.88, 0.02)	0.07
Water %	Age	0.26 (-0.13, 0.65)	0.20
Water %	BMI	-0.14 (-0.59, 0.31)	0.56
Log(amp)	Diameter	-0.40 (-0.77, -0.03)	0.04
Log(amp)	Age	-0.32 (-0.67, 0.03)	0.09
Log(amp)	BMI	0.21 (-0.19, 0.62)	0.31
Scatter power	Diameter	-0.30 (-0.60, 0.00)	0.07
Scatter power	Age	-0.36 (-0.71, -0.01)	0.05
Scatter power	BMI	0.18 (-0.20, 0.57)	0.36

4.3.4 NIR Information Relative to Radiographic Density

The subjects in this study were chosen with various radiographic densities. In general, it was found that the scattering amplitude appears to increase with increases in radiographic density. The statistical analysis of these data (presented in Table 4.5) shows that the extremely dense category was different from the fatty category, for both NIR scattering parameters. It is possible that further numbers of subjects would allow a more significant discrimination among these density categories as well, based on NIR scattering. Fig. 4.5 shows the mean of the scattering power and amplitude for each radiographic density

category. Nondense (i.e., fatty and scattered categories) breast tissue has the lowest hemoglobin and water content, whereas dense breast tissue has the highest water percentage and hemoglobin concentration. When a multivariate analysis of the data is completed, as shown in Table 4.5, no significant difference in Hb_T , oxygen saturation, or water content occurred among the radiographic density groups. Although hemoglobin may appear to increase with radiographic density, this increase is a result of other factors.

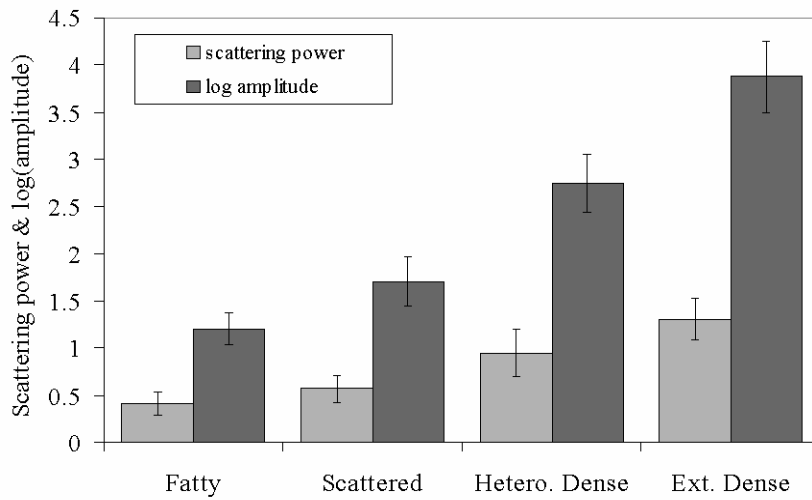


Figure 4-5: NIR scattering power and amplitude are plotted as a function of the four radiographic density classifications with average values from all patients shown by the shaded bars and the standard deviation between subjects shown as the error bars. A significant difference exists between fatty and extremely dense categories for both parameters (Table 5). Hetero: heterogeneous; Ext.: extremely.

4.3.5 Trends Between NIR Parameters

It is important to assess whether duplicate or complementary information exists between the NIR parameters, themselves. A multivariate test was performed to estimate the Pearson's correlation coefficient and the P values for significance between Hb_T , S_tO_2 , water, scattering power, and amplitude. The results are included in Table 4.6, and indicate that Hb_T is uncorrelated to S_tO_2 and water, but statistically correlated to the two scattering parameters

although with modest degrees of linearity. S_tO_2 is significantly correlated to water content with stronger linearity, but not to the scattering parameters.

Table 4-5: A comparison of mean standardized values for NIR properties among radiographic density groups and statistical P values for difference from the fatty group.

NIR property	Subject Radiographic Density	95% Confidence interval	Comparison to Fatty group, p-value
Hb _T	Fatty	-0.22 (-0.93, 0.49)	
Hb _T	Scattered	0.45 (-0.70, 1.60)	0.42
Hb _T	Het. Dense	-0.53 (-1.43, 0.37)	0.23
Hb _T	Extr. Dense	0.11 (-1.27, 1.48)	0.87
SO ₂ %	Fatty	0.40 (-0.55, 1.35)	
SO ₂ %	Scattered	0.16 (-1.37, 1.69)	0.83
SO ₂ %	Het. Dense	0.56 (-0.65, 1.77)	0.35
SO ₂ %	Extr. Dense	0.92 (-0.90, 2.75)	0.31
Water %	Fatty	0.09 (-0.72, 0.90)	
Water %	Scattered	-0.02 (-1.32, 1.28)	0.98
Water %	Het. Dense	0.36 (-0.69, 1.40)	0.48
Water %	Extr. Dense	-1.20 (-2.75, 0.34)	0.12
Log(Scatt. Amp.)	Fatty	-0.44 (-1.18, 0.29)	
Log(Scatt. Amp.)	Scattered	-0.39 (-1.58, 0.79)	0.50
Log(Scatt. Amp.)	Het. Dense	-0.48 (-1.42, 0.46)	0.30
Log(Scatt. Amp.)	Extr. Dense	-1.60 (-3.01, -0.19)	0.03
Scatter power	Fatty	-0.57 (-1.29, 0.15)	
Scatter power	Scattered	-0.48 (-1.65, 0.69)	0.40
Scatter power	Het. Dense	-0.67 (-1.58, 0.24)	0.14
Scatter power	Extr. Dense	-1.76 (-3.16, -0.36)	0.02

As expected, the scattering parameters are highly linearly correlated to each other, because they are estimated from the same model fit to the data. Figures 4.6 and 4.7 depict two of these trends, namely oxygen saturation versus Hb_T (i.e., uncorrelated in this data set)

in a , and scattering power versus Hb_T in b (i.e., correlated in this data set with modest linearity). These are further examined in *Chapter 10*.

Table 4-6: Correlation coefficients among the derived NIR properties with corresponding P values for testing for the presence of an association between properties

	Hb_T	$SO_2\%$	Water %	Log (Scatt. Amp)	Scatter power
Hb_T	1.0	0.32 ($p=0.13$)	-0.00 ($p=1.0$)	0.43 ($p=0.03$)	0.45 ($p=0.03$)
$S_tO_2\%$		1.0	-0.68 ($p<0.001$)	0.05 ($p=0.80$)	0.04 ($p=0.87$)
Water %			1.0	0.24 ($p=0.03$)	0.26 ($p=0.23$)
Log (Scatt. Amp)				1.0	0.99 ($p<0.001$)

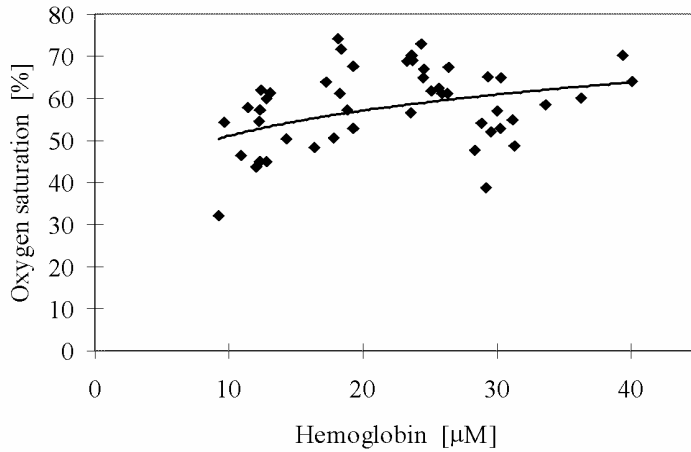


Figure 4-6: Subject NIR parameter oxygen saturation is plotted against Hb_T .

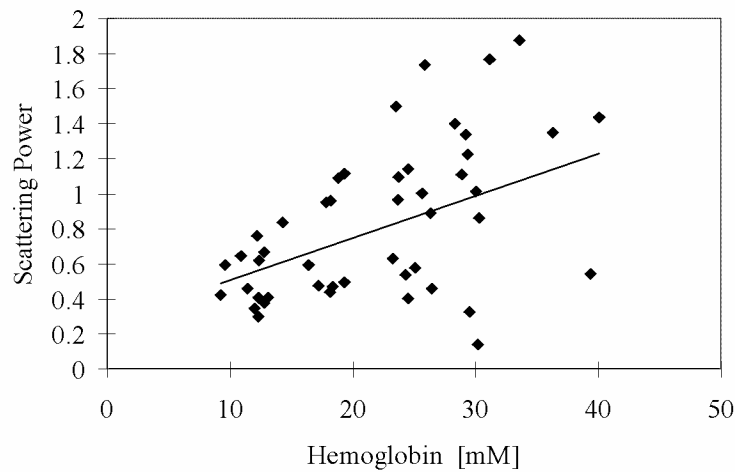


Figure 4-7: Scattering power versus Hb_T . for the normal patient pool of data.

4.4 Discussion

The goal of this work has been to examine the breast tissue information available from the NIR-derived measures of Hb_T , oxygen saturation, water concentration, scattering power, and scattering amplitude. These parameters are a direct consequence of tissue function and structure and should provide properties that are different, yet complementary to those obtained in x-ray mammography. The prelude to this study has been to ensure quantitative accuracy when imaging with the clinical experimental system at Dartmouth. To this end, the results in *Chapter 3* have shown that the three absorption-derived measures (Hb_T , S_tO_2 , and water) are separated well, without significant model-derived cross talk. The preclinical phantom measurements confirmed that oxygen saturation can be imaged, while simultaneously imaging Hb_T and water accurately, and the data suggest that a level of less than 10% error is incurred in this situation.

An important aspect of this work is the spectral correlation with clinical characteristics such as age, breast size, and BMI based on whole-breast data. Imaging the whole breast contrasts with earlier studies that have interrogated a portion of the breast, usually the superficial regions. Results from spectroscopy studies may also misrepresent spatial changes in transmitted spectra as being related to the tissue, whereas, in some cases, they may have more to do with the exterior breast geometry. In this study, the tissue was encircled with a fiber optic array, the measurements of reflected and transmitted light from which were analyzed with geometry-specific numerical modeling of the light propagation, an approach shown to provide the most accurate prediction of tissue optical properties, and

therefore, the most accurate prediction of whole-breast concentrations of Hb_T , S_tO_2 , water, and scattering.

The subject population studied here presented a reasonable cross-section of radiographic densities, ages, breast diameters, and BMIs. The fact that age, BMI, breast size, and radiographic density are themselves statistically correlated with modest linearity, suggests that they do not yield much independent information, yet when correlating the NIR parameters to these factors we do observe significant correlations to specific clinical parameters. For example, BMI, which should provide a reasonable measure of breast fat content, is most strongly correlated to Hb_T , which would indicate a decreased amount of functional tissue involving a lower vascular density. BMI was not significantly correlated to the other NIR properties, suggesting that Hb_T provides a measurement that appears unique to the composition of the breast and one that is not possible to obtain radiographically. Further studies of Hb_T in tumors and its correlation to histologically assessed vascular density are required (carried out in later *Chapter 8*). Measurements in animal tissues and tumors generally confirm that Hb_T concentration as measured by NIR spectroscopy is a linear function of the total vascular density¹⁰²⁻¹⁰⁴.

The scattering parameters measured from normal breast tissue also appear to yield new information. The numbers (Table 4.4) indicate that optical scattering (both amplitude and power) is most strongly correlated to the breast diameter, subject age, and possibly breast density. Because the structural matrix of tissue and its vascularity contribute to scattering, it would appear that age (Fig. 4.4*b*) and breast diameter (Fig. 4.3*a*) are major indicators of extravascular breast tissue characteristics. Further, the scattering parameters

were the only ones to correlate to changes in radiographic density. This makes sense assuming that radiographic density is dominated by changes in the structural composition of the breast (i.e., fat and fibroglandular tissue components) and that these same contributions to scattering occur both in x-ray interactions (i.e., Compton scattering) and in the NIR optical range (i.e., Mie scattering). Thus, although it could be argued that radiographic density provides a measure similar to the optical scattering coefficients, it may be that measuring the optical scattering coefficients provides a good indicator of breast density. Because breast density is strongly correlated to risk of cancer development²³, a measurement of optical scattering density may provide a nonionizing surrogate for radiodensity.

Measurement of tissue water content may be an important indicator for the breast as well. Water concentration was not correlated to any of the four clinical parameters investigated here, and was found to be uncorrelated to Hb_T (Table 4.6); however, indications are that it could be correlated to breast diameter ($P=0.07$). Water content in the breast is presumably dominated by contribution from extravascular spaces, because the fraction of blood vessel volume is generally less than 1%; yet, the water percentages measured in these subjects were in the 40–60% range. Thus, the measurement of water is a direct indication of the water in the interstitial and cellular compartments. Studies have shown that water and fat content are inversely related, which also supports the idea that the NIR water parameter is an extravascular measurement.

The fourth NIR parameter that was recovered was oxygen saturation of the breast. This parameter did not vary much over the subject pool, which suggests that the normal breast maintains a consistent oxygen extraction fraction. The only trend that appeared to

indicate possible correlation was subject age ($P=0.06$). Further studies with more enrollments might determine whether this correlation is truly significant. In tumor tissue where metabolic imbalance is present, a reduction in oxygen saturation might be expected, and has been reported in selected cases¹⁰⁵. Animal studies also support the hypothesis that reduced oxygen saturation occurs in more aggressive tumors with disorganized vascular patterns^{102, 106}. Further study of oxygen saturation as correlated to tumor growth rate and vascular density should provide important information about the extent to which this parameter supplies unique information.

In summary, the NIR measurements indicate that the absorbing and scattering components of breast tissue all occur in different proportions within the normal subject population and that demographic trends exist that help us determine what the significance of these measurements may be. Each of the five derived parameters has a unique correlate to subject characteristics, and the trends observed can be explained by what would be expected as normal physiologic variation in the population. Further analysis of breast tissue composition and correlation to NIR spectroscopic parameters will help to firmly establish the accuracy of these measurements. Studies of how these parameters vary spatially within the breast and how they vary in pathologically altered breast tissue will also help to determine what clinical value may be present in this measurement system. Promising avenues of research may lie in the study of how Hb_T, oxygen saturation, water, and NIR scattering vary between stages or types of breast pathologies. Such characterization is attempted in *Chapter 8*.

5. Multi-Stage Reconstruction Approach for Improved Quantification of Small Objects

5.1 Introduction

The process of obtaining the optical properties from the measurements of fluence at the periphery of the domain is a complex problem. Several models have been developed and of particular interest is the diffusion approximation to the radiation transport equation. Described in *Chapter 2*, this approximation is widely used because it can be computationally fast and robust when implemented using the finite element approach, providing a flexible way to model arbitrary tissue volumes⁴². Image reconstruction results have shown accurate spatial recovery of heterogeneities, however the common consensus seems to be that the spatial resolution is poor, which results physically from the dominance of scattering within tissue^{41, 48}. There is also some limitation on the ability to uniquely separate absorption and scattering coefficients when both variations exist within tissues, although empirical methods have been devised to minimize this problem¹⁰⁷. Even when absorption and scattering images can be recovered (as in most cases), the quantitative characterization of heterogeneities in terms of their absorption coefficient has been found to decrease as the size of the heterogeneity decreases¹⁰⁸, which is a side effect of having images that are essentially low-pass filtered in spatial frequency.

Studies have shown that optical properties are recovered to within 15% of true value in cases of anomalies of size 25mm (placed just off center)⁵³, and 25% for heterogeneities of size 17mm¹⁰⁷; however, for an object of 10mm, the error limit can be much higher. In 3-D modeling of diffusion theory, studies^{51, 109} have shown that the recovery of optical properties are significantly underestimated(only 15% of the true value could be reached for an object of diameter 8mm⁵¹). Since, this inaccuracy affects the resultant chromophore concentrations, the ability to quantify hemoglobin, oxygen saturation and water suffers as a result.

Several studies have focused on developing innovative approaches to solving the problem of maximizing the accuracy of imaging small objects. For example, Jiang and Paulsen implemented a technique to modify the objective function in order to minimize both the least square error and the total-variation of the field, which provided reconstruction of objects with sharp edges, thereby minimizing the total variation between pixels within the field⁷⁵. Other alternative objective functions are possible, and several have been attempted with limited success^{110, 111}. Eppstein et al introduced the idea of using successive zonation approaches in image reconstruction, similar to the multi-grid methods used in larger scale relaxation methods¹¹². Another concept along these lines is to use *a-priori* information about the size and position of the tumor to enhance the quantitative accuracy of absorption and scattering of tumors as demonstrated by Schweiger et al⁴⁹, Pogue et al⁵⁰, Dehghani et al^{51, 52}. This kind of high accuracy characterization would be especially useful to have in imaging of small objects. However, the *a-priori* information is typically obtained from MRI and requires a combined MRI-NIR system, which is currently unavailable in most cases. While all of the techniques noted above have their strengths and weaknesses, one overriding issue is the

need for a problem-dependent calibration factor in the objective function, or the inclusion of *a-priori* information in the process.

The work in this chapter was directed towards developing an algorithm for increased accuracy in quantification of heterogeneities without *a-priori* information and without a strong need for empirically derived calibration factors. It applies a variant of the zonation technique proposed by Eppstein et al¹¹², and follows a systematic investigation of how to accurately implement the approach. Specifically, the existing reconstruction algorithm has been modified to first start with the standard Newton minimization approach followed by zonation methods to reduce the problem to one that is uniquely defined and does not require regularization. The modification examined is a 3-step reconstruction where step 1 consists of the existing algorithm which gives the approximate size and position of the anomaly while step 2 repeats this reconstruction with a two-parameter regularization scheme where the anomaly (detected as a region of interest from step 1) is given a lower regularization compared to the background, yielding more freedom to update in areas with the largest change in optical properties. This type of reconstruction allows the heterogeneity to recover its true size, and the knowledge of size and position of the anomaly are extracted from this second step. Step 3 is a region-based reconstruction that uses the second step results as a priori information, to produce a quantitatively accurate value for the optical parameters. This method substantially improves the image accuracy and has been validated using simulated and experimental data for anomalies between the sizes of 10mm and 20mm with differing contrasts and positions. Finally the algorithm is applied to clinical subject data to examine how it changes the observed contrast in a tumor relative to the background breast properties.

5.2 Methods

The image reconstruction is based on the frequency domain diffusion equation used to model light propagation in highly scattering media^{35, 91}. This is explained in *Chapter 2*. Briefly, the core of the reconstruction scheme is a Newton-Raphson minimization method for iteratively updating the optical property parameters based on minimization of the standard sum of squared differences between the measured and calculated optical fluence (Φ) at specific detector locations. This type of error is a measure of the fit of the model to the measured data, and often referred to as the projection error and is commonly used as a surrogate measure of the convergence of the algorithm.

5.2.1 Step 1: Levenberg-Marquart reconstruction algorithm

The use of Levenberg Marquardt regularization is explained in *Chapter 2*. The Levenberg-Marquart technique gives the solution by iteratively solving:

$$\Delta\mu = (\mathfrak{J}^T \mathfrak{J} + \lambda I)^{-1} \mathfrak{J}^T \Delta\Phi \quad (5.1)$$

where \mathfrak{J} is the Jacobian matrix consisting of derivatives of Φ with respect to μ_a and κ for each source-detector location pair; where μ_a is the absorption coefficient and κ is the diffusion coefficient given by:

$$\kappa(r) = \frac{1}{3[\mu_a(r) + \mu_s'(r)]} \quad (5.2)$$

with μ_s' being the reduced scattering coefficient. $\Delta\mu$ in Equation 5.1 is the vector containing the perturbations of μ_a and κ , and $\Delta\Phi = (\Phi_{meas} - \Phi_{cal})$ where Φ_{meas} and Φ_{cal} are the measured and calculated fluence detected at the boundary. I is the identity matrix and λ is the regularizing factor that stabilizes the solution (i.e. matrix inversion). The value of λ in Equation 5.1 obviously determines the nature of the relationship. If λ is too high, it dominates the relationship in Equation 5.1 and successive iterations do not yield much change in the update vector. However, if this damping factor is too small, then the problem will be dominated by noise in the data. Previously, it was found empirically that a starting value of λ in the range of 1000 to 1 reasonably recover the optical images⁷⁴, and noise begins to dominate for starting regularization values below 1. The stopping criterion is met when the projection error is within 2% of the previous iteration's error. This typically occurs at 10-12 iterations, and all the reconstructions in step 1 in this study have begun with $\lambda = 10$. This algorithm when implemented, recovers spatial heterogeneities in approximately the correct position¹⁰⁷. Because of the ill-posed nature of the problem, the size of the anomaly is typically blurred with an approximately Gaussian-shaped profile¹¹³, and the average quantification of optical properties is underestimated, with this underestimation depending on the heterogeneity size^{107, 113}. However, since this reconstruction recovers the heterogeneity in its approximate position, this is used as step 1 of the three-step procedure.

5.2.2 Step 2: Two region regularization

Since the regularization parameter governs the smoothness or freedom of the pixels to change more from one iteration to the next, if a lower regularization parameter is specified in a region of interest (ROI) compared to the background, the pixels in the ROI have more opportunity to update so that the properties ultimately reach the true value, and

the ROI reaches the true size. In step 2 of the multi-stage reconstruction, λ in Equation 5.1 is rewritten as

$$\lambda(k) = \begin{cases} \lambda_1, k \in ROI \\ \lambda_2, k \notin ROI \end{cases} \quad (5.3)$$

where λ_1 and λ_2 are two selected regularization parameters, with $\lambda_1 < \lambda_2$.

The ROI to be given lower regularization is determined by full width half maximum (FWHM) criterion on the final absorption or scattering coefficient images (when the algorithm has iterated to stopping criterion) from step 1. ROI computed this way is the region containing all the reconstructed nodes having optical parameters greater than or equal to a threshold defined as the difference between maximum and half of the difference between the maximum and mean of the parameter throughout the image. It is assumed that FWHM gives a reasonable measure of the size of the recovered heterogeneity. Due to the blurring effect, the ROI defined from step 1 typically encompasses the actual heterogeneity as well as a transition zone. In comparison, when the final images from the second step are regionized in the same way using FWHM, a more accurate size estimate of the heterogeneity is obtained. The quantitative accuracy of the property value recovery from step 2 may still deviate from the true value, but it is expected to be closer to the true values relative to step 1. The best numerical values to use for λ_1 and λ_2 will depend on the object size as well as its contrast and position. In our algorithm, we have examined a series of values for λ_1 and λ_2 and chosen the optimal pair based on the projection error behavior-the pair giving the lowest projection error at the last iteration (when error change is less than 2%) is used.

5.2.3 Step 3: Region based reconstruction using spatial information from step 2

Step 3 of the process is a region-based reconstruction which has been applied previously in the context of using *a-priori* information⁴⁹⁻⁵¹. The implementation of this algorithm has been described in detail in⁵¹. In short, it consists of homogenizing regions in the mesh, by updating selected zones uniformly so that the final image consists of a significantly reduced set of parameter values which represent the property estimates for the individual regions. This type of reconstruction where the number of unknowns have been reduced to the number of regions, has shown quantitative accuracy of 97% and 93.4% in absorption and scatter for an 8mm object as shown by Dehghani et al⁵¹ using 3-D reconstruction. Simulations in 2-D have indicated similar high accuracy, given precise information about the size and position of the heterogeneity, as reported in the results section. In the third step, the geometric constraints are derived from step 2. The mesh is assigned regions through the zonation of areas based upon FWHM peaks in the absorption or scatter images from step 2. This algorithm has proved to be sensitive to accurate position and size estimates for the anomaly, and hence, the approximate ROI size obtained from step 1 has proved to be inadequate for accurate quantification. Step 3 can be given an initial guess obtained by averaging the optical coefficients in step 2 ROI and a regularization factor of 100. It can also be given the same initial guess as the two previous steps, and both converge to the same result with nearly identical projection error, the only difference in the final result being the number of iterations in which it converges.

5.3 Results

The results presented in the following sections focus on the need for quantitative accuracy in NIR tomography (*Section 5.3.1*) and demonstrate the application of the 3-step

reconstruction to simulated and experimental data and the sensitivity of the algorithm to both contrast and position of the anomaly (*Section 5.3.2*). *Section 5.3.3* shows promising results when applied to clinical patient data with an abnormality. While these results are specific to breast imaging, the concept can be extended to all 2-D or 3-D FEM applications of the diffusion approximation for improved quantification in an ROI.

5.3.1 The advantage of a priori information

The boundary data at modulation frequency 100MHz was generated using the forward solver (Equations 2.1-2.3)⁴⁵ for a circular disc of diameter 86mm (mesh contains 1785 nodes) with a single absorbing heterogeneity. The model had a background $\mu_a = 0.005 \text{ mm}^{-1}$ and $\mu_s' = 1 \text{ mm}^{-1}$; and data for *Sections 5.3.1 and 5.3.2* were generated for differing absorption coefficient in the anomaly ranging from 1.2 to 4.0 times the background in increments of 0.2. This type of data was generated for a circular object of diameter 10mm, 15mm and 20mm. Random Gaussian-distributed noise (1%) was added as in all simulated data (amplitude and phase) used in this study (1% noise has been established to be the level of shot noise in the experimental system¹⁰⁸). The object was positioned 10mm from the edge in all cases. The initial guess for the reconstructions from all three steps, was obtained from calibration of the data⁶⁹ with a homogenous set of measurements generated on the same mesh with 1% noise. As noted, the initial guess for steps 2 and 3 can also be obtained from the average reconstructed values from the previous stage of the reconstruction. There is no difference in the two approaches except in the number of iterations required for the solution to converge.

Figure 5.1(a) shows the average value for absorption coefficient recovered in the region of interest for different diameters of the anomaly (10, 15 and 20mm), for varying contrast, based on step 1. The reconstruction was stopped when the projection error was less than 2% of the previous iteration and a starting regularization parameter of 10 was used in all cases. The average value was computed as the mean of the absorption coefficient within the FWHM of the peak absorption coefficient. The high frequency noise near the boundary typically found in the images due to hypersensitivity close to the boundary, was removed from consideration during the regionization. Figure 5.1(a) shows data that indicates quantitative accuracy suffers as the diameter of the anomaly decreases. Specifically, the mean % error with respect to the true value used to generate the data has increased from 28% for a 20mm object, to 38% for a 15mm object, to 47.3% for a 10mm object.

A simple analysis has been pursued to evaluate how this percent error in absorption coefficient estimates propagates into the estimation of chromophore concentrations. The analysis begins with a known set of chromophore concentrations (Hb_T , S_tO_2 and water) and obtains the absorption coefficients corresponding to these concentrations using matrix multiplication $(\mu_a) = [\varepsilon](c)$ where ε is the molar absorption spectra at the six wavelengths available in our system, as evaluated in *Chapter 3*¹⁴ and c is the concentration of deoxyhemoglobin, oxyhemoglobin and water). Random noise was added to these set of absorption coefficients at the six chosen wavelengths, and the concentrations were recovered using a constrained linear least-squares fit. This analysis was carried out for a starting concentration of total hemoglobin=30 μ M, oxygen saturation=60% and water=60% (typical concentration found in the breast tissue⁵), and the percent error estimate used is the mean of 1000 such repetitions. This is explained in further detail in *Chapter 6*. The results

show that, using the current six wavelengths used by the Dartmouth system, an error of nearly 50% in the reconstructed absorption coefficient for an anomaly of 10mm diameter, can result in as much as 70% error in our estimation of water content in the breast. Since the accuracy in these parameters is likely a key determinant of the diagnostic utility of NIR information, this analysis shows the importance of quantitative accuracy in recovering the optical absorption coefficient, especially in small objects.

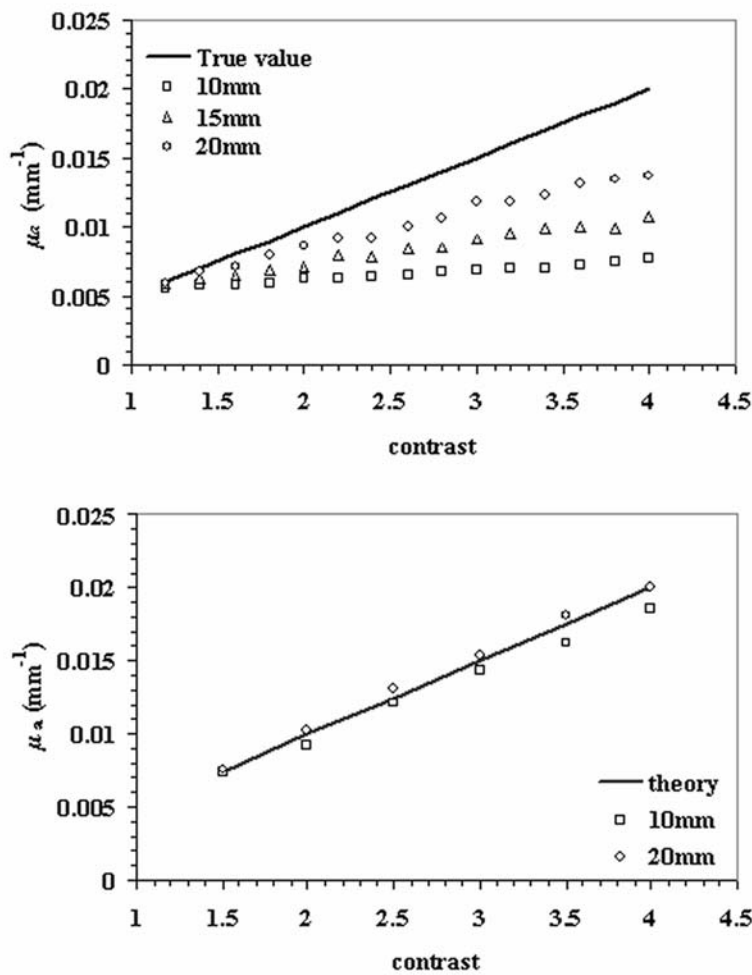


Figure 5-1: (a) Average reconstructed absorption coefficients plotted as a function of contrast for heterogeneities of different diameters compared to the true values, which illustrate the bias error as the size of the heterogeneity decreases. (b) Same as Figure 5.1(a) for 10mm and 20mm heterogeneities using region-based reconstruction with a priori information on the position and size of the inclusion.

If the size and position of the anomaly is known *a-priori* without steps 1 and 2, this information can directly be incorporated in our region-based reconstruction (step 3), to recover the average optical properties in the ROI and background. Results from such a reconstruction for an anomaly of size 10mm and 20mm for varying contrasts has shown in Figure 5.1(b), where data was generated in a similar fashion as above, with 1% noise. Accurate results with less than 6% error are obtained for objects of both 10mm as well as 20mm diameter (5.35% for 10mm and 2% for 20mm). Hence, knowledge of anomaly position and size is extremely useful and important in cases of objects of 10mm in size. The next part of the study is targeted at extracting this information from the existing reconstruction.

5.3.2 Application of three stage reconstruction

Figures in 5.2 shows the application of the three stage reconstruction to the data generated in Section I where the quantification of the average property estimate has been improved by the final stage of the reconstruction. As noted earlier, the regularization parameter for step 1 is 10, whereas for step 2, the optimal pair of the starting parameters has been chosen by searching over all sets of possible parameters, with λ_1 in the range 10-25 (varied in steps of 5), and λ_2 in the range 1-10 (in steps of 1). This range of parameters was chosen empirically after testing the algorithm for different ratios of λ . The pair giving the lowest projection error at the last iteration has been chosen for step 2 and the regularization pair so obtained varies with contrast and size of the anomaly. The results from this stage are carried on to step 3. There is improvement in accuracy from a 47.3% mean error in step 1 to a 27.3% mean error in the final step of this 3-stage reconstruction. There are certain spurious

oscillations in the curve for step 3, and these oscillations probably stem from very small scale fluctuations present in the results from step 1, since step 1 provides the starting estimate for the ROI. There are certain artifacts in the image arising from the small size of the anomaly and the underdetermined nature of the reconstruction problem, which are also a possible reason for the oscillations. The reduced scattering coefficient is found to stay constant in the ROI, with a standard deviation of 0.06 mm^{-1} , for varying contrast in absorption coefficient and there is a 12% increase in the mean of the reduced scattering coefficient resulting from step 3.

The same analysis was carried out for data from an anomaly of 15mm diameter where the results obtained from the final stage of the 3-step reconstruction have been compared to the theoretical values and the original results in Figure 5.2(b). As in the case of the 10 mm anomaly, Figure 5.2(b) is encouraging and shows increased quantitative accuracy. Specifically, the error has dropped to 13% in the final reconstruction step compared to 38% in original algorithm. Figure 5.2(c) shows analogous results for a 20mm diameter anomaly. As expected, the algorithm achieves better quantification of larger objects (mean error of 5.5% in final step, compared to 28.2% in the original reconstruction). The background absorption is found to stay constant for all three anomaly sizes illustrating that the background is not strongly affected by the three stage algorithm.

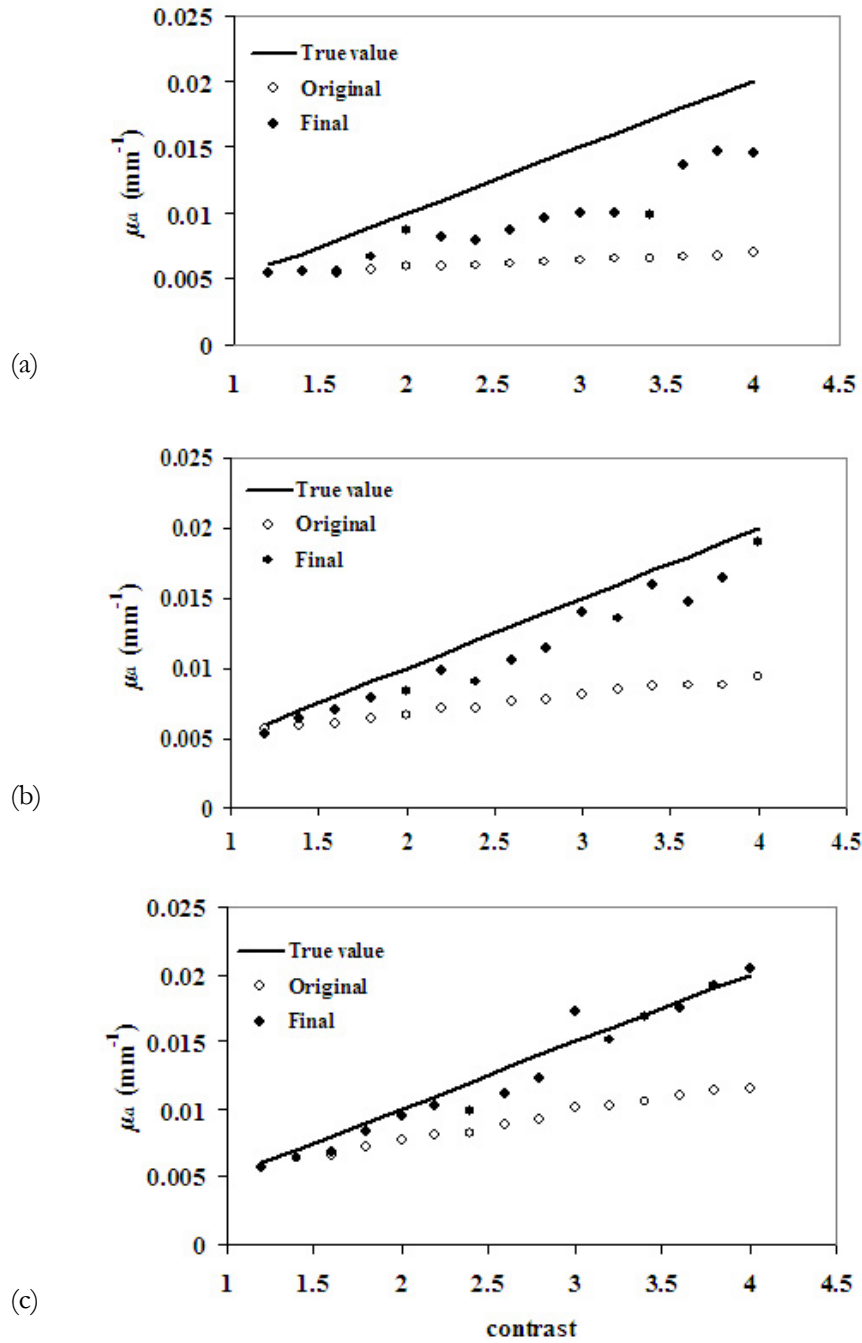
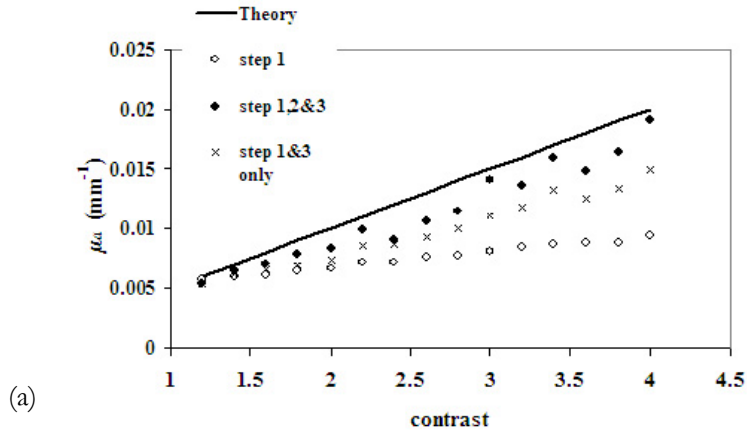


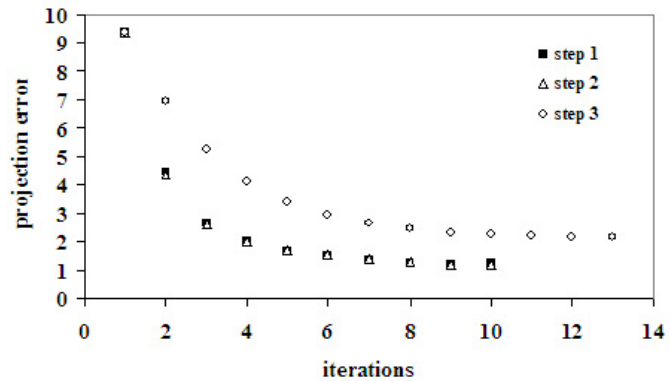
Figure 5-2: (a) The average reconstructed absorption coefficients in the heterogeneity are shown for the 10mm diameter anomaly, obtained using the original reconstruction (stage 1) and using a final step of the three stage reconstruction. These are compared against the true values for differing contrast levels. (b) same, using a 15mm diameter anomaly. (c) using a 20mm diameter anomaly.

In order to illustrate the importance of the sequence of steps in the three-stage reconstruction, a comparison of the results obtained by the three stage reconstruction, with using just steps 1 and 3, is shown in Figure 5.3(a), for the 15mm anomaly case. The mean percent error improvement by using the three stage reconstruction is 13% compared to 24% observed by using just steps 1 and 3. The plot of projection error as a function of iterations for different reconstruction steps, (15mm anomaly, contrast = 2.2 case), is shown in Figure 5.3(b). The projection error in step 3, which generates the most accurate average optical parameters, is higher than step 1 and 2, which is expected since this is a homogenous estimate in the anomaly and background, and a two-unknown problem is not sufficient to compensate for high frequency variations near the boundary. This observation is consistent in all the studies done including the experimental and patient data. Figure 5.3(c) shows the difference in the projection error between starting the third step with same initial guess as the previous steps relative to using an average of parameters from the previous steps of reconstruction. Both converge to the same projection error in step 3; and the quantitative values of the recovered optical properties were also found to be almost identical.

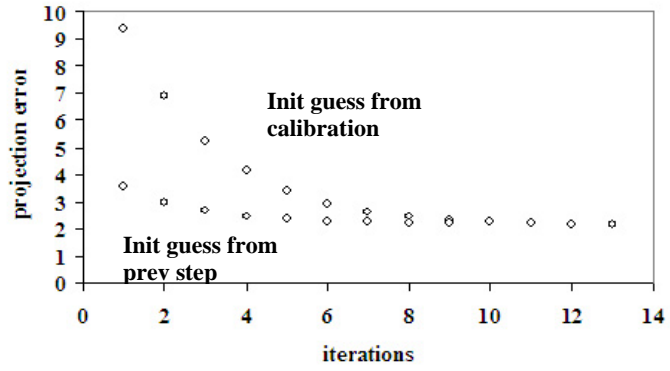
The results shown in Figure 5.2 indicate that the three stage reconstruction yields improved quantification for all degrees of contrast studies; however, all of the results have been based on a single location of the anomaly. Application of the algorithm for different anomaly positions at a fixed contrast (2:1, ROI relative to background) has been explored. Data was generated as before for an anomaly with the same background properties as for Figures 1 and 2 ($\mu_a = 0.005 \text{ mm}^{-1}$ and $\mu_s' = 1 \text{ mm}^{-1}$) with 1% random noise. This time the position of the anomaly was varied starting 10mm from the edge to center in steps of 3mm, for both 10mm and 20mm diameters. After calibration, the 3-step reconstruction was carried



(a)



(b)



(c)

Figure 5-3: (a) Comparison of average reconstructed absorption coefficient in the heterogeneity for the 15mm anomaly, obtained using just step 1, using steps 1 and 3, without step 2, and using the sequence of steps 1, 2 and 3, which shows the advantage of the sequence of three stage algorithm.(b) Projection error versus iteration number for the three steps of the reconstruction algorithm, when recovering an image from simulated data for a 15mm diameter anomaly with a contrast of 2.2 with the background. (c): Projection error versus iteration number for the final step of reconstruction, using an initial guess from calibration compared to an initial guess from the previous step of reconstruction.

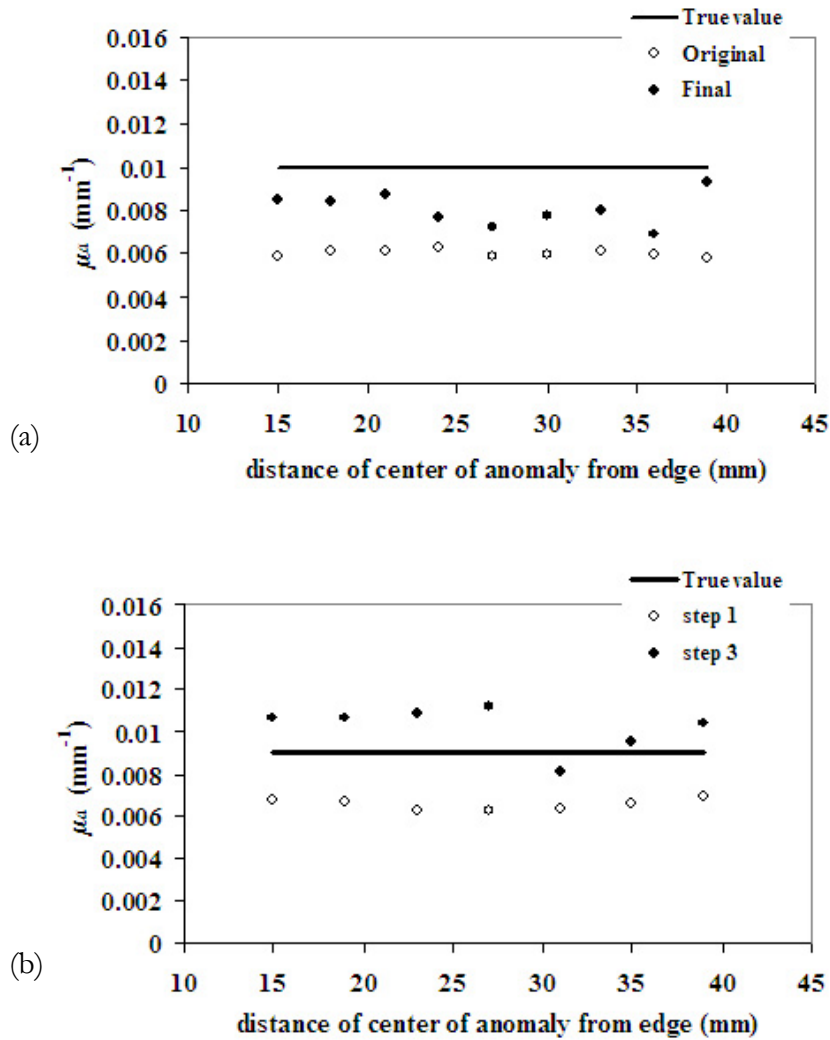


Figure 5-4: (a) Average reconstructed absorption coefficient in the inclusion for different positions of a 10mm region obtained from the original reconstruction (stage 1 only) and the final step of the 3-stage algorithm. Results are also compared with true values. The measurement data was simulated and the position of the inclusion was varied from a location 10mm from edge to the center, in increments of 3 mm. (b) same, for experimental data is used from a 10 mm object. The position was varied from a location 10mm from edge to the center, in increments of 4 mm.

out and Figure 5.4(a) shows the reconstructed average absorption coefficient for step 1 (original reconstruction) and step 3 (final stage) along with the theoretical value. As seen from the Figure, the final step provides better quantification compared to step 1. Overall,

the reconstruction shows variation with the position but no clear trend is visible. The mean error was decreased from 40% in step 1 to 19.47% in the final step. The variation in the reconstructed values in the final stage for different positions was 9.32% of their mean, suggesting that the 3-step algorithm is largely insensitive to position of the anomaly.

To show the improvement in quantification and insensitivity to position using experimental data, data with similar parameters was used, as collected by Xiaomei Song¹¹⁵. Specifically, an 84mm cup phantom was made of epoxy resin, with India ink for absorption and titanium dioxide for scattering¹⁰⁸, (optical properties measured by the system) with a wall thickness of 5mm. This cup was filled with Intralipid solution of the same optical properties as the phantom ($\mu_a = 0.0045 \text{ mm}^{-1}$ and $\mu_s' = 1.12 \text{ mm}^{-1}$, measured independently). A cylindrical rod of diameter 10mm (made similarly as the cup phantom) with optical properties of $\mu_a = 0.009 \text{ mm}^{-1}$ and $\mu_s' = 1.5 \text{ mm}^{-1}$ was moved starting 10mm from the edge to the center, in 4mm increments where measurements were acquired using the Dartmouth frequency domain NIR system¹⁰⁰. The 3-step reconstruction was carried out on the data and the results are shown in Figure 5.4(b). The graph shows that there is improvement in accuracy using the 3-step reconstruction, and again similarly to Figure 5.4(a), the variation in the absorption coefficient offers no clear trend. The error has been reduced from 27.56% in step 1 to 16.26% in step 3. There is an overshoot in the absorption coefficient values in some positions, which may be due to experimental artifacts.

Figures 5.5(a) and 5.4(b) show the analyses for a 20mm anomaly. The simulations were performed in the same way for different positions of the anomaly and the trends are similar to Figure 5.4(a): the simulated data shows improvement in accuracy from 23.2% in

original reconstruction to 9.8% in final stage. The same experiments were also conducted for a rod of diameter 20mm and quantification has been improved from 19.64% to 6.8% in this case.

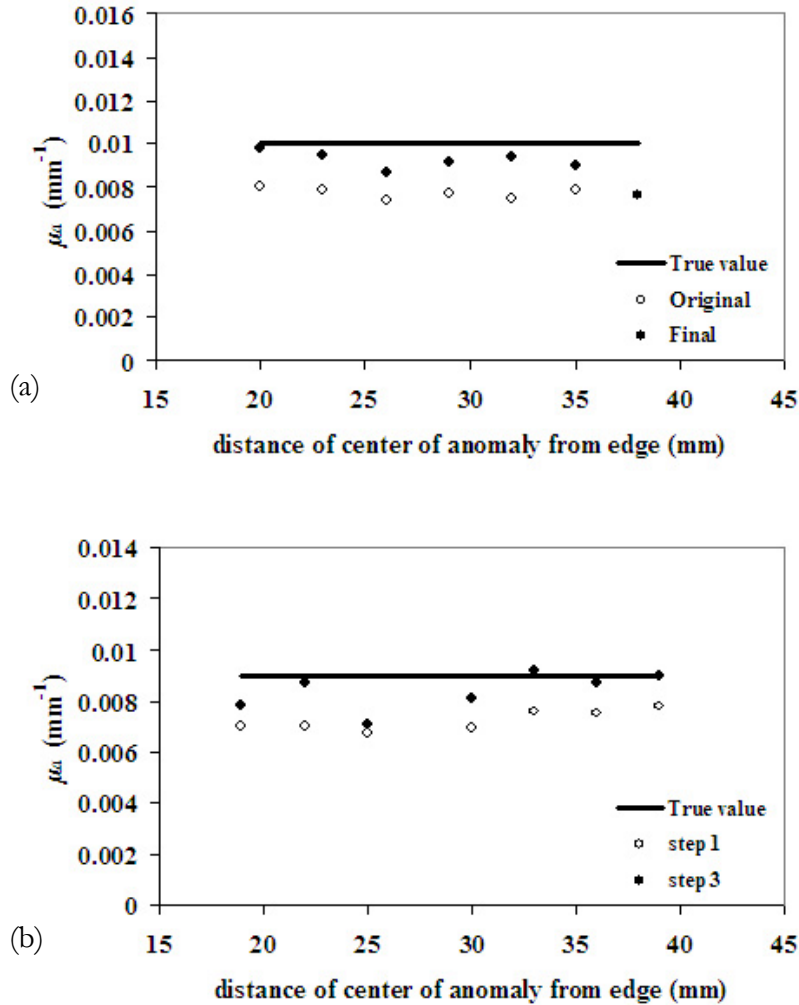


Figure 5-5: (a) Average reconstructed absorption coefficient in the inclusion for different positions of a 20mm anomaly (similar to Figure 5.4) using simulated data; (b) for experimental data. The position of the inclusion was varied from 10mm from the edge to the center, in increments of 3 mm.

5.3.3 Clinical abnormality: absorption and scattering heterogeneity in different positions

All the results presented in the previous sections had either an absorption-only heterogeneity or both absorption and scattering heterogeneity located in the same position. However, in the clinical environment, breast images with abnormalities may contain absorption and scattering heterogeneities of different sizes and in different positions. The algorithm can still be applied in this case where the regionization from step 1 is based on both absorption and scattering images and these regions are assigned lower regularization compared to the background for step 2. This ensures that both absorption and scattering heterogeneities are under-damped, and hence can update to the true size and quantitative property value. The regionization from step 2 is again absorption and scatter based, and the model is divided into different zones so that the region-based reconstruction for step 3 can generate accurate average optical parameters in the assigned areas. This algorithm was implemented and explored with simulated data using background properties $\mu_a = 0.01 \text{ mm}^{-1}$ and $\mu'_s = 1.0 \text{ mm}^{-1}$ and a 15 mm absorption anomaly having twice the background ($\mu_a = 0.02 \text{ mm}^{-1}$) located with center coordinates at (0,-20) and a 15 mm scattering object of $\mu'_s = 1.5 \text{ mm}^{-1}$ with center coordinates close to (0, 20) and 1% random Gaussian noise. It was found that the scattering object always appears in reduced size compared to its true extent while the absorption object is exaggerated. Empirically, it was found, increasing the scattering region obtained by FWHM of the scattering image by 20% of its radius and decreasing the absorption region by 20% of its radius in stages works with simulated data to bring the regionized size to its original expanse. The recovered size as it emerges in step 3 was found to be almost identical to the original 15mm size of the anomalies, and there was no

observable shift in position. The images from the three steps are shown in Figures 5.6(a), (b) and (c). An accurate quantification with 13% error in μ_a and 5.8% error in μ_s' was found in the final step and the values for the background and the anomaly for the initial and final steps are reported in Table 5.1.

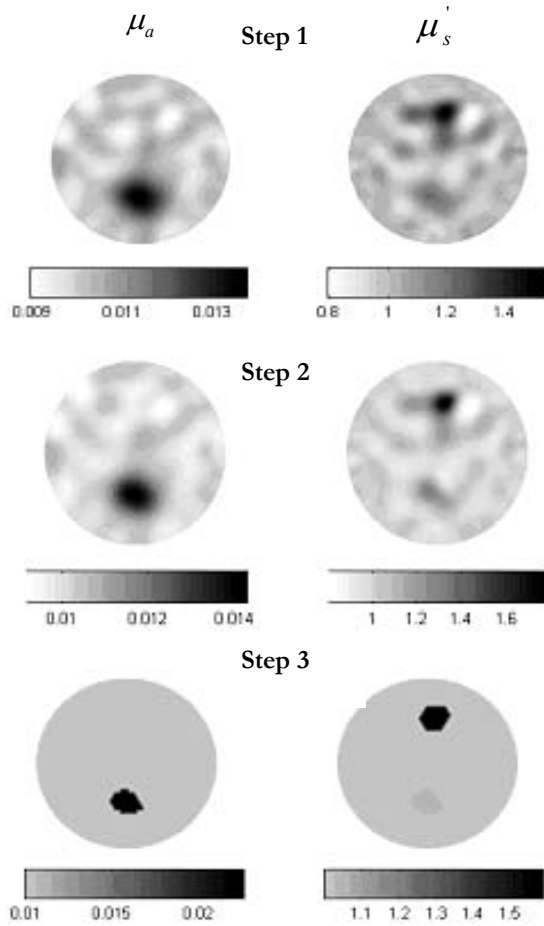


Figure 5-6: (a), (b), (c): Reconstructed images from the three stages of reconstruction, respectively, using simulated measurement data with 1% Gaussian-noise generated from a phantom with background properties of: $\mu_a = 0.01 \text{ mm}^{-1}$ and $\mu_s' = 1.0 \text{ mm}^{-1}$ and a 15mm absorption object near 6 o'clock with $\mu_a = 0.020 \text{ mm}^{-1}$ and 15 mm scattering object with $\mu_s' = 1.5 \text{ mm}^{-1}$ near 12 o'clock.

Table 5-1 The average reconstructed parameters for the three stages of reconstruction quantified from regions in the final images, when applied to the simulated data shown in Figure 5.6.

	Average μ_a in anomaly (mm⁻¹)	Average μ_a in background (mm⁻¹)	Average μ_s in anomaly (mm⁻¹)	Average μ_s in background (mm⁻¹)
Step 1	0.0128	0.0101	1.3977	1.0117
Step 2	0.0132	0.0101	1.5938	1.0115
Step 3	0.0226	0.0099	1.5865	1.0015

This algorithm was automated and implemented on measurements from the left breast of a Caucasian subject of age 38yrs, diagnosed with an intraductal carcinoma from biopsy. Mammograms showed that the cancer was in the 6:30 clock face position and 3cm from the nipple. The NIR breast exam was completed within an imaging study which has approval by the Dartmouth Institutional Review Board where all subjects participate under informed consent. Figure 5.7 shows the application of the 3-step algorithm on this clinical data measured at 785nm. From the reconstructed images in step 1, we can see that the increased absorption appears at the position of the tumor and increased scattering contrast presents in a different position. These two regions were given lower regularization, and step 2 was carried out, which yields comparable images to step 1. Step 3 shows the 3-region reconstruction where the background, absorption anomaly and scattering anomaly whose size and position was obtained from step 2, were updated uniformly. Table 5.2 shows the average absorption and scattering values from the three steps, and as seen, the absorption coefficient is much higher in step 3 compared to step 1 and step 2 and likely more accurate relative to previous results. The contrast has been enhanced in the final stage through increased absorption at the site of tumor and lower background values.

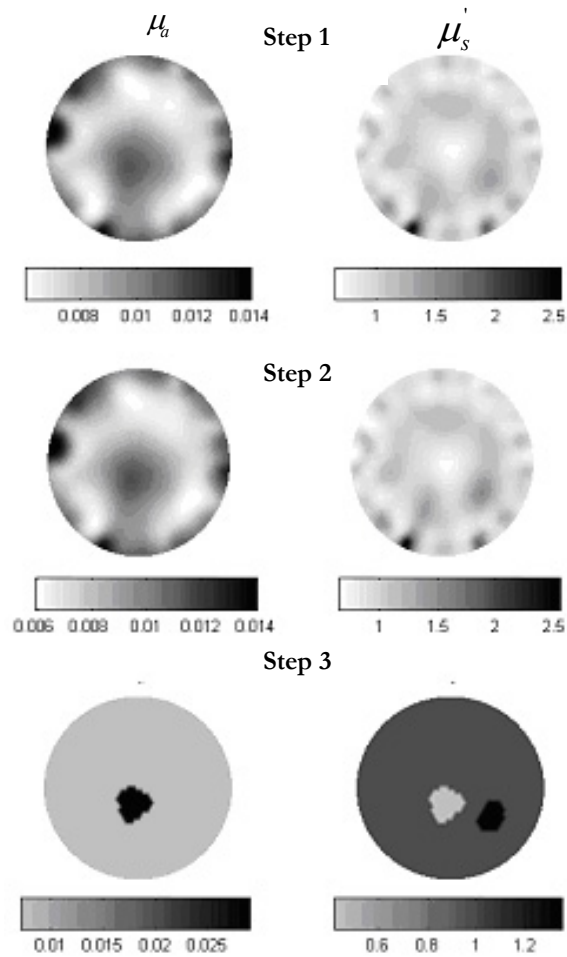


Figure 5-7: (a), (b), (c) Reconstructed images from the three stages of the reconstruction, using clinical data at 785nm wavelength from the left breast of a subject having an intraductal carcinoma in the lower region of the breast. The measurements were recorded 30mm from the nipple.

Table 5-2: The average reconstructed parameters from the three stages of reconstruction when applied to an image from the clinical data, discussed in Figure 5.7.

	Average μ_a in anomaly (mm⁻¹)	Average μ_a in background (mm⁻¹)	Average μ_s' in anomaly (mm⁻¹)	Average μ_s' in background (mm⁻¹)
Step 1	0.010455	0.0085	0.9251	1.0033
Step 2	0.010584	0.008523	0.9175	1.0036
Step 3	0.02904	0.007645	0.4245	1.002

5.4 Discussion

The primary benefit of NIR diffuse optical tomography arises from the ability to image tissue volumes that characterize the breast functional status. Early iterations of the reconstruction can yield images with the correct heterogeneity locations, but at these early iterations the quantitative values of optical parameters are significantly underestimated (by near 50% or more). Later iterations show more noise and artifacts in the image but the quantitative values of optical properties recovered are closer to the true values. The focus of the current study has been quantitative property accuracy rather than overall image quality and hence, all reconstructions have been allowed to proceed until the projection error reduction is less than 2%. The simple analysis in Section 5.3.1 has shown that a 50% error in quantifying the absorption coefficient of an object, translates into nearly 70% error in estimation of its water content, which indicates the importance of quantification in NIR tomography.

The three stage reconstruction has been implemented on simulated data with 1% random Gaussian noise for a range of typical contrasts in tumors of up to a maximum absorption of 4 times the background. The results show improved quantification in 10mm, 15mm and 20mm diameter region data by bringing the reconstructed optical property values closer to tolerable error limits. The background absorption was found to stay constant and hence improved contrast has also been observed using this method. The graphs in Figure 5.2 show that the algorithm yields results which are insensitive to contrast compared to the original single step algorithm where the higher contrasts were more difficult to recover. The algorithm has been tested for variation in position of the anomaly (from edge to center) and

insensitive to object position because changes expected in positioning are treated in the first two steps. This trend was also evident in experimental data for anomaly sizes of 10mm and 20mm, and the experimental results show improved quantification as well, with error reductions from 28% to 16% in the 10mm case and from 20% to 7% in the 20mm case.

The results in Section 5.3.3 indicate that the algorithm can accommodate both absorption and scattering heterogeneities, where accurate values within error limits of 15% for absorption and 6% for scattering have been obtained in simulated data with 1% random Gaussian noise. The algorithm has been successfully applied to clinical data and the tabular column in Table 5.2 shows a much higher contrast of 3.8 in the absorption coefficient between tumor and background in the final step compared to 1.23 in the original reconstruction. The main drawback with patient data is that there is no knowledge of the true optical properties; however studies performed in phantoms and with simulated data suggest that the values from the final step of reconstruction are much closer to the actual properties relative to the original reconstruction. Tromberg et al²⁸ showed measurements with a frequency domain photon migration (FDPM) system where a contrast of approximately 3 fold was observed between tumor versus normal sites when the probe was placed just 5mm lateral of the tumor center. Our results also show that quantification of contrast in the focal region has been increased substantially when the tumor is zoned through region based reconstruction. The images of patient data in Figure 5.7 also demonstrate the tradeoff between image quality and quantitative accuracy. In the three-stage reconstruction, the images from the final step contain homogeneous regions in the breast, and characterize the main anomalies. These may not be the best images since different kinds of tissue, such as glandular, fatty and fibrous are present in the breast. However, the

regionization improves the reliability of the modality in quantifying chromophore concentrations in the tumor, at the cost of characterization of other heterogeneities in the breast. Since this characterization is available from step 1, it is not completely lost and the information from the final step is more reliable in quantifying the optical properties of the tumor.

Finally, the method of defining the two regularization parameters in step 2 by the projection error approach is very robust since this includes the change in these parameters due to changes in contrast and size of the anomalies. The algorithm is automated and can easily be executed in a multiprocessor computing environment. Future studies (*Chapter 6*) show the importance of such improved quantification by analyzing the effects of error in μ_a in total hemoglobin, oxygen saturation and water content.

6. Error Models: Interpreting effects of Error in Absorption in Chromophore Concentrations' Recovery

6.1 Introduction

Near-infrared imaging applied in breast cancer allows functional information to be obtained that may be used to diagnose tumors based on their metabolic and functional status represented through vascularization, oxygenation and water content. Light absorption is caused by different absorbing chromophores in tissue such as hemoglobin, oxy-hemoglobin and water. Hence, by obtaining images of the absorption coefficients (μ_a) at multiple wavelengths, one can spectrally de-convolve the contributions from each of these chromophores, to obtain images of total hemoglobin, oxygen saturation and water content.

The Dartmouth optical tomography system permits multi-slice multi-wavelength frequency domain measurements to be obtained from the periphery of the breast. Image reconstruction is carried out using a finite element model to the diffusion approximation, the breast tissue being in the scatter-dominated regime in the NIR wavelength range. Details of these processes can be found in *Chapter 2*. While tumors in the breast have been detected in this manner as a contrast in absorption/hemoglobin images^{6, 27, 28} higher than the surrounding normal tissue, the dominance of scattering makes it difficult to obtain accurate

quantification of these parameters⁴⁷. *Chapter 5* has shown that *a-priori* spatial information obtained through a preliminary first pass reconstruction can be used in a multi-step recovery procedure and improves the quantification of μ_a . However, this quantification is not infallible in that, error in recovery of absorption coefficients still exists. Such error can vary from nearly 50% without priors to 30% with spatial priors for small anomalies (in the order of 10mm) and is in the range of 5-15% for medium sized tumors of sizes 15mm and 20mm.

The general trend in recovery of absorption properties is an underestimation, where the magnitude of underestimation depends on the tumor size^{53, 107, 116}. Since, the chromophore concentrations are obtained from μ_a at six wavelengths, their quantification suffers as well. The molar absorption coefficients (absorption per unit concentration) of these chromophores, differs with wavelength, and accordingly, depending on the concentration, the mean error in recovery of μ_a , will have different effects. For example, for a highly de-oxygenated tissue sample being imaged, the error in quantification of μ_a at 661 nm, will have a dominant effect on recovery of de-oxy hemoglobin, since this particular chromophore is the dominant absorber at this wavelength. The work in this chapter performs a systematic evaluation of the propagation of the error in transforming absorption into chromophore information, by incorporating a random error model (simulating the random error due to limited wavelength availability) and a systematic error model (simulating the negative bias observed in reconstruction).

6.2 Materials and Methods

Simulations were carried out using the FEM solver for image reconstruction as described in *Chapter 2*, for establishing the trend of negative bias in image reconstruction. The forward data for amplitude and phase was generated using the forward model and 1% random Gaussian noise was added to mimic an experimental setting⁴³. The absorption and reduced scattering coefficient images were reconstructed and mean error was calculated as the difference between the true property value and the average in the anomaly, whose size was defined by a FWHM criterion.

For the error models studied in this chapter, the spectral fit to Beer's law was used, given by:

$$\mu_a = [\varepsilon]c \quad (6.1)$$

so that the concentration vector c is calculated in a least squares constrained fit by putting the absorption coefficients at different wavelengths in the vector on the left hand side and the molar absorption spectra ε for the chromophores for the corresponding wavelengths on the right hand side. In this way, the concentrations of oxy and de-oxy hemoglobin and water were obtained as well as extended indices given by $Hb_T = HbO_2 + Hb$ (in μM), and oxygen saturation as $S_tO_2 = HbO_2 / Hb_T \times 100$ (in %). The error models were used to study the associated propagation for use of the six wavelengths currently used in the Dartmouth optical tomography system (described in *Chapter 2*), as well as effects of extending the number of wavelengths as well as their range to 600-1000nm.

6.3 Results

6.3.1 Negative Bias in Recovery of μ_a

The quantitative reliability of chromophore concentration estimation depends significantly on the accuracy of the spectral optical property estimates. *Chapter 5* evaluated the error trends in recovery of anomalies of sizes 10, 15 and 20mm. Described in Section 5.3.1; Figure 6.1 shows the recovered mean in the anomaly (of differing sizes and contrasts), calculated from the reconstructed images using simulated data. This Figure indicates that quantitative accuracy suffers as the diameter of the anomaly decreases, and the mean % error with respect to the true value used to generate the data, has increased from 28% for a 20mm object, to 38% for a 15mm object, to 47.3% for a 10mm object.

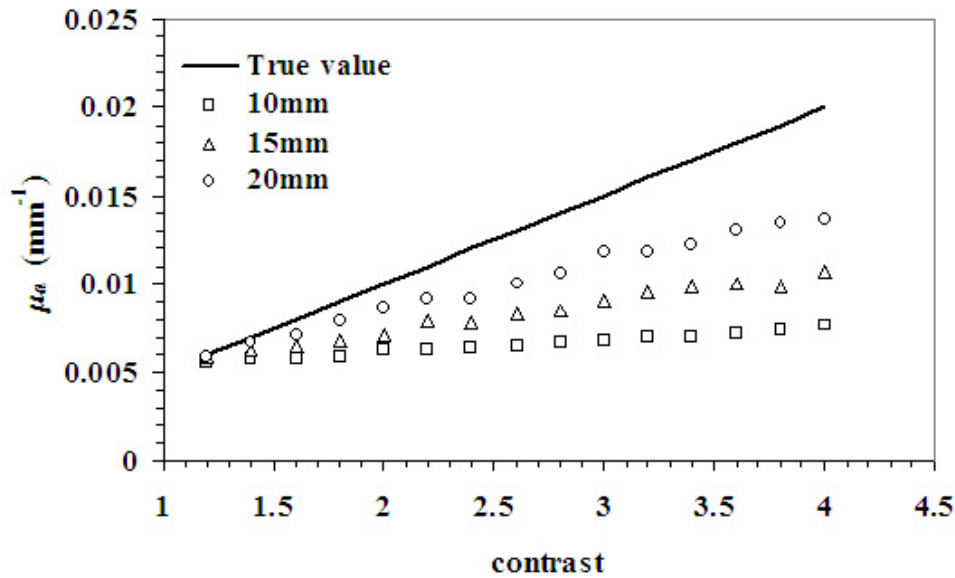
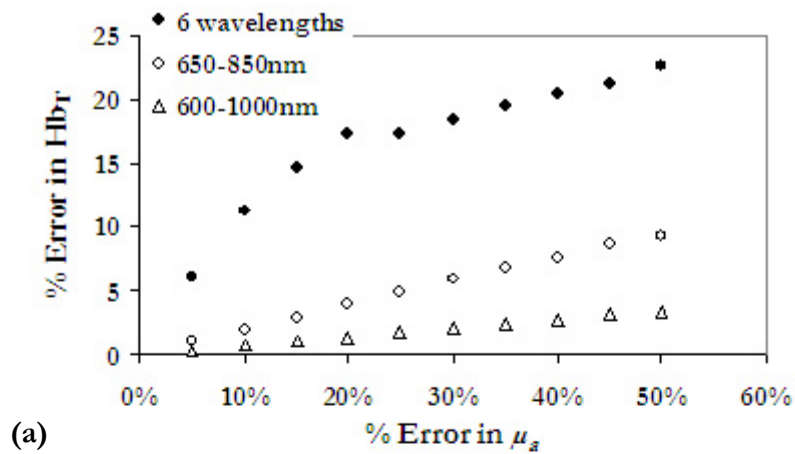


Figure 6-1: Reconstructed absorption coefficient for different sized inclusions, as a function of the contrast relative to the background absorption. These are simulated data with region of interest values taken from the final images.

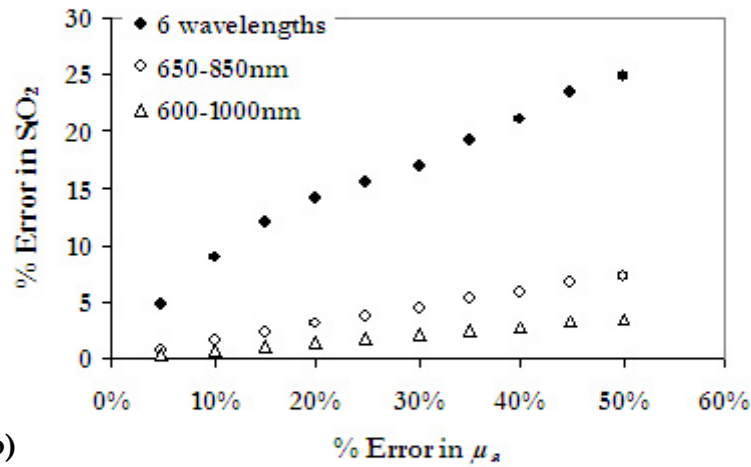
6.3.2 Random Error Propagation Model: Effects of Increasing Wavelengths

It is useful to analyze how the % error projects onto the estimation of the chromophore concentrations. Towards this purpose, a systematic error propagation analysis was carried out by starting with a known set of chromophore concentrations (known Hb_T , S_tO_2 and water) and obtaining the absorption coefficients corresponding to these concentrations using the simple matrix multiplication from Equation 6.1. In the random error model, a random noise level was added to these set of absorption coefficients at the 6 wavelengths, and the concentrations were recovered back using a constrained linear least-squares fit, so that the % error manifested in the concentrations as a results of error in absorption coefficients could be estimated. This analysis was carried out for a starting concentration of $Hb_T=30\mu M$, $S_tO_2=60\%$ and water=60% (typical concentration found in the breast tissue⁵), where the % error in the final chromophore concentrations retrieved, was the mean from 1000 such runs (where the results have converged) of adding random noise. The results (Figure 6.2) show that, using the current six wavelengths used by the Dartmouth clinical system, the “reasonable error limit” of 15% in μ_a recovery still results in nearly 50% error in quantification of water, though the error limit is closer to 15% for recovery of Hb_T and S_tO_2 . The high % error of nearly 50% currently found in the reconstructed absorption coefficient for an anomaly of 10mm diameter, can result in around 70% error in the estimation of water content in the breast. Since the accuracy of these parameters are the key factors in diagnosis, this kind of analysis shows how important it is to have quantitative accuracy in the optical absorption coefficient, which is especially low in small objects.

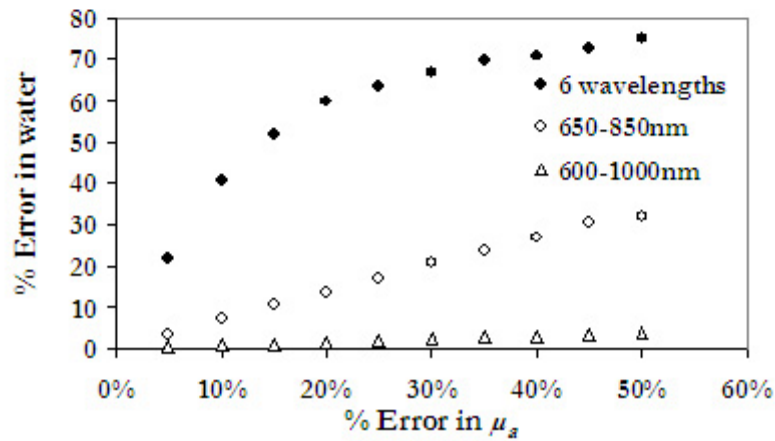
Carrying this analysis to the next step, the levels of quantification, if information from the entire useful spectrum is available, is considered next. In Figure 6.2, similar analysis as above was carried out, but the calculation was extended to incorporate two cases: (a) all the wavelengths in interval of 2nm, between 650-850nm (101 wavelengths) and (b) between 600 -1000nm (201 wavelengths) were assumed available. As expected, the levels of error drop. This signifies that chromophore information is more immune to accuracy in quantification of μ_a in the presence of so many wavelengths, with 600-1000nm range giving the best results. This is due to the fact that between 850nm and 1000nm, stronger features of water can be captured, improving the accuracy of its recovery. This type of analysis was also done for different starting concentrations (oxygen saturation = 20% instead of 60%, water = 30% instead of 60%), and the results showed higher % error values for the lower concentrations.



(a)



(b)



(c)

Figure 6-2:(a) The percent error in the calculated total hemoglobin value is estimated based upon spectral fitting with random errors assumed in the absorption coefficient, showing how the error would change with different numbers of wavelengths used in the measurements. In (b) the same error propagation calculation is shown for oxygen saturation and in (c) for water content.

6.3.3 Parabolic Error Propagation Models: Incorporating Negative Bias

A random error model is representative of a homogeneous estimate of μ_a , clinically observed images however, are closer to heterogeneous test objects. Results from Figure 6.1 indicate that the accuracy of μ_a depends on the size of the tumor/anomaly as well as the contrast in μ_a between the anomaly and the background. Figure 6.3 shows this error as a function of size and contrast; similar to the analysis in *Section 6.3.1*. Forward data was similarly generated for a test phantom with varying contrast in the inclusion, for different size inclusions (10, 15 and 20mm diameters) with 1% random Gaussian noise. 15% random variation was allowed in the optical properties, used to generate the data, in order to create a heterogeneous domain and the contrast scale was extended to 15 times the background, to observe the broader trend in recovery. The anomaly average value for μ_a was obtained from the reconstructed images and the percent error (calculated as the difference between true and recovered average divided by the true value) between the mean and the true values are shown in Figure 6.3. The graph shows a parabolic relationship in % error with the contrast variation, with the error saturating at higher contrasts, close to the maximum possible error of 100%.

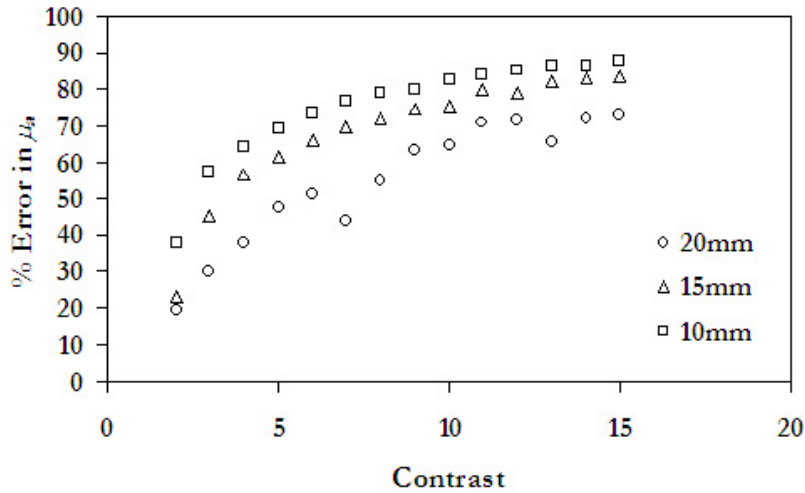


Figure 6-3: Error in recovery of μ_a as a function of contrast between the anomaly and background absorption for different inclusion sizes, shows a parabolic trend, with saturation at higher contrasts, due to inability of the reconstruction to recover steep changes between anomaly and background.

The error in recovery of μ_a does not, however depend on the wavelength (ignoring the measurement differences in the instrumentation system for different wavelengths). To illustrate this, forward data was generated for a test phantom containing a single anomaly of diameter 20mm, placed 10 mm from the edge, in a domain of total diameter 86mm. The phantom had background concentrations of 10 μ M Hb_T, 100% S_tO₂ and 100% water content. The anomaly had 30 μ M Hb_T and 100% water, and S_tO₂ was varied from 100% to 0% in steps of 5%. The images for the optical properties for each of the wavelengths were reconstructed, and Figure 6.4(a) shows the error in μ_a as a function of the wavelength; for 100% oxygenated situation, the errors at all the wavelengths are comparable, illustrating the independence to wavelength. However, the error at 661nm increases as the domain becomes more de-oxygenated, and this was found to be directly correlated to the contrast available between the anomaly and the background for μ_a (see Figure 6.4(b)) at 661nm. Hence, as

the contrast available increases, the current algorithm struggles in following the steep change in absorption between the anomaly and the surrounding domain, so that the percent error in quantifying the properties increases. Taking into consideration the observed results which indicate that error in recovery of absorption spectra is systematic with a negative bias, instead of having random fluctuations, a systematic error model was devised.

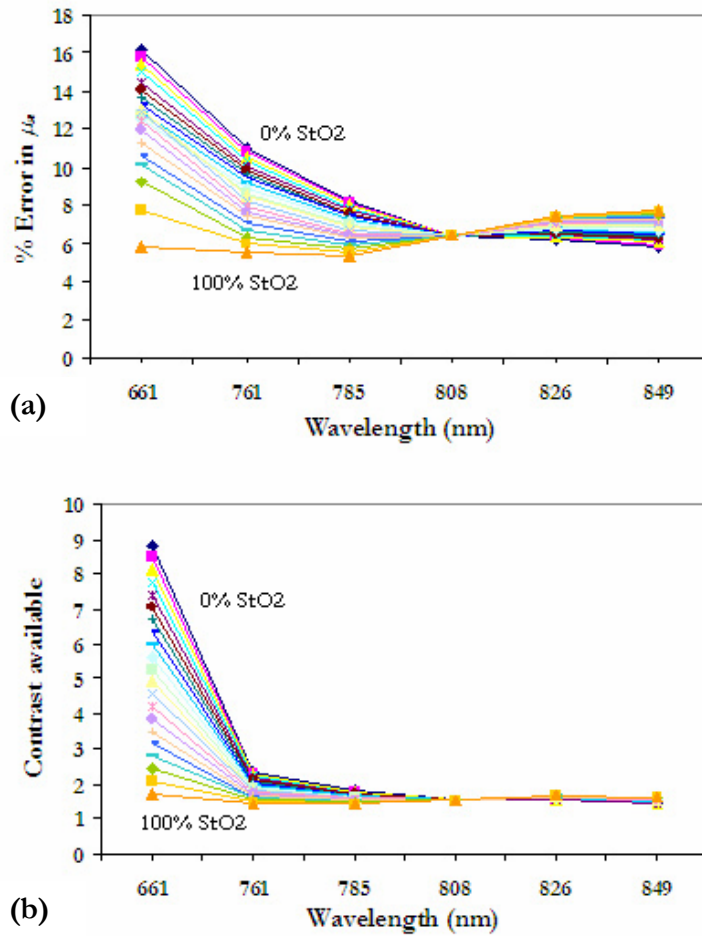


Figure 6-4:(a) Error in recovery of μ_a for different wavelengths as calculated from the reconstructed images; the different lines are for varying S_tO₂ from 100% to 0% in steps of 5%; (b) shows the true contrast available in μ_a between the anomaly and background, suggesting that the increasing error in (a) for lower S_tO₂ is because of the higher contrast (due to de-oxyhemoglobin absorption) available at 661nm.

This parabolic indication was implemented in an error model which adds % error in μ_a based on the contrast available in the anomaly versus background, given by:

$$y = A(x - x_1)(x - x_2) \quad (6.2)$$

where y is the % error added to μ_a for the particular wavelength, A is the percent noise to be added (to the lowest contrast wavelength), x is the contrast between the anomaly and background for the wavelength and x_1 and x_2 are the minimum and maximum contrasts possible. So, if 5% error is to be added to the lowest contrast wavelength, the noise added for the other five wavelengths depend on Equation 6.2. This systematic model when implemented gives a more complete description of the quantification of chromophores, and for six wavelengths, Figure 6.5 shows the situation. This error model is representative of the general trend observed in reconstruction, and may be different for differing types of reconstruction depending on the error observed. The results from this model do not differ significantly from the random error model, but provide a better understanding of the behavior of the image reconstruction process.

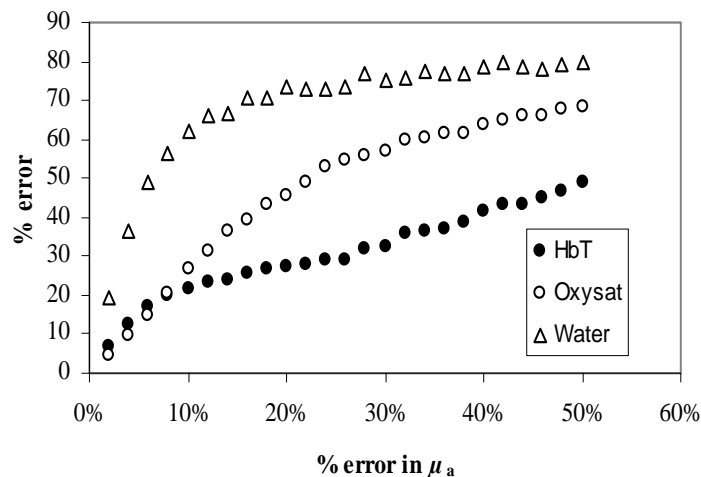


Figure 6-5: Error propagation in hemoglobin, oxygen saturation and water, is shown with the bias error model implemented, with current six wavelengths available.

6.4 Discussion

The accuracy in functional parameters such as hemoglobin, oxygen saturation and water content is a key factor in developing NIR tomography and the error propagation analysis presented here shows how important it is to have quantitative accuracy in the optical absorption coefficient. When information from the entire wavelength spectrum is incorporated, the levels of error decrease as expected, signifying that chromophore information is more immune to accuracy in quantification of μ_a in the presence of many wavelengths. The parabolic error model is representative of the general trend observed in reconstruction, and may be different for other types of reconstruction algorithms depending on the error observed. This analysis has stemmed the development of a novel reconstruction procedure described in the next chapter, which removes the intermediate process of recovering absorption and reduced scattering coefficient images for the breast, so that the error propagation from this step is eliminated. Instead, the chromophore concentration maps are directly obtained by use of *a-priori* spectral information. Another result of this analysis is the building of a spectroscopy system, which operates in conjunction with the tomography system, thus increasing the wavelengths of interrogation substantially. Overall, the analysis illustrates that the percent error in μ_a does not directly translate into the same error for total hemoglobin, oxygen saturation and water, and hence, it is important to take into consideration the propagation of this error, while evaluating the functional NIR parameters in a diagnostic setting.

7. Spectrally Constrained Direct Chromophore & Scattering Reconstruction

7.1 Introduction

While advances in the field have demonstrated qualitative, moderate resolution images useful for tracking changes in hemoglobin, oxygen saturation, water, and scatter, the current challenge faced is in improving quantitative accuracy and resolution. In-vivo studies have demonstrated levels of hemoglobin in tumors over twice that in normal breast^{6, 28} but the diagnostic utility of other near-infrared (NIR) parameters is still to be resolved. The quantification of chromophores and scattering parameters relies upon spectral decomposition of the optical properties' images acquired at a sparse number of discrete wavelengths instead of a complete spectrum. This sparse spectral sampling coupled with an image reconstruction process which is ill-posed and under-determined, tends to amplify errors in quantifying the spatially resolved parameters of the tissue.

A-priori information helps constrain the solution space and hence reduces the ill-posedness of this problem. In NIR imaging, this type of prior information, in the past, has been obtained from other modalities such as MRI or ultrasound, in the form of structural priors such as knowledge of location of the tumor, tissue boundaries etc^{50, 117-120}. However,

many of these studies demanded the exact knowledge of the tumor boundaries and while, the stability of the reconstruction was improved and faster convergence was shown^{50, 117-120} with results superior to a conventional no-priors type reconstruction, the effect of these priors on quantitative accuracy has not been determined clearly and such quantification may be biased by systematic errors and noise¹²¹. In addition, usage of prior information from simultaneous multi-modality type imaging takes away the advantage of NIR being a low-cost imaging system. Three dimensional reconstructions⁴⁶ exploit the availability of multiple planes of data and while they are time consuming, they provide a volume model for light propagation. In addition to these types of approaches, multi-wavelength NIR tomography offers a potential source of *a-priori* information in itself: the spectral behavior of absorbing chromophores and scattering mechanisms.

In prior work, the absorption and scattering coefficients were recovered from boundary measurements of amplitude and/or phase on the object of interest, such as the breast or brain, using computational models where both analytical and numerical approaches have been used by different research groups^{41, 48, 61, 122}. After recovery of these optical coefficients, a spectral fitting to known absorption signatures of oxyhemoglobin, deoxyhemoglobin and water is used to obtain concentrations of these absorbing chromophores. Similarly, the reduced scattering coefficients at separate wavelengths have been fit to give scatter amplitude (*a*) and scatter power (*b*), which are related to the structure of the tissue in terms of scatterer size and density. In this chapter, a novel reconstruction approach has been used, which implements the known spectral shapes of the chromophore and scattering models into the image formation process, thereby adding a spectral constraint into the reconstruction. The chromophore concentrations and scatter parameters are

estimated directly by incorporating the known Beer's law attenuation relation and Mie scattering behavior as constraints and using multi-wavelength measurements simultaneously; and thus removing the intermediate step of optical properties recovery.

This type of parameter reduction has been applied in electrical impedance tomography where Brandstatter et al¹²³ showed that by using multi frequency data and assuming a frequency dependence, the Cole model in their case, one can make the reconstruction better posed and more robust to noise in data. A similar application in microwave image reconstruction¹²⁴ provides evidence of reduced artifacts in the images as a result of coupling measurements from different frequencies. Corlu et al¹²⁵ have implemented this approach in NIR imaging using continuous wave measurements to find the optimal four wavelengths that reduce the crosstalk between absorption and scatter parameters. Their results from simulations are encouraging under the assumption that all change in scattering is due to scatter amplitude with scatter power kept constant. A similar approach to CW data has been implemented by Li et al¹²⁶ who have used two of three wavelengths under the assumption that there is no scattering perturbation. They have applied this method to find chromophore concentrations directly, and have shown in simulated and experimental data that their technique results in reduced image artifacts and parameter crosstalk.

In the approach implemented and studied in this chapter, the inclusion of spectral *a-priori* information is extended to the application of frequency-domain data, using six wavelengths simultaneously. A finite element model of the diffusion equation is used and the algorithm reconstructs images for five parameters: oxyhemoglobin, de-oxyhemoglobin, water fraction, scatter amplitude and scatter power, with no assumptions on scatter

amplitude or power. The model allows flexibility to additional wavelengths without much cost incurred on computational time. This spectrally constrained reconstruction has been implemented and its performance has been analyzed for robust handling of noisy data by studying the effects of increasing random Gaussian noise in amplitude and phase data. The results show that the new approach is more robust to noise in NIR measurements than the conventional method, handling up to 5% noise without significant cost on the quantitative accuracy. The method has been validated in homogeneous experiments following the variation of total hemoglobin, oxygen saturation and scattering individually. The results documented in the following sections demonstrate significantly improved images in both qualitative and quantitative aspects. Similar behavior was observed when implemented on simulated data with 1% random Gaussian noise, from a heterogeneous test phantom with concentrations and scattering mimicking breast tumors; and on experimental data obtained from a test setup of a gelatin phantom with a 25mm inclusion containing pig blood and Intralipid in saline. The crosstalk between different parameters has been substantially reduced by the spectral *a-priori* information and this is further validated along with examination of the effects of addition of longer wavelengths by a simulation containing five different heterogeneities for each of the reconstructed parameters.

7.2 Methods

7.2.1 Conventional Technique: Individual Optical Properties Recovery at Separate Wavelengths

Having obtained the measurements at the periphery of the imaging domain, image reconstruction is carried out by solving the diffusion equation⁶² for optical properties. This

has been described in *Chapter 2* in detail; briefly, this inverse problem being ill-posed, as often is the approach, we seek to minimize the least squares functional

$$\chi^2 = \sum_{j=1}^M (\phi_j^{meas} - \phi_j^{cal})^2, \quad (7.1)$$

where M is the total number of measurements at each wavelength, and ϕ_j^{meas} and ϕ_j^{alc} are the measured and calculated fluence at the boundary for each measurement point j . The minimization in Equation (7.1) is carried out by applying a Newton-Raphson iterative method⁶⁷ where the boundary data is calculated at a sufficiently close set of initial optical properties, along with the Levenberg Marquardt regularization¹²⁷ for stabilizing the inversion. The regularized solution is then given by:

$$\partial\mu = (\mathfrak{J}^T \mathfrak{J} + \lambda I)^{-1} \mathfrak{J}^T (\phi_{meas} - \phi_{cal}) \quad (7.2)$$

where \mathfrak{J} is the Jacobian, the matrix containing the sensitivity of the boundary data to a change in optical properties, $\mathfrak{J} = [\mathfrak{J}_{\mu_a}, \mathfrak{J}_{\kappa}]$ and $\partial\mu$ is the update in the optical properties given by $\partial\mu = (\partial\mu_a; \partial\kappa)$; where μ_a is the absorption coefficient in mm^{-1} and κ is the diffusion coefficient given by $\kappa = \frac{1}{3(\mu_a + \mu'_s)}$ in mm, and μ'_s is the reduced scattering coefficient in mm^{-1} . I is the identity matrix and λ is the regularizing factor that stabilizes the solution (i.e. matrix inversion). All reconstructions presented here using the conventional method used starting value for $\lambda = 10$ and the measure of convergence being that the change in χ^2 between successive iterations is less than an error tolerance limit. This limit is defined as 2%, based on simulation studies; and allows a balance between accuracy in property recovery, and high frequency noise in images. More details can be found in *Chapter 2*.

7.2.2 Spectral Fitting: Beer's law and Scatter Theory

Conventionally⁵³, once the optical properties at each wavelength are obtained, the calculation of the chromophore concentrations are performed using a constrained least squares fit to the Beer's law relation

$$\mu_a = [\varepsilon]c \quad (7.3)$$

where ε contains the molar absorption spectra of the absorbing chromophores and c is the concentration of these chromophores. Similarly, the μ'_s spectrum of tissue has been shown to fit well to an empirical approximation to Mie scattering theory^{81, 82} given by,

$$\mu'_s = a\lambda^{-b} \quad (7.4)$$

This was used to derive scatter amplitude (a) and scatter power (b) with wavelength in μm . The coefficient μ'_s has units mm^{-1} and b is dimensionless, so that a has units given by $10^{-3b}(\text{mm})^{b-1}$. Scattering power is governed by the shape or slope of scattering which is predominantly affected by the size^{83, 84}; the amplitude relates to the number density of the scatterers. Together, these parameters may reflect variations in breast structural composition due to different cellular, organelle and structural sizes/densities for fatty and glandular tissue.

7.2.3 Spectrally Constrained Direct Chromophore and Scattering Reconstruction

Using Beer's law and Scatter theory as spectral priors allows for a parametric-type reconstruction where multi-wavelength measurements are coupled together to reconstruct for "less" wavelength-dependent parameters like oxyhemoglobin, de-oxyhemoglobin and water concentrations as well as scatter amplitude and scatter power. In order to incorporate these spectral relationships into the reconstruction directly, the least squares function is

rewritten as $\chi^2 = \sum_{j=1}^{Mn} (\phi_j^{meas} - \phi_j^{cal})^2$, so that the sum includes measurements over all wavelengths (Mn), where n is the number of wavelengths available (6 in our case, in the range 660-850nm). Instead of estimating the optical properties at each wavelength and then spectrally de-convolving the chromophore concentrations (Equations 7.3 and 7.4), these constraints can be incorporated into the reconstruction to directly determine oxyhemoglobin, de-oxyhemoglobin, water, scatter amplitude and scatter power, thus reducing the parameter space from 12 images (μ_a and μ_s at 6 wavelengths) to 5 parametric images. Assuming that we know $\mathfrak{I}_{\mu_a} = \frac{\partial \phi}{\partial \mu_a}$ and $\mathfrak{I}_{\kappa} = \frac{\partial \phi}{\partial \kappa}$ as calculated using the Adjoint method in the conventional approach, in the new approach the measurements at all wavelengths are coupled together, and the relationships in Equations 7.3 and 7.4 are combined to create a new set of relationships, which for each wavelength, is represented by Newton's method as:

$$\partial \phi_{\lambda} = \mathfrak{I}_{c,\lambda} \partial c + \mathfrak{I}_{a,\lambda} \partial a + \mathfrak{I}_{b,\lambda} \partial b \quad (7.5)$$

where

$\mathfrak{I}_{c,\lambda} = \frac{\partial \phi}{\partial c} \Big|_{\lambda} = \frac{\partial \phi}{\partial \mu} \frac{\partial \mu}{\partial c} \Big|_{\lambda}$, for each chromophore (c) in the model. From Equation 7.3, we get

$\partial \mu = \varepsilon \partial c$, so that, substituting for $\frac{\partial \mu_a}{\partial c}$,

$$\mathfrak{I}_{c,\lambda} = \frac{\partial \phi}{\partial c} \Big|_{\lambda} = \frac{\partial \phi}{\partial \mu} \varepsilon \Big|_{\lambda} = \left(\frac{\partial \phi}{\partial \mu} \Big|_{\lambda} \right) \otimes (\varepsilon_{\lambda}^{c1,c2,c3}) = \mathfrak{I}_{\mu,\lambda} \otimes (\varepsilon_{\lambda}^{c1,c2,c3}) \quad (7.6)$$

where \otimes refers to the Kronecker tensor product.

Similarly,
$$\mathfrak{S}_{a,\lambda} = \left. \frac{\partial \phi}{\partial a} \right|_{\lambda} = \left. \frac{\partial \phi}{\partial \kappa} \frac{\partial \kappa}{\partial a} \right|_{\lambda} \quad (7.7)$$

Rewriting $\frac{\partial \kappa}{\partial a} = \left(\frac{\partial \kappa}{\partial \mu'_s} \right) \left(\frac{\partial \mu'_s}{\partial a} \right)$, and knowing that $\kappa = \frac{1}{3(\mu_a + \mu'_s)}$, we get

$$\frac{\partial \kappa}{\partial \mu'_s} = \frac{1}{3} \left(\frac{-1}{(\mu_a + \mu'_s)^2} \right) = \frac{1}{3} (-9\kappa^2) = -3\kappa^2, \text{ and } \frac{\partial \mu'_s}{\partial a} = \lambda^{-b}$$

Substituting these expressions in Equation 7.7 leads to

$$\mathfrak{S}_{a,\lambda} = \left. \frac{\partial \phi}{\partial a} \right|_{\lambda} = \left. \frac{\partial \phi}{\partial \kappa} \frac{\partial \kappa}{\partial a} \right|_{\lambda} = \mathfrak{S}_{\kappa} (-3\kappa^2) (\lambda^{-b}) \Big|_{\lambda} \quad (7.8)$$

Similarly, for the scatter power:

$$\mathfrak{S}_{b,\lambda} = \left. \frac{\partial \phi}{\partial b} \right|_{\lambda} = \left. \frac{\partial \phi}{\partial \kappa} \frac{\partial \kappa}{\partial b} \right|_{\lambda} = \left(\frac{\partial \phi}{\partial \kappa} \right) \left(\frac{\partial \kappa}{\partial \mu'_s} \right) \left(\frac{\partial \mu'_s}{\partial \ln \mu'_s} \right) \left(\frac{\partial \ln \mu'_s}{\partial b} \right) \Big|_{\lambda} \quad (7.9)$$

Knowing that, $\frac{\partial \ln \mu'_s}{\partial \ln \mu'_s} = \frac{1}{\mu'_s} \frac{\partial \mu'_s}{\partial \ln \mu'_s} = \mu'_s$ and from (7.4), $\ln \mu'_s = \ln a - b \ln \lambda$, then

it is found that $\frac{\partial \ln \mu'_s}{\partial b} = -\ln \lambda$. Substituting these relations produces

$$\mathfrak{S}_{b,\lambda} = \left. \frac{\partial \phi}{\partial b} \right|_{\lambda} = \left. \frac{\partial \phi}{\partial \kappa} \frac{\partial \kappa}{\partial b} \right|_{\lambda} = \mathfrak{S}_{\kappa} (-3\kappa^2) (\mu'_s) (-\ln \lambda) \Big|_{\lambda} \quad (7.10)$$

The overall system of equations is assembled by substituting the relations from (7.6), (7.8)

and (7.10) into Equation 7.5:

$$\begin{pmatrix} \partial \phi_{\lambda 1} \\ \partial \phi_{\lambda 2} \\ \vdots \\ \partial \phi_{\lambda n} \end{pmatrix} = \begin{bmatrix} \mathfrak{S}_{c1,\lambda 1} & \mathfrak{S}_{c2,\lambda 1} & \mathfrak{S}_{c3,\lambda 1} & \mathfrak{S}_{a,\lambda 1} & \mathfrak{S}_{b,\lambda 1} \\ \mathfrak{S}_{c1,\lambda 2} & \mathfrak{S}_{c2,\lambda 2} & \mathfrak{S}_{c3,\lambda 2} & \mathfrak{S}_{a,\lambda 2} & \mathfrak{S}_{b,\lambda 2} \\ \vdots & & & & \\ \mathfrak{S}_{c1,\lambda n} & \mathfrak{S}_{c2,\lambda n} & \mathfrak{S}_{c3,\lambda n} & \mathfrak{S}_{a,\lambda n} & \mathfrak{S}_{b,\lambda n} \end{bmatrix} \begin{pmatrix} \partial c_1 \\ \partial c_2 \\ \partial c_3 \\ \partial a \\ \partial b \end{pmatrix} \quad (7.11)$$

The size of the left hand vector is number of wavelengths multiplied by the number of measurements per wavelength while the size of the right hand side vector is number of chromophores and scatter parameters multiplied by the number of nodes for updating each parameter in the mesh. The individual Jacobian matrices for each chromophore were computed using a dual mesh technique¹²⁸, on a 2000 node mesh for forward diffusion calculations and a 425 node mesh for image reconstruction. Equation 7.11 was implemented by building the new Jacobian (5×425 by 480×6) and the same Levenberg-Marquardt regularization scheme was applied as the conventional approach, so that the final iterative procedure is of the same form as given by Equation 7.2. The starting value for regularization was chosen as 10 empirically; values in the range 1000-1 reasonably recovered the images. The computation time was approximately 25 minutes for typically 5-7 iterations, the measure of convergence being when the projection error was less than 2% of previous iteration value. Additional constraints based on physiologically possible values for the parameters were applied at each iteration so that Hb_T does not exceed $200\mu\text{M}$ (based on typical concentrations found in the breast), oxygen saturation is in the range $[0, 100\%]$ and water in the range $[0, 100\%]$. Scatter amplitude is similarly bounded so that at each iteration, the values lie in the range $[0, 3.0]$ in units of $10^{-3b}(\text{mm})^{b-1}$ and scatter power in the range $[0, 3.0]$ (based on previous studies³¹), so that together they cover the possible range for reduced scattering coefficient. This range is $[0, 6.2] \text{ mm}^{-1}$ for 785nm. These constraints are applied only at the boundary of these ranges; which is in the case of highly noisy data; in the majority of reconstructions, the constraints do not come into place, as the updated values at different iterations lie well within the range. The approach can easily be extended to additional wavelengths without any computational expense in the inversion process since the size of the new Hessian for the inversion in step 7.11 depends on number of nodes of the mesh

and not on the number of measurements, though the number of wavelengths will influence the calculation of individual Jacobians. The algorithm typically converges in lower number of iterations than the conventional method, and no spatial filtering has been necessary since the noise in the images is already damped by the spectral constraints.

7.3 Results

7.3.1 Effect of Noise in Amplitude and Phase Measurements

It is expected that the spectral-constrained nature of this new algorithm will make the reconstruction more immune to noise in measurements as compared to the conventional method since data over all available wavelengths are coupled. Larger noise in the data is typically observed at 661nm for tissues containing lower oxygenation (due to high absorption of de-oxyhemoglobin) and 849nm (due to water absorption), and in higher scattering cases. By the *a-priori* spectral constraints, these absorption and scattering features are embedded into the image formation process, and as it will be demonstrated, the presence of high noise in data is suppressed. In order to test the hypothesis of reduced noise-sensitivity of the spectral method, amplitude and phase data at six wavelengths were simulated using the finite element model for a homogeneous phantom of diameter 86mm having concentrations of 30 μ M HbO₂, 30 μ M Hb, 60% water and scatter amplitude =1 in units of 10^{-3b}(mm)^{b-1} ; scatter power = 1. This yields total hemoglobin of 60 μ M and S_tO₂ = 50% and μ'_s at 785nm = 1.27 mm⁻¹, which are concentrations typically found in the breast. Random Gaussian distributed noise was added to the amplitude and phase measurements in a systematic manner from 0.5% to 5%, as a percentage of each measurement and the spectrally constrained reconstruction was carried out on this data. The conventional technique of reconstructing each wavelength separately and then carrying out the spectral fit

was also applied to this data for comparison purposes. The mean and standard deviation for the reconstructed images from both techniques for each of the parameters were calculated from the images, excluding 15mm from the boundary to remove contributions from high frequency boundary artifacts. These are plotted in Figure 7.1; the results are shown for the cases with no-noise, 1% noise and 5% noise.

For the noiseless data reconstruction, both techniques show accurate recovery of all five parameters (mean is within 3% of true value) with an average standard deviation of 0.5% of the mean for the spectral method and 3.7% for the conventional technique. For the 1% and 5% noise cases, the standard deviation increases as expected; however, this increase is much more evident in the images from the conventional technique than the spectral method. The results from the spectral method does not differ significantly from the conventional technique for total hemoglobin and oxygen saturation images; however, noise is significantly suppressed in the water and scatter images from the spectral method. For 1% noise in data, the mean is still within 5% of the true value for both methods, but the standard deviation in water has reduced from 40% in conventional method to 12% of the mean for the spectral technique. Even in the 5% noise case, the spectral method shows reasonable recovery of mean values for the parameters (accurate within 10 % on an average) with 15.3% standard deviation (as percent of the mean). These results indicate that in the presence of large noise in the NIR data, the spectrally-constrained reconstruction outperforms the conventional method, since all the data are coupled. This illustrates that the problem is now better-posed⁷⁰, in terms of stability, making the solution less sensitive and more stable, to noise in measured data.

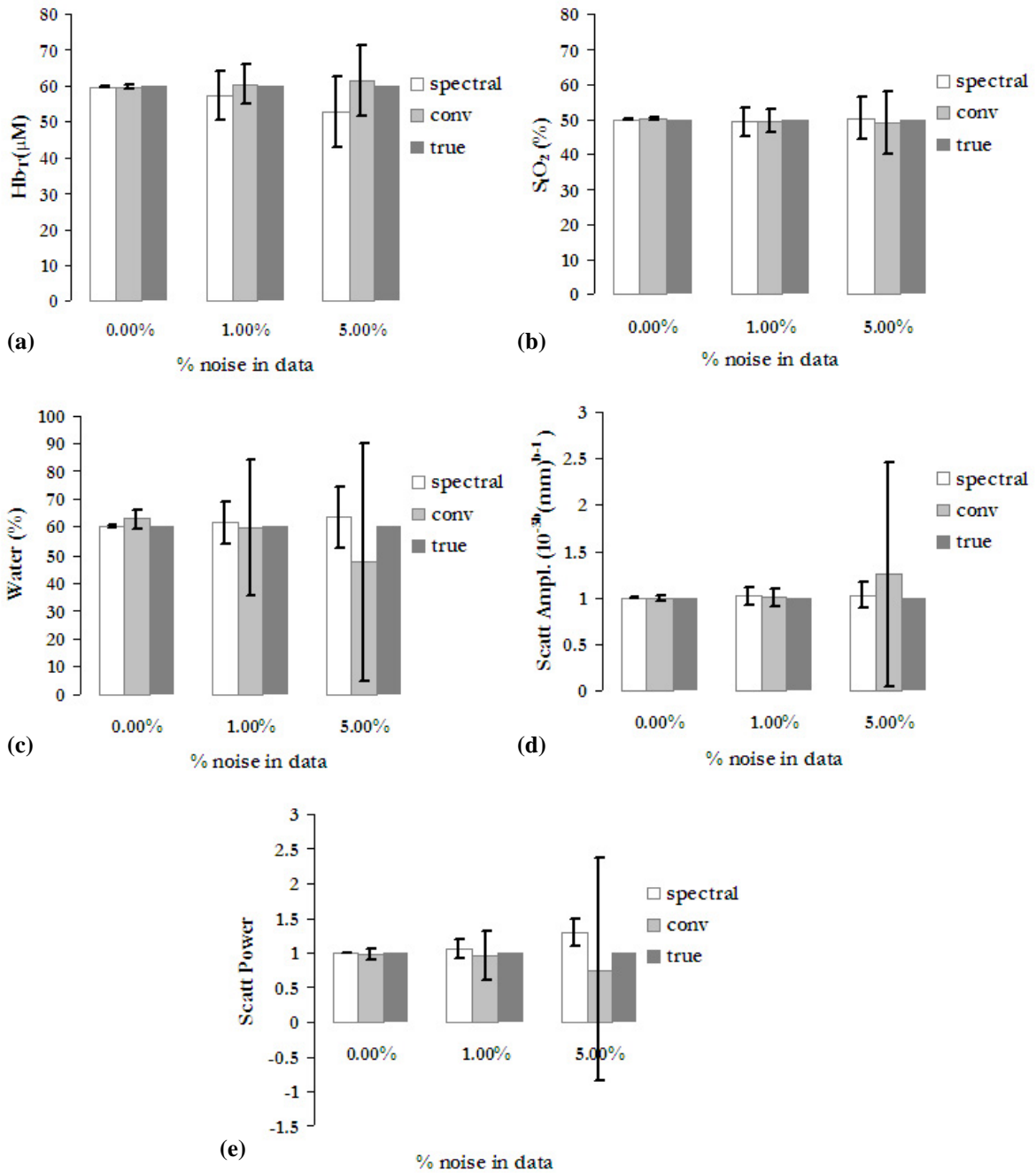


Figure 7-1: Recovered mean values with standard deviation error bars are shown for (a) hemoglobin, (b) oxygen saturation (SO₂), (c) water (%), (d) scatter amplitude, and (e) scatter power. These were estimated from the interior of a homogeneous field, reconstructed with different levels of noise in the original data. Values for the new spectrally-constrained reconstruction are shown alongside results from the conventional approach.

7.3.2 Tumor-simulating Phantom results

In order to test the recovery of heterogeneities in the imaging field, amplitude and phase measurements were generated for a heterogeneous phantom using the finite element forward solver and 1% random Gaussian noise was added to mimic experimental noise⁴³. This phantom was of diameter 86mm, and contained an inclusion of size 20mm, with higher hemoglobin representative of tumors; such that the total hemoglobin contrast was 3:1, with respect to the background. The anomaly also had lower oxygen saturation of 30% compared to the background at 60%, representing hypoxic conditions^{28, 129}, and contrast in scatter amplitude, with value 1.5, compared to 1.2 in background. Water and scatter power were maintained homogeneous at 60% and 0.6 respectively. The spectrally constrained direct chromophore and scattering reconstruction was applied to this data, with an initial guess for the parameters mid-way between the anomaly and background concentrations, to analyze recovery of both background and anomaly values. In addition, the conventional method of reconstructing at each wavelength separately and then applying least squares fit to Beer's law and Mie theory, was also applied. Figure 7.2 shows the corresponding images obtained using each method, compared to the true images shown in the top row. The conventional method needed spatial filtering at each iteration in the individual wavelengths reconstruction whereas no filtering was applied to the spectral reconstruction. Both procedures were terminated when the projection error changed by less than 2% between successive iterations and both used a starting value for regularization as 10.

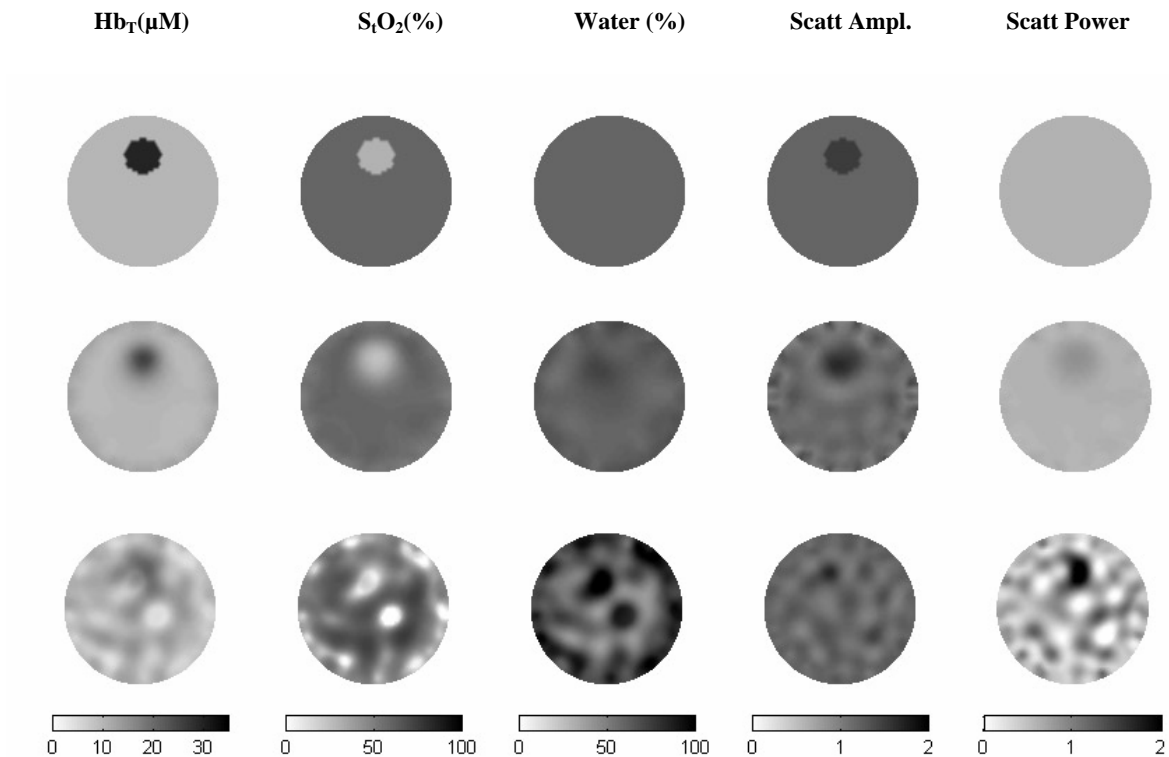


Figure 7-2: Recovered NIR parameter images are shown for a heterogeneous phantom with true values in the top row, as reconstructed from simulated data with 1% random Gaussian noise added. The middle row shows images obtained using the spectrally-constrained reconstruction and the bottom row shows the same set of images using the conventional method of applying least squares fitting to images of absorption and reduced scattering coefficients, and then sequentially fitting for chromophore images.

The Figure above shows fewer high frequency spatial artifacts in all the five NIR parameter images in the spectral reconstruction compared to the conventional technique. Quantitative accuracy is improved in addition to the reduced standard deviation, with the spectrally constrained method giving results accurate with less than 15% error overall, and this error limit being at 43% for the conventional technique. There is also a reduction in cross-talk observed between hemoglobin and water, from 30% in conventional method to 7% in the spectral reconstruction. The pseudo increase in scatter power in the conventional recovery owing to crosstalk possibly from de-oxyhemoglobin, has been reduced substantially

as well in the spectral prior method. The smooth recovery of the hypoxic oxygen saturation by the spectral technique is encouraging and is accurate with less than 1% error.

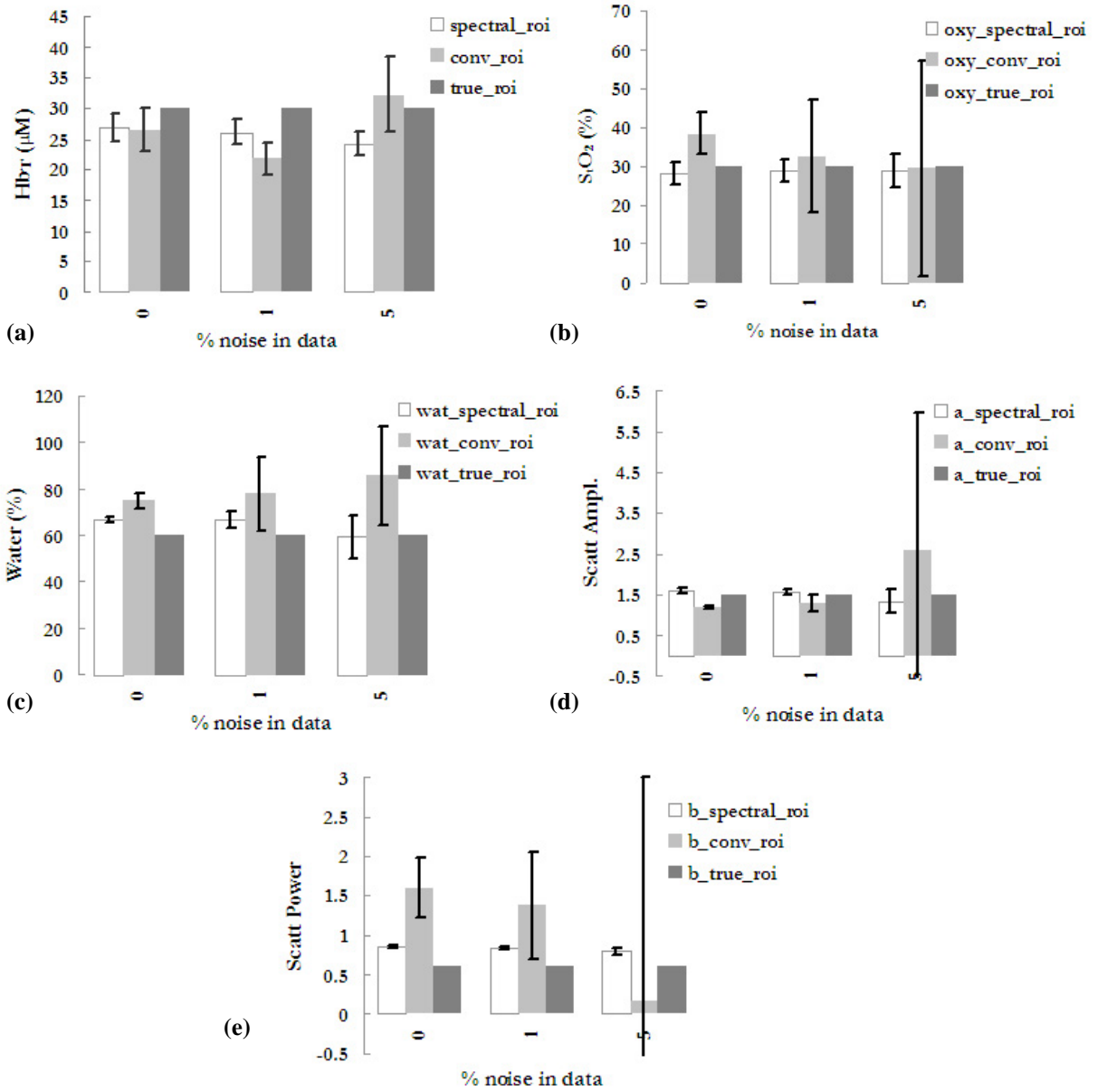


Figure 7-3: Mean and standard deviations from the images recovered using both spectrally constrained reconstruction and the conventional method are shown for the test phantom used in Figure 1, with increasing amounts of random Gaussian noise as the abscissa. The results are average values taken from the region of the heterogeneity, for (a) HbT in μM , (b) SiO_2 in %, (c) water in %, (d) scatter amplitude and (e) scatter power. The background values were observed to stay constant for both methods.

Further, to test the noise-sensitivity of this algorithm similar to the approach in *Section 7.3.1*, increasing amounts of random Gaussian noise from 0 to 5% in steps of 0.5% was added to the simulated amplitude and phase measurements for this test phantom. This was used to reconstruct for the five NIR parameters and the mean and standard deviation in the NIR parameters in the region of interest (ROI), as recovered from both conventional and direct spectral reconstruction have been plotted (see Figure 7.3) alongside the true values. The ROI was defined from the Hb_T image based on the FWHM criterion, where the threshold was defined midway between the mean and the maximum of the image, and the ROI contained all nodes having Hb_T value above this threshold. At 1% noise, which is the level found in our tomography system⁴³, the reduction in standard deviations in oxygen saturation (Figure 7.3(b)), water (Figure 7.3(d)) and scatter power (Figure 7.3(e)) are most striking. The trend is continued at 5% noise in the amplitude and phase data (5% is possibly the limit of noisy data found typically in such measurement systems). The spectrally constrained technique still gives quantification accurate within 15% of true values overall at this level of noise, but this is not the case in the conventional method, where the high standard deviations in the images make it impossible to obtain useful NIR information.

7.3.3 Reduced Standard Deviation in Homogeneous Experimental Data

In order to assess the mean and standard deviation from homogeneous images in experimental data, measurements were collected on a liquid tissue-simulating phantom within a plastic circular container of 90 mm diameter, consisting of 1% pig blood in buffered saline and 1% Intralipid concentration. The blood hematocrit was measured before the experiment with a clinical co-oximeter that showed 1% of the pig blood contained 9.3 μM of hemoglobin for this sample. The expected values for scatter amplitude and scatter power

were derived from the work of van Staveren et al⁸². Using the expression given by van Staveren et al with the units suitably modified produces the following equation, $\mu'_s = 0.928\lambda^{-1.4} - 0.16\lambda^{-2.4}$. Incorporating the higher order term into the scatter amplitude factor (since the amplitude factor of the second term is much lower than of the first term) by assuming that $\mu'_s = 1\text{mm}^{-1}$ at 800nm, the scatter amplitude (a) = 0.73 and scatter power (b) = 1.4. Water and oxygen saturation are expected to be close to 100%, since the phantom was an oxygenated liquid solution. Both the spectral and conventional techniques were applied to this data, and the mean and standard deviation from the reconstructed images have been plotted in Figure 7.4(a) along with the expected values.

Figure 7.4(a) shows reduced standard deviation in the images obtained from the spectral method, compared to the conventional technique. The mean values for the parameters are accurate to within 6 % on average, for the spectral scheme and to within 11% for the conventional method. As with the simulations, no spatial filtering has been applied to the spectral reconstruction, whereas the conventional method uses a mean filter. Both methods use the same initial regularization parameter (equal to 10 in this study). The main improvement here was the suppression of noise in the water and scattering images using the spectral technique. Figure 7.4(b) shows the reconstructed images from both methods along with a cross-section profile of the middle plane. The spatial variation in the cross-section is less in the spectral technique and some of the boundary artifacts in hemoglobin, water and scatter power images are reduced. The hemoglobin and water images from the conventional technique show some crosstalk between the images. A central artifact can be seen in the Hb_T image where there is a decrease in its value, with saturation in the water image at this same region (=100%). The scatter parameter images, especially scatter power, show considerable

noise, possibly due to crosstalk between the two scatter parameters, and between scatter and de-oxyhemoglobin.

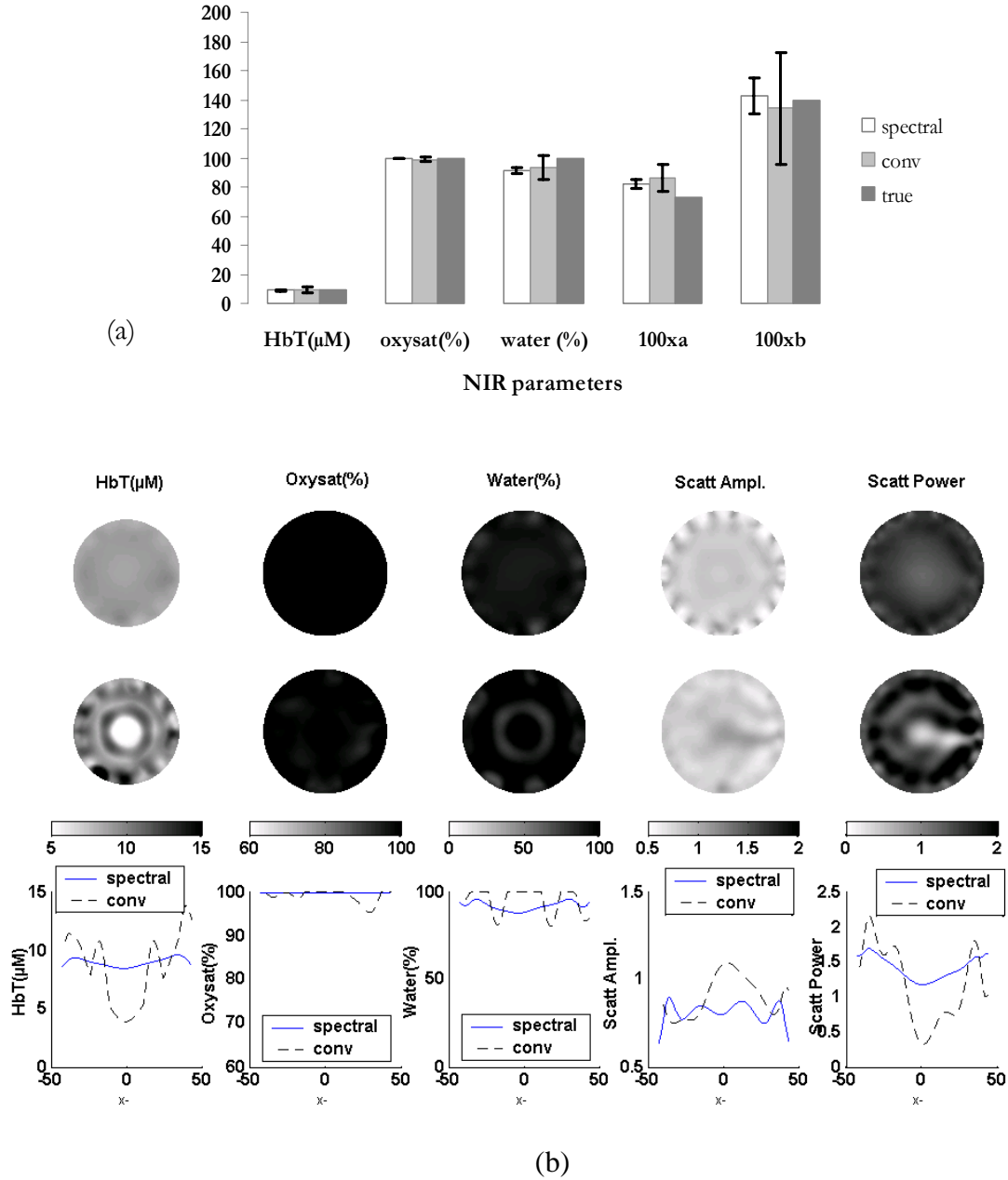


Figure 7-4: Recovered mean values with standard deviation error bars are shown in (a) from reconstructed data with a 90 mm diameter liquid phantom containing 1% Intralipid with 9.3 μM total hemoglobin. Values for the spectrally constrained reconstruction are shown alongside those obtained with the conventional reconstruction approach and the true theoretical values. In (b) the images from this phantom are shown for comparison, with the spectrally-constrained reconstruction (top row), the conventional reconstruction (middle row) and profile plots from the mid-plane of these images (bottom row).

7.3.4 Scattering Parameter Validation

Having shown that spectral reconstruction is superior to the conventional approach, in terms of reduced sensitivity to noise in the data and suppression of artifacts in the images, the following sections focus on validating the accuracy of the spectral reconstruction. One of the key advantages of the spectral method over the conventional technique is the reduction of noise in water and scatter parameters. The implementation of this technique on frequency domain measurements allows separation of absorption and scatter, and this along with multi-wavelength capability allows modest separation of scatter amplitude and scatter power. In order to test the cross-talk and noise in the scatter parameters with experimental measurements and follow their variation, the Intralipid concentration was varied in the liquid phantom solution containing 1% blood, from 0.75% to 1.5% in steps of 0.25% (the data from 1% Intralipid has also been used for Figure 7.4). Amplitude and phase measurements were taken for each concentration, and the spectrally constrained reconstruction was applied to the data. The total hemoglobin was constant through the varying concentrations of Intralipid, and the water and oxygen saturation were 100% for all data sets. The mean value along with standard deviation from the images have been plotted for scatter amplitude and scatter power in Figure 7.5(a), Figure 7.5(b) shows the average μ'_s at 661nm and 785nm. Figure 7.5(c) shows the total hemoglobin and 7.5(d) shows the oxygen saturation and water content. The scatter amplitude varies linearly with concentration; and shows more variation (range of 0.6-1.25) than scatter power (range of 1.3-1.53). Scatter power values are comparable to the expected value of 1.4 from van Staveren et al⁸², showing a mean of 1.4 ± 0.1 through the change in concentrations. The mean μ'_s at 785nm varies linearly (slope ≈ 1) with the change in % Intralipid and the value approximately doubles (0.89mm^{-1} versus

1.7mm⁻¹) when concentration doubles from 0.75% to 1.5% Intralipid, which is encouraging. The reduced scattering coefficient at 661nm also shows a similar trend. The total hemoglobin stays constant with change in scattering with a mean of 8.2μM±0.8, and oxygen saturation shows a mean value of 99.3 ±1.2%, close to expected value of 100%. Water shows an average of 92.4%±4.2% and some crosstalk can be seen between hemoglobin and water at the higher Intralipid concentrations due to the high scattering medium.

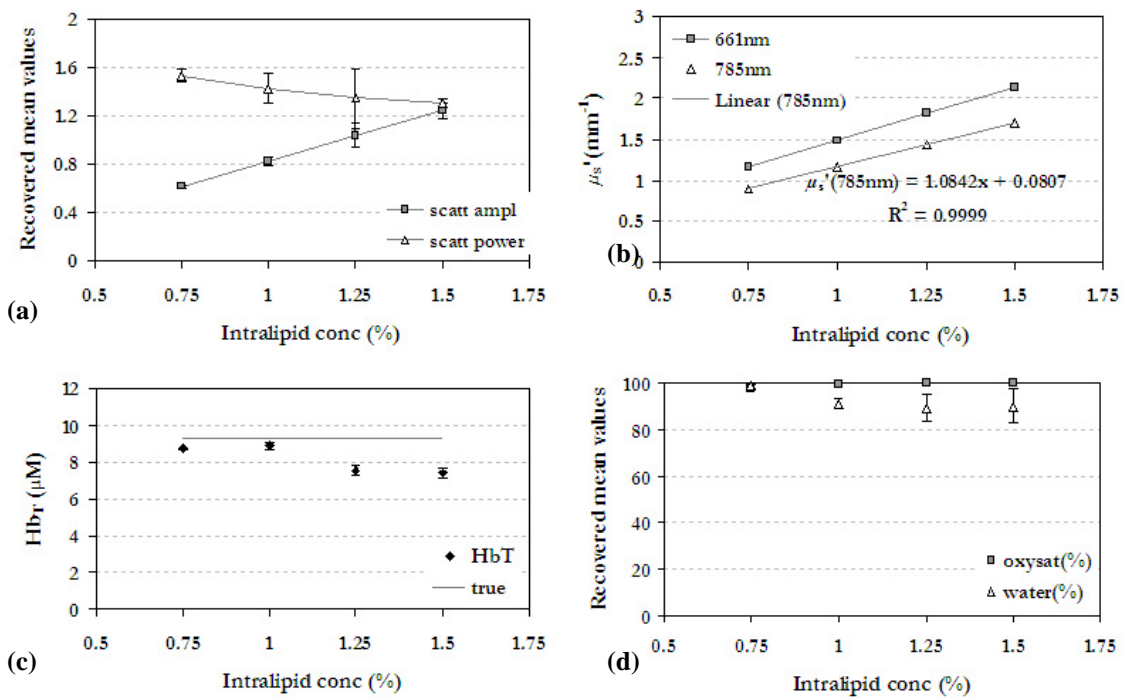


Figure 7-5: Recovered mean values are shown from a series of phantoms where the scattering coefficient was systematically varied through differing concentrations of Intralipid, between 0.75% and 1.5%. The estimated scattering power and amplitudes are shown in (a) and the reduced scattering coefficients at 661 and 785 nm are shown in (b). The total hemoglobin, which did not vary, is shown in (c) along with a line corresponding to the theoretical value. In (d) the oxygen saturation and water values are shown, which also did not vary. Both have theoretical estimates of 100%. Error bars represent the standard deviation of all pixels within the interior 60 mm of the region imaged.

7.3.5 Oxygen Saturation Validation

Malignant tumors typically have lower pO_2 values for oxygen due to hypoxia²⁶, and it is useful to verify that the spectrally constrained reconstruction can follow these hypoxic conditions. The relationship of oxygen saturation to variation in partial pressure of oxygen has a well-characterized behavior given by the Hill Curve. This curve has been obtained previously for the conventional method and published in¹¹⁴. Data was acquired using a phantom solution containing 1% whole blood and 1% Intralipid in saline, in a thin-walled plastic container, 70mm in diameter. The 1% whole blood was found to have 18 μ M hemoglobin, and the oxygenation of the solution was reduced by varying the pO_2 values from 150mm to 0mm Hg by addition of yeast. The pO_2 was independently measured using a chemical microelectrode, after calibration of the electrode overnight in saline solution. By varying the pO_2 gradually, using a small amount of yeast and making measurements over this period of time, the pO_2 eventually reduced to zero, and a complete set of data over the required range was obtained. The spectral reconstruction of this data gave Hb_T , S_tO_2 , water, scatter amplitude and scatter power images from which the mean and standard deviation have been plotted in Figure 7.6. The oxygen saturation in Figure 7.6(a) follows the theoretical Hill curve⁹³ reasonably well with a mean error of 7.7%, with the worst accuracy close to zero pO_2 (possibly due to noisier data, owing to high de-oxy hemoglobin absorption) and higher accuracy when it is above 80% saturation. For pO_2 below 20mm Hg, oxygen saturation is still accurate to within 15%, with a low standard deviation in the images.

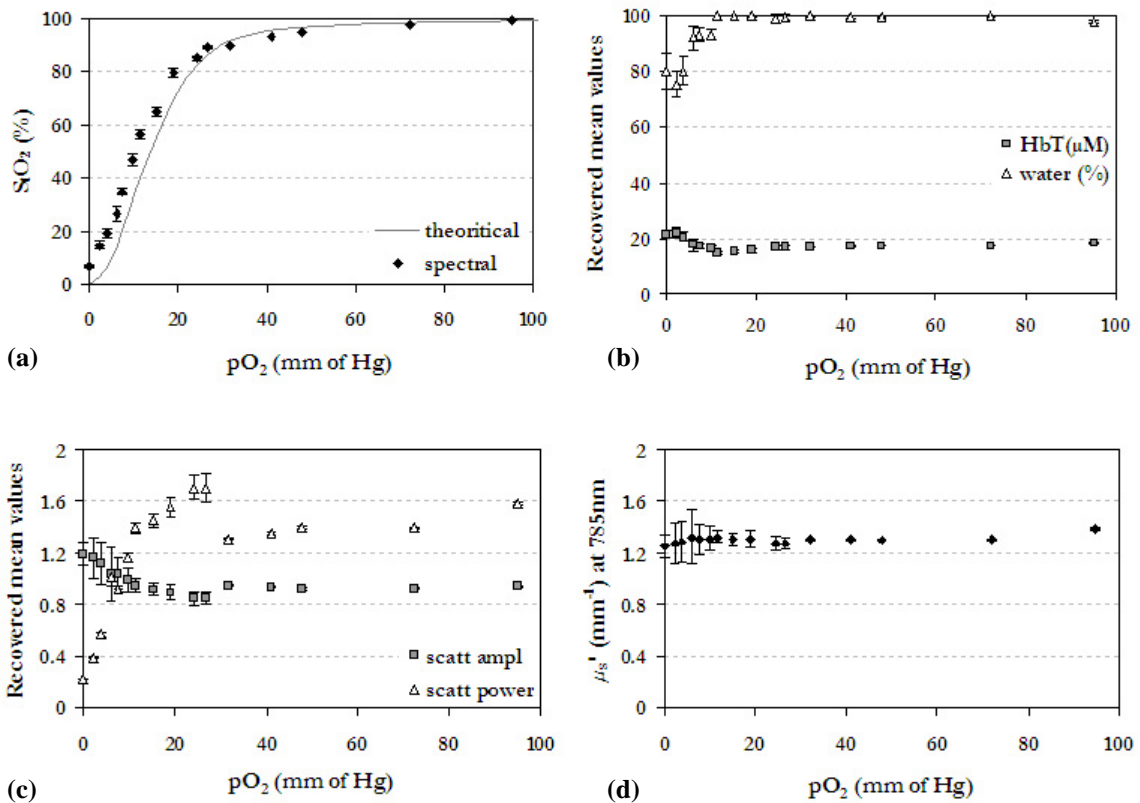


Figure 7-6: Estimated mean values are shown from homogeneous reconstructions of a phantom with varying oxygen partial pressure (pO_2) of the solution, induced by addition of yeast. The oxygen saturation is shown in (a) along with the theoretical estimate from the Hill curve. The total hemoglobin and % water are shown in (b), with the theoretically estimated values of 18 μM and 100% respectively, and should not vary with changes in oxygenation. The scatter power and amplitude are shown in (c) and should not vary, and the reduced scattering coefficient at 785 nm is also shown in (d).

With variation of pO_2 total hemoglobin concentration stayed approximately constant (Figure 7.6(b)) with a mean value of $17.5 \pm 2.1 \mu M$, which is within 97% of the true value given above, and water exhibited a mean value of $94.2\% \pm 8.3\%$. Both parameters show some crosstalk at pO_2 values below 11 mm Hg, which is possibly unavoidable due to the limited number of wavelengths used in this data. Both scatter amplitude and scatter power stay approximately constant until a pO_2 of 11 mm Hg, beyond which both show some variation, which could be the result of crosstalk between the two parameters. Above 11 mm Hg, scatter

amplitude has value of 0.92 ± 0.04 in units of $10^{-3b}(\text{mm})^{b-1}$ and scatter power has values 1.49 ± 0.14 . The reduced scattering coefficient, however, stays constant throughout, as shown for 785nm, in Figure 7.6(d), with a mean of $1.3 \pm 0.03 \text{ mm}^{-1}$.

7.3.6 Total Hemoglobin Validation

The final experimental homogeneous data set involved varying the total hemoglobin while keeping oxygen saturation, water and scatter parameters constant. This was accomplished using a similar liquid phantom, with 1% Intralipid in saline, and varying the concentration of whole blood. The hematocrit level was measured by a clinical co-oximeter giving 1% blood equivalent to $22\mu\text{M}$ total hemoglobin. The blood concentration was varied from 0.2% to 1% in steps of 0.2% and amplitude and phase measurements were obtained for each level. After calibration, the spectrally constrained reconstruction was applied to the data, and the recovered mean and standard deviation from the NIR parameters are plotted in Figure 7.7. The theoretical water and oxygen saturation values were 100%, as the phantom was a liquid oxygenated solution.

Figure 7.7(a) shows that the total hemoglobin followed the variation in % blood linearly, and is quantitatively accurate with a mean percent error of 6.2%. Oxygen saturation stayed constant with change in blood concentration in Figure 7.7(b), with a mean value of $98.9 \pm 0.6 \%$. The same trend was found in water, with mean value $98.2\% \pm 1.5\%$. Scatter amplitude and scatter power, shown in Figure 7.7(b), are also independent of the variation in blood concentration, with scatter amplitude of 0.65 ± 0.01 . Scatter power had a mean value of 1.39 ± 0.08 , and this agreed well with the estimated 1.4 derived from van Staveren et al⁸².

The reconstruction converged in 4-6 iterations for the different concentrations, and no spatial filtering was applied in the reconstruction.

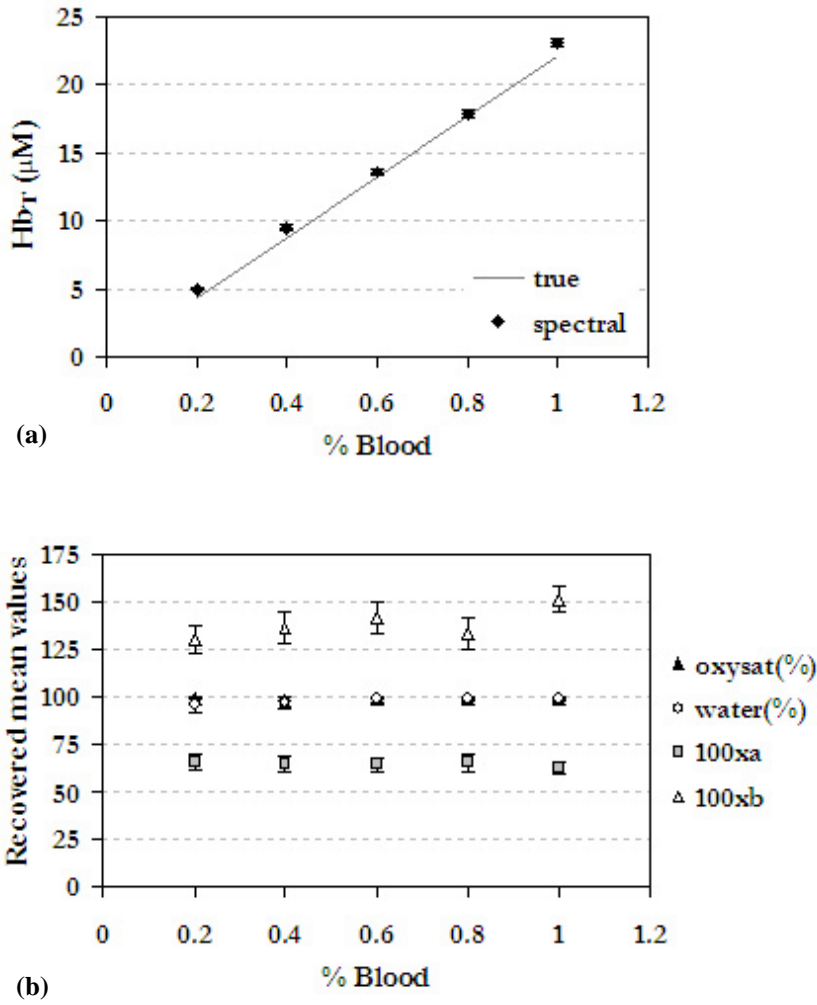


Figure 7-7: The reconstructed mean and standard deviation values are shown from phantoms with varying concentrations of blood where total hemoglobin is graphed in (a) alongside the theoretical value shown by a dotted line. The recovered values of oxygen saturation (%), water (%), scattering amplitude (a) and scattering power (b) are shown in (b), all of which are not expected to vary with changes in total % blood. The scatter parameters are multiplied by 100 to allow them to be displayed on the same graph as oxygen saturation and water.

7.3.7 Application to Heterogeneous Experimental Measurements: Phantom Study

In order to test the spectrally-constrained algorithm on an experimental measurements on a heterogeneous phantom, a phantom using gelatin with whole blood added for absorption and Titanium dioxide for scatter, was made. The recipe for this phantom is given in the appendix. Two such gelatin phantoms with a diameter of 8.2cm were obtained from the same mixture, one of which was maintained in its homogeneous state, and the other had a 2.5cm hole drilled 1cm from the boundary. This hole was filled with a saline solution containing 4% pig blood (the hematocrit level of the blood was measured by a clinical co-oximeter so that 4% blood = 43.2 μ M total hemoglobin) with 0.75% Intralipid for scattering. The background chromophore concentrations and scatter for the gel were determined by imaging the phantom in its homogeneous state and using the mean from the reconstructed NIR images, ignoring contributions close to the boundary (taken empirically to be 12% of the total diameter); earlier experiments have shown that concentrations obtained this way are quantitatively accurate¹³⁰. The inclusion had a contrast of nearly 2:1 in total hemoglobin and was expected to have 100% oxygen saturation and water content. The scattering images were expected to be almost homogeneous because 0.75% Intralipid was measured to be similar in scattering quantitatively to the background gelatin in the phantom. Amplitude and phase data were collected on this heterogeneous phantom and image reconstruction was carried out using both the conventional technique of separate wavelength reconstruction as well as the spectrally-constrained procedure. The top row in Figure 7.8 shows recovered images for the five NIR parameters, followed by the images generated with the spectrally-constrained reconstruction and the images from the conventional technique (in the bottom-most row).

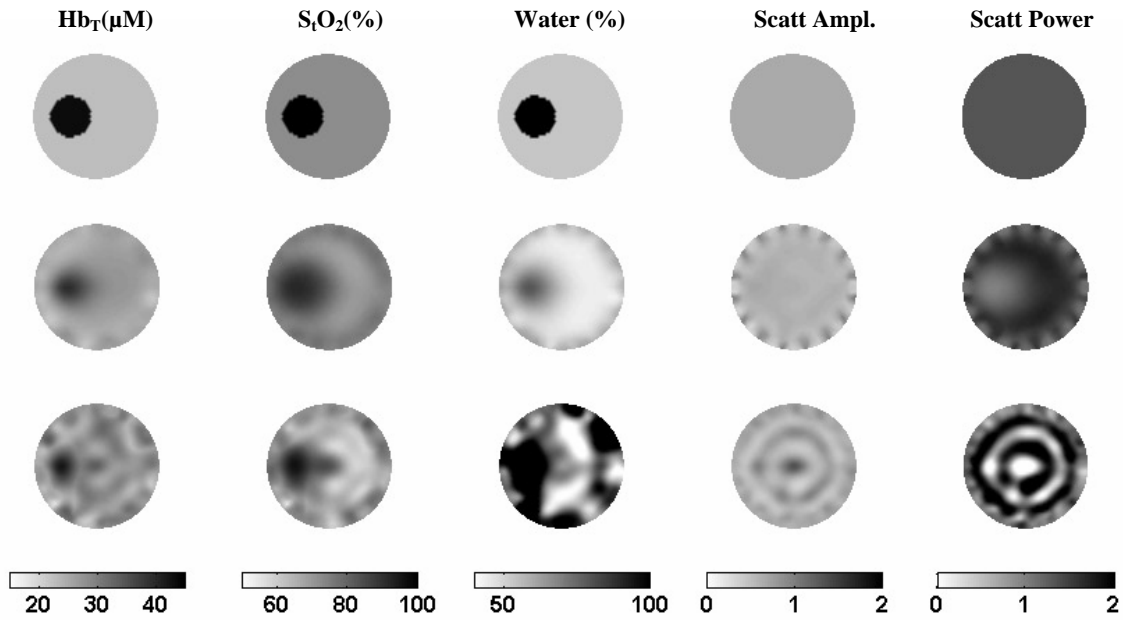


Figure 7-8: Comparison of images obtained with the spectrally constrained direct chromophore reconstruction and the conventional technique of independent optical property at separate wavelengths recovery on measurements from a gelatin phantom with a 2.5cm inclusion. The gelatin phantom contained whole blood and TiO₂ for scattering and the inclusion was filled with 4% pig blood and 0.75% Intralipid in buffered saline. The expected images are shown in the top row for HbT (μM), oxygen saturation (%), water (%), scatter amplitude and scatter power. The spectral method images appear in the second row while conventional technique images are located in the bottom-most row.

The images obtained with the spectrally constrained reconstruction are qualitatively much smoother and more accurate than their conventional counterparts. The simultaneous use of six wavelengths of data along with the spectral priors makes the inverse problem better posed and this along with the parameter reduction procedure provides the smoothness in the spectral images. Images from the conventional technique have more spatial artifacts, including higher cross-talk between oxy-hemoglobin and water, which have similar spectral behavior, resulting in under-estimation of total hemoglobin in the anomaly and saturation of water. In order to obtain the mean, peak and standard deviation in the anomaly, a FWHM regionization was performed on the images, using the total hemoglobin

image for the spectral method and the oxygen saturation image for the conventional technique. While the peak in total hemoglobin still reaches 98% of the true value, the mean in the anomaly is lower (80.6%) with significant standard deviation ($\sim 10\%$ of the mean). The scatter images from the conventional method suffer from a ring-type artifact, which arises from the difficulty in separating the two scatter parameters. This results in high standard deviation in the images, close to 25% of the mean for scatter amplitude and 82% of the mean for scatter power in the anomaly region. This has been circumvented in the spectrally constrained reconstruction through prior information related to scattering, providing well-defined limits for scatter amplitude and power. The standard deviation is now reduced to 2.3% of the mean for scatter amplitude and 7% for scatter power. The mean of the scatter amplitude in the anomaly region is quantitatively accurate with a mean error of 3.3% (reduced from 7% for the conventional method); and similarly for scatter power, the mean error is reduced to 19% from 32.4% for the conventional technique.

The spectral shapes of oxy-hemoglobin and water embedded into this reconstruction minimizes the crosstalk between these parameters and provides accuracy in total hemoglobin in the anomaly within 91.6 % of expected value for the peak and within 84% for the average and standard deviation reduced by almost half, to 4.83% of the mean. Water content has been underestimated by 20.3% using the spectral method. This may be due to the steep difference in background and anomaly water content (typically not observed in a patient), making it difficult to recover the high contrast in the anomaly. A possible solution to improving the accuracy of water content is the use of data in the longer wavelength range (850-1000nm) and is examined in simulations in *Section 7.3.10* ahead, which will incorporate stronger features of water.

7.3.8 Variation of Hemoglobin in Heterogeneous Phantom Experiment

In order to study the behavior of the spectrally-constrained algorithm in tracking changes in total hemoglobin, the inclusion's blood concentration was varied systematically from 20 to 44 μ M and measurements were taken. The images for total hemoglobin recovered using the spectral priors in the reconstruction, following this change in hemoglobin concentration are shown below, with comparison to the images obtained using the conventional technique along with the expected images.

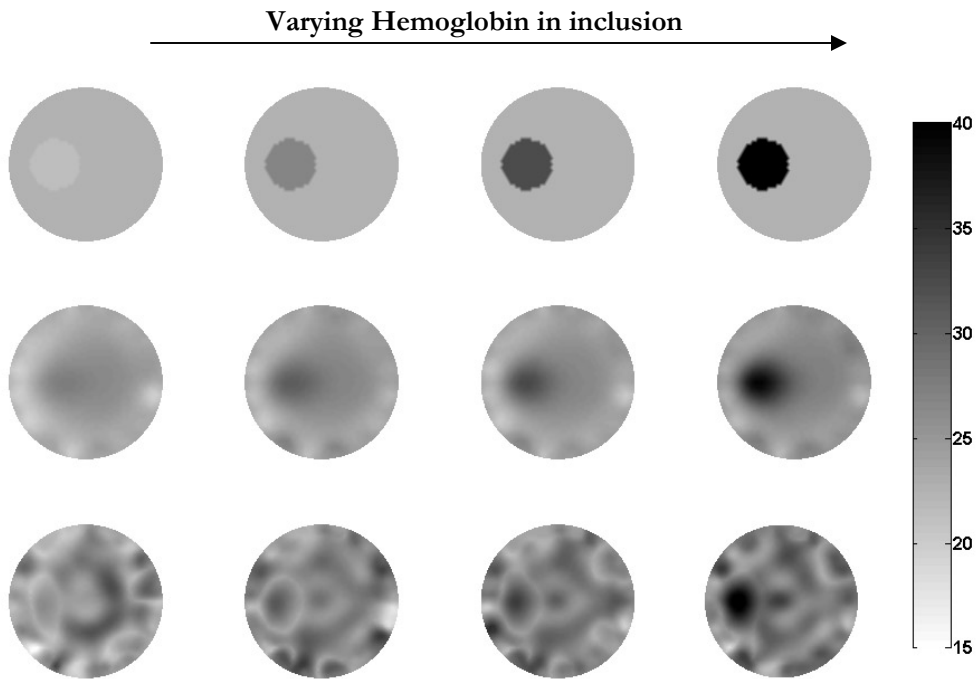


Figure 7-9: Images of a gelatin phantom whose inclusion HbT concentration was varied from 20-44 μ M. Top row shows true images for HbT. Images obtained by application of spectral priors appear in second row while the bottom row contains the images resulting from the conventional technique. The images for all other parameters (oxygen saturation, water and scatter) remained nearly constant with the HbT change.

The images shown in Figure 7.9 are consistent with images from previous experiments and simulations, with images obtained using spectral priors not only appearing smoother but also following the variation more accurately than the conventional method without the use of the priors. The mean with standard deviation for all the NIR parameters,

in the region of the anomaly are plotted below in Figure 7.10. The anomaly region was obtained using the FWHM segmentation described before in *Section 7.3.2*.

The mean in the anomaly recovered from the spectral method tracked this change in blood concentration with a mean error of 12.3%. While the average is similar to that obtained from the conventional method, the spectral method shows lower standard deviation in all the cases, as a result of reduced high frequency spatial noise, except the first concentration (where concentration in anomaly was slightly lower than the background) as shown by the error bars in Figure 7.10(a). The other parameters stayed constant through this change, as shown in Figure 7.10(b), with lower standard deviation for the spectral method (<5% overall compared to 23.5% for conventional, as percent of mean). Oxygen saturation remained accurate within 88% for both methods. While water stayed constant as expected through this change for both techniques, it did show some underestimation as found before in Figure 7.8. A significant improvement was observed in the accuracy of scatter with the mean error in scatter power reducing by nearly half, from 27% for the conventional method to 13% for the images from the spectrally constrained reconstruction. Figure 7.10(c) also shows the dramatic decrease in standard deviation in scatter power for the spectral (graph on left side) compared to the conventional method (shown on right side).

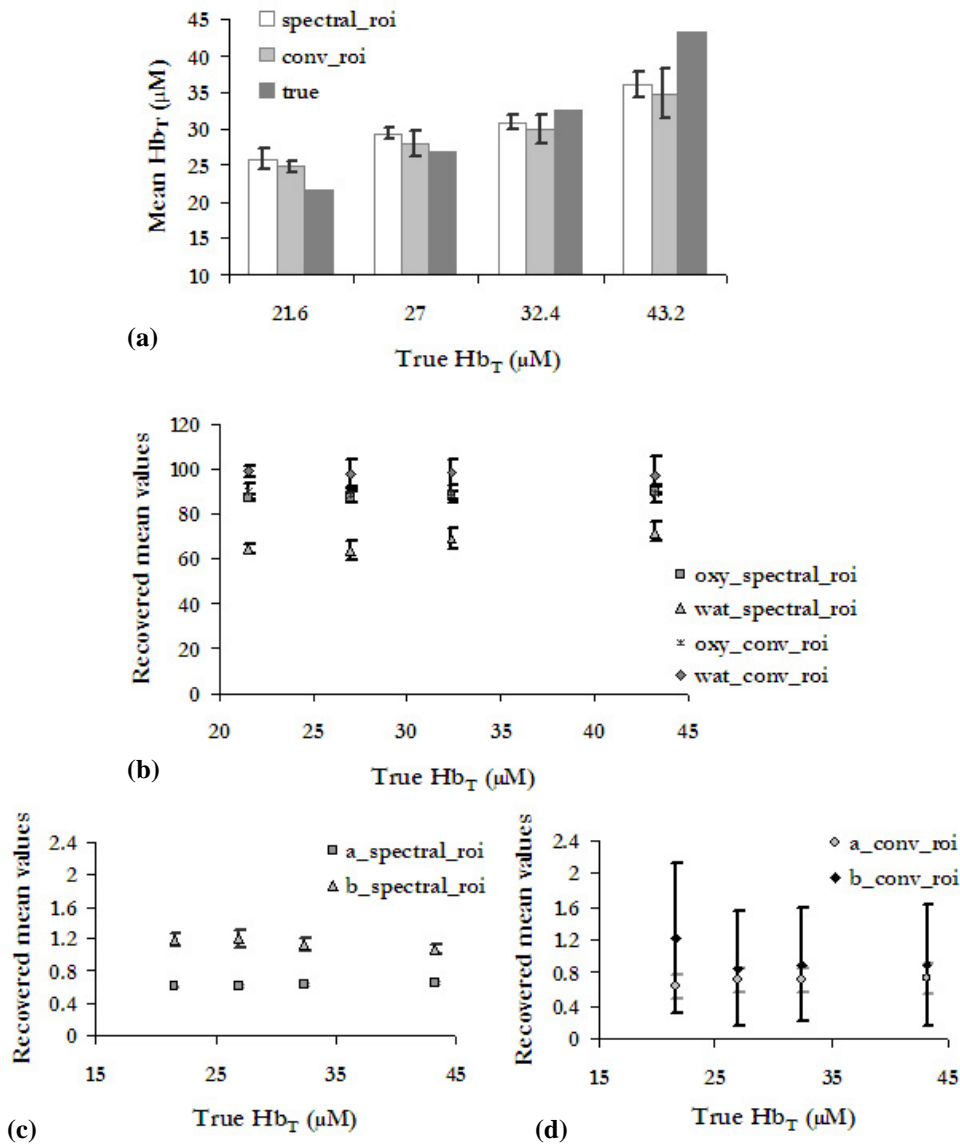


Figure 7-10: The mean and standard deviation in the anomaly region from images recovered by spectrally constrained direct reconstruction and conventional separate wavelengths property recovery following change in hemoglobin concentration in the anomaly for (a) Hb_T (μM). The other parameters did not vary as shown by (b) Oxygen saturation (%) and water (%) for both methods; (c) scatter amplitude and power for spectral method and (d) scatter amplitude and power for conventional procedure.

7.3.9 Variation of Scattering in Heterogeneous Phantom Experiments

Scattering was similarly followed by varying the Intralipid concentration in saline, in the 25mm inclusion in the gelatin phantom, from 0.75% to 1.75% in steps of 0.25%; and

keeping the total hemoglobin fixed. Such a change would result in an increase in the number density of scatterers while their size remains the same. The Mie theory approximation to scattering behavior in the regime where scatterer size is comparable to the wavelength, predicts that the number density only changes the magnitude of the scattering coefficients, but not their slope⁸³. This means that an increase in Intralipid concentration would translate to change in scatter amplitude with scatter power remaining unchanged. The test phantom was imaged by the clinical system and the amplitude and phase data obtained was used for both types of reconstruction. The images for scatter amplitude following the change in Intralipid percent, obtained using the spectrally constrained procedure are shown in Figure 7.11, along with the images from the conventional method and the expected images. The expected values were obtained from the homogeneous experiment results which were shown to be quantitatively accurate in section 3.4.

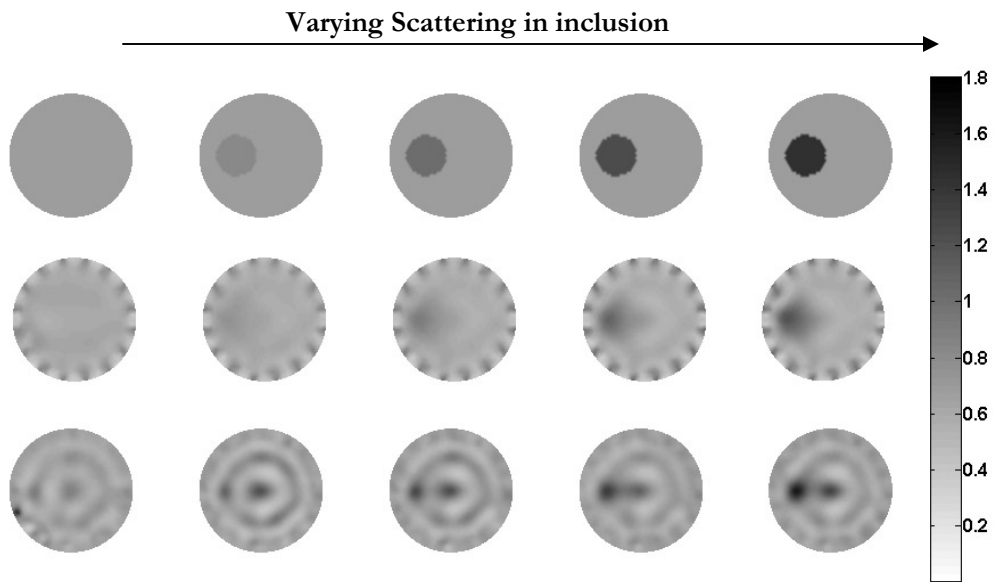


Figure 7-11: Following variation in scattering by imaging a gelatin phantom whose inclusion Intralipid concentration was varied from 0.75 to 1.75% in steps of 0.25%. Top row shows true images for scatter amplitude (in units of $10^{-3b}(\text{mm})^{b-1}$, b being scatter power) with images obtained by application of spectral priors in second row and bottom row containing these images for the conventional technique. The images for all other parameters (Hb_T, oxygen saturation, water and scatter) stayed nearly constant with this change.

While the images for both the spectral and conventional methods in Figure 7.11 show a localized increase in scatter amplitude in the region of the anomaly, the conventional method retains a ring type artifact found in previous experiments (Figure 7.8) potentially due to crosstalk with scatter power. This makes it difficult to discern the inclusion in the conventional images for the first three contrast changes in the experiment. This is eliminated in the spectrally reconstructed images, which show a smoother variation with change in scattering. Artifacts close to the boundary exist in the spectral scattering images and this may illustrate the need for a higher regularization compared to the other parameters in the direct reconstruction. The recovered average values in the ROI (as defined from FWHM criterion previously in *Section 7.3.2*) for scatter amplitude and power are plotted in Figure 7.12 (a) and (b) for both techniques.

Scatter amplitude reconstructed using the direct spectrally constrained procedure follows this variation in Intralipid percent successfully with a mean error of 17.6%, with the error increasing from 3% at lower Intralipid percent to 27.5% at higher Intralipid concentrations due to scattering. The accuracy in scatter amplitude from both methods is comparable; however the images using conventional method for this parameter are confounded by artifacts resulting in much higher standard deviation. Scatter power stays constant as expected, with a mean value of 1.19 ± 0.16 for the conventional reconstruction procedure and 1.23 ± 0.03 from the spectral method, comparable to expected value of 1.4 from van Staveren et al⁸². Figure 7.12 is consistent with the trend of lower error bars in quantification of scatter power, found in the previous sections. The total hemoglobin,

oxygen saturation and water content are expected to stay constant with scattering variation and the Figures 7.12(c) and (d) show this trend.

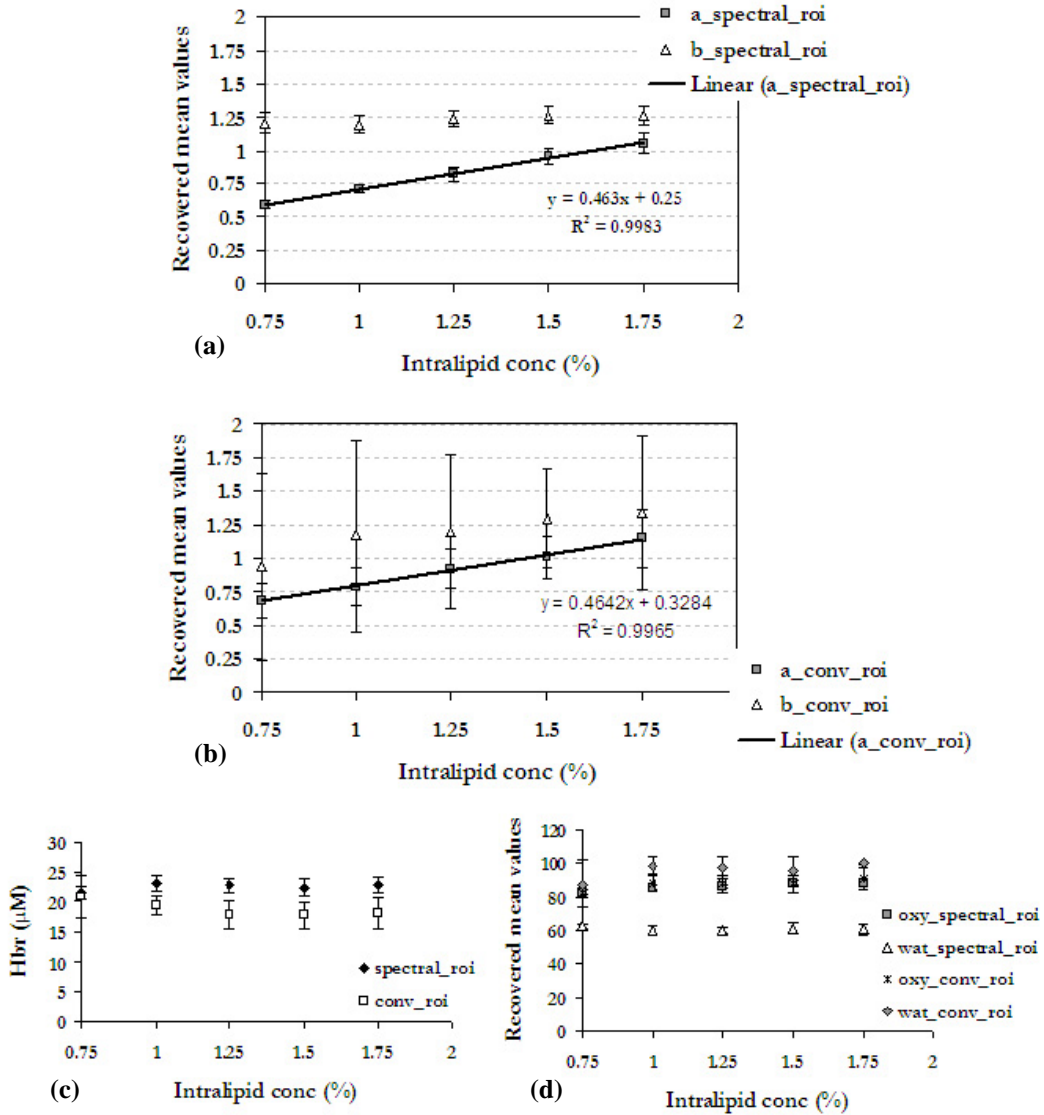


Figure 7-12: The mean and standard deviation in the anomaly region for scatter amplitude and scatter power from images recovered by (a) spectrally constrained direct reconstruction and (b) conventional separate wavelengths property recovery, following change in Intralipid concentration in the anomaly. Scatter power is expected to stay constant with this change with linear variation in scatter amplitude. The other parameters did not vary as shown by (c) $\text{Hb}_T(\mu\text{M})$ and (d) Oxygen saturation (%) and water (%) for both methods.

7.3.10 Addition of Wavelengths: Case Study

Validation in simulations and experiments using a single heterogeneity have shown clearly that the addition of spectral priors in the image formation process to directly reconstruct for chromophore concentrations and scatter provides a significant improvement in image quality and quantification of these parameters, over the existing conventional method. The information content in the images is improved and this is especially significant in oxygen saturation where hypoxic conditions could be tracked; in water content where the saturation occurring previously due to crosstalk from oxy-hemoglobin has been eliminated and in scatter where the artifacts in the image have been substantially reduced. However, the water image in Figure 7.8 (*Section 3.7*) shows a quantitative underestimation; not fully reaching the true value of 100% in the anomaly. This is explainable by the lack of sufficient wavelengths in the 850-1000nm where water features are stronger; so that steep contrasts in water could not be tracked.

In order to test out this hypothesis and demonstrate the effect of increasing the number of wavelengths for interrogation of tissue, a simulation with 1% random Gaussian noise in the amplitude and phase data has been carried out. Here, the test phantom contained five heterogeneities, one for each of the five reconstructed parameters. This case study would be ideal to study the cross-talk between the parameters as well. Frequency domain measurements were generated using the forward finite element model solver for background concentrations of 6 μ M oxyhemoglobin, 4 μ M de-oxyhemoglobin, 40% water, scatter amplitude = 1 and scatter power = 0.4, all falling in the normal range of values typically observed in breast tissue³¹. A contrast of 3:1 between anomaly and background values was given for HbO₂ and Hb in separate heterogeneities. Water was increased to 70%

in a third anomaly along with contrast of 1.5 in scatter amplitude in a fourth anomaly and 25% contrast in scatter power in the fifth heterogeneity. The wavelengths of use are shown below in Figure 7.13 with the molar absorption spectra at these wavelengths taken from Prahl⁷⁶ for oxy and de-oxyhemoglobin and Hale and Quarry⁴ for water. After addition of noise in the data generated for 14 wavelengths almost evenly distributed to span the range of 660-960nm, the spectrally constrained direct chromophore reconstruction was carried out using six of the wavelengths (used in the current system) and compared against the images obtained by applying the method to all of the 14 wavelengths along with the true images in Figure 7.14.

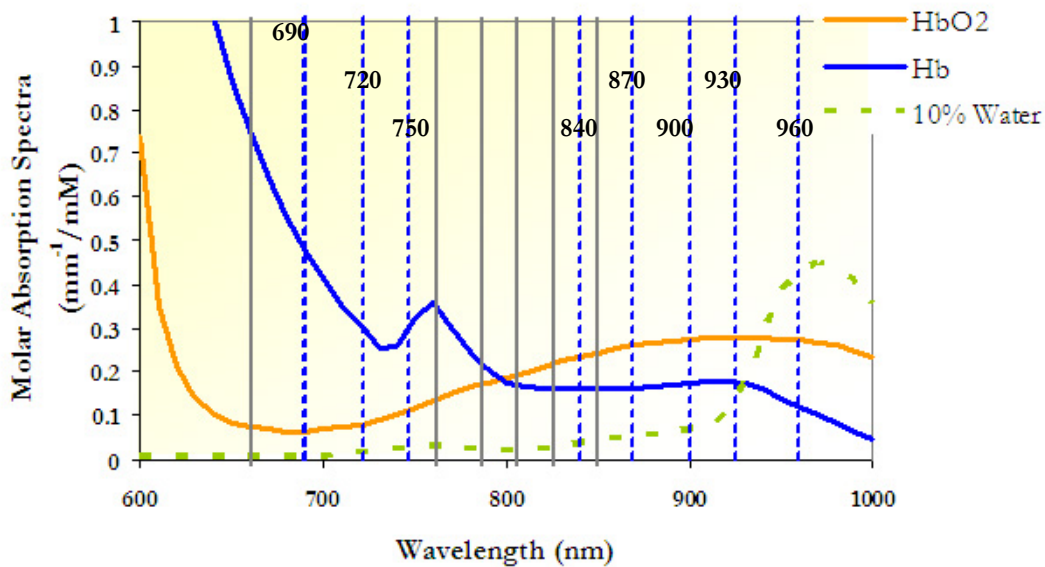


Figure 7-13: The molar absorption spectra for the absorbing chromophores^{4, 76} (oxyhemoglobin-HbO2, de-oxyhemoglobin-Hb and water (multiplied by 10 to fit on the same scale) is shown in Figure. The gray bold lines show the current six wavelengths of use and the blue dotted lines with labels show the wavelengths added to these, to study the behavior of the spectral reconstruction to increasing number of wavelengths.

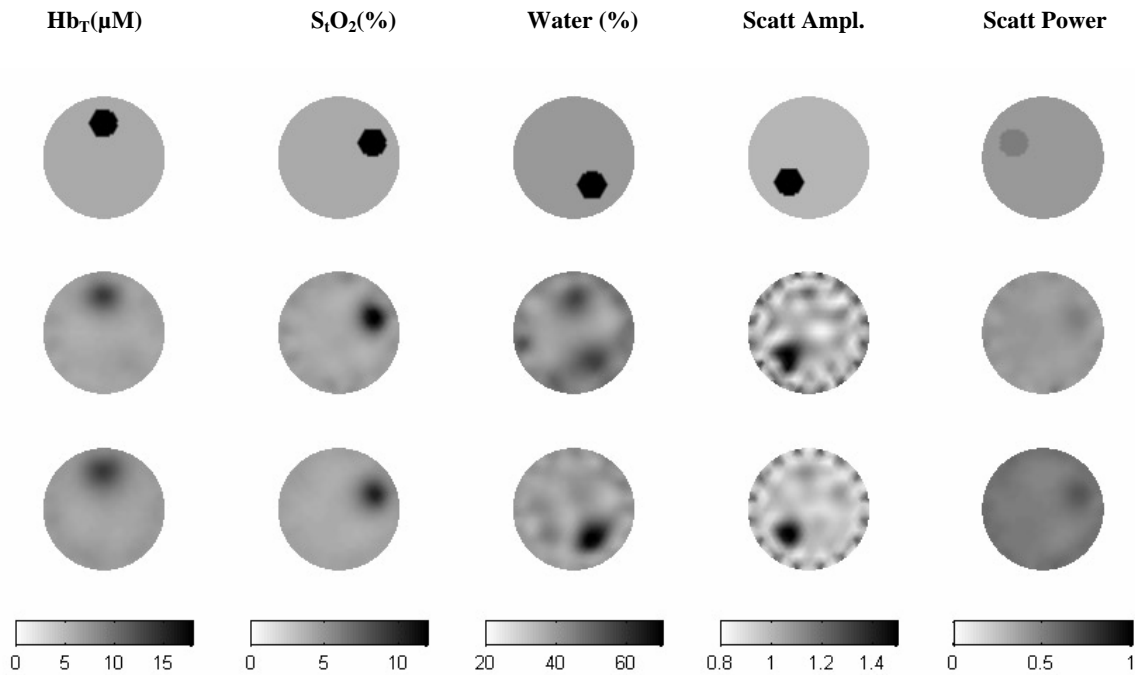


Figure 7-14: Top row shows the true images (Hb_T (μM), Oxygen saturation (%), water (%), scatter amplitude and scatter power) for the test phantom used to generate frequency domain measurements. Middle row shows the images recovered by the spectral technique using six of the wavelengths (currently in use in the clinical instrumentation) and bottom row shows the images obtained by the use of fourteen wavelengths almost uniformly distributed in the range 660-960nm which includes the six wavelengths used for middle row images.

The images recovered using six wavelengths in Figure 7.14 show accurate recovery of oxy and de-oxyhemoglobin but the water image shows an underestimation as observed previously, with a peak of 53% compared to the true value of 70%. Crosstalk between oxyhemoglobin and water is also discernible in the image as a pseudo increase in water in the region of the oxyhemoglobin anomaly (12 o clock position). The use of all 14 wavelengths, which includes four wavelengths beyond 850nm, capturing more distinct features of water, eliminates this artificial anomaly in the water image; with the maximum in the real water heterogeneity at 5 o clock phase, reaching 73.7% comparable to the expected 70%. The

scatter power images for both cases are comparable and the scatter amplitude image shows better localization of the anomaly in the image recovered using all fourteen wavelengths.

The averages in the region of the five heterogeneities, for each of the parameters are plotted along with the standard deviations and the true values in Figure 7.15(a) for the spectrally constrained reconstructions using six wavelengths and fourteen wavelengths. Each of the anomalies were recovered using the FWHM criterion described before (*Section 3.2*) on the respective images with the exception of scatter power where the true image was used, because the crosstalk from de-oxyhemoglobin makes it difficult to clearly discern the anomaly. The low contrast (25%) between the scatter power inclusion and the background may also be responsible for this.

The background means are shown with standard deviations alongside the expected values in Figure 7.15(b). Both Figures show the improved accuracy in the quantification of water content by the addition of longer wavelengths in the range of 850-960nm. The average for water is now accurate with less than 5% difference from the true value compared to 16% for the six wavelengths recovery. Further, the crosstalk between oxyhemoglobin and water has been reduced from 11.6% for six wavelengths to 1.2% for the reconstruction using all fourteen wavelengths. The quantification for all other parameters is comparable for both cases.

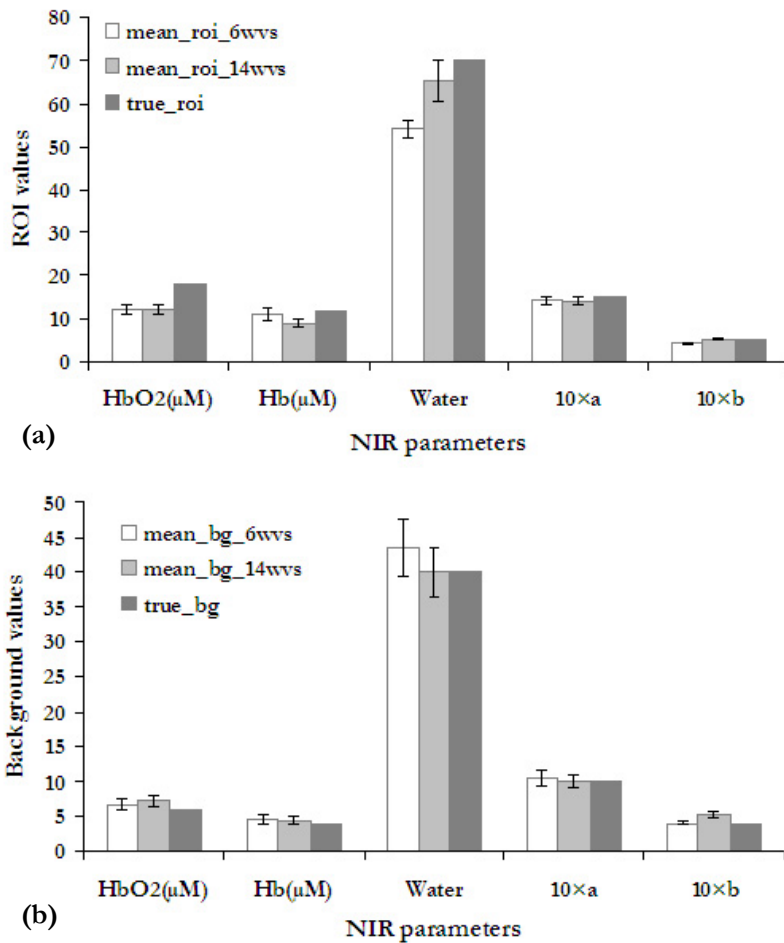


Figure 7-15: (a) Average and standard deviation for each of the NIR parameters in their respective heterogeneities, obtained by FWHM segmentation on the images. The images were recovered by the spectral reconstruction for two cases: current six wavelengths used in the clinical imager and the extension to 14 wavelengths uniformly sampling the entire range of 660-960nm. The test phantom consisted of five heterogeneities (one for each NIR parameter) with 1% random Gaussian noise in the simulated frequency domain data. (b) shows the background recovered means with standard deviations alongside true values.

7.4 Discussion

Spectral imaging offers the potential of truly realizing the potential of ‘hemoglobin imaging’, the key idea behind the innovation in the NIR research¹³¹. Initially, the field started out with obtaining images of absorption and reduced scattering coefficients at different

wavelengths individually, showing the possibility of contrasts between tumors and surrounding tissue^{45, 107, 132, 133}. This was followed by utilizing multi-wavelength data acquisition capability to permit recovery of chromophore concentrations and extended indices such as hemoglobin, oxygen saturation, scatter amplitude and scatter power^{6, 28}. However, in so far, this was done by a linear least squares fit (or constrained linear least squares, as detailed in *Chapter 2*, to bound the parameters) which did not utilize the spectral behavior in the recovery of the optical properties themselves. NIR tomographic imaging of breast tissue being in a scatter-dominated regime, the inverse problem itself is ill-posed with insufficient measurements at the boundary of the domain utilized to create property maps of the entire domain, using the diffusion equation; and is susceptible to instability due to noise in the data (this noise being inevitable because of the scattering). Hence, a method providing more robust behavior to such noise would certainly be a welcome addition to the field. The possibility offered by a spectrally constrained direct chromophore and scattering reconstruction is a natural progression of a basic hypothesis: use of as much inherent priori information as available as long as they don't contradict one another. The approach presented here uses simultaneously all six wavelengths of frequency domain measurements and incorporates the Beer's law for absorption and Mie theory for scattering as constraints. Unlike other fields (microwave imaging¹²⁴) where such models may not be readily available, these models for absorption and scatter form the basis of NIR imaging. As with any model, there are certainly some key assumptions: absorption has been assumed as the contribution from three chromophores-oxy and deoxy hemoglobin and water. Lipid absorption has been ignored and Quaresima et al⁹⁷ have shown this absorption to be negligible at the current wavelengths of use. Mie theory assumes that the scatterers are homogeneous spheres⁸² and studies on red blood cells and yeast^{85, 86} have shown this to be a reasonable approximation.

Finally, the diffusion equation itself is an approximation for light propagation in a scatter-dominated regime¹³⁴, and is widely accepted as being valid for breast tissue.

The results documented here hold up this hypothesis and spectral *a-priori* information along with parameter reduction in the reconstruction has a key role in:

- 1) Reducing sensitivity of the reconstruction to noise in measured data by making the problem better posed with simultaneous use of six wavelengths of measurements
- 2) Decrease in crosstalk between parameters: oxyhemoglobin and water having similar spectra, are better separable now because of the incorporation of their individual spectral features. Similarly, de-oxyhemoglobin and scatter both have a decreasing trend but are sufficiently different in *a-priori* information.
- 3) Improvement in quantitative accuracy as demonstrated in averages rather than peak, in tumor and surrounding tissue from the reconstructed images.
- 4) Qualitatively enhanced information content in the images permitting easier detection of tumors.

Each of these have been validated in simulated data with noise and experimental measurements. The results from *Section 7.3.1* show improved robustness of the reconstruction to increased amounts of noise in the data. The frequency domain instrumentation in use has typically 1% noise in amplitude and 0.5 degrees in phase⁴³, and at this noise level, using simulated data from a homogeneous phantom, water images show a reduction in standard deviation from 32% to 10% (as percent of the mean) in going from the conventional to the spectral approach. Even at a 5% noise level, the spectral approach shows recovery of the parameters accurate within 10% on an average, with significantly reduced standard deviation as compared to the conventional method. In heterogeneous

phantoms, this trend prevailed as well, with the spectrally constrained reconstructions using data from a test phantom with a simulated tumor (*Section 7.3.2*), giving accurate quantification (mean error within 15%) even for 5% noise scenario. The reconstructed images from the simulated test phantom in Figure 7.2 show the extent of the effect of incorporating priors: the images are not only smoother, but hypoxia could be clearly discernible in the oxygen saturation image, a vast improvement over the conventional oxygen saturation images, and was accurate to within 99%. Crosstalk in water from oxyhemoglobin was reduced from 30% to 7% and scatter showed much superior recovery. The reduction in noise in the images is also tangible in homogeneous experimental data, and the NIR parameter images in Figure 7.4 show the suppression of the artifacts in the images, similar to the trend in simulated data.

The Hill curve relationship between oxygen saturation (S_tO_2) and pO_2 of oxygen was followed by the spectral method in the graphs of Figure 7.6, which showed that S_tO_2 was accurate with a mean error of 7.7%. Total hemoglobin estimates remained constant through this change in pO_2 producing a mean that is accurate to 97% of the expected value. Water content also showed this trend having a mean of 94.2% which compared well with the predicted value of 100%. Though some variation was found in scatter amplitude and scatter power, μ'_s at 785nm remained constant with change in oxygenation with a mean of $1.3 \pm 0.03 \text{ mm}^{-1}$. The standard deviations in the oxygen saturation images remain low, even at lower oxygenation. This translates into successful recovery of S_tO_2 in malignancies without significant noise or crosstalk between scatter parameters and de-oxy hemoglobin. Total hemoglobin recovered by the spectral approach was separately validated using experimental data obtained by varying blood concentration from 0.2 to 1% in a homogeneous phantom

set up. Quantitatively accurate results with a mean percent error of 6.2% were obtained. No crosstalk between any of the parameters was observed during this variation as shown in Figure 7.7(b), where oxygen saturation, water, scatter amplitude and scatter power remained unchanged and close to predicted values. The reconstructions from the gelatin heterogeneous phantom set up shown in Figure 9, backed this trend with the spectral method successfully tracking the change in hemoglobin with mean error of 12.3% with other parameters remaining constant. The quantification in scatter power (expected to stay constant) was improved with the mean error reducing by nearly half using the spectral method, in comparison to the conventional approach.

Scattering is another area where the constraints from Mie theory incorporated into the reconstruction significantly improve the quantification of the scatter amplitude and power. Recent studies have used scattering to study structural variations. For example, Poplack et al¹³⁵ showed in a normal cohort of 23 women that there is a significant decrease in the reduced scattering coefficient (μ'_s) at 785 nm with increasing body mass index (BMI) and that adipose tissue was less scattering than glandular tissue, as expected. The same trend was observed by Durduran et al⁵ in a subject pool of 52 volunteers. Cerussi et al²⁷ used the fit of μ'_s to Mie theory approximation to show that scatter power decreases with increasing BMI in a group of 30 healthy women. Pogue et al²⁵ showed that scattering power and scatter amplitude could successfully separate categories of fatty and scattered breasts from extremely dense breasts ($p < 10^{-4}$) in a survey of 39 women with normal mammography. Since the risk of cancer is strongly correlated to the breast density²³, this separation of breast densities in a non-invasive manner could prove very useful. Though these trends may prove

to be promising in the future, their quantitative accuracy must be validated in phantom studies. Hence, it is important to investigate the accuracy and standard deviation in these parameters in order to fully exploit the NIR information. In the homogeneous experimental setup in *section 3.3*, the recovered mean for scatter amplitude and scatter power agreed well with predicted values from Van Steveran et al⁸². Change in scattering, obtained by varying Intralipid concentration in a homogeneous phantom solution, was successfully followed (Figure 7.5) where scatter amplitude varied linearly, and scatter power showed a mean of 1.4 ± 0.1 during the changes in concentration. The results were consistent with theoretical predictions that a change in Intralipid concentration should affect only the amplitude of the scatter⁸³. The crosstalk between scatter parameters and chromophore concentrations was minimal with total hemoglobin, oxygen saturation and water content staying constant through this change (Figures 7.5(c) and 7.5(d); except at the highest scattering concentration of Intralipid (1.5%). The trend was continued in the gelatin phantom setup where the inclusion scattering was varied (*Section 7.3.9*): again, the spectral method showed accurate quantification with error as low as 3% at the lowest Intralipid concentration and overall mean error of 17.6% in tracking the change. The scatter power stayed constant with a mean of 1.23 ± 0.03 from the spectral method compared to a mean of 1.19 ± 0.16 from the conventional technique, the former agreeing closer to the expected value. The recovered scatter amplitude images shown in Figure 7.11 demonstrate that change in scattering is more qualitatively traceable using the spectral priors. One aspect that needs further investigation is the sensitivity to heterogeneities in scatter power. Figure 7.14 showed that the addition of wavelengths, while improving localization in scatter amplitude, does not demonstrate the same trend in scatter power. It may be that low contrasts in scatter power (25% in the simulation study) between anomaly and background cannot be recovered; and scatter power

is more accurate in quantifying bulk tissue. The hypothesis that scatter power is associated with particle size^{83, 84} backs such bulk quantification and it would be important in the future, to assess how much of change in scatter power, a significant change in size yields.

Water is an important measure of breast physiology; however, its quantitative accuracy from NIR tomography is yet to be validated. In the past, several studies have used a fixed water content in tissue (such as assuming 30-31% fraction in tissue) in order to allow spectral fitting of hemoglobin levels^{5, 136}, or have used radiological data¹³⁷ because the availability of insufficient wavelengths and the crosstalk between water and oxyhemoglobin have prevented quantitatively accurate recovery of the water absorption. McBride et al¹³⁸ and Cerussi et al²⁷ have shown that using sparse spectral image data from a subject with assumptions about the bulk concentration for water and lipids could have up to 15% influence on Hb_T and oxygen saturation estimates. In recent studies, water has been shown to have significant variation with breast size in normal subject studies³¹, with values between subjects varying significantly from 10% up to 70%. This large range was observed in a 30 subject population as shown by Cerussi et al²⁷, and values of 21% to 82% were observed in a 26 subject population given by Srinivasan et al³¹. These large numbers suggest that water is a measure of the extravascular space, since the vascular space is clearly less than 2% in most breast tissues. Thus water gives different information than that of hemoglobin, about the physiology of the breast and spatial changes are expected in water due to differing content in the fatty and glandular tissue, which vary with composition of the breast. The change in water content during the course of the menstrual cycle has been followed by Cubeddu et al, showing an increase in water in the second half of the cycle⁵⁴ for one patient. Shah et al⁷ have shown an increase of up to 28.1% in water in the luteal phase in a single volunteer and

Pogue et al²⁵ have shown individual variations in 7 subjects with a mean value of nearer 2.5%. In a study following the effect of neoadjuvant chemotherapy¹³⁹ in a subject with a palpable adenocarcinoma using optical white-light spectroscopy, water showed the most dramatic change, dropping 67% over the course of three treatment cycles. These studies have shown important trends in water content. However, in order to improve the clinical utility of the recovered values, it is important to show that they are quantitatively accurate estimates as well. The results shown here provide evidence of improvement in the quantification of water using the spectrally constrained approach, over the conventional method of fitting for the chromophore and scattering parameters from optical property reconstructions. Improved information is observable in the water images which are now artifacts-free from crosstalk with oxyhemoglobin and saturation at 100%. Figures 7.1, 7.2 and 7.3 show the reduced standard deviation using simulated data from homogeneous and heterogeneous imaging fields and Figure 7.8 (obtained from the gelatin experiment) is most representative of this aspect in the images. The spectral method using the current six wavelengths is certainly no end-all solution: an underestimation in reaching steep changes between background and anomaly is still a problem. The solution to this was analyzed in *Section 7.3.10* where the inclusion of data at wavelengths in the 850-1000nm range suitably encompassing the entire range of 660-960nm, improved the recovery of water. Water is then accurate to less than 5% mean error and the image in Figure 7.14 is demonstrative of this and the further reduction in crosstalk from oxyhemoglobin (reduced to 1.2% from 11.6% error initially).

The spectrally constrained approach is inherently robust due to the addition of *a-priori* spectral behavior. It requires less spatial filtering whereas the conventional technique

benefits from a mean filter to prevent excessive noise in the images. This new approach also converges faster, and is readily extendable to 3-D models as well. Use of data at additional wavelengths can be easily implemented without much computational burden in the inversion process. This has been integrated with spatial priors, obtained from a combined MRI-NIR system to achieve benefits of both types of priors, and is discussed in *Chapter 9*.

As the use of NIR tomography expands, spectrally constrained reconstruction should add considerable value in obtaining quantitatively accurate estimates of different NIR parameters. The use of frequency domain measurements allows good separation of chromophore and scattering and together with the spectral approach, we obtain the realization of true ‘hemoglobin imaging’ with desirable features of reduced crosstalk between the parameters, suppression of image artifacts, insensitivity to noise in the measurements and finally, accurate quantification and qualitatively improved images of the NIR parameters.

8. Characterization of Breast Tumors In-Vivo using Spectrally Constrained Direct Reconstruction

8.1 Introduction

Near-Infrared (NIR) imaging of tissue can potentially provide quantitatively accurate estimates of physiologically important parameters such as hemoglobin, oxygen saturation, water fraction, lipid fraction and scattering indices^{6, 17, 105, 140-142}. However, past approaches to NIR tomography have suffered from using too few wavelengths, and simplistic strategies for spectral deconvolution. The major benefits of the direct spectral reconstruction are well established^{130, 143} (documented in *Chapter 7*) to be improvements in the accuracy of quantification of oxygen saturation, water fraction and scattering parameters. The relevance of improved accuracy in these parameters is significant, as these parameters provide fundamental metabolic information about tissue which is not obtained with any other imaging modalities today.

The value of oxygen saturation in particular could be significant, if sufficient accuracy can be achieved in estimating this parameter with an imaging method. Tissue hypoxia is found in breast cancers due to metabolic imbalance between oxygen supply and consumption²⁶, which has significant potential in diagnosis as well as prognosis for radiation

treatment. On average, the mean partial pressure of oxygen (pO_2) is lower in malignancies than in surrounding tissues (typically ≤ 20 mm Hg)²⁶. This presents a difficult situation for radiotherapy which is ineffective when pO_2 is less than 5 mm Hg¹²⁹. Tumor oxygenation may serve to predict its response to radiation treatment as suggested by its critical role in modifying the dose response curve¹⁴⁴ and may also be related to the likelihood of occurrence of distant metastases as well¹⁴⁵. Vaupel et al¹⁴⁶ have shown that although hypoxia did not correlate with tumor size, tumor location, grade or stage, it did depend critically on whole blood hemoglobin levels; even mild anemia in breast cancer subjects causes the development of hypoxia. Pretreatment hemoglobin levels¹⁴ can also aid in predicting tumor response to primary chemotherapy. While the hemoglobin levels referred to here were baseline values, those measured by NIR imaging for the normal tissue surrounding the tumor may also be representative of the oxygen carrying capacity of the blood in the breast.

Conover et al¹⁴⁷ used NIR spectroscopic measurements in vivo on subcutaneous rat mammary adenocarcinomas to show correlation with cryospectrophotometry estimates of oxygen saturation on rapidly frozen sections of the same tumors. These studies suggested that NIR may be able to detect hypoxic regions even when their distribution occurs on a spatial scale that is beyond the resolution limit of NIR. Tromberg et al²⁸ observed a decrease in oxygen saturation in spectroscopic studies on a palpable mass diagnosed as ductal carcinoma in situ (DCIS). In a related study which monitored neoadjuvant chemotherapy using spectroscopy¹³⁹, they found an initial tissue oxygen saturation decrease in the lesion with respect to the surrounding tissue followed by a slight peak, when tracked over a 10 week course of treatment. Spectroscopic methods, however suffer from over-sampling of the superficial bulk tissue, which while suitable for palpable tumors, may misrepresent spatial

changes in deeper lesions. Tomographic imaging methods sample more broadly and provide a better representation of the whole breast volume. In a study¹³³ using time domain instrumentation with two wavelengths and a water contribution fixed at 30%, lower oxygen saturation was observed in images of two carcinomas. Heffer et al¹⁴⁸ used an ‘oxygenation index’, generated from frequency domain measurements, to show a decrease in carcinomas. In previous work at Dartmouth, McBride et al¹³⁸ used an NIR tomography system to image a subject with a 2.5cm infiltrating ductal carcinoma, and although an increase in hemoglobin was observed, reduction in oxygen saturation was not found. Dehghani et al⁴⁶ used three-dimensional modeling to obtain tomographic images from a patient with a infiltrating ductal carcinoma and reported an increase in blood oxygen saturation level, contrary to expectation. Grosenick et al⁵⁵ surveyed results from 50 carcinomas using a dual wavelength time domain instrument and showed good separation of tumors from healthy tissue based on total hemoglobin. However, in their study oxygen saturation both increased and decreased at the location of tumors such that no clear hypoxic trend was evident. In the current study, the spectrally constrained direct chromophore and scattering reconstruction, shown to be quantitatively superior and stable to noise in phantom measurements, has been applied to study malignancies.

Another NIR parameter of significant interest is scattering. Optical scattering has been correlated to mammographic density³¹ which is a major risk factor in the development of cancer²³. A recent study³⁰ to assess NIR transillumination spectroscopy as related to mammographic density and cancer risk, showed that optical spectroscopy predicted the radiological assessment of density with a principal components analysis (PCA) model in the range of 90% with an odds ratio comparable to mammography. In breast cancer locations,

scattering is certainly expected to increase because the tumor cells stimulate endothelial cell proliferation¹⁴⁹ which increases the cellular density. In addition, the tortuous tumor vessel network is held together by dense fibrotic connective tissue³² which may be optically dense, owing to the presence of different sized scatterers relative to the surrounding tissue. Spectroscopic studies have shown this increase in scattering in a palpable carcinoma¹⁵⁰. In this paper, scattering is analyzed at the location of the tumor from tomographic images obtained through spectrally constrained direct reconstruction.

8.2 Methods

As part of a clinical trial to investigate alternate imaging modalities for diagnosis of breast cancer, NIR imaging was carried out on women with mammographically-detected abnormalities. All clinical work was approved by the institutional committee for the protection of human subjects at Dartmouth, and informed consent was obtained from all participants. The women were imaged in the prototype NIR tomography system at the Dartmouth Hitchcock Medical Center (DHMC). The mammograms were interpreted by a radiologist specializing in breast imaging (Dr. Steve .P. Poplack). The clinical information utilized in the study included the radiographic density, the location of the tumor and its size, in addition to architectural features. The breast radio-density was categorized according to the BI-RADS system¹⁵¹ as classifications of (1) almost entirely fat, (2) scattered fibroglandular tissue, (3) heterogeneously dense, or (4) extremely dense. Pathologic studies were completed following biopsy (Dr. Wendy A. Wells) to provide tumor histologic type, grade and size. In addition, using reproducible, computer-assisted image processing methodology described elsewhere¹⁵², the mean vessel density of the tumor and the ratio of malignant epithelium to surrounding stroma (epithelial to stroma ratio) were also assessed.

The results from six women with breast tumors, three of which were diagnosed as infiltrating ductal carcinomas, one with fibrosis and two with fibrocystic disease; were analyzed here using the spectrally constrained direct chromophore and scattering reconstruction. The contrast between the tumor and background was documented along with interpretation of the images and their correlation to mammography, pathology and the physiology of the different types of cancers.

8.3 Results

8.3.1 Case Studies 1, 2&3: Infiltrating Ductal Carcinomas (IDCs)

NIR tomographic images were obtained from a 73 year old female volunteer (patient ID #1035) with breast cancer. The left craniocaudal and magnified close-up mediolateral views of the mammogram are shown in Figures 8.1(a) and (b). They revealed a peripherally located spiculated mass of size 2.5 cm (maximum focal diameter) at 2:30 in clock face position with architectural distortion occurring over a much larger area (up to 6cm). The patient also went through ultrasonography which confirmed the existence of a hypoechoic irregular mass in the same location. Multiple simple cysts were also evident. Following a 1.1cm core needle biopsy, the tumor was diagnosed as infiltrating ductal carcinoma with lobular features. The subject underwent the NIR clinical exam two weeks after the biopsy; the images obtained by applying spectrally constrained reconstruction, along with the conventional method of recovering the optical properties at separate wavelengths, are shown in Figure 8.1(c). The mid-plane (marked to contain the tumor) measurements at five wavelengths, excluding 849nm, were used and the breast diameter was 10.4cm corresponding to this plane. The breast density was categorized as heterogeneously dense

(category 3) and pathological examination of the tumor through the biopsy sample revealed a vessel density of 0.9%.

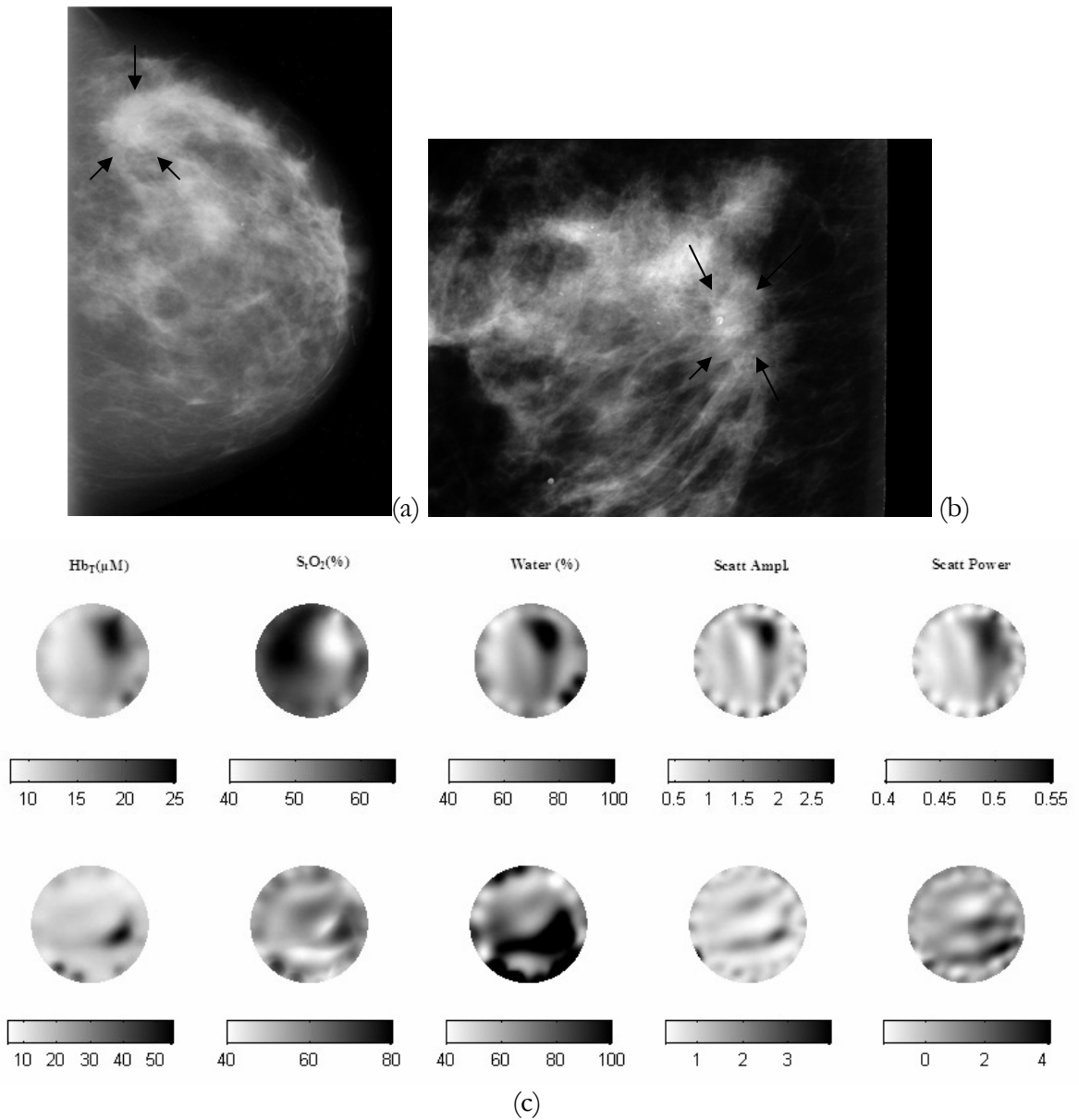


Figure 8-1: (a) left craniocaudal mammogram and (b) magnified close-up mediolateral mammogram from the left breast of a 73yr old woman with a 2.5cm spiculated mass (marked with black arrows) diagnosed as infiltrating ductal carcinoma by core-needle biopsy (patient ID #1035). (c) top row shows images for Hb_T(μM), S_O₂ (%), water (%), scatter amplitude and scatter power obtained using the spectrally constrained direct chromophore reconstruction; bottom row shows the images of the same using the conventional separate wavelength approach. Images in top row correspond well with tumor location (given as 2:30 clock face position, close to the periphery) from the mammogram.

The total hemoglobin image obtained from the spectral reconstruction shows a localized increase at the site of the tumor along with a reduction in oxygen saturation. The oxygenation decrease, an indication of an hypoxic situation in the tissue, is not observable in the images from the conventional method. This finding is consistent with results generated from simulated data (with 1% random Gaussian noise)¹⁵³ and other experiments which showed that the spectral method is quantitatively and qualitatively superior when tracking a change in oxygenation. Imaging of the tumor oxygenation response is a strong indicator of the potential of NIR tomography to study hypoxic fractions in malignancies. The increase in hemoglobin is consistent with earlier studies⁶ and the theory that angiogenic activity results in increased vascularity^{32, 149}. The conventional method shows higher values for total hemoglobin in the tumor, compared to the spectral method, with the water content saturating in most of the image, at 100%. Corlu et al^{130, 143} have also reported this trend in a carcinoma, indicating a false-increase in hemoglobin with the conventional technique, possibly due to a cross-talk between oxy-hemoglobin and water. The water image using the conventional method shows significant artifacts; however, the artifacts are removed in the spectral method in which case water shows a clear increase at the location of the tumor. This is consistent with the expected physiological changes in a tumor which include a leaky vasculature formed in the process of angiogenesis that is responsible for creating an interstitium containing inflammatory cells, fibroblasts and other enzymes facilitating cell growth¹⁴⁹.

The scatter images from the conventional method are more artifacts-ridden with abnormally high values for amplitude at certain locations as well as negative values for power, that do not correspond to the scattering model predictions. However, with the spectral approach, both scatter amplitude and power show a localized increase at the site of the tumor. Scatter amplitude from the Mie theory approximation, is found to be more sensitive to the number density of the scatterers whereas their size is usually governed by the slope of scattering or the scatter power⁸³. Hence, we expect the change in scatter amplitude due to cell proliferation to be more localized than scatter power. The contrast in scatter power is possibly due to fibrosis occurring in malignancies which explains the increased optical density.

It is evident that the images from the spectrally constrained reconstruction show physiological changes more clearly, with undeniable improvement in image quality. The accuracy of the method has already been validated and henceforth only the spectral method is used to analyze breast cancer images presented. Based on the five NIR parameter images from the top row in Figure 8.1(c), the average in the tumor and the background were obtained from a FWHM criterion applied to the total hemoglobin image. This ensures that the tumor size, while close to the true size, is specific to the NIR imaging modality and defined accordingly. The criteria has been applied successfully in earlier studies¹¹⁶. Figure 8.2 shows the results when the approach is applied to the images above from the spectrally constrained reconstruction. The total hemoglobin increased to a maximum of 24.5 μM in the tumor, while the background had a mean of 13.2 μM , resulting in a contrast of 86% in tumor versus surrounding tissue. A decrease in oxygen saturation was observed at the location of the tumor reducing by nearly 13% from an average of 56.4% in the background to 43.6% in

the tumor. Water showed an average increase of up to 89% in the cancer relative to 65% in the background, which may also be due to the existence of the cysts found in the sonogram. The tumor also showed a contrast of nearly twice that of scatter amplitude (mean of 0.98 in the background to 2.0 in the tumor). The contrast in scatter power was less pronounced, though an increase in tissue density at the cancer location could still be observed.

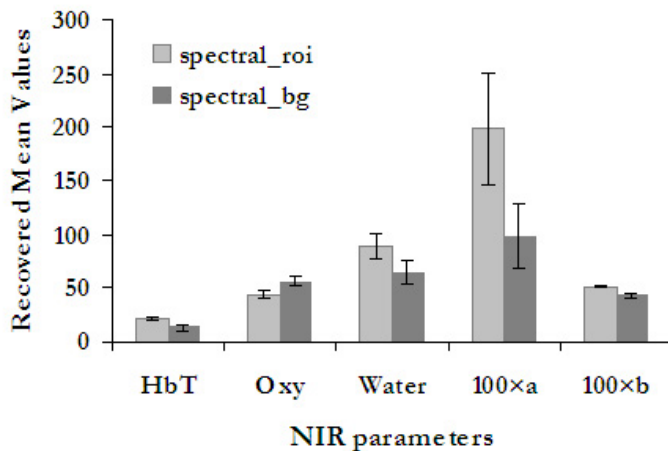


Figure 8-2: The average for the five NIR parameters along with standard deviation in the region of the tumor and the background (for the patient corresponding to Figure 8.1). The tumor was defined by segmentation of the images obtained from the spectrally constrained direct chromophore reconstruction using the FWHM criterion. The tumor exhibits increases in total hemoglobin (Hb_T), water and scatter with decreases in oxygenation, compared to the surrounding tissue.

In the second case, the NIR clinical examination was carried out on a 37 year old female volunteer (patient ID# 1077) to image a palpable mass. Mammography revealed a 3cm irregular lesion centrally located at the 6:30 clock face position, with ill-defined margins in both the left craniocaudal and left mediolateral oblique mammograms (left craniocaudal mammogram and magnified view are shown in Figures 8.3(a) and (b)). The tumor was 5cm from the chest wall. The patient underwent ultrasonography which showed a solid mass

larger than 5cm in size (Figure 8.3(c)). The tumor was confirmed by a biopsy to be an infiltrating ductal carcinoma. Pathology studies on the resected specimen indicated a vessel

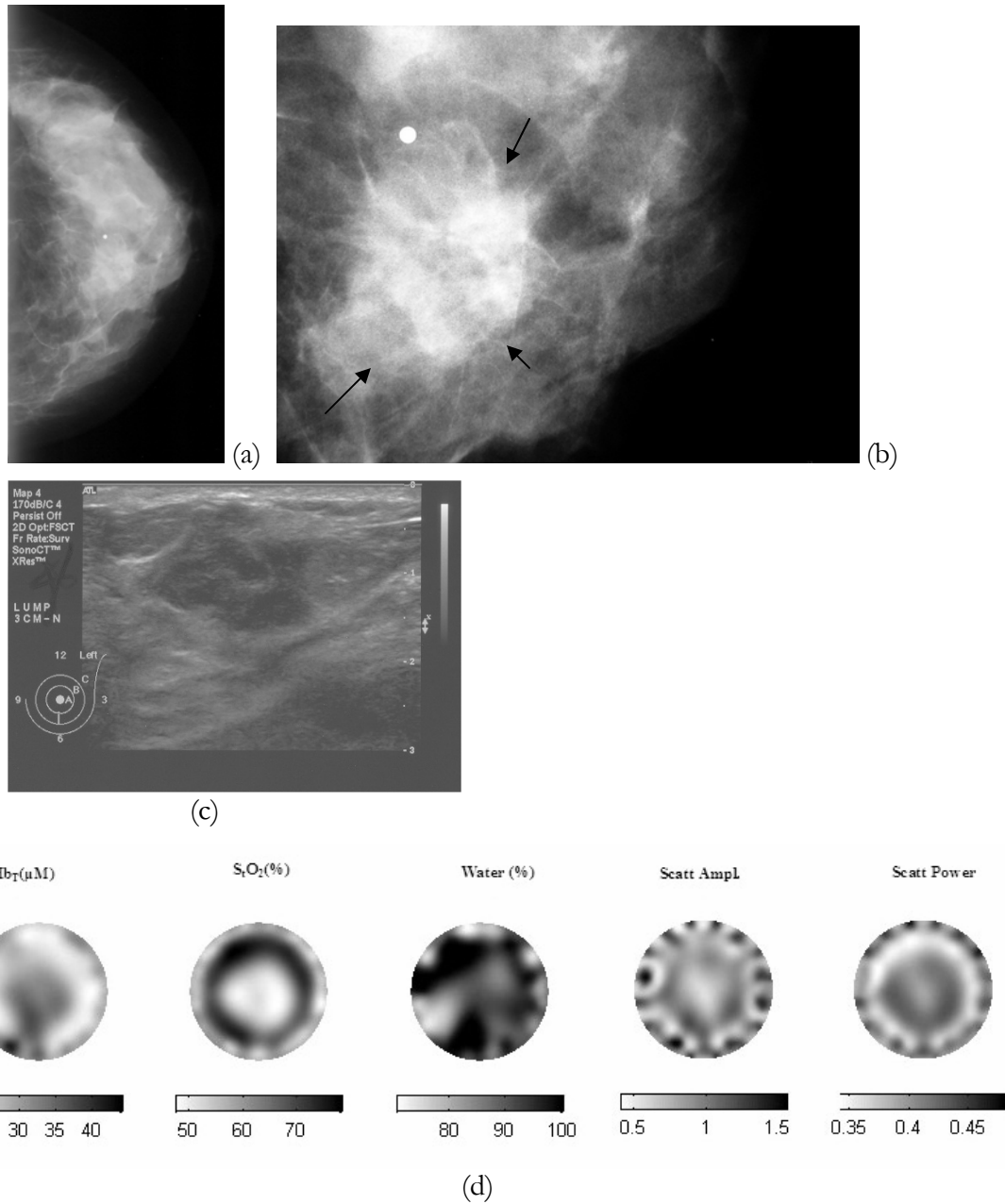


Figure 8-3: (a) left craniocaudal mammogram, (b) magnified view of mammogram and (c) ultrasound images from the left breast of a 37yr old woman with a 3cm irregular mass (indicated with black arrows) centrally located at 6:30 on the clock face; diagnosed as infiltrating ductal carcinoma through biopsy (patient ID #1077) (d) images for Hb_T(μM), S_tO₂ (%), water (%), scatter amplitude and scatter power obtained using the spectrally constrained direct chromophore reconstruction. The tumor is most clearly visible in the Hb_T image.

density of 0.74 %. The radiographic classification of the breast was heterogeneously dense. The amplitude and phase data were obtained from the periphery of both breasts and the measurements at five wavelengths (excluding 849nm) from the tumor-bearing left breast were used by the spectral reconstruction to provide the tomographic images shown in Figure 8.3(d) for the lowest plane closest to the nipple, where the breast diameter was 8.5cm.

A localized increase in total hemoglobin was found in the location given by the mammogram, increasing to a peak of $37\mu\text{M}$ in the tumor. Oxygen saturation showed a decrease with respect to the breast background reducing to a minimum of 47.4%, consistent with the prediction of hypoxia in malignancies. A contrast in water was also observed, increasing at the site of the cancer. Scattering did not change appreciably at the cancer site, though the cross-section reveals a mild peak (increasing to 1.1 with respect to a background minimum of 0.5). The lack of a higher contrast in scatter may be due to the fact that the subject was younger in age and had a radiographically dense breast (category 3) so that scattering in general is high.

Figure 8.4 shows the mean and standard deviation for all five reconstructed parameters in the cancer and surrounding tissue following the same FWHM segmentation procedures. Total hemoglobin increased from an average of $27.7\mu\text{M}$ in the normal tissue to a peak of $37\mu\text{M}$ (equivalent to a contrast of 34%) and an average of $34.4\mu\text{M}$ in the tumor. The oxygen saturation reduced by 6.4% in the cancer, from an average of 61.7% in the surrounding tissue. Water increase in the location of the cancer was not as predominant as in the previous case; it changed by less than 5%. This may be due to the large size of the tumor,

averaging out the change between the tumor and the surrounding tissue. Scatter amplitude and power remained nearly unchanged in their averages between tumor and the background.

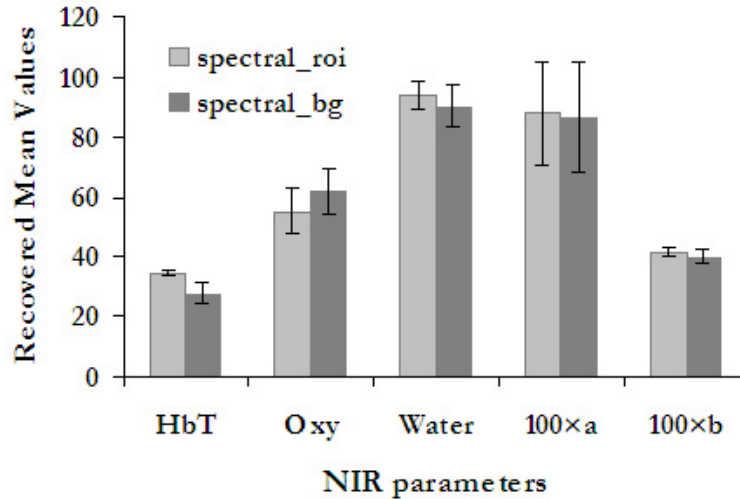


Figure 8-4: The average and standard deviation for the five NIR parameters in the region of the tumor and the background (for patient corresponding to Figure 6). The tumor was defined by segmentation of the images obtained using the spectrally constrained direct chromophore reconstruction and FWHM criterion. The tumor exhibits an increase in total hemoglobin (Hb_T) and water, with decreases in oxygenation, compared to the surrounding tissue.

In the final cancer case presented here, the subject was a 73 yr old female volunteer (patient id # 2034) whose mammogram (see Figure 8.5(a) and (b)) revealed an approximately 2cm focal density with subtle associated architectural distortions in the lower outer left breast at the 4:30 clock position. Just below this was an approximately 1cm focal asymmetric density with ill-defined margins, also in the lower, outer left breast. The first abnormality was 6cm in depth from the nipple and the second adjacent abnormality was 8cm in depth from the nipple. Ultrasound directed to the lower, outer left breast at 4:30, approximately 4.5cm from the nipple, demonstrated the two adjacent abnormalities with a questionable hypoechoic bridge between them. The two abnormalities collectively measured 2.5cm in greatest diameter. The radio-density of the breast belonged to category 2, the scattered type.

Excisional biopsy confirmed the tumor as an infiltrating ductal carcinoma with a vessel density of 0.71. On excision, there was a single lesion with a fatty interface and the pathology size of the tumor was 2.5cm. The NIR exam used six wavelengths the images obtained, are shown in Figure 8.5(c) for total hemoglobin, oxygen saturation, water and scatter.

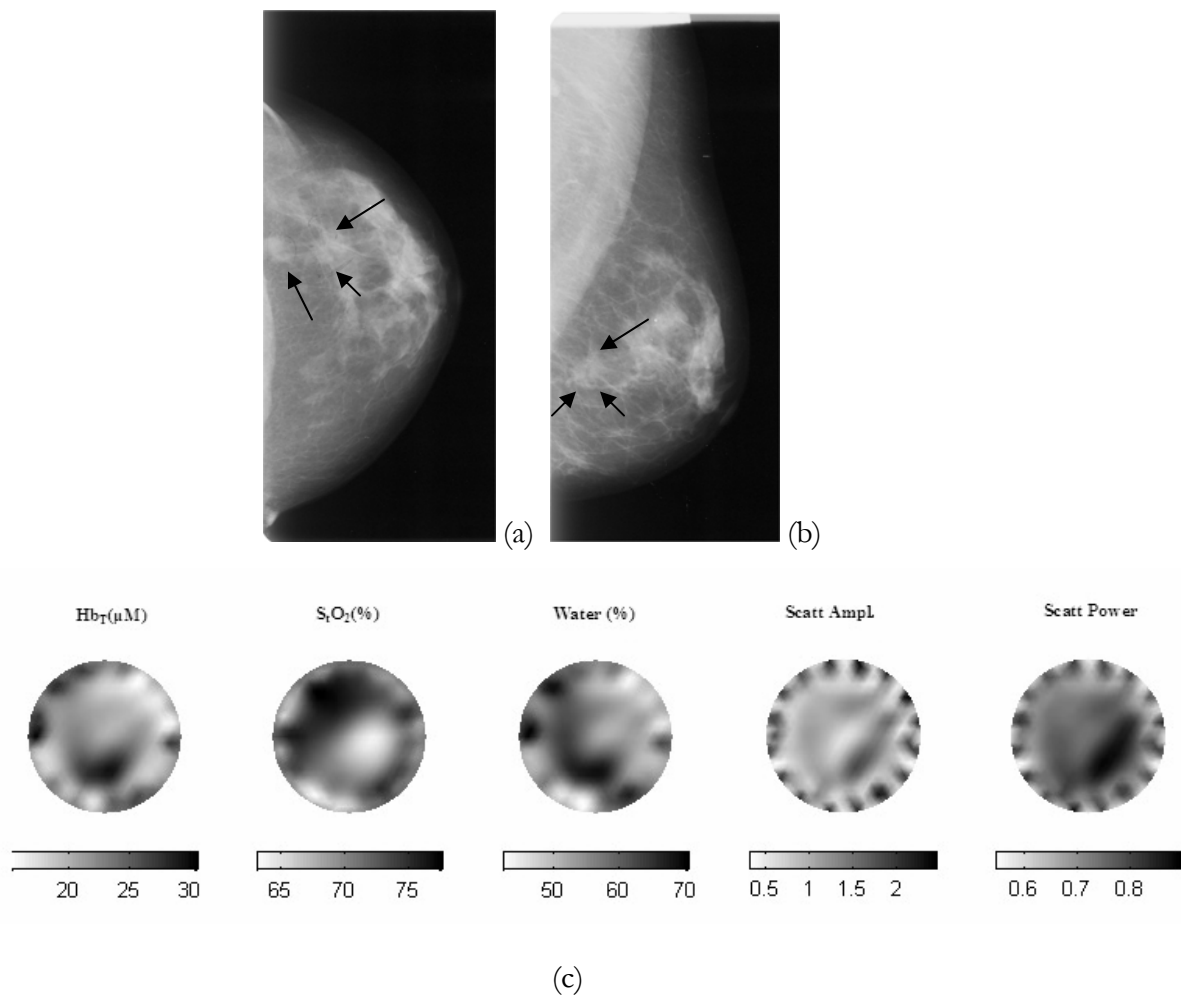


Figure 8-5: (a) Left craniocaudal mammogram, (b) left mediolateral oblique mammogram for a 73 yr old subject, revealed two abnormalities close to each other in the lower outer left breast, diagnosed by excision biopsy as infiltrating ductal carcinoma and 2.5cm in size (patient ID #2034). The mass is indicated with black arrows. (c) NIR tomographic images obtained using amplitude and phase measurements at the periphery of the breast and the spectrally constrained reconstruction approach. The tumor is visible in total hemoglobin, water and scatter as a localized increase and in oxygen saturation, as a decrease.

Total hemoglobin showed an increase at the 6:00 clock position, slightly different from the location of 4:30 given by the Radiologist. Oxygen saturation and scatter show the tumor at the right location, with a reduction in oxygen saturation observed at the cancer site to a minimum of 64%. The water content in the tumor showed an increase with respect to the background with a maximum value of 68%. Both scatter amplitude and power also showed a contrast discerning the cancer from the surrounding tissue. The cancer observed in the images in Figure 8.5(c) was regionized using the FWHM approach to zone into the tumor which placed it in the correct location (corresponding to the mammograms). The average and standard deviation was obtained in the lesion and plotted alongside the mean in the surrounding normal tissue in Figure 8.6. The maximum in total hemoglobin in the tumor increased by 36% relative to the background. Oxygenation and water content did not change substantially but scatter amplitude increased at the location of the cancer by 39%. Scatter power showed a contrast with a value of 0.85 compared to 0.72 in the background.

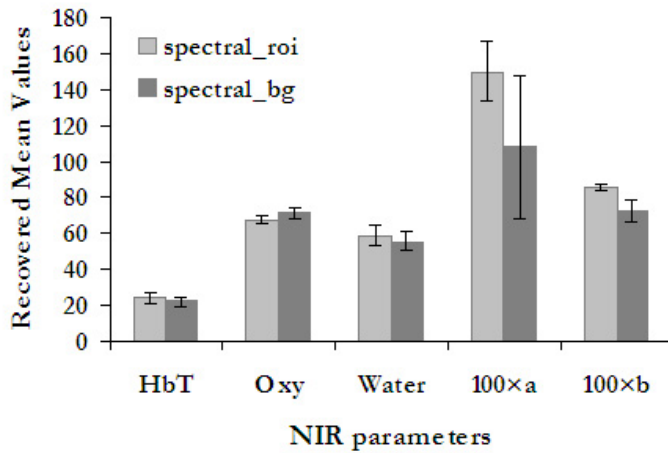


Figure 8-6: The average and standard deviation for total hemoglobin, oxygen saturation, water and scatter amplitude (*a*) and power (*b*) (multiplied by 100 to fit in the same Figure) obtained from the images in 8.5(c) The tumor was segmented using a FWHM criterion from the scatter power image, which shows the cancer most clearly, corresponding to location from mammogram.

8.3.2 Case Study 4: Fibrosis

Also studied here are subjects with benign conditions, specifically, fibrosis (a benign, localized lesion comprising an abundance of scar-like, dense stromal collagen in proportion to a reduced epithelial component); and fibrocystic disease. The mammogram of a 49yr old female volunteer (patient id #2135) showed a peripheral tumor in a scattered type breast. The left craniocaudal and mediolateral oblique mammograms (see Figure 8.7) revealed an approximately 5cm area of asymmetric density in the upper outer quadrant of the left breast; the cone compression views of the mammograms gave it the appearance of normal glandular tissue. Ultrasound of the majority of this area showed dense fibroglandular tissue; however, at the 2:30 clock position, 10 cm from the nipple, was an approximately 2.7 x 1.7 x 1.2 cm ill-defined hypoechoic area with dense posterior acoustic shadowing, giving the suspicion of local fibrosis. There were several tiny cysts in the same area. The patient's symptoms and concerning ultrasound lead to a core biopsy which confirmed the lesion as fibrosis, a benign condition, with a vessel density of 0.33. The NIR clinical examination was carried out two days prior to the biopsy. It consisted of collecting three planes of frequency domain data where the measurements from plane 0 (which contained the tumor), closest to the chest wall (at six wavelengths), was used to reconstruct for the NIR parameters. The spectral approach was used and the images are shown in Figure 8.7(c).

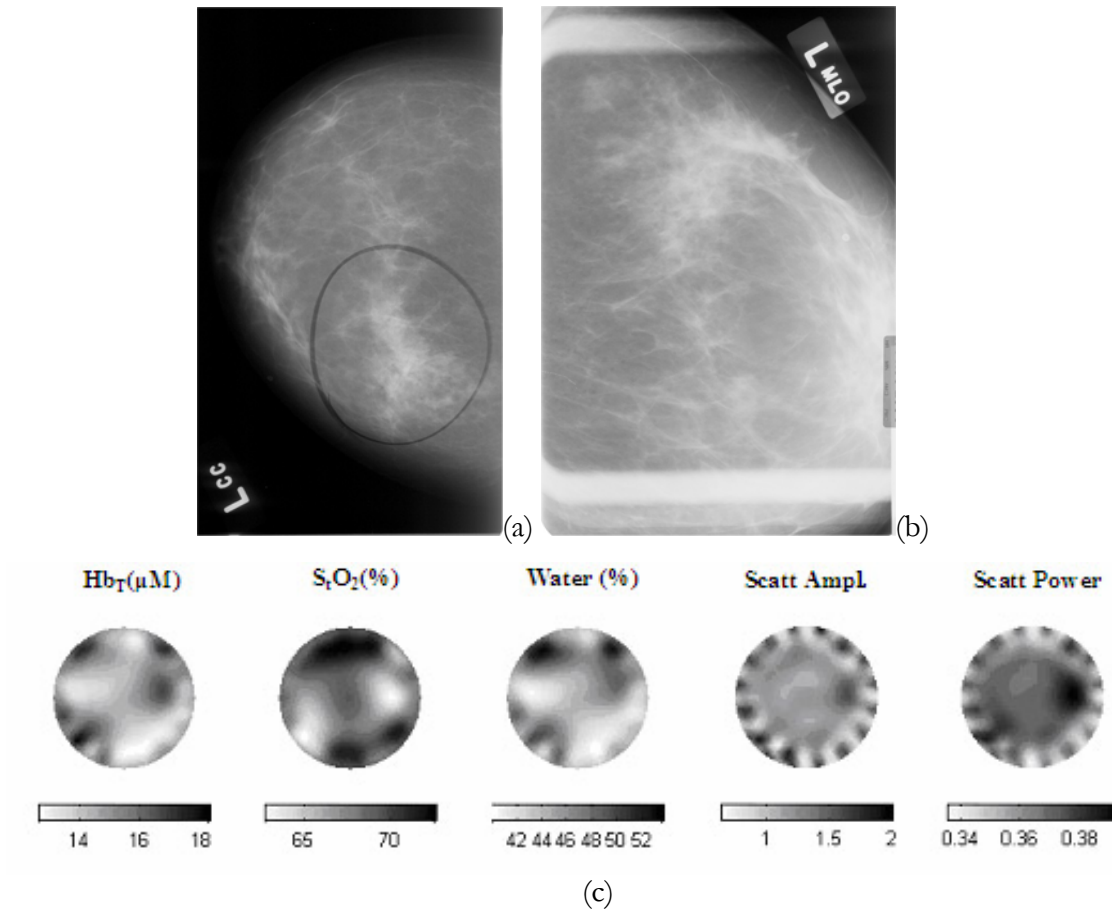


Figure 8-7: (a) Left craniocaudal mammogram, (b) left mediolateral oblique mammogram magnified for a 49 yr old subject showing a 2.7cm mass in the 2:30 clock position, diagnosed by core biopsy as the benign condition, fibrosis (patient ID #2135) (c) NIR tomographic images obtained by applying the spectral reconstruction on the frequency domain data from the plane closest to the chest wall containing the tumor. The tumor is most clearly discernible in total hemoglobin and scatter in the 3:00 clock position with oxygen saturation and water having almost homogeneous images.

The tumor is most clearly visible in total hemoglobin and scatter amplitude and power. Total hemoglobin showed a slight increase whereas the contrast in scatter is more pronounced. Since the vessel density is much lower compared to the malignancies documented here, the contrast in total hemoglobin is also expected to be low. Fibrosis contains a higher density of tissue which explains the increases observed in the scattering parameters. Scatter amplitude increased to a maximum of 1.6 and a lower contrast is observed in scatter power. Water content exhibited a contrast but overall, has a small range

from 42 to 52% overall. Oxygenation varied by less than 5% between tumor and background. The tumor and background averages are shown along with standard deviations in Figure 8.8 using the regionization scheme employed in all of the earlier cases. The same trend is visible, with a contrast in the tumor of less than 10% of the surrounding tissue in total hemoglobin and scatter amplitude showing the most dominant change, increasing by 22% in the tumor, from a background value of 1.2.

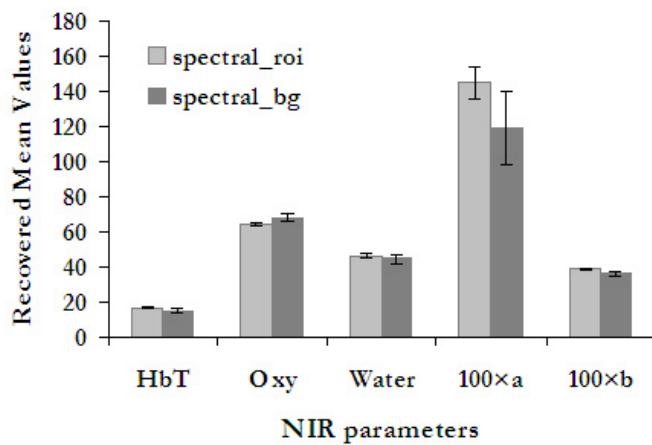


Figure 8-8: The average for the five NIR parameters along with standard deviation, in the region of the tumor and the background for a subject with fibrosis (mammogram and NIR images in Figure 8.7). The tumor exhibits a small increase in total hemoglobin (10%) and a larger increase in scatter amplitude (22%) with respect to the surrounding tissue; other NIR parameters do not show much change.

8.3.3 Case Study 5 & 6: Fibrocystic Disease (FCD)

Frequency domain measurements were obtained from a 50 year old female volunteer whose mammogram revealed a 0.7 x 0.5 cm ill defined mass in the upper-inner left breast, approximately 9cm deep to the nipple (patient ID #1079). Although portions of the margins were fairly well-circumscribed, at least half was ill-defined or obscured. The lesion was non-calcified and non-palpable and the ultrasound exam showed no sonographic abnormality.

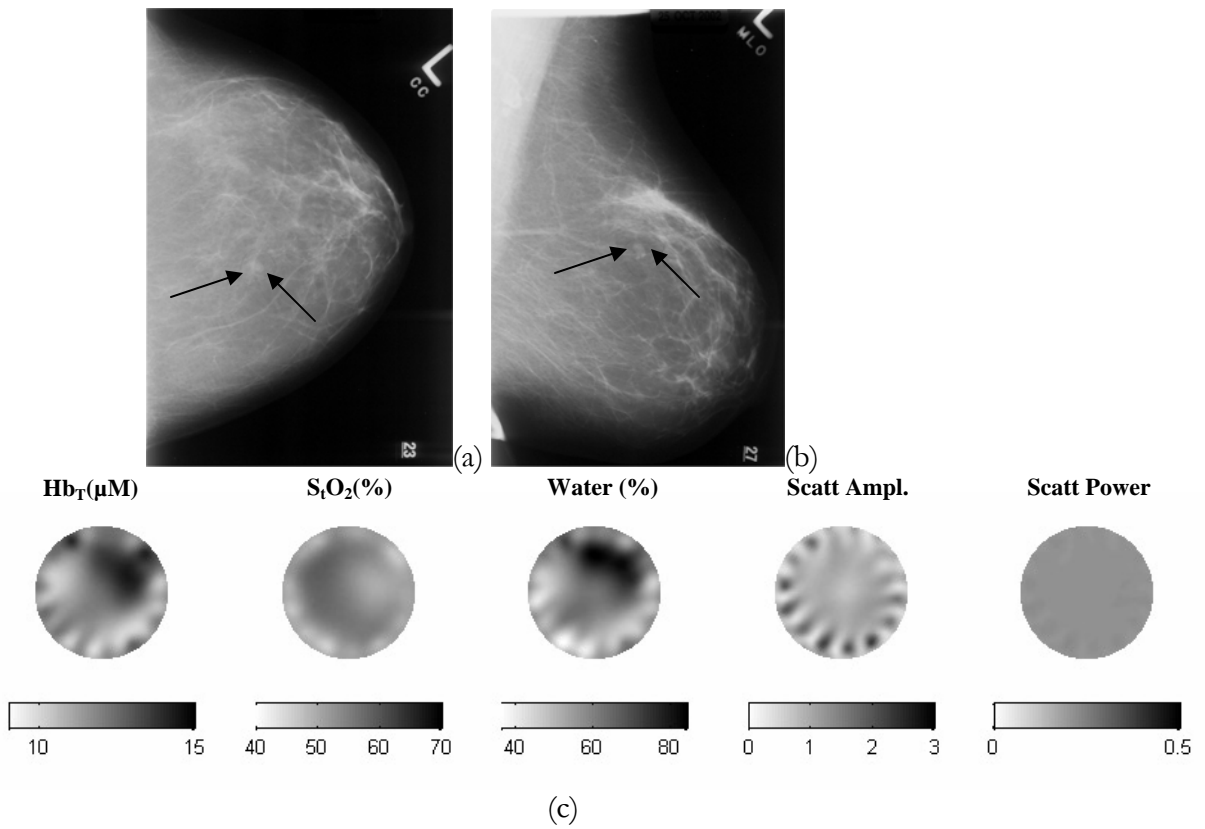


Figure 8-9: (a) Left craniocaudal mammogram, (b) left mediolateral oblique mammogram for a 49 yr old subject, showing an 7 x 5 mm ill-defined mass at 12:00 clock position, diagnosed by stereotactic guided biopsy as the benign condition, FCD (patient ID #1079). (c) Recovered images for the NIR parameters are shown as reconstructed with the spectral approach, using frequency domain data from the periphery of the breast. Contrast is observed at location of the lesion, in total hemoglobin and water, and no decrease in oxygen saturation is observed. (d) Mean values and standard deviation, in the tumor (segmented using FWHM criterion as for previous cases) and surrounding tissue; most dominant contrast is in water.

A stereotactic guided biopsy revealed the lesion as the benign condition of Fibrocystic Disease (FCD). The NIR parameter images using the spectrally constrained technique have been shown here (see Figure 8.9(c)) using the boundary measurements from plane 1 (taken two days before biopsy). The total breast diameter was measured to be 10.2cm in this plane, where the location of cyst was marked, and given by the Radiologist as upper inner quadrant, 11.00-12.00 clock position. The tumor is visible in the 12.00 position in the total hemoglobin and water images. There is a contrast of 25% in the Hb_T image, between the maximum in the tumor and background mean, lower than that found in the malignancies (34-86%). In addition, no decrease in oxygenation is observed, with this parameter remaining almost homogeneous. Water shows an increase of up to a maximum value of 85% at the site of the tumor, which corresponds well with theory that FCDs may contain fluid filled cysts. Since the physiology of this disease is complex, and may vary from distinct masses to diffuse masses³², the additional increases in hemoglobin and water found close to the tumor may very well be physiologically true. The radiodensity category of the breast of this subject was given to be fatty/scattered type with less of glandular tissue, and the recovered background hemoglobin ($\sim 10\mu\text{M}$) agrees well with the expected lower vascularity in such tissue. In addition, the low values of scatter power correspond well with a previous hypothesis that scattering may be a non-invasive indicator of radio-density³¹. The comparison of the mean in the lesion versus the background is plotted in Figure 8.9(d), applying the FWHM criterion on the images; and shows the same trend, with the dominant contrast in water increasing by nearly 24% from a background content of 57%.

Another female volunteer with FCD imaged with the NIR modality was a 61 year old woman (patient ID #1059) with multiple cysts, whose mammogram did not reveal any

abnormality (see Figure 8.10 (a) and (b)). Ultrasound showed the lesion, 1.1cm in size, centrally located at 9.30 on the clock face in the right breast and core biopsy confirmed FCD. The subject had a breast density belonging to category 3 (heterogeneously dense), which probably explains why it was difficult to find the cysts, in both the craniocaudal and mediolateral oblique mammograms. The volunteer was taken through the NIR clinical exam and all six wavelengths were used for the tissue interrogation. The images are shown in Figure 8.10(c); the lesion is clearly distinguishable in hemoglobin and scatter as a localized increase in the expected position. There is also a centralized decrease in oxygenation which may confound the diagnosis of this lesion; however, examination of the contralateral breast images (shown in Figure 8.10(c), bottom row) revealed a similar trend which leads to the conclusion that this change in oxygen saturation is more likely due to the metabolic activity of glandular relative to adipose tissue. Water showed an increase consistent with the previous FCD case study analyzed suggesting that water content is a likely indicator of cysts containing fluids. Scatter amplitude also showed a contrast and this maybe an indicator of denser tissue enveloping the cysts. This is also the primary change not visible in the contralateral breast.

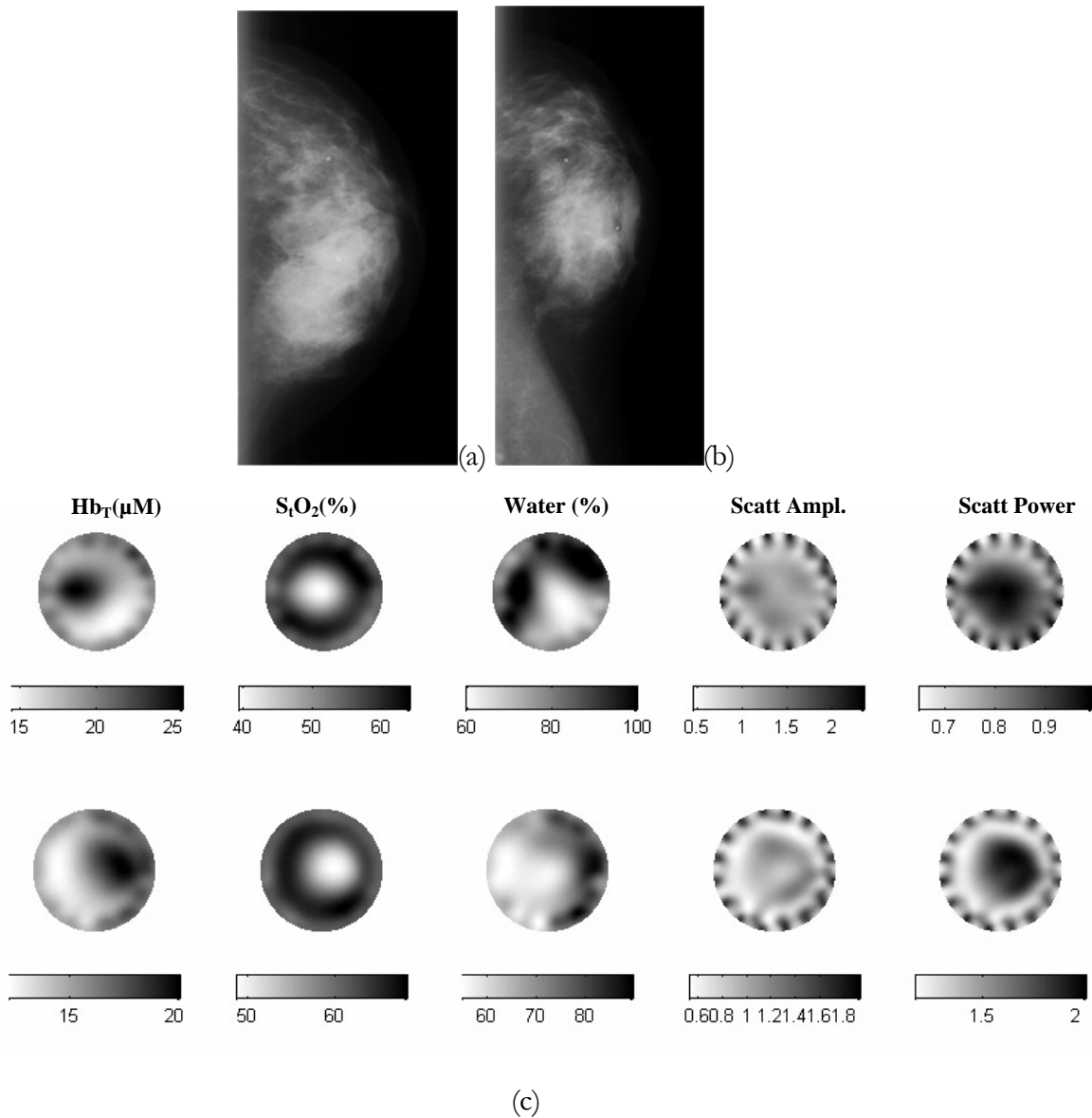


Figure 8-10(a) Right craniocaudal and (b) right mediolateral oblique mammograms for a 61 yr old subject (patient ID #1059). The mammograms showed no abnormality. Ultrasound revealed a 1.1cm lesion at the 9:30 clock position diagnosed as FCD. (c) top row shows the images obtained using the spectral reconstruction for the right breast; bottom row shows the images for the contralateral normal breast. Both show a trend of decreasing oxygenation corresponding to an increasing hemoglobin; likely occurring as a result of fibroglandular tissue rather than tumor location.

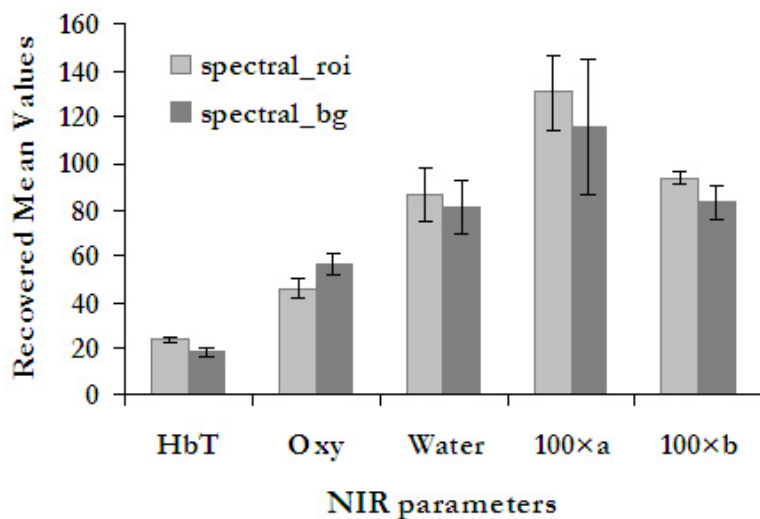


Figure 8-11: Average and standard deviation in the benign lesion (discussed in Figure 8.10) and the surrounding tissue. The tumor was segmented using the FWHM criterion on the NIR images; while a decrease in oxygenation is observed, this may be due to fibroglandular tissue. Water shows a contrast and scatter as well, over the background.

8.4 Discussion

Studies have established that the neovasculature, hypoxia and cellular microenvironment have a major impact on tumor detection and treatment^{144, 149}. NIR tomography is an imaging method directly related to the functional processes occurring in tumors. Hemoglobin is a measure of the vascularization; oxygen saturation offers a measure of tissue oxygenation which relates to tissue partial pressure of oxygen and hence to a direct measure of hypoxic fractions in tumors. Water is a measure of the microenvironment and cellular compartments³¹ and scattering is related to cell density and fibrosis. These together provide a noninvasive manner to study changes in the breast due to malignancies and benign lesions.

While correlation plots of NIR cancer and benign clinical data are useful to identify overall trends separating malignant from benign disease, (an example is the hemoglobin-oxygen saturation plot shown in Grosenick et al⁵⁵) the reality may be that separating the two is more complicated. Certain features of benign conditions, such as fibrocystic disease, present difficulties in diagnosing it from cancer, when based only upon mammographic image features³². NIR tomography is undergoing several clinical trials evaluating its role in aiding breast lesion diagnosis^{6, 28}; however, defining the particular NIR characteristics expected in different types of tumors is not yet well defined. While NIR gives estimates of oxygenation in the tumor and surrounding tissue, hypoxia is not a sole indicator in tumor diagnosis, as Okunieff et al¹⁴⁴ showed that some malignancies may not have pO_2 values less than 5mm Hg. In the three case studies presented here for infiltrating ductal carcinomas each had reduction in oxygen saturation. However, the change varied from a decrease of 4% to 13% from the surrounding oxygenation, indicating that if this decrease is accurate, the contrast available is likely subtle. A similar decrease was also observed in the FCD case study (patient id #1059), where the reduction was more likely due to the higher metabolism of fibroglandular tissue; this was verified by a similar trend of a central lower oxygenation in the normal contralateral breast, corresponding to both a more vascularized tissue region as well as an increase in scatter power indicative of higher radio-density. Thus, it would seem that oxygen saturation alone is not sufficient to separate cancer from FCD. Hence, it is likely more useful to examine the characteristics of different tumors in the NIR images along with the comprehensive data sets which are available from mammograms, ultrasound and potentially MR images.

The NIR images presented here are consistent with physiological changes expected. Total hemoglobin showed a localized increase in the malignancies with a higher contrast (34-86% increase in the lesion with respect to the surrounding tissue) compared to the benign lesions (10-28% increase in lesion compared to background). Hemoglobin also seemed to correlate with vessel density, obtained through biopsy of tumor tissue, where higher vessel density has been associated with higher hemoglobin content. Using the six cases studied here along with other tumors imaged (n=12, 7 cancers and 5 benign lesions, size > 8mm), Figure 8.12 shows this trend. The data does not include the patient with FCD (patient id #1059), whose mammogram did not show a lesion; and whose NIR images show an increase in hemoglobin, more likely indicating glandular tissue. The Figure supports an interesting observation: typically 1% human blood in its normal state contains ~20-25 μM blood; and 1% vessel density from the graph shows a correspondence of 1% blood = 26 μM . This trend has to be validated in a larger number of clinical cases.

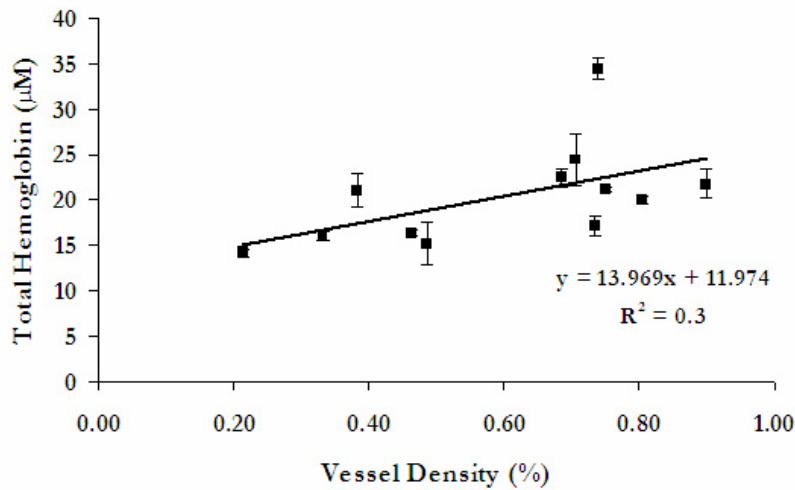


Figure 8-12: The average total hemoglobin and standard deviation in the location of the lesions from 12 tumors imaged in-vivo (7 cancers and 5 benign lesions) including the case-studies reported in this paper, plotted against vessel density in the tumor obtained from pathology, indicates a possible correlation.

All three carcinomas studied here showed a localized change in all five NIR images; the same was not true in the benign conditions. In the subject with fibrosis, the dominant change was in scatter amplitude, consistent with the densely packed fibrous tissue. In cancers, the contrast in scatter amplitude agreed with an expectation of cell proliferation resulting in higher number density of scatterers in the cancers. This yields the encouraging conclusion that scatter amplitude could be an emerging indicator of the density of localized tissues, which when interpreted along with total hemoglobin, oxygenation and water, may enable separation of malignant and benign disease. Scatter power, on the other hand, may be more indicative of bulk radiodensity of the breast^{25, 31, 135}. Scattering was found to correlate inversely with E/S ratio in preliminary studies and this will be investigated with the spectral approach in future work.

Water content in the images studied here, obtained using the spectrally constrained direct reconstruction, has yielded increased information, compared to the conventional approach of separate wavelength recovery. In all three malignancies, water showed an increase with respect to the surrounding tissue coinciding with the physiological expectation of a leaky endothelium. Water was the dominant mechanism of contrast in the FCDs (see images in Figure 8.9 and 8.10) along with scatter change for one of the cases (patient #1059).

Overall, using the spectrally constrained direct reconstruction approach, the NIR images studied here offer an example of qualitative ways of characterizing different types of lesions. The analysis when performed on a larger number of clinical cases will present distinctive features of tumors useful in diagnosis. The physiological changes observable here can be extended to monitoring response to therapy, predicting risk of malignancy or

aggressiveness of tumors. At this stage of development, the role of NIR imaging in diagnosis is still uncertain; however, through algorithm improvement and case study analysis, the potential value of the NIR parameters become clearer. It is likely that this system can be used to measure physiological changes which are not observable in other imaging modalities, and further patient imaging sessions will help determine those parameters and indications where the system will have its most important impact.

9. Combination of Spectral and Spatial *A-Priori* Information

9.1 Introduction

Chapter 5 investigated the use of spatial priors in a multi-step reconstruction procedure, where knowledge of the location of a tumor is obtained from a first pass recovery of absorption and scattering coefficients. Researchers have shown that this form of priors relating to anatomical structure also obtainable from other modalities such as MRI or ultrasound, when used in the reconstruction procedure, improves the stability of the estimation process and results in faster convergence to a higher resolution and more accurate image^{50, 117-119}. Pogue et al⁵⁰ applied structural data from MR to obtain high resolution images in the rat cranium. Schweiger and Arridge⁴⁹ studied the use of *a priori* information, and showed that while results superior to those without priors were obtained, exact knowledge of the tissue boundaries was required. Ntziachristos et al¹¹⁸ applied a similar approach to breast tissue, using *a priori* information to over-determine the inverse problem. However, this also involved exact information on tumor location, and while the authors showed quantification improvements, they also suggested that the results may be biased by systematic errors and noise¹²¹. Brooksby et al¹¹⁹ reported a method for encoding MRI priors into a spatially varying regularization, thereby eliminating the requirement that the spatial

constraints be error-free. In that study, phantom data at a single wavelength was used to show that quantitative accuracy and spatial resolution of optical property images could be improved without increasing vulnerability to systematic errors. While all these studies have shown that image resolution, and algorithm stability and convergence can be enhanced through anatomical priors, the net effect on quantitative spectroscopic accuracy is less clear.

Spectral priors relating to the spectral shapes of the absorbing chromophores and the scattering behavior, have been implemented into the reconstruction procedure (*Chapter 7*); and the results have demonstrated substantial improvements in quantification of the NIR functional parameters. In this chapter, the next logical step of combining both spectral priors (implemented as in *Chapter 7*) and spatial priors from MR(based on the work of Brooksby et al¹¹⁹) has been carried out. This was a collaborative effort with Ben Brooksby and allowed a comparison between spectral and spatial priors, as well as the extension of the benefits of spectral priors on quantification, for the MRI-NIR system⁵² at Dartmouth. The reconstruction that resulted from the synergy of the two types of priors was applied to measurements obtained from simulations, experiments and clinical studies and has been relevantly documented here.

9.2 Materials and Methods

9.2.1 Instrumentation

The MRI-NIR system built at Dartmouth has been documented by Brooksby et al¹⁵⁴. Briefly, this device allows frequency domain measurements to be taken from the periphery of the breast as the patient lies inside a 1.5 T whole body MRI (GE Medical Systems). Data is collected at six wavelengths (660-850nm) and in a similar fashion to the stand-alone NIR

tomography system⁴³, with 16 source fibers and 15 detector locations for each source delivery, in a circular geometry. The NIR and MRI data acquisition systems run in parallel and typically T1 volume is acquired which is used to generate a 2-D (or 3-D) mesh in the plane of the optical measurements. After amplitude and phase data calibration for the NIR measurements, an initial estimate for the optical properties (conventional method)/chromophore concentrations (spectral method) were obtained.

9.2.2 Image Reconstruction

The conventional approach of image reconstruction was explained in *Chapter 2*. Briefly, it uses a finite element model for the diffusion equation with the iterative Newton Raphson scheme and Levenberg Marquardt regularization. The spectral approach implements the Beer's law and scatter theory as constraints and directly reconstructs for chromophore concentrations and scatter parameters (*Chapter 7*). In order to incorporate these spectral relationships into the reconstruction directly, the least squares functional minimized, is written as $\chi^2 = \sum_{j=1}^{Mn} (\phi_j^{meas} - \phi_j^{cal})^2$, where M is the total number of measurements at each wavelength, and ϕ_j^{meas} and ϕ_j^{cal} are the measured and calculated fluence at the boundary for each measurement point j and the sum includes all wavelength measurements (Mn), where n is the number of wavelengths available (6 in our case). The Newton's method produces a relationship, which along with regularization is given by:

$$(\tilde{\mathfrak{F}}^T \tilde{\mathfrak{F}} + \lambda I) \partial c = \tilde{\mathfrak{F}}^T \partial \phi, \quad (9.1)$$

where ∂c is the update in chromophores and scatter, $\partial \phi = \left(\phi^{meas,\lambda} - \phi_k^{cal,\lambda} \right)_{\lambda=1:n}$ and $\tilde{\mathfrak{S}} = \left[\mathfrak{S}_{c,\lambda}, \mathfrak{S}_{a,\lambda}, \mathfrak{S}_{b,\lambda} \right]_{\lambda=1:n}$ and $\mathfrak{S}_{c,\lambda}$, $\mathfrak{S}_{a,\lambda}$ and $\mathfrak{S}_{b,\lambda}$ represent the Jacobians for each of the chromophore and scattering parameters.

In order to introduce a spatial constraint, the minimization functional is modified to include a penalty term for *a-priori* information on tissue structure, given by:

$$\chi^2 = \sum_{j=1}^{Mn} \left(\phi_j^{meas} - \phi_j^{cal} \right)^2 + \beta \sum_{j=1}^{Mn} L(\mu_j - \mu_{0,j})^2 \quad (9.2)$$

where β is the regularizing factor for the spatial prior and L is a matrix generated from MRI-derived spatial data, acting on the solution μ . This matrix links all of the locations (nodes) in a particular type tissue (glandular or fatty) so that a second differential operator is approximated within each region. L is given by:

$$L_{i,j} = \begin{cases} 1, & i = j \\ \frac{-1}{n}, & i_{region} = j_{region} \\ 0, & i_{region} \neq j_{region} \end{cases} \quad (9.3)$$

where n is the total number of nodes in a region (glandular or fatty). This is similar to total variation minimization⁷⁵ because it allows sharp boundaries to exist but it provides the flexibility to encode these boundaries from MRI information. The spatial prior technique has been applied separately without the spectral constraints as documented in Brooksby et al¹¹⁹ and results have led to image improvements. Applied with the spectral prior, the final matrix equation becomes

$$\left(\tilde{\mathfrak{S}}^T \tilde{\mathfrak{S}} + \lambda I + \beta L^T L \right) \partial c = \tilde{\mathfrak{S}}^T \partial \phi \quad (9.4)$$

where $\tilde{\mathfrak{S}}$, ∂c , and $\partial\phi$ are defined as in Eq. (9.1), λ is the Levenberg-Marquardt regularization parameter, and β is the regularizing factor for the spatial prior. All the reconstructions presented here were carried out on a dual-mesh scheme (2000-400 nodes mesh pair) and the method incorporating Equation 9.4 usually converged in 10-14 iterations. The stopping criterion was also consistently followed to be χ^2 error change less than 2% between successive iterations.

9.3 Results

9.3.1 Heterogeneous Phantom Experiments: Test Case

Measurements from the gelatin phantom experiment described in *Chapter 7* is used here as a test for the spectral-spatial constraints method. Specifically, the new reconstruction implementing these constraints was applied to the test case shown in Figure 7.8. Figure 9.1(a) shows a photograph of this phantom and the exact knowledge of the location of the heterogeneity was obtained from this photograph and used to provide the spatial a priori information. The spectral priors were derived, as before, from the Beer's law and Scatter theory. The measurements for this phantom were taken using the stand-alone NIR system described in *Chapter 2*. Figure 9.1(b) (top row) shows the true properties of the phantom with an inclusion containing $[\text{Hb}_T]$ nearly twice that of the background, along with images reconstructed with four different algorithms. The first algorithm uses no priors—absorption and reduced scattering coefficients are reconstructed at each wavelength separately, then spectrally decomposed to produce images of $[\text{Hb}_T]$, S_tO_2 , water fraction, A, and b (2nd row). The second, third, and fourth algorithms incorporate spatial, spectral, and both spatial and spectral priors, respectively, and their corresponding images appear in the third, fourth, and fifth rows of Fig. 9.1(b).

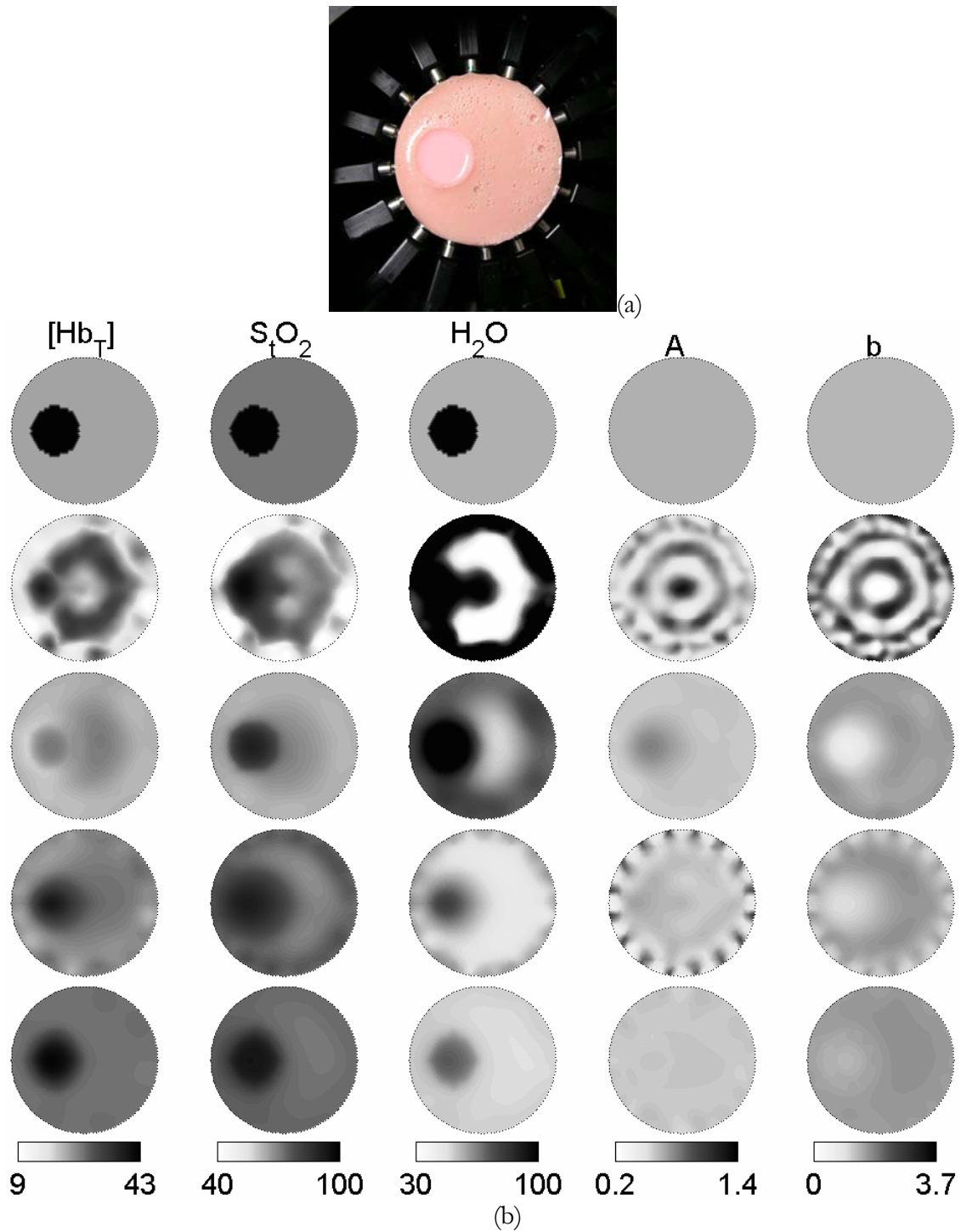


Figure 9-1: (a) Photograph of gelatin phantom used to provide a priori information regarding position of anomaly; (b) Reconstructed images of total hemoglobin concentration (μM), percent hemoglobin oxygen saturation, water fraction, scattering amplitude, and scattering power, for the gelatin phantom, using algorithms which incorporate different degrees of a priori information. The top row shows the true values, the second shows the reconstruction which uses no priors, the third uses spatial constraints, the fourth uses spectral constraints, and the bottom uses both spectral and spatial priors.

These results clearly show that the conventional method (no priors) yields images having considerable artifacts (as in Figure 7.8 and explained in *Section 7.3.7*). The application of spatial priors removes these artifacts, so that the heterogeneity is clearly visible and matches its expected size and shape. However, $[Hb_T]$ contrast is significantly underestimated. The recovered mean in the region of anomaly reaches only 61% of the true value (maximum within 63% of truth). This is probably because of the fact that, while the spatial constraints provide knowledge of anomaly size and location (in the form of the regularizing term in Equation 9.4) which enables accurate recovery of size and shape and smoothness in the images; the underlying model still involves recovery of individual wavelengths optical properties, where the accuracy obtained at each wavelength may indeed be improved¹¹⁹; but this does not necessarily translate to a cumulative improvement in quantification of chromophore concentrations and scattering. This aspect has been discussed in *Chapter 6* in detail, which shows that a reasonable error limit such as 15% in absorption coefficients can result in nearly 50% error in quantification of water.

Spectral priors, on the other hand, allow the shapes of the chromophores and scattering behavior with wavelength embedded in the reconstruction which along with the usage of all six wavelengths measurements simulatenously, shows substantial improvement in the quantification with mean of $[Hb_T]$ reaching 84% of the true value (maximum within 92%). Finally, the application of both constraints results in images with further reduction in artifacts close to the boundary, and quantification of $[Hb_T]$ within 91.5% of the true value for the mean (maximum within 98%). The spatial priors now, acting on the underlying spectral reconstruction, allows the same benefits of smoothness and recovery of accurate

size and shape, and is coupled with accurate quantification from the use of spectral a priori information. As a result of this, the high frequency noise close to the boundary, observed in the scatter amplitude and scatter power images for the spectral technique, have been eliminated.

The experiment was carried further for the same setup, using four different blood concentrations in Intralipid solution as inclusions ($22-43 \mu\text{M}$ $[\text{Hb}_T]$, $S_t\text{O}_2=100 \%$, $\text{Water}=100 \%$, $A=0.65$, $b=1.35$). Figure 9.2 shows the mean property values recovered in the region of interest (as found by FWHM regionization) for each change in $[\text{Hb}_T]$, by applying the four methods of reconstruction (no priors, spatial, spectral, and spectral-spatial priors). As suggested in Fig. 9.1(b), these results indicate that while the standard deviation in the region of interest is reduced using spatial constraints (leading to much smoother images), the quantitative values are underestimated, and may even be degraded relative to the reconstruction without any priors. The spectrally constrained technique produces more accurate results for $[\text{Hb}_T]$, and including both priors gives the best results: accurate quantification along with reduced standard deviation.

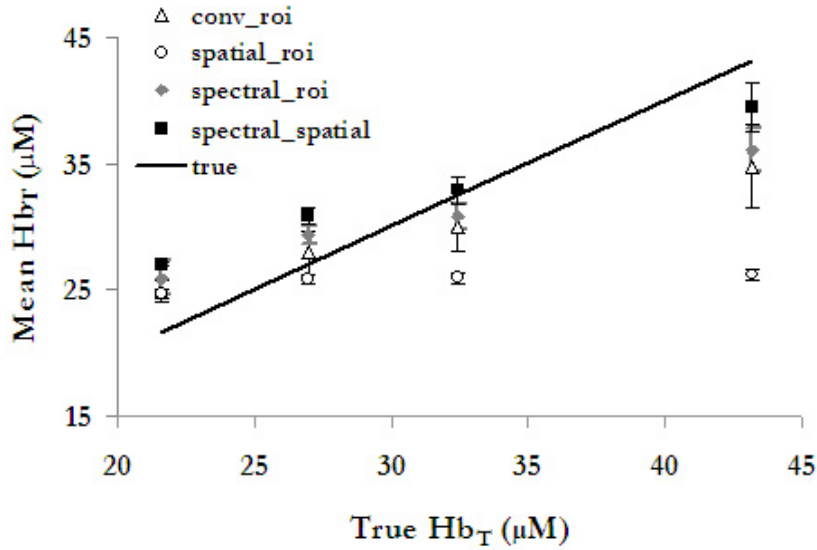


Figure 9-2: Mean reconstructed values of $[Hb_T]$ (μM), S_tO_2 (%), Water (%), A , and b , in the region of the inclusion using four algorithms. As the total hemoglobin concentration in the phantom cavity increases, so does the reconstructed value. When the blood concentration is high, the best results are achieved when both spectral and spatial priors are used in the reconstruction, with spectral priors following close. As expected, S_tO_2 , water, a , and b within the cavity remain constant for each solution (not shown here). Generally, when no priors are used, the standard deviation of the property values within the region is the highest.

9.3.2 Application to Clinical Data from Normal Subject

The combined NIR-MRI imaging system was used¹⁵⁴ in a case study to estimate the properties of normal breast tissue. A 43 yr old pre-menopausal female volunteer with heterogeneously dense breasts underwent the MRI and NIR examination, this provided the T1 volume weighted images as well as frequency domain data; thus a FEM mesh generated from the MRI was used in the reconstruction to obtain NIR parameters. The locations (nodes) of this mesh were each associated with grayscale intensity in the co-registered MRI, and were classified as representing either fibroglandular or adipose tissue. Figure 9.3 shows the tissue properties estimated with the four procedures used in the phantom studies. The images obtained for the NIR parameters using an unconstrained reconstruction are noisy

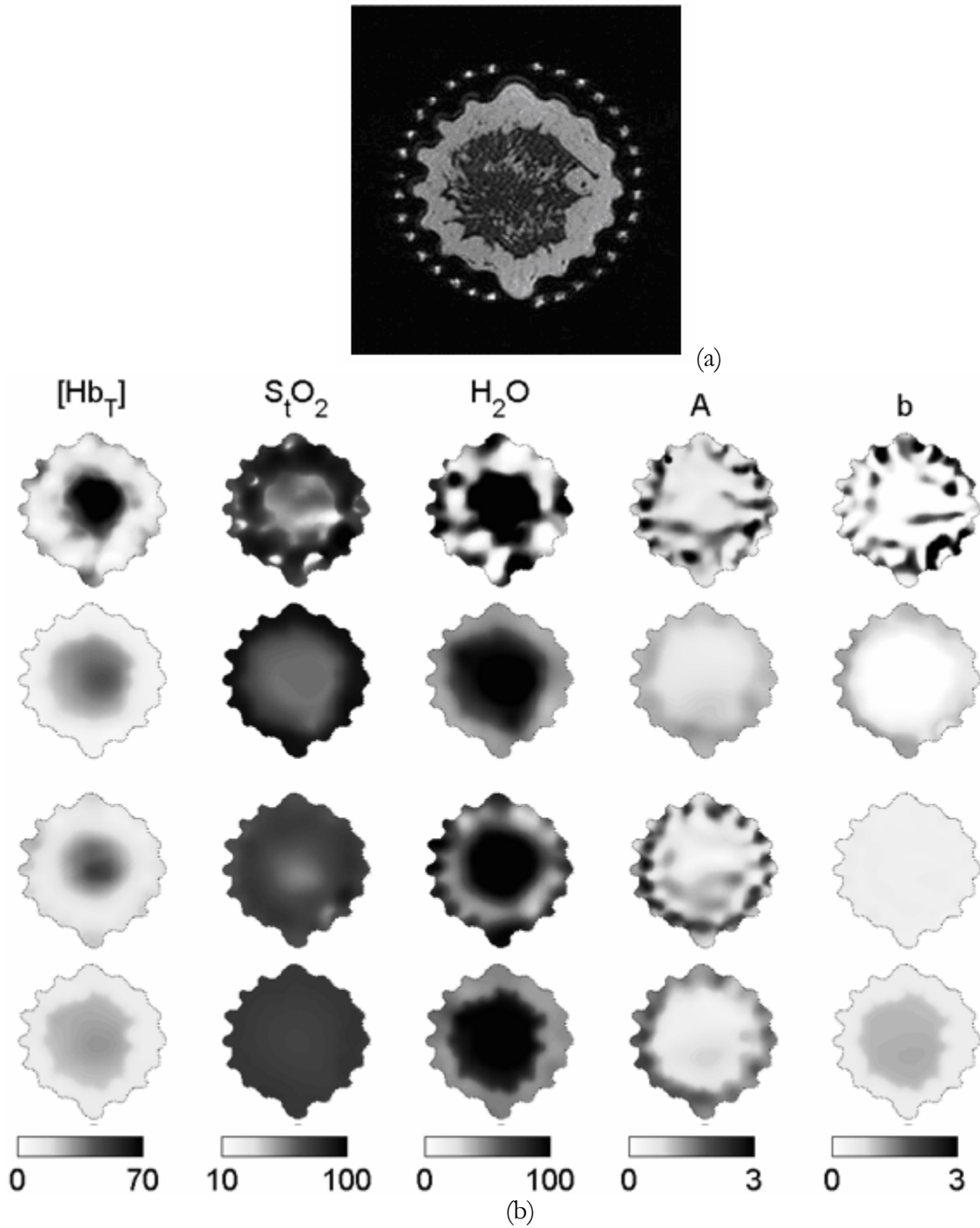


Figure 9-3:(a) MRI of a healthy 43yr old female volunteer, used to provide spatial priors regarding tissue boundaries, for the reconstruction; (b)Breast tissue property images estimated using four different reconstruction methods. First (top), only the outer boundary of the imaging domain, and the location of the optical fiber measurement sites are specified. Second, a spatially constrained algorithm was used. Third, spectral constraints were applied and chromophore concentrations and scattering parameters were reconstructed directly. Fourth (bottom), both spatial and spectral constraints were combined.

and exhibit boundary artifacts. While the total hemoglobin image shows higher values for glandular tissue compared to adipose tissue, the oxygen saturation, water and scatter images are more artifacts-ridden making it difficult to see any trends between the different types of tissue in the normal breast. The spatial priors act on these images, making them smoother, but preserve the trends in chromophore and scattering quantification. For example, the scatter power shows a decrease in the glandular tissue (row 2) similar in value to that obtained without priors (row 1). However, previous studies have suggested that glandular tissue having smaller particle size, may have higher values for scatter power than fat⁸³. Hence, the results from the spatially constrained reconstruction, while appearing smoother, may be misleading. The scatter power image obtained by application of the spectrally constrained method (row 3) is more quantitatively acceptable; and consistent with results from *Chapter 7* and *8*, the images show lesser artifacts and more useful information, particularly in oxygen saturation, water and scatter. Finally, including the spatial priors within this spectral method (row 4) produces the most intuitively appealing image for this parameter by also showing the layered structure of the breast tissue. We observed elevated $[Hb_T]$ (25:13 μM), water (91:49 %), and scattering power (1.0:0.5) in the glandular zone relative to adipose tissue using the combined priors, which matches the higher degree of vascularization expected³².

9.4 Discussion

This collaborative project was done to test the proof of principle: that incorporation of spectral and spatial constraints together will provide the most accurate characterization of breast tissue. Intes et al¹⁵⁵ have demonstrated a similar result in a study using simulated frequency domain measurements without noise by reconstructing for blood volume and

oxygen saturation with the spatial priors applied in a Bayesian framework. Li et al¹⁵⁶ also showed results in simulations, by using continuous wave measurements and reconstructing for the chromophores (no scatter) with MR providing the priors for water and lipids. In the current chapter, all five NIR parameters (oxy and d-oxyhemoglobin, water and scatter amplitude and power) were directly reconstructed using spectral constraints based on their absorption and scattering behavior with wavelength, without any assumptions on their values and applied to experimental and clinical data. The spatial constraints allowed sufficient flexibility in recovering different regions by incorporating a soft prior that allows update in all the pixels in a region while minimizing their variation. The conclusions derived from this study are multifold:

- 1) Application of spatial a priori information alone, while enhancing the image quality (in terms of high frequency noise), can provide lower quality functional parameter quantification.
- 2) The use of spectral priors improves the quantification of these parameters (HbT, oxygen saturation, water and scatter) substantially, while suffering from lower resolution.
- 3) Application of spatial constraints in the spectral reconstruction enhances the quality of the functional images further, while retaining the benefit of higher accuracy from the spectral priors.

The quantification in terms of the average in the region of the anomaly for the phantom in Figure 9.2 was not substantially different between the use of spectral and the use of both spectral and spatial priors; and the spectral priors by themselves recover the glandular and adipose layers reasonably well. However, the image resolution in terms of recovering the

complex layered structure of a normal breast, was best with the use of both the spectral and spatial a priori information. The aspect of anatomical priors may especially become important for observing smaller tumors; and in such cases, the combination of priors will especially be useful. When both spatial and spectral priors were applied in a healthy volunteer, glandular tissue showed higher $[Hb_T]$, water, and scattering power compared to fatty tissue, consistent with expectations. The results from a single patient imaged using the combined MRI-NIR system shown here demonstrates the general trend in image recovery with application of both priors; Ben Brooksby's thesis¹⁵⁷ explores this further by application to clinical data from more normal asymptomatic patients.

10. Analysis of Normal Patient Data using Spectrally Constrained Direct Reconstruction

10.1 Introduction

Chapter 4 dealt with analyzing results from imaging healthy asymptomatic women, in order to establish trends and correlation between the functional parameters provided by optical imaging, and clinical demographic parameters such as age, body mass index (BMI), breast diameter and radiographic density. A bulk-average reconstruction approach, which treated the breast as a single homogeneous breast, was used to study these trends; the results showed interesting, statistically significant correlations, some of which are consistent with physiological predictions³¹.

Presented in this chapter is a renewed analysis of normal breast tissue: here, a novel reconstruction approach utilizing the spectral behavior of chromophores and scatterers in tissue as priors, has been used to obtain functional images of the breast. This reconstruction approach, introduced and validated in *Chapter 7*, has been shown to provide improved quantification as well as better separation between the chromophore concentrations and scattering parameters. In lieu of this development in imaging as well as a larger patient pool

(n=60 subjects), the images from healthy female volunteers so obtained were analyzed statistically in order to test for similar correlations as before.

10.2 Methods

The NIR tomography system based at Dartmouth was utilized to perform all the examinations. Written consent was obtained from all the volunteers and the examination protocol was approved by the institutional committee. The subjects imaged were under supervision (of Christine Kogel) to ensure comfort and pressure sensors were appropriately placed to prevent compression of the breast. The pendant breast was imaged in the radial configuration and frequency domain measurements (amplitude and phase) were obtained. After calibration, the spectrally constrained direct chromophore reconstruction (for details, see *Chapter 7*) was used to obtain the functional images of both left and right breasts. The statistical analysis on the averages from these images, were done by the biostatistician at DHMC, Jennifer Gibson.

10.3 Results

10.3.1 Patient Demographic Information

Having obtained measurements of amplitude and phase from three planes on the breast, the data was calibrated and used to obtain images of total hemoglobin, oxygen saturation, water, scatter amplitude and power, by the use of the direct spectral reconstruction. Artifacts are typically found close to the boundary; this is more likely an imaging system artifact rather than physiological in nature. Hence, 12% of the total breast diameter, from the boundary, was ignored, and the rest of the imaging field, for each of the NIR parameters, was used to compute the average and standard deviation. This was carried

out for all the 60 subjects and table 10.1 shows the mean with standard deviation as well as the total range for the clinical and NIR parameters.

Table 10-1: Average and standard deviation for demographic and NIR parameters from 60 normal subjects

Property	Mean \pm SD	Range
BMI (kg/m ²)	25 \pm 4	18-36
Age (yrs)	57 \pm 10.8	41-79
Breast Diameter (mm)	80.6 \pm 13.9	49-124
Hb _T (μ M)	16.6 \pm 4.6	6-31
S _t O ₂ (%)	68.3 \pm 7.2	46-96
Water (%)	51.5 \pm 14.1	28-94
Scatt Ampl.	1.2 \pm 0.25	0.59-2.2
Scatt Power	0.7 \pm 0.44	0.1-3

10.3.2 Correlations between functional and demographic parameters

A random-coefficients regression model was used to test for correlations between each of the NIR functional parameters with the clinical data. Both left and right breast data were used; and the model allowed for correlation between them for each subject. The coefficients along with standard errors and p-values are shown in table 10.2. *P*-values lower than 0.05 indicate a statistically significant difference from a slope of zero, for the fit between the clinical parameter (x) and the functional property (y), indicating a partial correlation between them.

From table 10.2, total hemoglobin was found to have a statistically significant correlation with BMI with a p-value <0.001. Figure 10.1(a) shows this relationship in a cluster plot of total hemoglobin averages with the respective standard deviations, plotted against BMI, for all the subjects. The analysis also indicates that oxygen saturation has a

significant relationship with both BMI as well as breast diameter (p-values of 0.012 and 0.006 respectively). When plotted on a cluster plot, it was hard to see any correlation visually; but it is possible that separating categories of BMI will yield a better indication. Water shows a statistically significant correlation to age and BMI and Figure 10.1(b) shows the graph of water plotted against BMI, and is representative of this trend. Scatter amplitude and power correlate with different factors: amplitude with breast diameter and scatter power correlates with age. Both these correlations are plotted in Figures 10.2 (a) and (b).

Table 10-2: Estimated partial correlations with standard error of NIR parameters relative to demographic factors such as age, BMI and breast diameter

NIR parameter	subject parameter	coefficient (SE)	F p-value
Hb _T	Age	-0.04 (0.03)	0.27
Hb _T	BMI	-0.47 (0.12)	<.001
Hb _T	Breast diameter	-0.06 (0.03)	0.064
S _t O ₂ (%)	Age	-0.07 (0.06)	0.25
S _t O ₂ (%)	BMI	-0.54 (0.21)	0.012
S _t O ₂ (%)	Breast diameter	0.16 (0.06)	0.006
Water (%)	Age	-0.45 (0.10)	<.001
Water (%)	BMI	-0.95 (0.33)	0.005
Water (%)	Breast diameter	-0.15 (0.09)	0.1
Scatt Ampl	Age	0.002 (0.002)	0.28
Scatt Ampl	BMI	0.009 (0.007)	0.18
Scatt Ampl	Breast diameter	-0.010 (0.002)	<.001
Scatt Power	Age	-0.010 (0.003)	0.005
Scatt Power	BMI	-0.009 (0.011)	0.44
Scatt Power	Breast diameter	-0.004 (0.003)	0.19

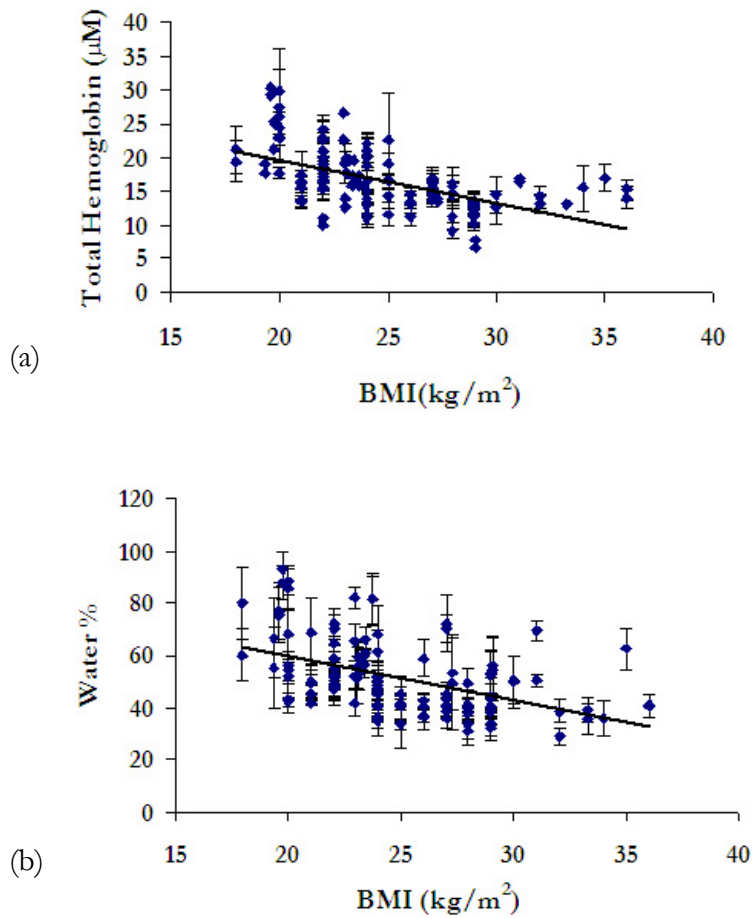
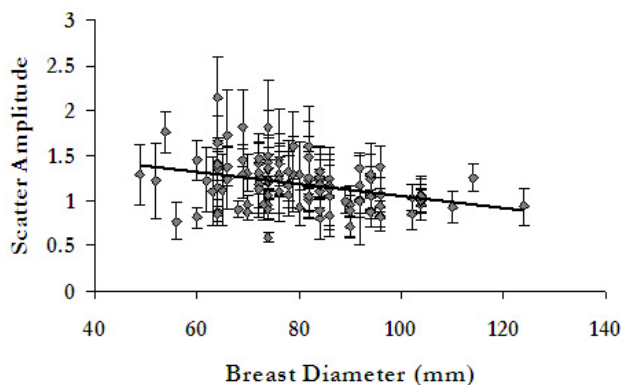


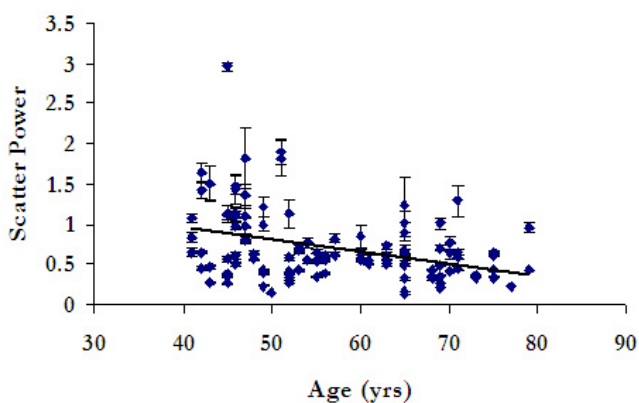
Figure 10-1:(a) Total hemoglobin plotted against BMI and (b) Water plotted against BMI using data from left and right breasts, for 60 healthy subjects. Both showed a statistically significant correlation ($p < 0.001$ for (a) and $p = 0.005$ for (b)).

10.3.3 Correlations between functional parameters and radiographic density

Another subject parameter of considerable importance is the patient breast density. This was determined from the mammogram and classified in four categories according to BI-RADS¹⁵¹: as 1) fatty, 2) scattered 3) heterogeneously dense and 4) extremely dense. The functional parameters were tested for correlations with each of the radio-density groups in a random coefficients regression model. Table 10.3 shows the information, similar to Table 10.2, for this statistical model.



(a)



(b)

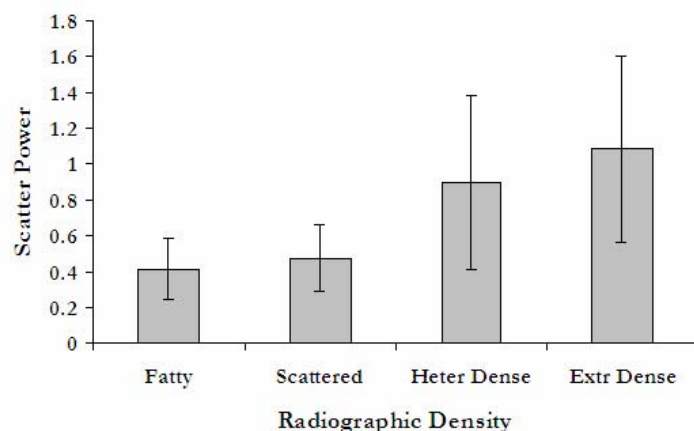
Figure 10-2:(a) Scatter amplitude versus diameter and (b) scatter power versus age; both showed statistically significant correlations with p values <0.001 and 0.005 respectively.

Among the correlations tested for, it was found that oxygen saturation can separate heterogeneously dense and extremely dense subjects from fatty subjects with p -values of 0.038 and 0.035 respectively. The other parameter which could do this separation was scatter power; Figure 10.3(a) shows this relationship in a plot between scatter power and the radio-graphic density groups. In addition to the analysis in Table 10.3; it was also found that water could separate heterogeneously dense and extremely dense patients from subjects with scattered type breasts, with p -values of 0.03 and 0.005 respectively. This can be seen from Figure 10.3 (b) as well, where the water content average for fatty and scattered type breasts

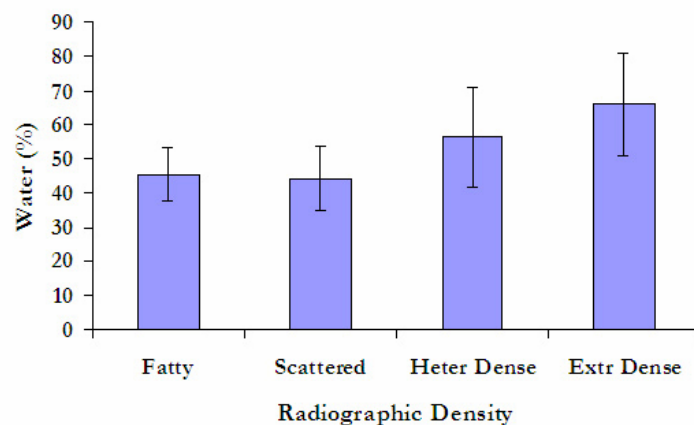
are similar, but scattered is different from heterogeneously dense as well as extremely dense categories. Scatter amplitude could separate heterogeneously dense from scattered; (p-value of 0.008) and scatter power could separate both heterogeneously dense as well as extremely dense from scattered (<0.001 and 0.001 p values respectively).

Table 10-3: Results of statistical analysis testing for separation of the radiographic density categories using NIR parameters

NIR Parameters	Radio-density groups	Coefficient (SE)	T p-value
Hb _T	Fatty	Reference	
	Scattered	-0.95 (1.22)	0.44
	Het. Dense	-0.16 (1.30)	0.9
	Extr. Dense	1.10 (1.76)	0.53
S _t O ₂ (%)	Fatty	Reference	
	Scattered	-2.32 (2.23)	0.3
	Het. Dense	-5.00 (2.38)	0.038
	Extr. Dense	-6.89 (3.23)	0.035
Water(%)	Fatty	Reference	
	Scattered	-3.80 (3.45)	0.27
	Het. Dense	1.69 (3.67)	0.65
	Extr. Dense	8.13 (4.98)	0.11
Scatt Ampl	Fatty	Reference	
	Scattered	0.014 (0.073)	0.85
	Het. Dense	-0.130 (0.078)	0.1
	Extr. Dense	-0.023 (0.106)	0.82
Scatt Power	Fatty	Reference	
	Scattered	0.011 (0.117)	0.92
	Het. Dense	0.33 (0.12)	0.01
	Extr. Dense	0.47 (0.17)	0.006



(a)



(b)

Figure 10-3: (a) NIR scatter power as a function of radiographic density: the average for the subjects in each category is plotted along with standard deviation. Statistical analysis showed that scatter power could separate fatty from heterogeneous dense and extremely dense category, with a p-values 0.01 and 0.006. (b) Water as a function of radio-density: water could separate scattered from heterogeneously dense and extremely dense categories with p values 0.03 and 0.005 respectively.

10.3.4 Correlations between the functional parameters

In order to test for correlations between the NIR parameters themselves, in order to assess how much independent information was obtained, a multi-variate test to calculate the Pearson's correlation coefficient was performed. The results are shown in Table 10.4 where the correlation coefficients are given along the p-values. Total hemoglobin appears to correlate with water (Figure 10.4(a) and scatter power (Figure 10.4(b)) with modest linearity (p-values <0.001 for both) and water also correlated with scatter power with a strong level of

linearity, with p -value < 0.001 . Scatter amplitude and power correlate with each other, as expected; since both are estimated from spectral constraints from an empirical approximation to Mie theory.

Table 10-4: Correlation coefficients among the derived NIR properties with corresponding p -values

	Hb _T	S _t O ₂ (%)	Water(%)	Scatt Power	Scatt Ampl.
Hb _T	1	0.237($p=0.068$)	0.569($p<0.001$)	0.494($p<0.001$)	-0.117($p=0.37$)
S _t O ₂		1	-0.079($p=0.55$)	0.094($p=0.47$)	-0.184($p=0.16$)
Water			1	0.743($p<0.001$)	-0.235($p=0.071$)
Scatt Power				1	0.468($p=0.0002$)
Scatt Ampl.					1

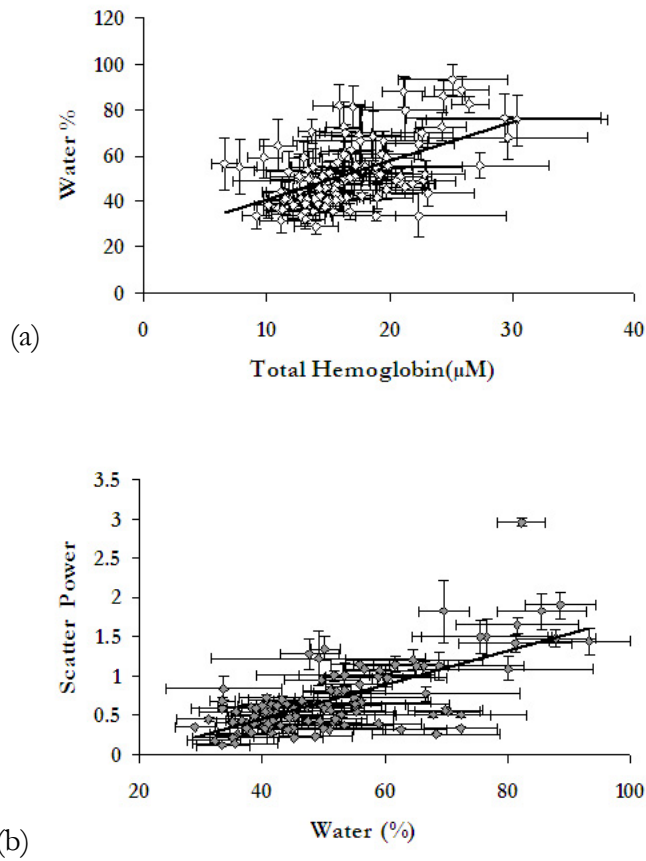


Figure 10-4:(a) Water versus total hemoglobin and (b) scatter power versus water; both showed statistically significant correlations with p -values < 0.001 .

10.4 Discussion

Studies on healthy breast tissue offer an insight into the physiological relationships between clinical factors and the functional information available through NIR imaging. The spectral approach to image reconstruction allows for improved quantification, especially significant in parameters like water and scatter, which were artifact-ridden in the conventional approach (without spectral priors). Among the correlations found here, some are consistent with the earlier study in *Chapter 4*; however some new correlations mainly involving water and scatter, were also observed.

Among the significant correlations between the demographic factors such as age, BMI and breast diameter and the functional parameters such as total hemoglobin, oxygen saturation, water and scatter, Hb_T was found to correlate with BMI (p -value <0.001). This is consistent with earlier studies by our group as well as other researchers^{5, 25, 135}. The body mass is indicative of the fat content of the breast, and hence higher BMI values represent breasts predominantly composed of adipose tissue, and hence having a lower vascularity (compared to glandular composition). The inverse relationship between water and adipose tissue is well known, and hence the inverse correlation between water content and BMI is also consistent with theoretical predictions. Water was also found to correlate with age with a statistically significant p -value < 0.001 . Cerussi et al²⁷ showed some indication of this relationship; and age has been shown to affect the proliferative activity of the breast¹⁵⁸; post-menopausal women were also found to have lower water content than pre-menopausal women⁷. Hence the correlation using water as a parameter agree with physiology, and also illustrate the improvement in water information, since these correlations were not available in *Chapter 4*.

Scatter amplitude and power show a better separation in this analysis using the Mie theory approximation as a constraint in the reconstruction. Previously, both scatter amplitude and power were found to correlate with breast diameter and separate the radiographic density categories. In this renewed analysis, scatter amplitude was found to correlate only with breast diameter (p-value <0.001), but not with radio-graphic density; whereas scatter power was found to correlate with age (p-value = 0.005) as well as yield a separation between differing density categories. In the previous chapters, images using the spectral approach illustrated that scatter power was more indicative of bulk tissue composition such as glandular and adipose tissue structures. The trend in Figure 10.3(a) backs this hypothesis. This was observed in earlier studies as well; and recently, it has been shown that NIR has potential to determine the breast density with accuracy of up to 90%; corresponding to the parenchymal density pattern from mammograms³⁰. Since breast density is related to risk of cancer²³; as well as decreased mammographic sensitivity²⁴; NIR offers the potential to non-invasively characterize both. Since denser breasts have higher contribution from fibroglandular tissue; water is also expected to increase with density: Figure 10.3(b) validates this trend. Finally, the correlation between water and total hemoglobin shows that the higher vascularity found in breast tissues which are more glandular, also tend to have higher water content. Water also correlated with scatter power, probably due to the same rationale: glandular tissue has higher scattering properties.

It should be noted at this point that the changes observed here are actually thought to be volume fraction changes, rather than actual compositional changes in the adipose and fibroglandular tissue (which are separate in MRI images). These fractional areas are thought to be the factors that change with age and BMI such that the trends observed here are likely

surrogate measures of how breast partitioning is altered with age or by differing BMI or what radiographic density actually means. Overall, this study used a larger patient pool than before (*Chapter 4*) and the spectral approach; and the relationships showed an indication of the heterogeneity between subjects, as well as new correlations regarding better separation of water and scatter.

11. Concluding Remarks

This thesis has explored methods to improve tissue characterization using NIR tomography, by examining the image reconstruction and the process of obtaining spectral parameters. The body of work presented here marks a major transition, moving from a focus on studying optical properties' recovery, to the direct recovery and study of the NIR functional parameters themselves, such as total hemoglobin, oxygen saturation, water and scatter; the primary source of contrast in optical breast imaging.

The use of spectral priors to obtain chromophore concentrations gives a significant improvement in quantification over the multistage reconstruction with spatial priors used before. Spectral priors allowed the spectral shapes of the chromophores as well as the approximation to Mie theory for scattering, to be embedded into the image reconstruction procedure. The multi-wavelength frequency domain measurements were coupled together and used simultaneously, to reconstruct directly for oxy and de-oxy hemoglobin, water, scatter amplitude and scatter power. This type of parametric reconstruction made the inverse problem better posed in terms of stability of the process to noise in data and showed superior quantification as well as improved qualitative images of NIR parameters.

There was still some under-estimation in the quantification of water content and simulation results, using additional wavelengths beyond 850nm, to capture stronger water features, illustrated an improvement in accuracy. It would be beneficial to follow this aspect more in detail, in an experimental setting. Currently, a broad-band spectroscopy system is being built at Dartmouth, to be used in conjunction with the frequency domain imager. The frequency domain data when reconstructed with the spectrally constrained reconstruction, yields images of scatter amplitude and power. These can then be used; along with continuous wave broadband data, to obtain quantitatively, better estimates for water.

The studies here have recovered images of scatter amplitude and power based on an empirical approximation to Mie theory. When this relationship was used as a constraint in the direct-spectral reconstruction, the quantification of scatter amplitude and power improved dramatically, increasing the information content available from scattering. These parameters have been found to correlate with radiographic density and provide a non-invasive surrogate measure of the density of the tissue^{25, 135}. Recent studies are demonstrating the ability to recover the size and density from scatter amplitude and power, based on Mie theory^{83, 159}. Researchers have shown that the size of tumor cells may be different from normal cells⁸⁴; Future studies in this direction may strengthen the potential of scattering as a diagnostic indicator.

The spectral approach was used to study malignant and benign disease, through a series of case-studies to establish distinctive features of these, useful in diagnosis. A major improvement was the ability to characterize hypoxia through oxygen saturation images of

cancers. Total hemoglobin, water and scatter provided physiological measures of changes in malignancies, all of these demonstrating contrasts in the tumor compared to surrounding tissue. The characteristics of benign disease (fibrocystic disease and fibrosis studied here) were different, with dominant contrast in water (consistent with fluid filled cysts) or scatter (due to scarred collagen tissue in fibrosis). Some potential gray zones exist in diagnosis, in separation of higher metabolism of normal glandular tissue from a metabolically active cancer and the study of the NIR images along with corresponding MR images can aid in this area. More clinical cases studied in this manner will help establish diagnostic indicators. Analysis of healthy breast tissue was carried out and results demonstrated the improved information content in water and scatter through the spectral approach and established physiological indicators of volume fraction changes in the breast, with age, size, and body - mass and radiographic density.

By establishing quantitative accuracy in the NIR functional parameters as a focus, and validating the imaging process, physiological changes in normal and diseased tissue were characterized here. These changes represented through hemoglobin, oxygen saturation, water and scatter can be extended to monitor response to therapy, predict risk of malignancy and aggressiveness of tumors.

Appendix A

Given below is the recipe for the gelatin phantom used in Chapter 7 and 9.

Materials Used:

20% Gelatin (240gms of Sigma-Aldrich Inc. G2625, Gelatin from porcine skin, Type A, 175 Bloom)

80% Buffered Saline (960ml)

1% Pig blood (12ml; hematocrit level measured: 1% blood~10.8 μ M total hemoglobin)

Titanium Dioxide (2.2gms of Sigma-Aldrich Inc. T-8141, Titanium (IV) Oxide (TiO₂))

Anti-bacterial (1 g of Sigma-Aldrich Inc. EDS, Ethylenediamine-tetraacetic acid (C₁₀H₁₆N₂O₈) (EDTA))

Procedure:

1. Mix gelatin in water; stir in smoothly to keep air bubbles at a minimum.
2. Heat up to 40 degrees centigrade in the microwave; remove the bubbles, if any, which would have risen to the top.
3. After cooling up to 30 degrees, put on the stir-plate and slowly add blood and Antibacterial.
4. Slowly add TiO₂ till all of it is mixed in.
5. Pour the mixture into two bottles; one with a rod 25mm in diameter to create a hole.
6. Cool down the mixtures in the refrigerator (at -20degrees C) for half hr: the phantoms are ready for use.

Appendix B

This appendix gives the input and output filenames used in data generation and reconstruction programs, as well as a brief over-view of the main programs. All the code was written in Matlab; and structured to work with NIRFAST.

The first step in the entire spectral toolbox is that the wavelengths to be used are given explicitly by the user, in the form of an array: For e.g., the current six wavelengths are given in the form:

```
wv_array = [661; 761; 785; 808; 826; 849]
```

Next, the extinction coefficients at different wavelengths are stored in a file (called 'excoeff.dat' for the current tool box); the format is as below, and units for the spectra are in mm^{-1}/mM for HbO_2 and Hb spectra; and mm^{-1} for water. This file can include any number of wavelengths; only the values for the wavelengths specified by the user (as `wv_array`) will then be used.

<i>Wvs</i>	<i>HbO₂</i>	<i>Hb</i>	<i>Water</i>
661	0.074074074	0.85	0.00148
761	0.118518519	0.329166667	0.00428
785	0.15	0.205555556	0.00378
808	0.174074074	0.161111111	0.00332
826	0.227777778	0.161111111	0.00396
849	0.237037037	0.155555556	0.00578

All the codes for the spectral approach are easily extendable to multiple chromophores. (given by a single variable 'nc' in the beginning of the code).

File naming Conventions

All the filenames are made to be consistent with clinical data; hence, simulated data also has to be stored in the same format. Filenames for Data: given patient id: 'patid' and left or right breast: 'left' or 'right'; along with plane number (0,1 or 2) and repetition number; and the wavelength array, data is stored in files below (given as an example for a patid of '1035', left breast; at 661 and 761nm, for plane 0 and repetition 1) :

```
'pat1035_left_661nm_plane0_rep1.paa'  
'pat1035_left_761nm_plane0_rep1.paa' etc
```

Phantom data for the same patient is stored as

```
'pat1035_phantom_661nm_plane0_rep1.paa'  
'pat1035_phantom_761nm_plane0_rep1.paa' etc.
```

Calibrated data is stored as below for same inputs for each wavelength:

```
'pat1035_left_661nm_plane0_rep1.cal'  
'pat1035_left_761nm_plane0_rep1.cal'
```

The spectral calibration stores an initial guess for HbO₂, Hb, water, scatter amplitude and scatter power, in filenames:

```
Pat1035_left_plane0_rep1_hb1.cal  
Pat1035_left_plane0_rep1_hb2.cal  
Pat1035_left_plane0_rep1_wat.cal  
Pat1035_left_plane0_rep1_sa.cal  
Pat1035_left_plane0_rep1_sp.cal
```

This is done by the program 'cal_spectral.m' which uses the Beer's law and Scatter theory fits to absorption and scattering coefficients from a homogeneous calculation; to obtain the initial guesses.

The forward data can be generated given a set of concentrations and scattering; with data stored in the same file format above. For this purpose, 'forward_chromo.m' is to be used. The true concentrations and scatter can be generated also using 'add_conc_heter.m' which

adds anomalies in desired locations and stores the values inputted by the user in files that can be used to generate the forward data. The tutorial has this sequence: users should refer to it.

Image Reconstruction

After having the patid, left or right side, plane and repetition; and calibration to generate the initial guesses, the image reconstruction program can be used. This is called 'recon_spectral.m'. The program is made to work with the dual mesh basis; or pixel basis; though all the reconstructions performed in this work used the dual mesh basis. The program is called using the following command:

```
[mesh1,pj_error] = recon_spectral('circle2000_86','circle400_86',100,patid,LR,plane,rep,...  
'excoeff.dat',wv_array,iterations,regn_param,filter_n);
```

The first mesh is the typically used fine mesh followed by the coarse mesh containing 425 nodes. The third input is the frequency, followed by patient parameters, the extinction coefficient file, wavelengths to be used. The last three parameters are the number of iterations (the program stops earlier if the projection error change between successive iterations is less than 2%); the regularization parameter (typically given as 10) and the filter (usually 1).

All the parameters given as inputs by the user, as well as projection errors and regularization parameters for each iteration, are stored in a log file given as:
'pat1035_left_plane1_rep0_spectral.log'

The solution for the chromophore concentrations and scatter amplitude and power are stored automatically, at each iteration, in filenames below (as given by Dr. Shudong Jiang):

HbO₂: 'pat1035_left_hb1_plane0_rep1.sol'
Hb: 'pat1035_left_hb2_plane0_rep1.sol'
Water: 'pat1035_left_wat_plane0_rep1.sol'
Hb_T: 'pat1035_left_hbT_plane0_rep1.sol'
S₀O₂: 'pat1035_left_StO_plane0_rep1.sol'
Scatt Ampl: 'pat1035_left_SCa_plane0_rep1.sol'

Scatt Power: 'pat1035_left_SCP_plane0_rep1.sol'

In addition the final iteration solutions are stored separately for easy access, in similar filenames as above, in the format:

Hb_T: 'pat1035_left_hbT_plane0_rep1_final.dat'

S_tO₂: 'pat1035_left_StO_plane0_rep1_final.dat'

Water: 'pat1035_left_wat_plane0_rep1_final.dat'

Scatt Ampl: 'pat1035_left_SCa_plane0_rep1_final.dat'

Scatt Power: 'pat1035_left_SCP_plane0_rep1_final.dat'

The solutions can be plotted for either the final iteration (from files above) or any particular iteration. The program used for this is 'read_spectral_clinical.m' and uses the below format:

```
[hbt,oxysat,wat,sa,sp]=read_spectral_clinical(mesh,patid,LR,plane,rep,iteration);
```

where iteration is given as 0, if final iteration is to be plotted.

Users are recommended to use the spectral tool box when working with direct spectral reconstruction and are referred to the tutorial: 'tutorial_spectral.m' to get acquainted with the tool-box usage.

References

1. V.V. Tuchin, *Tissue optics: light scattering methods and instruments for medical diagnosis*. Tutorial texts in optical engineering. Vol. 38. 1999: SPIE. 200.
2. F.F. Jobsis, "Non-invasive, infra-red monitoring of cerebral and myocardial oxygen sufficiency and circulatory parameters.." *Science*, vol. 198 pp. 1264-1267.1977.
3. J.-L. Boulnois, "Photophysical processes in recent medical laser developments: a review." *Lasers in Medical Science*, vol. 1 pp. 47-66.1986.
4. G.M. Hale and M.R. Querry, "Optical constants of water in the 200-nm to 200-um wavelength region." *Appl. Opt.*, vol. 12(3) pp. 555-563.1973.
5. T. Durduran, R.Choe, J.P.Culver, L.Zubkov, M.J.Holboke, J.Giammarco, B.Chance and A.G.Yodh, "Bulk optical properties of healthy female breast tissue." *Phys. Med. Biol.*, vol. 47 pp. 2847-2861.2002.
6. B.W. Pogue, S.P. Poplack, T.O. McBride, W.A. Wells, O.K. S., U.L. Osterberg, and K.D. Paulsen, "Quantitative Hemoglobin Tomography with Diffuse Near-Infrared Spectroscopy: Pilot Results in the Breast." *Radiology*, vol. 218(1) pp. 261-6.2001.
7. N. Shah, A. Cerussi, C. Eker, J. Espinoza, J. Butler, J. Fishkin, R. Hornung, and B. Tromberg, "Noninvasive functional optical spectroscopy of human breast tissue." *Proceedings of the National Academy of Sciences of the United States of America*, vol. 98(8) pp. 4420-5.2001.
8. J.C. Hebden, Gibson, A., Yusof, R. M., Everdell, N., Hillman, E. M., Delpy, D. T., Arridge, S. R., Austin, T., Meek, J. H., Wyatt, J. S., "Three-dimensional optical tomography of the premature infant brain." *Phys. Med. Biol.*, vol. 47(23) pp. 4155-66.2002.
9. G. Strangman, Boas, D. A. and Sutton, J. P., "Non-invasive neuroimaging using near-infrared light." *Biol. Psychiatry*, vol. 52 pp. 679-693.2002.
10. J.S. Wyatt, "Cerebral oxygenation and haemodynamics in the foetus and newborn infant." *Phil. Trnas. R. Soc. Lond. B*, vol. 352 pp. 697-700.1997.

11. E. Gratton, Fantini, S., Franceschini, M. A., Gratton, G. and Fabiani, M., "Measurements of scattering and absorption changes in muscle and brain." *Phil. Trans. R. Soc. Lond. B*, vol. 352 pp. 727-735.1997.
12. P. Van der Zee, Cope, M., Arridge, S. R., Essenpreis M., Potter, L. A., Edwards, A. D., Wyatt, J. S., McCormick, D. C., Roth, S. C., Reynolds, E. O., et al, "Experimentally measured optical pathlengths for the adult head, calf and forearm and the head of the newborn infant as a function of inter-optode spacing." *Adv Expt Med Biol*, vol. 316 pp. 143-53.1992.
13. I.V. Meglinski, Matcher, S. J., "Computer simulation of the skin reflectance spectra." *Computer Methods and Programs in Biomedicine*, vol. 70 pp. 179-186.2003.
14. A. Bottini, A. Berruti, M.P. Brizzi, A. Bersiga, D. Generali, G. Allevi, S. Aguggini, G. Bolsi, S. Bonardi, G. Bertoli, P. Alquati, and L. Dogliotti, "Pretreatment haemoglobin levels significantly predict the tumour response to primary chemotherapy in human breast cancer." *Br J Cancer*, vol. 89(6) pp. 977-82.2003.
15. B.C. Wilson and M.S. Patterson, "The physics of photodynamic therapy." *Phys. Med. Biol.*, vol. 31 pp. 327-360.1986.
16. T. Johansson, Thompson, M. S., Stenberg, M., Klinteberg, C. A., Andersson-Engels, S., Svanberg, S. and Svanberg, K., "Feasibility study of a system for combined light dosimetry and interstitial photodynamic treatment of massive tumors." *Applied Optics*, vol. 41(7) pp. 1462-1468.2002.
17. B. Chance, Q. Luo, S. Nioka, D.C. Alsop, and J.A. Detre, "Optical investigations of physiology: a study of intrinsic and extrinsic biomedical contrast." *Phil. Trans. R. Soc. Lond. B*, vol. 352 pp. 707-716.1997.
18. M. Cutler, "Transillumination as an aid in the diagnosis of breast lesions." *Surg. Gyn. Obst.*, vol. 48 pp. 721-729.1929.
19. D.J. Watmough, "Transillumination of breast tissues: factors governing optimal imaging of lesions." *Radiol.*, vol. 147 pp. 89-92.1982.
20. R.J. Bartrum and H.C. Crow, "Transillumination light scanning to diagnose breast cancer: a feasibility study." *Am. J. Roentg.*, vol. 142 pp. 409-414.1984.
21. J.G. Elmore, M. B. Barton, V. M. Mocerri, S. Polk, P. J. Arena and S. W. Fletcher, "Ten-Year Risk of False Positive Screening Mammograms and Clinical Breast Examinations." *The New England Journal of Medicine*, vol. 338(16) pp. 1089-1096.1998.

22. S.P. Poplack, A.N. Tosteson, M.R. Grove, W.A. Wells, and P.A. Carney, "Mammography in 53,803 women from the New Hampshire mammography network." *Radiology*, vol. 217 pp. 832-840.2000.
23. M.T. Mandelson, N. Oestreicher, P.L. Porter, D. White, C.A. Finder, S.H. Taplin, and E. White, "Breast density as a predictor of mammographic detection: comparison of interval- and screen-detected cancers." *J Natl Cancer Inst*, vol. 92(13) pp. 1081-7.2000.
24. D.S.M. Buist, P.L. Porter, C. Lehman, S.H. Taplin, and E. White, "Factors contributing to mammography failure in women aged 40-49 years." *Journal of the National Cancer Institute*, vol. 96(19) pp. 1432-40.2004.
25. B.W. Pogue, S. Jiang, H. Dehghani, C. Kogel, S. Soho, S. Srinivasan, X. Song, S.P. Poplack, and K.D. Paulsen, "Characterization of hemoglobin, water and NIR scattering in breast tissue: analysis of inter-subject variability and menstrual cycle changes relative to lesions." *J. Biomed. Opt.*, vol. 9(3) pp. 541-552.2004.
26. P. Vaupel, K. F., and O. P., "Blood Flow, Oxygen and Nutrient Supply, and Metabolic Microenvironment of Human Tumors : A Review." *Cancer Research*, vol. 49 pp. 6449-6465.1989.
27. A. Cerussi, D. Jakubowski, N. Shah, F. Bevilacqua, R. Lanning, A. J. Berger, D. Hsiang, J. Butler, R. F. Holcombe, B. J. Tromberg, "Spectroscopy enhances the information content of optical mammography." *J. Biomed. Opt.*, vol. 7(1) pp. 60-71.2002.
28. B.J. Tromberg, N. Shah, R. Lanning, A. Cerussi, J. Espinoza, T. Pham, L. Svaasand, and J. Butler, "Non-invasive in vivo characterization of breast tumors using photon migration spectroscopy." *Neoplasia (New York)*, vol. 2(1-2) pp. 26-40.2000.
29. K. Blyschak, M. Simick, R. Jong, and L. Lilge, "Classification of breast tissue density by optical transillumination spectroscopy: optical and physiological effects governing predictive value." *Med. Phys.*, vol. 31(6) pp. 1398-414.2004.
30. M.K. Simick, R. Jong, B. Wilson, and L. Lilge, "Non-ionizing near-infrared radiation transillumination spectroscopy for breast tissue density and assessment of breast cancer risk." *Journal of Biomed Opt*, vol. 9(4) pp. 794-803.2004.
31. S. Srinivasan, B.W. Pogue, S. Jiang, H. Dehghani, C. Kogel, S. Soho, J.J. Gibson, T.D. Tosteson, S.P. Poplack, and K.D. Paulsen, "Interpreting hemoglobin and water

- concentration, oxygen saturation and scattering measured in vivo by near-infrared breast tomography." *PNAS*, vol. 100(21) pp. 12349-12354.2003.
32. S. Thomsen, and D. Tatman, "Physiological and Pathological Factors of Human Breast Disease That can Influence Optical Diagnosis." *Ann. N. Y. Acad. Sci.*, vol. 838 pp. 171-193.1998.
 33. S.J. Graham, P.L. Stanchev, J.O.A. Lloyd-Smith, M.J. Bronskill, and D.B. Plewes, "Changes in fibroglandular volume and water content of breast tissue during the menstrual cycle observed by MR imaging at 1.5 T." *JMRI*, vol. 5 pp. 695-701.1995.
 34. N. Shah, A. Cerussi, D. Jakubowski, D. Hsiang, J. Butler, and B. Tromberg, "Spatial variations in optical and physiological properties of healthy breast tissue." *Journal of Biomed Opt*, vol. 9(3) pp. 534-540.2004.
 35. M.S. Patterson, C. B., and B.C. Wilson, "Time resolved reflectance and transmittance for the non-invasive measurement of tissue optical properties." *Appl. Opt.*, vol. 28 pp. 2331-2336.1989.
 36. B. Chance, Nioka, S., Kent, J., McCully, K., Fountain, M., Greenfield, R., Holtom, G., "Time-resolved spectroscopy of hemoglobin and myoglobin in resting and ischemic muscle." *Analy. Biochem.*, vol. 174 pp. 698-707.1988.
 37. B.W. Pogue, Patterson, M. S., Jiang, H., Paulsen, K. D., "Initial assessment of a simple system for frequency domain diffuse optical tomography." *Phys. Med. Biol.*, vol. 40 pp. 1709-1729.1995.
 38. S. Fantini, Franceschini-Fantini, M. A., Maier, J. S., Walker, S. A., Barbieri, B. and Gratton, E., "Frequency-domain multichannel optical detector for noninvasive tissue spectroscopy and oximetry." *Opt. Eng.*, vol. 34 pp. 32-42.1995.
 39. E.L. Hull, M.G. Nichols, and T.H. Foster, "Quantitative broadband near-infrared spectroscopy of tissue-simulating phantoms containing erythrocytes." *Physics in Medicine & Biology*, vol. 43(11) pp. 3381-404.1998.
 40. A. Kienle, Lilge, L., Patterson, M. S., Hibst, R., Steiner, R. and Wilson, B. C., "Spatially resolved absolute diffuse reflectance measurements for noninvasive determination of the optical scattering and absorption coefficients of biological tissue." *Applied Optics*, vol. 35 pp. 2304-2314.1996.

41. K.D. Paulsen, and Jiang, H., "Spatially varying optical property reconstruction using a finite element diffusion equation approximation." *Med. Phys.*, vol. 22(6) pp. 691-701.1995.
42. S.R. Arridge, Schweiger, M.,Hiraoka, M.,Delpy,D.T, "A finite element approach for modeling photon transport in tissue." *Med. Phys.*, vol. 20(2) pp. 299-309.1993.
43. T.O. McBride, B.W. Pogue, S. Jiang, U.L. Osterberg, and K.D. Paulsen, "A parallel-detection frequency-domain near-infrared tomography system for hemoglobin imaging of the breast in vivo." *Review of Scientific Instruments*, vol. 72(3) pp. 1817-1824.2001.
44. T.O. McBride, "Spectroscopic reconstructed near infrared tomographic imaging for breast cancer diagnosis", in *Thayer School of Engineering*. 2001, Dartmouth College. p. 200.
45. H. Jiang, K.D. Paulsen, U.L. Osterberg, B.W. Pogue, and M.S. Patterson, "Optical image reconstruction using frequency-domain data: simulations and experiments." *J. Opt. Soc. Am. A*, vol. 13(2) pp. 253-266.1996.
46. H. Dehghani, Pogue, B. W., Poplack, S. P. and Paulsen, K. D., "Multiwavelength three-dimensional near-infrared tomography of the breast: initial simulation, phantom, and clinical results." *Applied Optics*, vol. 42(1) pp. 135-145.2003.
47. M.S. Patterson, B.C. Wilson, and D.R. Wyman, "The propagation of optical radiation in tissue II. Optical properties of tissues and resulting fluence distributions." *Lasers Med. Sci.*, vol. 6 pp. 379-390.1990.
48. S.R. Arridge and M. Schweiger, "Image reconstruction in optical tomography." *Phil. Trans. R. Soc. Lond. B*, vol. 352 pp. 717-726.1997.
49. M. Schweiger, Arridge, S. R., "Optical tomographic reconstruction in a complex head model using apriori region boundary information." *Phys. Med. Biol.*, vol. 44 pp. 2703-2721.1999.
50. B.W. Pogue and K.D. Paulsen, "High resolution near infrared tomographic imaging simulations of rat cranium using apriori MRI structural information." *Opt. Lett.*, vol. 23(21) pp. 1716-8.1998.
51. H. Dehghani, B.W. Pogue, J. Shudong, B. Brooksby, and K.D. Paulsen, "Three-dimensional optical-tomography: resolution in small-object imaging." *Applied Optics*, vol. 42(16) pp. 3117-3128.2003.

52. B. Brooksby, Dehghani, H., Pogue, B. W., Paulsen, K. D., "Near infrared (NIR) tomography breast image reconstruction with apriori structural information from MRI: algorithm development for reconstructing heterogeneities." *IEEE Journal of Selected Topics in Quantum Electronics on Lasers in Medicine and Biology*.2003-in press.
53. T.O. McBride, B.W. Pogue, E. Gerety, S. Poplack, U.L. Osterberg, and K.D. Paulsen, "Spectroscopic diffuse optical tomography for quantitatively assessing hemoglobin concentration and oxygenation in tissue." *Appl. Opt.*, vol. 38(25) pp. 5480-90.1999.
54. R. Cubeddu, C. D'Andrea, A. Pifferi, P. Taroni, A. Torricelli and G. Valentini, "Effects of the Menstrual Cycle on the Red and Near-infrared Optical Properties of the Human Breast." *Photochemistry & Photobiology*, vol. 72(3) pp. 383-391.2000.
55. D. Grosenick, H. Wabnitz, K.T. Moesta, J. Mucke, M. Moller, C. Stroszczynski, J. Stossel, B. Wassermann, P.M. Schlag, and H. Rinneberg, "Concentration and oxygen saturation of haemoglobin of 50 breast tumours determined by time-domain optical mammography." *Phys Med Biol*, vol. 49(7) pp. 1165-81.2004.
56. B.W. Pogue, Patterson, M. S., "Frequency domain optical absorption spectroscopy of finite tissue volumes using diffusion theory." *Phys. Med. Biol.*, vol. 39 pp. 1157-1180.1994.
57. M.G. Nichols, Hull, E. L. and Foster, T. H., "Design and testing of a white-light, steady-state diffuse reflectance spectrometer for determination of optical properties of highly scattering systems." *Applied Optics*, vol. 36(1) pp. 93-104.1997.
58. S.R. Arridge and W.R.B. Lionheart, "Nonuniqueness in diffusion-based optical tomography." *Optics Letters*, vol. 23(11) pp. 882-884.1998.
59. S.R. Arridge, "Optical tomography in medical imaging." *Inverse Problems*, vol. 15(2) pp. R41-R93.1999.
60. F. Bevilacqua, Berger, A. J., Cerussi, A. E., Jakubowski, D. and Tromberg, B. J., "Broadband absorption spectroscopy in turbid media by combined frequency-domain and steady-state methods." *Applied Optics*, vol. 39(34) pp. 6498-6507.2000.
61. M.S. Patterson, B.C. Wilson, and D.R. Wyman, "The propagation of optical radiation in tissue I. models of radiation transport and their application." *Lasers Med. Sci.*, vol. 6 pp. 155-168.1990.

62. A. Ishimaru, *Wave propagation and scattering in random media*. Vol. 1. 1978: Academic Press, Inc., New York.
63. R.A.J. Groenhuis, Ferwerda, H. A., ten Bosch, J. J., "Scattering and absorption of turbid materials determined from reflection measurements. I.Theory.." *Appl. Opt.*, vol. 22(16) pp. 2456-2462.1983.
64. A. Kienle and M.S. Patterson, "Determination of the optical properties of turbid media from a single Monte Carlo simulation." *Phys Med Biol*, vol. 41 pp. 2221-2227.1996.
65. T.J. Farrell, Patterson, M. S., Wilson, B. C., "A diffusion theory model of spatially resolved, steady-state diffuse reflectance for the noninvasive determination of tissue optical properties." *Med. Phys.*, vol. 19(4) pp. 879-888.1992.
66. M. Schweiger, S.R. Arridge, M. Hiraoka, and D.T. Delpy, "The finite element method for the propagation of light in scattering media: boundary and source conditions." *Med. Phys.*, vol. 22 pp. 1779-1792.1995.
67. B. Kaltenbacher, "Some Newton-type methods for the regularization of nonlinear ill-posed problems." *Inverse Problems*, vol. 13 pp. 729-753.1997.
68. M. Hanke, "A regularizing Levenberg-Marquardt scheme, with applications to inverse groundwater filtration problems." *Inverse Problems*, vol. 13 pp. 79-95.1997.
69. T.O. McBride, B.W. Pogue, U.L. Österberg, and K.D. Paulsen, "Strategies for Absolute Calibration of Near Infrared Tomographic Tissue Imaging", in *Oxygen Transport to Tissue XXI*, J.F. Dunn, Swartz, H. M., Editor. 2001, Lengerich: Pabst.
70. A. Kirsch, *An introduction to the mathematical theory of inverse problems*. Vol. 120. 1996: Springer-Verlag, NY Inc. 282.
71. P.C. Hansen, "Rank-deficient and discrete ill-posed problems: numerical aspects of linear inversion."1998.
72. D.W. Marquardt, "An algorithm for least squares estimation of nonlinear parameters." *J. Soc. Ind. Appl. Math.*, vol. 11 pp. 431-441.1963.
73. W.H. Press, S.A. Teukolsky, W.T. Vetterling, and B.P. Flannery, *Numerical Recipes in Fortran*. 2nd ed. 1992, New York: Cambridge University Press.
74. B.W. Pogue, McBride, T. O., Prewitt, J., Osterberg, U. L., Paulsen, K. D., "Spatially variant regularization improves diffuse optical tomography." *Appl. Opt.*, vol. 38(13) pp. 2950-61.1999.

75. K.D. Paulsen, Jiang, H., "Enhanced frequency-domain optical image reconstruction in tissues through total-variation minimization." *Appl. Opt.*, vol. 35(19) pp. 3447-3458.1996.
76. S. Prahl, "Optical Absorption of Hemoglobin." <http://omlc.ogi.edu/spectra/hemoglobin/index.html>,
77. S. Wray, Cope, M., Delpy, D. T., Wyatt, J. S., Reynolds, E., "Characterization of the near infrared absorption spectra of cytochrome aa3 and haemoglobin for the non-invasive monitoring of cerebral oxygenation." *Biochem. Biophys. Acta*, vol. 933 pp. 184-192.1988.
78. A. Dunn and R. Richards-Kortum, "Three-dimensional computation of light scattering from cells." *Ieee Journal of Selected Topics in Quantum Electronics*, vol. 2(4) pp. 898-905.1996.
79. A.H. Hielscher, J.R. Mourant, and I.J. Bigio, "Influence of particle size and concentration on the diffuse backscattering of polarized light from tissue phantoms and biological cell suspensions." *Appl Opt*, vol. 36(1) pp. 125-135.1997.
80. R. Drezek, A. Dunn, and R. Richards-Kortum, "Light scattering from cells: finite difference time-domain simulations and goniometric measurements." *Appl Opt*, vol. 38(16) pp. 3651-61.1999.
81. J.R. Mourant, T. Fuselier, J. Boyer, T.M. Johnson, and I.J. Bigio, "Predictions and measurements of scattering and absorption over broad wavelength ranges in tissue phantoms." *Applied Optics*, vol. 36(4) pp. 949-957.1997.
82. H.J. van Staveren, C.J.M. Moes, J. van Marle, S.A. Prahl, and J.C. van Gemert, "Light scattering in Intralipid - 10% in the wavelength range of 400-1100nm." *Applied Optics*, vol. 30(31) pp. 4507-4514.1991.
83. X. Wang, B.W. Pogue, S. Jiang, X. Song, K.D. Paulsen, C. Kogel, S.P. Poplack, and W.A. Wells, "Approximation of Mie scattering parameters in near-infrared tomography of normal breast tissue in vivo." *Journal of Biomed Opt.*2005 (in press).
84. J.R. Mourant, A.H. Hielscher, A.A. Eick, T.M. Johnson, and J.P. Freyer, "Evidence of intrinsic differences in the light scattering properties of tumorigenic and nontumorigenic cells." *Cancer Cytopathology*, vol. 84(6) pp. 366-74.1998.
85. J.M. Steinke and A.P. Shepherd, "Comparison of Mie theory and the light scattering of red blood cells." *Appl Opt*, vol. 27 pp. 4027-4033.1988.

86. B. Beauvoit, H. Liu, K. Kang, P.D. Kaplan, M. Miwa, and B. Chance, "Characterization of absorption and scattering properties for various yeast strains by time-resolved spectroscopy." *Cell Biophysics*, vol. 23(1-3) pp. 91-109.1993.
87. M. Cope, "The Application of Near infrared Spectroscopy to Noninvasive Monitoring of Cerebral oxygenation in the New born Infant.." *Ph.D thesis*.1991.
88. W.G. Zijlstra, Buursma, A., and Meeuwse-van der Roest, "Absorption Spectra of Human Fetal and Adult Oxyhemoglobin, De-oxyhemoglobin, Carboxyhemoglobin, and Methemoglobin." *Clinical Chemistry*, vol. 37(9) pp. 1633-1638.1991.
89. R.M. Pope and E.S. Fry, "Absorption spectrum (380-700nm) of pure water. II. Integrating cavity measurements." *Appl Opt*, vol. 36(33) pp. 8710-8723.1997.
90. S.J. Matcher, Elwell, C. E., Cooper, C. E., Cope, M., and Delpy, D. T., "Performance Comparison of Several Published Tissue Near-Infrared Spectroscopy Algorithms." *Analytical Biochemistry*, vol. 227 pp. 54-68.1995.
91. M.S. Patterson, Moulton, J. D., Wilson, B. C., Berndt, K. W., Lakowicz, J. R., "Frequency-domain reflectance for the determination of the scattering and absorption properties of tissue." *Appl. Opt.*, vol. 30(24) pp. 4474-4476.1991.
92. H.J. van Staveren, C.J.M. Moes, J. van Marle, S.A. Prahl, and M.J.C. van Gemert, "Light Scattering in Intralipil-10% in the wavelength range of 400-1100nm." *Applied Optics*, vol. 30(31) pp. 4507-4514.1991.
93. N. Varjavand, "The Interactive Oxyhemoglobin Dissociation Curve." <http://www.ventworld.com/resources/oxydisso/dissoc.html>.2002.
94. P.C. Stomper, B.J. Van Voorhis, V.A. Ravnkar, and J.E. Meyer, "Mammographic changes associated with postmenopausal hormone replacement therapy: a longitudinal study.." *Radiology*, vol. 174(2) pp. 487-490.1990.
95. P.C. Stomper and R.S. Gelman, "Mammography in symptomatic and asymptomatic patients." *Hematology-Oncology Clinics of North America*, vol. 3(4) pp. 611-40.1989.
96. K. Suzuki, Yamashita, Y., Ohta, K., Kaneko, M., Yoshida, M., Chance, B., "Quantitative measurement of optical parameters in normal breasts using time-resolved spectroscopy: In vivo results of 30 Japanese women." *J. Biomed. Opt.*, vol. 1(3) pp. 330-334.1996.

97. V. Quaresima, S.J. Matcher, and M. Ferrari, "Identification and quantification of intrinsic optical contrast for near-infrared mammography." *Photochem. Photobiol.*, vol. 67 pp. 4-14.1998.
98. A.E. Cerussi, A.J. Berger, F. Bevilacqua, N. Shah, D. Jakubowski, J. Butler, R.F. Holcombe, and B.J. Tromberg, "Sources of absorption and scattering contrast for near-infrared optical mammography." *Academic Radiology*, vol. 8(3) pp. 211-8.2001.
99. B.W. Pogue, M. Testorf, T. McBride, U. Osterberg, and K. Paulsen, "Instrumentation and design of a frequency-domain diffuse optical tomography imager for breast cancer detection." *Opt. Express*, vol. 1(13) pp. 391-403.1997.
100. T.O. McBride, B.W. Pogue, S. Jiang, U.L. Osterberg, and K.D. Paulsen, "Development and Calibration of a Parallel Modulated Near-Infrared Tomography System for Hemoglobin Imaging In Vivo." *Rev. Sci. Instr.*, vol. 72(3) pp. 1817-1824.2001.
101. H. Dehghani, B. W. Pogue, J. Shudong, B. Brooksby and K. D. Paulsen, "Three Dimensional Optical Tomography : Resolution in Small Object Imaging." *Applied Optics*.2002-in press.
102. E.L. Hull, D.L. Conover, and T.H. Foster, "Carbogen-induced changes in rat mammary tumour oxygenation reported by near infrared spectroscopy." *British Journal of Cancer*, vol. 79(11-12) pp. 1709-16.1999.
103. H. Liu, B. Chance, A.H. Hielscher, S.L. Jacques, and F.K. Tittel, "Influence of blood vessels on the measurement of hemoglobin oxygenation as determined by time-resolved reflectance spectroscopy." *Med. Phys.*, vol. 22(8) pp. 1209-17.1995.
104. M. Firbank, E. Okada, and D.T. Delpy, "Investigation of the effect of discrete absorbers upon the measurement of blood volume with near-infrared spectroscopy." *Phys. Med. Biol.*, vol. 42(3) pp. 465-77.1997.
105. B.J. Tromberg, Coquoz, O., Fishkin, J. B., Pham, T., Anderson, E. R., Butler, J., Cahn, M., Gross, J. D., Venugopalan, V., Pham, D., "Non-invasive measurements of breast tissue optical properties using frequency-domain photon migration." *Phil. Trans. R. Soc. Lond. B*, vol. 352 pp. 661-668.1997.
106. H.L. Liu, Y.L. Song, K.L. Worden, X. Jiang, A. Constantinescu, and R.P. Mason, "Noninvasive investigation of blood oxygenation dynamics of tumors by near-infrared spectroscopy." *Applied Optics*, vol. 39(28) pp. 5231-5243.2000.

107. T.O. McBride, B.W. Pogue, S. Jiang, U.L. Osterberg, K.D. Paulsen, and S.P. Poplack, "Initial studies of in vivo absorbing and scattering heterogeneity in near-infrared tomographic breast imaging." *Opt. Lett.*, vol. 26(11) pp. 822-824.2001.
108. B.W. Pogue, C. Willscher, T.O. McBride, U.L. Osterberg, and K.D. Paulsen, "Contrast-detail analysis for detection and characterization with near-infrared diffuse tomography." *Medical Physics*, vol. 27(12) pp. 2693-2700.2000.
109. A. Gibson, R.M. Yusof, H. Dehghani, J. Riley, N. Everdell, R. Richards, J.C. Hebden, M. Schweiger, S.R. Arridge, and D.T. Delpy, "Optical tomography of a realistic neonatal head phantom." *Appl Opt*, vol. 42(16) pp. 3109-16.2003.
110. H.W. Engl and W. Grever, "Using the L-curve for determining optimal regularization parameters." *Numer. Math*, vol. 69 pp. 25-31.1994.
111. A. Neumaier, "Solving ill-conditioned and singular linear systems: a tutorial on regularization." *SIAM Rev.*, vol. 40(3) pp. 636-666.1998.
112. M.J. Eppstein, D.E. Dougherty, T.L. Troy, and E.M. Sevick-Muraca, "Biomedical optical tomography using dynamic parameterization and Bayesian conditioning on photon migration measurements." *Appl. Opt.*, vol. 38(10) pp. 2138-2150.1999.
113. X. Song, B.W. Pogue, T.D. Tosteson, T.O. McBride, S. Jiang, and K.D. Paulsen, "Statistical analysis of nonlinearly reconstructed near-infrared tomographic images: Part II--Experimental interpretation." *IEEE Trans Med Imaging*, vol. 21(7) pp. 764-72.2002.
114. S. Srinivasan, B.W. Pogue, S. Jiang, H. Dehghani, and K.D. Paulsen, *Validation of hemoglobin and water molar absorption spectra in near-infrared diffuse optical tomography*. Optical Tomography and Spectroscopy of Tissue V: Proceedings of SPIE,, ed. B. Chance, et al. Vol. 4955. 2003. 407-415.
115. X. Song, "Statistical analysis and evaluation of near infrared tomographic imaging system", in *Thayer School of Engineering*. 2005, Dartmouth College.
116. S. Srinivasan, Pogue, B. W., Dehghani, H., Jiang, S., Song, X. and Paulsen, K. D., "Improved quantification of small objects in near-infrared diffuse optical tomography." *Journal of Biomed Opt.*, vol. 9(6) pp. 1161-71.2004.
117. M. Schweiger and S.R. Arridge, "Optical tomographic reconstruction in a complex head model using apriori region boundary information." *Phys. Med. Biol.*, vol. 44 pp. 2703-2721.1999.

118. V. Ntziachristos, A.G. Yodh, M.D. Schnall, and B. Chance, "MRI-guided diffuse optical spectroscopy of malignant and benign breast lesions." *Neoplasia*, vol. 4(4) pp. 347-354.2002.
119. B. Brooksby, S. Jiang, H. Dehghani, B.W. Pogue, K.D. Paulsen, J. Weaver, C. Kogel, and S.P. Poplack, "Combining near infrared tomography and magnetic resonance imaging to study in vivo breast tissue: implementation of a Laplacian-type regularization to incorporate MR structure." *Journal of Biomedical Optics*, vol. submitted.2004.
120. A.H. Hielscher and S. Bartel, "Use of penalty terms in gradient-based iterative reconstruction schemes for optical tomography." *J. Biomed. Opt.*, vol. 6(2) pp. 183-192.2001.
121. V. Ntziachristos, A.G. Yodh, M. Schnall, and B. Chance, "Concurrent MRI and diffuse optical tomography of breast after indocyanine green enhancement." *Proceedings of the National Academy of Sciences of the United States of America*, vol. 97(6) pp. 2767-72.2000.
122. A.D. Klose and A.H. Hielscher, "Iterative reconstruction scheme for optical tomography based on the equation of radiative transfer." *Medical Physics*, vol. 26(8) pp. 1698-1707.1999.
123. B. Brandstatter, K. Hollaus, H. Hutten, M. Mayer, R. Merwa, and H. Scharfetter, "Direct estimation of Cole parameters in multifrequency EIT using a regularized Gauss-Newton method." *Physiol Meas*, vol. 24(2) pp. 437-48.2003.
124. Q. Fang, P.M. Meaney, S.D. Geimer, A.V. Streltsov, and K.D. Paulsen, "Microwave image reconstruction from 3-D fields coupled to 2-D parameter estimation." *IEEE Trans Med Imaging*, vol. 23(4) pp. 475-84.2004.
125. A. Corlu, T. Durduran, R. Choe, M. Schweiger, E.M. Hillman, S.R. Arridge, and A.G. Yodh, "Uniqueness and wavelength optimization in continuous-wave multispectral diffuse optical tomography." *Opt Lett*, vol. 28(23) pp. 2339-41.2003.
126. A. Li, Q. Zhang, J.P. Culver, E.L. Miller, and D.A. Boas, "Reconstructing chromosphere concentration images directly by continuous-wave diffuse optical tomography." *Opt Lett*, vol. 29(3) pp. 256-8.2004.
127. K. Levenberg, "A method for the solution of certain nonlinear problems in least squares." *Q. Appl. Math*, vol. 2 pp. 164-168.1944.

128. K.D. Paulsen, P.M. Meaney, M.J. Moskowitz, and J.M. Sullivan, "A dual mesh scheme for finite element based reconstruction algorithms." *IEEE Trans Med Imaging*, vol. 14(3) pp. 504-514.1995.
129. M. Hockel, P.Vaupel, "Tumor Hypoxia : Definitions and Current Clinical, Biologic, and Molecular Aspects." *J. Natl. Cancer Inst.*, vol. 93(4) pp. 266-276.2001.
130. S. Srinivasan, Pogue, B. W., Jiang, S., Dehghani, H. and Paulsen, K. D., "Spectrally constrained chromophore and scattering NIR tomography provides quantitative and robust reconstruction." *Appl Opt*, vol. 44(10) pp. 1858-69.2005.
131. F.F. Jobsis, "Non-invasive, infra-red monitoring of cerebral and myocardial oxygen sufficiency and circulatory parameters." *Science*, vol. 198 pp. 1264.1977.
132. S. Fantini, Walker, S. A., Franceschini, M. A., Kaschke, M., Schlag, P. M., Moesta, K. T., "Assessment of the size, position, and optical properties of breast tumors in vivo by noninvasive optical methods." *Appl. Opt.*, vol. 37(10) pp. 1982-89.1998.
133. V. Chernomordik, D.W. Hattery, D. Grosenick, H. Wabnitz, H. Rinneberg, K.T. Moesta, P.M. Schlag, and A. Gandjbakhche, "Quantification of optical properties of a breast tumor using random walk theory." *Journal of Biomed Opt*, vol. 7(1) pp. 80-87.2002.
134. M.S. Patterson, Wilson, B. C., Wyman, D. R., "The propagation of optical radiation in tissue: I. Models of radiation transport and their application." *Lasers Med. Sci.*, vol. 6 pp. 155-168.1992.
135. S.P. Poplack, K.D. Paulsen, A. Hartov, P.M. Meaney, B.W. Pogue, T.D. Tosteson, M.R. Grove, S.K. Soho, and W.A. Wells, "Electromagnetic breast imaging: average tissue property values in women with negative clinical findings." *Radiology*, vol. 231(2) pp. 571-80.2004.
136. D. Grosenick, K.T. Moesta, H. Wabnitz, J. Mucke, C. Stroszczyński, R. Macdonald, P.M. Schlag, and H. Rinneberg, "Time-domain optical mammography: initial clinical results on detection and characterization of breast tumors." *Appl Opt*, vol. 42(16) pp. 3170-86.2003.
137. D.R. White and H.Q. Woodard, "Average soft-tissue and bone models for use in radiation dosimetry." *Br. J. Radiol.*, vol. 60 pp. 907-13.1987.
138. T.O. McBride, B.W. Pogue, S. Jiang, U.L. Osterberg, K.D. Paulsen, and S.P. Poplack, "Multi-spectral near-infrared tomography: a case study in compensating for

- water and lipid content in hemoglobin imaging of the breast." *J. Biomed. Opt.*, vol. 7 pp. 72-79.2002.
139. D.B. Jakubowski, A.E. Cerussi, F. Bevilacqua, N. Shah, D. Hsiang, J. Butler, and B.J. Tromberg, "Monitoring neoadjuvant chemotherapy in breast cancer using quantitative diffuse optical spectroscopy: a case study." *J Biomed Opt*, vol. 9(1) pp. 230-8.2004.
 140. X. Intes, J. Ripoll, Y. Chen, S. Nioka, A.G. Yodh, and B. Chance, "In vivo continuous-wave optical breast imaging enhanced with Indocyanine Green." *Med. Phys.*, vol. 30(6) pp. 1039-47.2003.
 141. M.A. Franceschini, K.T. Moesta, S. Fantini, G. Gaida, E. Gratton, H. Jess, W.W. Mantulin, M. Seeber, P.M. Schlag, and M. Kaschke, "Frequency-domain techniques enhance optical mammography: initial clinical results.." *Proc. Nat. Acad. Sci USA*, vol. 94(12) pp. 6468-73.1997.
 142. X. Gu, Q. Zhang, M. Bartlett, L. Schutz, L.L. Fajardo, and H. Jiang, "Differentiation of cysts from solid tumors in the breast with diffuse optical tomography." *Acad. Radiology*, vol. 11(1) pp. 53-60.2004.
 143. A. Corlu, R. Choe, T. Durduran, K. Lee, M. Schweiger, S.R. Arridge, E.M. Hillman, and A.G. Yodh, "Diffuse optical tomography with spectral constraints and wavelength optimization." *Appl Opt*, vol. 44(11) pp. 2082-2093.2005.
 144. P. Okunieff, M.Hoeckel, E. P. Dunphy, K. Schlenger, C. Knoop and P. Vaupel, "Oxygen Tension Distributions are Sufficient to Explain the Local Response of Human Breast Tumors Treated with Radiation alone." *Int. J. Radiation Oncology Biol. Phys.*, vol. 26 pp. 631-636.1993.
 145. D.M. Brizel, Scully S.P., Harrelson J.M., Layfield L.J., Bean J.M., Prosnitz L.R. and Dewhirst M.W., "Tumor Oxygenation Predicts for the Likelihood of Distant Metastases in Human Soft Tissue Sarcoma." *Cancer Research*, vol. 56 pp. 941-943.1996.
 146. P. Vaupel, A. Mayer, S. Briest, and M. Hockel, "Oxygenation gain factor: a novel parameter characterizing the association between hemoglobin level and the oxygenation status of breast cancers." *Cancer Research*, vol. 63 pp. 7634-7637.2003.
 147. D.L. Conover, B.M. Fenton, T.H. Foster, and E.L. Hull, "An evaluation of near infrared spectroscopy and cryospectrophotometry estimates of haemoglobin oxygen

- saturation in a rodent mammary tumour model." *Physics in Medicine & Biology*, vol. 45(9) pp. 2685-700.2000.
148. E. Heffer, V. Pera, O. Schutz, H. Siebold, and S. Fantini, "Near-infrared imaging of the human breast: complementing hemoglobin concentration maps with oxygenation images." *Journal of Biomed Opt.*, vol. 9(6) pp. 1152-60.2004.
 149. B.S. Kuszyk, F.M. Corl, F.N. Franano, D.A. Bluemke, L.V. Hofmann, B.J. Fortman, and E.K. Fishman, "Tumor transport physiology: implications for imaging and image-guided therapy." *AJR*, vol. 177 pp. 747-753.2001.
 150. N. Shah, A. Cerussi, D. Jakubowski, D. Hsiang, J. Butler, and B. Tromberg, "The role of diffuse optical spectroscopy in the clinical management of breast cancer." *Disease Markers*, vol. 19 pp. 95-105.2003-2004.
 151. "Breast imaging reporting and data system (BIRADS™)". 1998, Reston[VA]: American College of Radiology.
 152. W.A. Wells, C.P. Daghlian, T.D. Tosteson, M.R. Grove, S.P. Poplack, S. Soho, and K.D. Paulsen, "Analysis of the microvasculature and tissue type ratios in benign and malignant breast tissue." *Analytical and Quantitative Cytology and Histology*, vol. 26 pp. 166-174.2004.
 153. S. Srinivasan, B.W. Pogue, S. Jiang, H. Dehghani, and K.D. Paulsen, "Spectrally constrained NIR tomography for breast imaging: simulations and clinical results." *Proc. SPIE*, vol. 2005(Photonics West).2005.
 154. B.A. Brooksby, S. Jiang, H. Dehghani, C. Kogel, M. Doyley, J.B. Weaver, S.P. Poplack, B.W. Pogue, and K.D. Paulsen, "Magnetic resonance-guided near-infrared tomography of the breast." *Review of Scientific Instruments*, vol. 75(12).2004.
 155. X. Intes, C. Maloux, M. Guven, B. Yazici, and B. Chance, "Diffuse optical tomography with physiological and spatial *a priori* constraints." *Phys Med Biol*, vol. 49 pp. N155-N162.2004.
 156. A. Li, G. Boverman, Y. Zhang, D. Brooks, E.L. Miller, M.E. Kilmer, Q. Zhang, E.M. Hillman, and D.A. Boas, "Optimal linear inverse solution with multiple priors in diffuse optical tomography." *Appl Opt*, vol. 44(10) pp. 1948-1956.2005.
 157. B. Brooksby, "Combining near infrared tomography and magnetic resonance imaging to improve breast tissue chromophore and scattering assessment", in *Thayer School of Engineering*. 2005, Dartmouth College.

158. C.S. Potten, R.J. Watson, G.T. Williams, S. Tickle, S.A. Roberts, M. Harris, and A. Howell, "The effect of age and menstrual cycle upon the proliferative activity of the normal human breast." *Br J Cancer*, vol. 58 pp. 163-170.1988.
159. C. Li and H. Jiang, "Measurement of particle-size distribution and concentration in heterogeneous turbid media with multi-spectral diffuse optical tomography." *Appl Opt*, vol. 44(10) pp. 1838-44.2005.

Tutorial Program

```
%%tutorial illustrating use of spectral reconstruction tool box
%% Subha 3/14/05
patid = input('enter a patid for this simulation/reconstruction');
LR = input('save as left or right breast? (left/right)');
plane = input('which plane?');
rep = input('which repetition number?');
%%wvs to be used:
wv_array = [661; 761; 785; 808; 826; 849];

yy = input('need to generate data? 1 for yes/0 for no');
if (yy == 1)
    mesh = load_mesh('circle2000_86');

    %%add a blob with diff conc, using command below: allows b/g conc to be given
    %%and resulting conc and scatter to be stored in file specified
    %% file for extinction coeff (contains wvs in first coln) has to be given as well as wvs
    %%the absorption coeff corresponding to conc, are also stored in a temp
    %%file
    [mesh] = add_conc_heter(mesh,'temp_store','excoeff.dat',wv_array);
    %%the conc are automatically stored in 'temp_store_hb1.paa', 'temp_store_hb2.paa' etc

    %% to generate forward data using above conc; the filenames to store the data, are automatically
    created, given a patient id,
    %% left or right side, plane and rep; this is so that it is consistent with clinical data
    forward_chromo('temp_store','circle2000_86',patid,LR,plane,rep,'excoeff.dat',wv_array);
    %% the first input is for conc, second input for mesh on which data is generated; rest are patid,
    side, plane and rep;
    %%followed by extinction coeff file and wvs at which data is generated
    %% if patid = 'heter', the data has now been stored in 'patheter_left_661nm_plane0_rep1.paa' etc

    %% for calibrating the data, if it has noise or is clinical data; you need a homogeneous phantom
    data set.
    %% if simulated data is used, generate data by similar method above, for homogeneous
    concentrations and scatter
    p = input('generate homogeneous data also? 1 for yes, 0 for no');
    if (p==1)
        %% for homog conc, don't add blob, just run the subroutine and input 0 when asked if blob to
        be added
        [mesh] = add_conc_heter(mesh,'homo_temp');
        forward_chromo('homo_temp','circle2000_86',patid,'phantom',0,rep,'excoeff.dat',wv_array);
        end
    end

    %% generating filenames to store calibrated data; for all the wvs

yy_1 = input('need to calibrate data? 1 for yes/0 for no');
if (yy_1 == 1)
    %%generating filenames for the data
```

```

    for i = 1:length(wv_array)
        data_anom(i,:) =
strcat('pat',patid,'_',LR,'_',num2str(wv_array(i)), 'nm_plane',num2str(plane),'_rep',num2str(rep),'.paa');
        data_ph(i,:) =
strcat('pat',patid,'_phantom_',num2str(wv_array(i)), 'nm_plane0_rep',num2str(rep),'.paa');
        mesh_cal(i,:) =
strcat('circle_',patid,'_',LR,'_',num2str(wv_array(i)), 'nm_plane',num2str(plane),'_rep',num2str(rep));
        data_cal(i,:) = strcat('pat',
patid,'_',LR,'_',num2str(wv_array(i)), 'nm_plane',num2str(plane),'_rep',num2str(rep),'.cal');
    end
    fconc = strcat('pat',patid,'_',LR,'_plane',num2str(plane),'_rep',num2str(rep));

    %%calibrating each wavelength
    for i = 1:length(wv_array)

newcaliberate(data_ph(i,:),data_anom(i:),'circle2000_86','circle2000_86',mesh_cal(i,:),data_cal(i,:));
    end
    %%spectral fit: %%the next statement stores the initial guesses for conc
    %%and scatter in appropriate files, to be used by the reconstruction below
    cal_spectral(patid,LR,plane,rep,fconc,wv_array,'excoeff.dat');
end

```

```

[mesh1,pj_error] =
recon_spectral('circle2000_86','circle400_86',100,patid,LR,plane,rep,'excoeff.dat',wv_array,20,10,1);
%%above command does the reconstruction and has a log file containing the details in
'heter_left_plane0_rep1_spectral.log'
%%the solutions for conc and scatter are stored for each iteration in
%%'heter_left_hbT_plane0_rep1.sol' etc; the final iteration values are also stored separately in
'heter_left_hbT_plane0_rep1_final.dat'
[hbt,oxysat,wat,sa,sp]=read_spectral_clinical(mesh,patid,LR,plane,rep,0);
%% giving iteration as 0 plots the final iteration solution

```

Clinical Reconstruction Program

```

function clinical_recon(patid,LR,plane,rep,fexcoeff,wv_array,dia);
%%single program to calibrate and reconstruct patient data
%%patid is patient id, eg: '1097', LR is 'left' or 'right'
%%plane is plane no. eg: 1, rep is rep no. eg: 0
%%fexcoeff is extinction file, which has wavelengths in first column
%%wv_array is wavelengths in nm, and dia is patient diameter.

%generate meshes
if (dia ~ =86)
    mesh_dia(dia,2000);
    mesh_dia(dia,400);
end
mesh1_fn = strcat('circle2000_',num2str(dia));
mesh2_fn = strcat('circle400_',num2str(dia));
%%filenames for calibration
for i = 1:length(wv_array)

```

```

    data_anom(i,:) =
strcat('pat',patid,'_',LR,'_',num2str(wv_array(i)), 'nm_plane',num2str(plane),'_rep',num2str(rep),'.paa');
    data_ph(i,:) =
strcat('pat',patid,'_phantom_',num2str(wv_array(i)), 'nm_plane0_rep',num2str(rep),'.paa');
    %data_ph(i,:) = strcat('pat',patid,'_phantom_',num2str(wv_array(i)), 'nm_plane0_rep0.paa');
    mesh_cal(i,:) =
strcat('clinical/',patid,'/circle_',patid,'_',LR,'_',num2str(wv_array(i)), 'nm_plane',num2str(plane),'_rep',
num2str(rep));
    data_cal(i,:) =
strcat('clinical/',patid,'/pat',patid,'_',LR,'_',num2str(wv_array(i)), 'nm_plane',num2str(plane),'_rep',nu
m2str(rep),'.cal');
end
fconc = strcat('clinical/',patid,'/pat',patid,'_',LR,'_plane',num2str(plane),'_rep',num2str(rep));

%%calibrating each wavelength
for i = 1:length(wv_array)
    newcaliberate(data_ph(i,:),data_anom(i,:),mesh1_fn,'circle2000_86',mesh_cal(i,:),data_cal(i,:));
end
%%spectral fit
cal_spectral(patid,LR,plane,rep,fconc,wv_array,fexcoeff);

%%reconstruction
[mesh1,pj_error] =
recon_spectral(mesh1_fn,mesh2_fn,100,patid,LR,plane,rep,fexcoeff,wv_array,15,10,1);

```

Reconstruction Program

```

function [mesh1,pj_error] =
recon_spectral(fwd_fn,recon_basis,frequency,patid,LR,plane,rep,fexcoeff,wv_array,iteration,lambda,f
ilter_n)
%%spectrally constrained reconstruction, Subha 2004
%%fwd_fn is the forward mesh name, recon_basis is second mesh basis,
%%patid gives patient id, eg: '1097', LR is 'left' or 'right'
%%plane is plane no. eg: 1, rep is rep no. eg: 0
%%fexcoeff is extinction coeff files, it has wavelength in first column, eg: 'excoeff.dat'
%%wv_array is all the wavelengths to be used, iteration is max iteration; recon. stops when proj
error<2%, or when
%%max iteration is reached, lambda is regularization parameter, eg 10 and filter_n is for mean filter,
usually 1.
%%Subha Modified vsn for clinical, 11/14/04
tic

%%nc : number of absorbing chromophores (scattering separate); nwn = number of wavelengths
nc = 3;
nwn = length(wv_array);

% if patid ~=char
%   patid = num2str(patid)
% end

%%generating filenames for obtaining initial guesses for conc./data at 6 wavelengths

```

```

fdata_bg = strcat('pat',patid,'_',LR);
fdata_end = strcat('_plane',num2str(plane),'_rep',num2str(rep));
[fc,fsa,fsp,fname,data_wv] = gen_filenames(fdata_bg,fdata_end,wv_array);
%%wavelength in micrometers.
wv_act = wv_array./1000;

%%filenames for storing solutions
output_fn = strcat('pat',patid,'_',LR,'_plane',num2str(plane),'_rep',num2str(rep),'_spectral');
conc_nim(1,:) = strcat('pat',patid,'_',LR,'_hb1_plane',num2str(plane),'_rep',num2str(rep),'.sol');
conc_nim(2,:) = strcat('pat',patid,'_',LR,'_hb2_plane',num2str(plane),'_rep',num2str(rep),'.sol');
conc_nim(3,:) = strcat('pat',patid,'_',LR,'_wat_plane',num2str(plane),'_rep',num2str(rep),'.sol');

hbt_nim = strcat('pat',patid,'_',LR,'_hbT_plane',num2str(plane),'_rep',num2str(rep),'.sol');
oxy_nim = strcat('pat',patid,'_',LR,'_StO_plane',num2str(plane),'_rep',num2str(rep),'.sol');
sa_nim = strcat('pat',patid,'_',LR,'_SCa_plane',num2str(plane),'_rep',num2str(rep),'.sol');
sp_nim = strcat('pat',patid,'_',LR,'_SCP_plane',num2str(plane),'_rep',num2str(rep),'.sol');

%reading concentration and scattering initial guesses from filenames above
mesh1 = load_mesh(fwd_fn);
conc_fine(1:length(mesh1.nodes),1) = load(fc(1,:));
conc_fine((length(mesh1.nodes) + 1): 2*length(mesh1.nodes),1) = load(fc(2,:));
conc_fine((2*length(mesh1.nodes) + 1): 3*length(mesh1.nodes),1) = load(fc(3,:));
sa_fine = load(fsa);
sp_fine = load(fsp);

%%Calculating extinction coefficient matrix, and initial guess for absorption
ee = load(fexcoeff);
E = [];
for ww = 1:nwn
    jj = find (ee(:,1)==wv_array(ww));
    E = [E;ee(jj,2:end)];
end

%E = load(fexcoeff);
for ii = 1:length(mesh1.nodes)
    mua_big(:,ii) =
E*[conc_fine(ii);conc_fine(ii+length(mesh1.nodes));conc_fine(ii+2*length(mesh1.nodes))];
end
mua_big = reshape(mua_big', length(mesh1.nodes)*nwn,1);

%%storing initial guess for mua and mus' in fine mesh for each wavelength
kappa_big = [];
for ww = 1 : nwn
    mesh1 = load_mesh(fwd_fn);
    mesh1.mua(:) = mua_big(((ww-1)*length(mesh1.nodes) + 1):ww*length(mesh1.nodes));
    mesh1.mus(:) = sa_fine.*wv_act(ww).^(-sp_fine);
    mesh1.kappa = 1./(3*(mesh1.mus + mesh1.mua));
    save_mesh(mesh1,fname(ww,:));
    kappa_big = [kappa_big;mesh1.kappa];
end

```

```

%% initializing projection error
pj_error = [];

% Initiate log file
fid_log = fopen([output_fn '.log'],'w');
fprintf(fid_log,'Forward Mesh = %s\n',fwd_fn);
fprintf(fid_log,'Second Mesh = %s\n',recon_basis);
fprintf(fid_log,'Frequency = %f MHz\n',frequency);
for ww = 1:nwn
    fprintf(fid_log,'Data at %d nm = %s\n',ww_array(ww), data_wv(ww,:));
end
fprintf(fid_log,'Initial Guess files = %s\n',fc(1,:));
fprintf(fid_log,'          = %s\n',fc(2,:));
fprintf(fid_log,'          = %s\n',fc(3,:));
fprintf(fid_log,'          = %s\n',fsa);
fprintf(fid_log,'          = %s\n',fsp);
fprintf(fid_log,'Initial Reg = %d\n',lambda);
fprintf(fid_log,'Filter = %d\n',filter_n);
fprintf(fid_log,'Output Files HbT = %s\n',hbt_nim);
fprintf(fid_log,'          Oxsyat = %s\n',oxy_nim);

fprintf(fid_log,'          Wat = %s\n',conc_nim(3,:));
fprintf(fid_log,'          Scatt ampl = %s\n',sa_nim);
fprintf(fid_log,'          Scatt Power = %s\n',sp_nim);

for it = 1:iteration

    %% interpolation of conc on coarse mesh
    mesh1 = load_mesh(fwd_fn);
    mesh2 = load_mesh(recon_basis);
    disp('calculating basis for dual mesh');
    if ischar(recon_basis)
        mesh2 = load_mesh(recon_basis);
        [mesh1.fine2coarse,mesh2.coarse2fine] = second_mesh_basis(mesh1,mesh2);
    else
        [mesh1.fine2coarse,mesh2] = pixel_basis(recon_basis,mesh1);
    end

    [conc,sa,sp] = interp2coarse(mesh1,mesh2,conc_fine,sa_fine,sp_fine);

    %% computing new Jacobian and ref data from each wavelength data
    [J,ref_big] = jacobian_spectral(fname,recon_basis,E,nwn,frequency,wv_act,sp);
    %% calculating anom data for six wavelengths
    anom_big = [];
    for ww = 1:nwn

        %% read data
        %% removing nearest S-D positions for all wvs data

```

```

%   if (ww==1)
%       [nlr,nlc] = size(mesh1.link);
%       dat_size = reshape(mesh1.link',nlr*nlc,1);
%       jnodes = find(dat_size(:)==0);
%   end
%
%   clear dat_size nlr nlc;
anom = load(data_wv(ww,:));
%anom(jnodes,:)=[];
anom(:,1) = log(anom(:,1));
anom(:,2) = anom(:,2)/180.0*pi;
anom(find(anom(:,2)<0),2) = anom(find(anom(:,2)<0),2) + (2*pi);
anom(find(anom(:,2)>(2*pi)),2) = anom(find(anom(:,2)>(2*pi)),2) - (2*pi);
anom = reshape(anom',length(anom)*2,1);

anom_big = [anom_big;anom];
clear anom;
end
data_big = [anom_big - ref_big];

pj_error = [pj_error sum(data_big.^2)];

disp('-----');
disp(['Iteration Number      = ' num2str(it)]);
disp(['Projection error      = ' num2str(pj_error(end))]);

fprintf(fid_log,'-----\n');
fprintf(fid_log,'Iteration Number      = %d\n',it);
fprintf(fid_log,'Projection error      = %f\n',pj_error(end));

if it ~= 1
p = (pj_error(end-1)-pj_error(end))*100/pj_error(end-1);
disp(['Projection error change = ' num2str(p) '%']);
fprintf(fid_log,'Projection error change = %f%%\n',p);
if (p) <= 2
disp('-----');
disp('STOPPING CRITERIA REACHED');
fprintf(fid_log,'-----\n');
fprintf(fid_log,'STOPPING CRITERIA REACHED\n');
break
end
end

%%% to normalize Jacobian w.r.t different SI units
N = [conc; sa; sp];
J = J*diag(N);

%calculating data difference

data_diff = J*data_big;

```

```

%%% build hessian
disp('Building Hessian');
[nrow,ncol]=size(J);
Hess = zeros(ncol);
Hess = J'*J;

clear J
%% Add regularization
if it ~= 1
    if ((sum(data_big.^2) < pj_error(end-1)))
        lambda = lambda./10^0.25;
    else
        lambda = lambda.*10^0.125;
    end
end
clear data_big;

reg = lambda*max(diag(Hess));
disp(['Regularization          = ' num2str(reg)]);
fprintf(fid_log,'Regularization          = %f\n',reg);
Hess = Hess+(eye(ncol).*reg);

disp('calculating concentrations and scattering');

foo = Hess\data_diff;

foo = foo.*N;

%%%update in values
for i = 1 : nc*length(mesh2.nodes)
    conc(i) = conc(i) + foo(i);
end
for i = (nc*length(mesh2.nodes) +1): ((nc+1)*length(mesh2.nodes))
    sa(i - nc*length(mesh2.nodes)) = sa(i - nc*length(mesh2.nodes)) + foo(i);
end
for i = ((nc+1)*length(mesh2.nodes) +1): ((nc+2)*length(mesh2.nodes))
    sp(i - (nc+1)*length(mesh2.nodes)) = sp(i - (nc+1)*length(mesh2.nodes)) + foo(i);
end
clear foo;

%%% constraining water to be less than 100%, sa and sp <3.0
[conc,sa,sp] = constrain_val(mesh2,conc,sa,sp);

%%%converting back to fine mesh
[conc_fine, sa_fine, sp_fine] = interp2fine(mesh1,mesh2,conc,sa,sp);

%%%filtering
disp('Filtering');
if (filter_n ~= 0)
    [conc_fine,sa_fine,sp_fine] = mean_filter_conc(mesh1,conc_fine,sa_fine,sp_fine,filter_n);
end

```

```

%% computing absorption and scatter coeff for each wavelength
clear mua_big;
for ii = 1:length(mesh1.nodes)
    mua_big(:,ii) =
E*[conc_fine(ii);conc_fine(ii+length(mesh1.nodes));conc_fine(ii+2*length(mesh1.nodes))];
end
mua_big = reshape(mua_big', length(mesh1.nodes)*nwn,1);
% mua_big = E_big*conc_fine;

for ww = 1 : nwn
    mesh1 = load_mesh(fname(ww,:));
    mesh1.mua(:) = mua_big(((ww-1)*length(mesh1.nodes) + 1):ww*length(mesh1.nodes));
    mesh1.mus = sa_fine.*wv_act(ww).^(-sp_fine);
    mesh1.kappa = 1./(3*(mesh1.mus + mesh1.mua));
    save_mesh(mesh1,fname(ww,:));
end
%%writes in coarse meshes
disp('writing files out...');
hbt(:,1) = (conc(1:length(mesh2.nodes)) + conc(length(mesh2.nodes)+1 :
2*length(mesh2.nodes))).*1000;
oxy(:,1) = ((conc(1:length(mesh2.nodes)).*1000)./hbt)*100;

for cc = 1:nc
    if (it==1)
        fid = fopen(conc_nim(cc,),'w');
    else
        fid = fopen(conc_nim(cc,),'a');
    end
    fprintf(fid,'solution %d ',it);
    fprintf(fid,'-size=%g ',length(mesh2.nodes));
    fprintf(fid,'-components=1 ');
    fprintf(fid,'-type=nodal\n');
    %%storing water as percent instead of fraction
    if (cc~=3)
        fprintf(fid,'%f ',conc(((cc-1)*length(mesh2.nodes) + 1) : cc*length(mesh2.nodes)));
    else
        fprintf(fid,'%f ',conc(((cc-1)*length(mesh2.nodes) + 1) : cc*length(mesh2.nodes)).*100);
    end
    fprintf(fid,'\n');
    fclose(fid);
end

if (it==1)
    fid = fopen(hbt_nim,'w');
else
    fid = fopen(hbt_nim,'a');
end
fprintf(fid,'solution %d ',it);
fprintf(fid,'-size=%g ',length(mesh2.nodes));
fprintf(fid,'-components=1 ');
fprintf(fid,'-type=nodal\n');
fprintf(fid,'%f ',hbt);

```

```

fprintf(fid,'\n');
fclose(fid);

if (it==1)
    fid = fopen(oxy_nim,'w');
else
    fid = fopen(oxy_nim,'a');
end
fprintf(fid,'solution %d ',it);
fprintf(fid,'-size=%g ',length(mesh2.nodes));
fprintf(fid,'-components=1 ');
fprintf(fid,'-type=nodal\n');
fprintf(fid,'%f ',oxy);
fprintf(fid,'\n');
fclose(fid);

if (it==1)
    fid = fopen(sa_nim,'w');
else
    fid = fopen(sa_nim,'a');
end
fprintf(fid,'solution %d ',it);
fprintf(fid,'-size=%g ',length(mesh2.nodes));
fprintf(fid,'-components=1 ');
fprintf(fid,'-type=nodal\n');
fprintf(fid,'%f ',sa);
fprintf(fid,'\n');
fclose(fid);

if (it==1)
    fid = fopen(sp_nim,'w');
else
    fid = fopen(sp_nim,'a');
end
fprintf(fid,'solution %d ',it);
fprintf(fid,'-size=%g ',length(mesh2.nodes));
fprintf(fid,'-components=1 ');
fprintf(fid,'-type=nodal\n');
fprintf(fid,'%f ',sp);
fprintf(fid,'\n');
fclose(fid);

end
%%storing only last iteration values in separate files
clear hbt_nim oxy_nim sa_nim sp_nim

wat_nim = strcat('pat',patid,'_',LR,'_wat_plane',num2str(plane),'_rep',num2str(rep),'_final.dat');
hbt_nim = strcat('pat',patid,'_',LR,'_hbt_plane',num2str(plane),'_rep',num2str(rep),'_final.dat');
oxy_nim = strcat('pat',patid,'_',LR,'_StO_plane',num2str(plane),'_rep',num2str(rep),'_final.dat');
sa_nim = strcat('pat',patid,'_',LR,'_SCa_plane',num2str(plane),'_rep',num2str(rep),'_final.dat');
sp_nim = strcat('pat',patid,'_',LR,'_SCP_plane',num2str(plane),'_rep',num2str(rep),'_final.dat');

```

```

fid = fopen(hbt_nim,'w');
fprintf(fid,'%f',hbt);
fprintf(fid,'\n');
fclose(fid);

fid = fopen(oxy_nim,'w');
fprintf(fid,'%f',oxy);
fprintf(fid,'\n');
fclose(fid);

fid = fopen(wat_nim,'w');
%%storing water as percent instead of fraction
fprintf(fid,'%f',conc((2*length(mesh2.nodes) + 1) : 3*length(mesh2.nodes)).*100);
fprintf(fid,'\n');
fclose(fid);

fid = fopen(sa_nim,'w');
fprintf(fid,'%f',sa);
fprintf(fid,'\n');
fclose(fid);

fid = fopen(sp_nim,'w');
fprintf(fid,'%f',sp);
fprintf(fid,'\n');
fclose(fid);

% close log file!
time = toc;
fprintf(fid_log,'Computation TimeRegularization = %f\n',time);
fclose(fid_log);

```

```

function [conc,sa,sp] = interp2coarse(mesh1,mesh2,conc_fine,sa_fine,sp_fine)
cc1_fine = conc_fine(1:length(mesh1.nodes));
cc2_fine = conc_fine((length(mesh1.nodes) + 1):2*length(mesh1.nodes));
cc3_fine = conc_fine((2*length(mesh1.nodes) + 1):3*length(mesh1.nodes));
for i = 1:length(mesh2.nodes)
    if mesh1.fine2coarse(i,1) ~= 0
        cc1(i,1) = (mesh1.fine2coarse(i,2:end) * ...
            cc1_fine(mesh1.elements(mesh1.fine2coarse(i,1),:)));
        cc2(i,1) = (mesh1.fine2coarse(i,2:end) * ...
            cc2_fine(mesh1.elements(mesh1.fine2coarse(i,1),:)));
        cc3(i,1) = (mesh1.fine2coarse(i,2:end) * ...
            cc3_fine(mesh1.elements(mesh1.fine2coarse(i,1),:)));
        sa(i,1) = (mesh1.fine2coarse(i,2:end) * ...
            sa_fine(mesh1.elements(mesh1.fine2coarse(i,1),:)));
        sp(i,1) = (mesh1.fine2coarse(i,2:end) * ...
            sp_fine(mesh1.elements(mesh1.fine2coarse(i,1),:)));
    elseif mesh1.fine2coarse(i,1) == 0
        dist = distance(mesh1.nodes,...

```

```

        mesh1.bndvtx,...
        [mesh2.nodes(i,1:2) 0]);
mindist = find(dist==min(dist));
mindist = mindist(1);
cc1(i,1) = cc1_fine(mindist);
cc2(i,1) = cc2_fine(mindist);
cc3(i,1) = cc3_fine(mindist);
sa(i,1) = sa_fine(mindist);
sp(i,1) = sp_fine(mindist);
    end
end
conc = [cc1;cc2;cc3];

```

```

function [conc_fine,sa_fine,sp_fine] = interp2fine(mesh1,mesh2,conc,sa,sp)
cc1 = conc(1:length(mesh2.nodes));
cc2 = conc((length(mesh2.nodes) + 1):2*length(mesh2.nodes));
cc3 = conc((2*length(mesh2.nodes) + 1):3*length(mesh2.nodes));
for i = 1:length(mesh1.nodes)
    cc1_fine(i,1) = (mesh2.coarse2fine(i,2:end) * ...
        cc1(mesh2.elements(mesh2.coarse2fine(i,1),:)));
    cc2_fine(i,1) = (mesh2.coarse2fine(i,2:end) * ...
        cc2(mesh2.elements(mesh2.coarse2fine(i,1),:)));
    cc3_fine(i,1) = (mesh2.coarse2fine(i,2:end) * ...
        cc3(mesh2.elements(mesh2.coarse2fine(i,1),:)));
    sa_fine(i,1) = (mesh2.coarse2fine(i,2:end) * ...
        sa(mesh2.elements(mesh2.coarse2fine(i,1),:)));
    sp_fine(i,1) = (mesh2.coarse2fine(i,2:end) * ...
        sp(mesh2.elements(mesh2.coarse2fine(i,1),:)));
end
conc_fine = [cc1_fine;cc2_fine;cc3_fine];

```

```

function [fc,fsa,fsp,fname,data_wv] = gen_filenames(fdata_bg,fdata_end,wv_array);
nwn = length(wv_array);
str1 = strcat(fdata_bg,fdata_end,'_hb1.cal');
str2 = strcat(fdata_bg,fdata_end,'_hb2.cal');
str3 = strcat(fdata_bg,fdata_end,'_wat.cal');
fc = [str1;str2;str3];
clear str1 str2 str3;
fsa = strcat(fdata_bg,fdata_end,'_sa.cal');
fsp = strcat(fdata_bg,fdata_end,'_sp.cal');

for i = 1:nwn
    fname(i,:) = strcat('circle_temp_',num2str(wv_array(i)));
    data_wv(i,:) = strcat(fdata_bg,'_',num2str(wv_array(i)),'nm',fdata_end,'.cal');
end

```

```

function [conc,sa,sp] = constrain_val(mesh2,conc,sa,sp);
jj = find(conc((2*length(mesh2.nodes) + 1):3*length(mesh2.nodes)) > 1.0);
conc(jj+2*length(mesh2.nodes)) = 1.0;
clear jj;
jj = find(conc((2*length(mesh2.nodes) + 1):3*length(mesh2.nodes)) < 0.0);

```

```

conc(jj+2*length(mesh2.nodes)) = 0.0;
clear jj;
%%constraining scatt ampl
jj = find(sa > 3.0);
sa(jj) = 3.0;
clear jj;
jj = find(sa < 0);
sa(jj) = 0;
clear jj;
%%constraining scatt power
jj = find(sp > 3.0);
sp(jj) = 3.0;
clear jj;
jj = find(sp < 0.);
sp(jj) = 0.;
clear jj;

```

Jacobian Function

```

function [J,ref_big] = jacobian_spectral(fname,recon_basis,E,nwn,frequency,vw_act,sp);
J_big = [];
J_big_sa = [];
J_big_sp = [];
ref_big = [];
[junk,nc] = size(E);
for ww = 1:nwn
    disp('Loading mesh1');
    mesh1 = load_mesh(fname(ww,:));
    disp('Loading mesh2');
    if ischar(recon_basis)
        mesh2 = load_mesh(recon_basis);
        [mesh1.fine2coarse,mesh2.coarse2fine] = second_mesh_basis(mesh1,mesh2);
    else
        [mesh1.fine2coarse,mesh2] = pixel_basis(recon_basis,mesh1);
    end

    %%calculating jacobian for absorption and scatter
    [Jwhole,data1]=jacobian(fname(ww,:),frequency,mesh1);
    % map jacobian onto coarse mesh
    [J,mesh2] = interpolatef2r(mesh1,mesh2,Jwhole.complete);

    J_mua(:,:) = J(:,length(mesh2.nodes)+1 : end);
    J_kappa(:,:) = J(:,1:length(mesh2.nodes));
    if (nc==4)
        J_big = [J_big;E(ww,1).*J_mua,E(ww,2).*J_mua,E(ww,3).*J_mua,E(ww,4).*J_mua ];
    else
        J_big = [J_big;E(ww,1).*J_mua,E(ww,2).*J_mua,E(ww,3).*J_mua];
    end
    J_big_sa = [J_big_sa;J_kappa*diag(-3*(mesh2.kappa.^2).*(vw_act(ww).^(-sp)))]];
    J_big_sp = [J_big_sp;J_kappa*diag((-3*(mesh2.kappa.^2).*(mesh2.mus)).*(-log(vw_act(ww))))];
    clear Jwhole JJ J_mua J_kappa;

```

```

ref(:,1) = log(data1.amplitude);
ref(:,2) = data1.phase;
ref(:,2) = ref(:,2)/180.0*pi;
ref(find(ref(:,2)<0),2) = ref(find(ref(:,2)<0),2) + (2*pi);
ref(find(ref(:,2)>(2*pi)),2) = ref(find(ref(:,2)>(2*pi)),2) - (2*pi);
ref = reshape(ref,length(ref)*2,1);
ref_big = [ref_big; ref];
clear ref;
end

%%building new big jacobian for conc/scatter
J = [J_big,J_big_sa,J_big_sp];
clear J_big J_big_sa J_big_sp;

function [val_int,recon_mesh] = interpolatef2r(fwd_mesh,recon_mesh,val)

% This function interpolates fwd_mesh into recon_mesh
% For the Jacobian it is an integration!
NNC = size(recon_mesh.nodes,1);
NNF = size(fwd_mesh.nodes,1);
NROW = size(val,1);
val_int = zeros(NROW,NNC*2);

for i = 1 : NNF
    if recon_mesh.coarse2fine(i,1) ~= 0
        val_int(:,recon_mesh.elements(recon_mesh.coarse2fine(i,1),:)) = ...
            val_int(:,recon_mesh.elements(recon_mesh.coarse2fine(i,1),:)) + ...
            val(:,i)*recon_mesh.coarse2fine(i,2:end);
        val_int(:,recon_mesh.elements(recon_mesh.coarse2fine(i,1),:)+NNC) = ...
            val_int(:,recon_mesh.elements(recon_mesh.coarse2fine(i,1),:)+NNC) + ...
            val(:,i+NNF)*recon_mesh.coarse2fine(i,2:end);
    elseif recon_mesh.coarse2fine(i,1) == 0
        dist = distance(fwd_mesh.nodes,fwd_mesh.bndvtx,recon_mesh.nodes(i,:));
        mindist = find(dist==min(dist));
        mindist = mindist(1);
        val_int(:,i) = val(:,mindist);
        val_int(:,i+NNC) = val(:,mindist+NNF);
    end
end

for i = 1 : NNC
    if fwd_mesh.fine2coarse(i,1) ~= 0
        recon_mesh.mua(i,1) = (fwd_mesh.fine2coarse(i,2:end) * ...
            fwd_mesh.mua(fwd_mesh.elements(fwd_mesh.fine2coarse(i,1),:)));
        recon_mesh.mus(i,1) = (fwd_mesh.fine2coarse(i,2:end) * ...
            fwd_mesh.mus(fwd_mesh.elements(fwd_mesh.fine2coarse(i,1),:)));
        recon_mesh.kappa(i,1) = (fwd_mesh.fine2coarse(i,2:end) * ...
            fwd_mesh.kappa(fwd_mesh.elements(fwd_mesh.fine2coarse(i,1),:)));
        recon_mesh.region(i,1) = ...
            median(fwd_mesh.region(fwd_mesh.elements(fwd_mesh.fine2coarse(i,1),:)));
    elseif fwd_mesh.fine2coarse(i,1) == 0

```

```

dist = distance(fwd_mesh.nodes,...
    fwd_mesh.bndvtx,...
    [recon_mesh.nodes(i,1:2) 0]);
mindist = find(dist==min(dist));
mindist = mindist(1);
recon_mesh.mua(i,1) = fwd_mesh.mua(mindist);
recon_mesh.mus(i,1) = fwd_mesh.mus(mindist);
recon_mesh.kappa(i,1) = fwd_mesh.kappa(mindist);
recon_mesh.region(i,1) = fwd_mesh.region(mindist);
end
end

```

Forward Program

```

%%%forward simulation, given conc in a data file
function forward_chromo(fconc,fn1,patid,LR,plane,rep,fexcoeff,wv_array)
%%fconc is filename used to get chromophore conc and scatter: eg: fconc = 'heter',then HbO2 conc is
obtained from 'heter_hb1.paa' etc.
%%%patid, LR ('left' or 'right'), plane (0,1,2)and rep are used to generate filenames:
%%%eg: patid = 'heter', for 'left', plane 1 and rep 1, data is stored in
'heter_left_661nm_plane1_rep1.paa'
%%%fn1 is mesh name, fexcoeff is name of extinction coeff file, contains wvs in first coln; wv_array
contains wvs for data is to be generated
%%%hb1 is HbO2, hb2 is Hb, sa is scatt ampl, and sp is scatter power
%%%Final Vsn Subha 11/14/04

str1 = strcat(fconc,'_hb1.paa');
str2 = strcat(fconc,'_hb2.paa');
str3 = strcat(fconc,'_wat.paa');
fc = [str1;str2;str3];
clear str1 str2 str3;
fsa = strcat(fconc,'_sa.paa');
fsp = strcat(fconc,'_sp.paa');
nwn = length(wv_array);
%%%file names for data and meshes with optical pptyes
fdata_bg = strcat('pat',patid,'_',LR);
fdata_end = strcat('_plane',num2str(plane),'_rep',num2str(rep));

for i = 1:nwn
    fname(i,:) = strcat('circle_',fconc,'_',num2str(wv_array(i)));
    data_wv(i,:) = strcat(fdata_bg,'_',num2str(wv_array(i)),'nm',fdata_end,'.paa');
end

%%%loading concentrations, scatter power and scatter amplitude
mconc = load(fc(1,:));
conc(1:length(mconc),1) = load(fc(1,:));
conc((length(mconc) + 1): 2*length(mconc),1) = load(fc(2,:));
conc((2*length(mconc) + 1): 3*length(mconc),1) = load(fc(3,:));
sa = load(fsa);
sp = load(fsp);

```

```

wv_act = wv_array./1000;

%% calculating absorption coefficients
mesh1 = load_mesh(fn1);
ee = load(fexcoeff);
E = [];
for ww = 1:nwn
    jj = find (ee(:,1) == wv_array(ww));
    E = [E;ee(jj,2:end)];
end

for ii = 1:length(mesh1.nodes)
    mua_big(:,ii) = E*[conc(ii);conc(ii+length(mesh1.nodes));conc(ii+2*length(mesh1.nodes))];
end

%% saving in meshes
for ww = 1 : nwn
    mesh1 = load_mesh(fn1);
    mesh1.mua(:) = mua_big(ww,:);
    %mesh1.mua(:) = mua_big(((ww-1)*length(mesh1.nodes) + 1):ww*length(mesh1.nodes));
    mesh1.mus(:) = sa.*wv_act(ww).^(-sp);
    mesh1.kappa = 1./(3*(mesh1.mus + mesh1.mua));
    save_mesh(mesh1,fname(ww,:));
    [data] = femdata(fn1,100,mesh1);
    foo = data.paa;
    fstr = data_wv(ww,:);
    save (fstr, 'foo', '-ASCII');
    %wv_big = [wv_big; wv_act(ww)*ones(length(mesh1.nodes))];
end

```

Plotting Solution Images

```

function [hbt,oxysat,wat,sa,sp]=read_spectral_clinical(mesh1,patid,LR,plane,rep,it)
%% displays concentration images along with cross section

%subha 2/27/04
%% display for iteration specified or final iteration (give it = 0).

if (it==0)
    hbt_nim = strcat('pat',patid,'_',LR,'_hbT_plane',num2str(plane),'_rep',num2str(rep),'_final.dat');
    oxy_nim = strcat('pat',patid,'_',LR,'_StO_plane',num2str(plane),'_rep',num2str(rep),'_final.dat');
    wat_nim = strcat('pat',patid,'_',LR,'_wat_plane',num2str(plane),'_rep',num2str(rep),'_final.dat');
    sa_nim = strcat('pat',patid,'_',LR,'_SCa_plane',num2str(plane),'_rep',num2str(rep),'_final.dat');
    sp_nim = strcat('pat',patid,'_',LR,'_SCP_plane',num2str(plane),'_rep',num2str(rep),'_final.dat');
    hbt = load(hbt_nim);
    oxysat = load(oxy_nim);
    wat = load(wat_nim);
    sa = load(sa_nim);
    sp = load(sp_nim);

else
    conc_nim(1,:) = strcat('pat',patid,'_',LR,'_hb1_plane',num2str(plane),'_rep',num2str(rep),'_sol');

```

```

conc_nim(2,:) = strcat('pat',patid,'_',LR,'_hb2_plane',num2str(plane),'_rep',num2str(rep),'.sol');
conc_nim(3,:) = strcat('pat',patid,'_',LR,'_wat_plane',num2str(plane),'_rep',num2str(rep),'.sol');

```

```

hbt_nim = strcat('pat',patid,'_',LR,'_hbT_plane',num2str(plane),'_rep',num2str(rep),'.sol');
oxy_nim = strcat('pat',patid,'_',LR,'_StO_plane',num2str(plane),'_rep',num2str(rep),'.sol');
wat_nim = strcat('pat',patid,'_',LR,'_wat_plane',num2str(plane),'_rep',num2str(rep),'.sol');
sa_nim = strcat('pat',patid,'_',LR,'_SCa_plane',num2str(plane),'_rep',num2str(rep),'.sol');
sp_nim = strcat('pat',patid,'_',LR,'_SCP_plane',num2str(plane),'_rep',num2str(rep),'.sol');

```

```

%%HbO2
fid = fopen(hbt_nim,'r');
if(fid==-1)
    disp('file does not exist');
    break;
end
for i = 1 : 2*it-1
    fgetl(fid);
end
hbt = fscanf(fid,'%g',inf);
fclose(fid);
%%Hb
fid = fopen(oxy_nim,'r');
for i = 1 : 2*it-1
    fgetl(fid);
end
oxysat = fscanf(fid,'%g',inf);
fclose(fid);
%%H2O
fid = fopen(wat_nim,'r');
for i = 1 : 2*it-1
    fgetl(fid);
end
wat = fscanf(fid,'%g',inf);
fclose(fid);
%%sa
fid = fopen(sa_nim,'r');
for i = 1 : 2*it-1
    fgetl(fid);
end
sa = fscanf(fid,'%g',inf);
fclose(fid);
%%sp
fid = fopen(sp_nim,'r');
for i = 1 : 2*it-1
    fgetl(fid);
end
sp = fscanf(fid,'%g',inf);
fclose(fid);
end

```

```

%%display

```

```

%%%HbO2, Hb and water
% mesh1 = load_mesh(fn1);
if isempty(hbt)
    disp("That iteration does not exist");
elseif length(mesh1.nodes)~=length(hbt)
    disp("The mesh is not compatible with solution file");
else
    figure;
    for cc = 1:3
        %figure (8)
        subplot(2,3,cc);
        if (cc == 1)
            val = hbt;
            str = 'HbT';
        elseif (cc==2)
            val = oxysat;
            str = 'Oxy';
        else
            val = wat;
            str = 'Wat';
        end

        %istr = num2str(cc);
        trisurf(mesh1.elements,mesh1.nodes(:,1),mesh1.nodes(:,2),mesh1.nodes(:,3),val);
        view(2); shading interp; axis equal;colorbar('horiz');
        %str = input('enter title of figure...');
        title(str);axis off;colormap(gray)
        h = flipud(colormap);
        colormap(h);

        %clear str;

    end

%%% Scatter Ampl.
%figure (10);
subplot(2,3,4);
trisurf(mesh1.elements,mesh1.nodes(:,1),mesh1.nodes(:,2),mesh1.nodes(:,3),sa);
view(2); shading interp; axis equal;colorbar('horiz');
title('Scatt Ampl.');
```

```

axis off;colormap(gray)
    h = flipud(colormap);
    colormap(h);

%%% for scatter power
subplot(2,3,5);
trisurf(mesh1.elements,mesh1.nodes(:,1),mesh1.nodes(:,2),mesh1.nodes(:,3),sp);
view(2); shading interp; axis equal;colorbar('horiz');
title('Scatt Power');
```

```

axis off;colormap(gray)
    h = flipud(colormap);
    colormap(h);
end

```